Universitat Autònoma de Barcelona

Towards Improvement of Preclinical Glioblastoma Management: Detection, Therapy and Assessment of Response Using Magnetic Resonance Techniques

Nuria Arias Ramos

Towards Improvement of Preclinical Glioblastoma Management: Detection, Therapy and Assessment of Response Using Magnetic Resonance Techniques

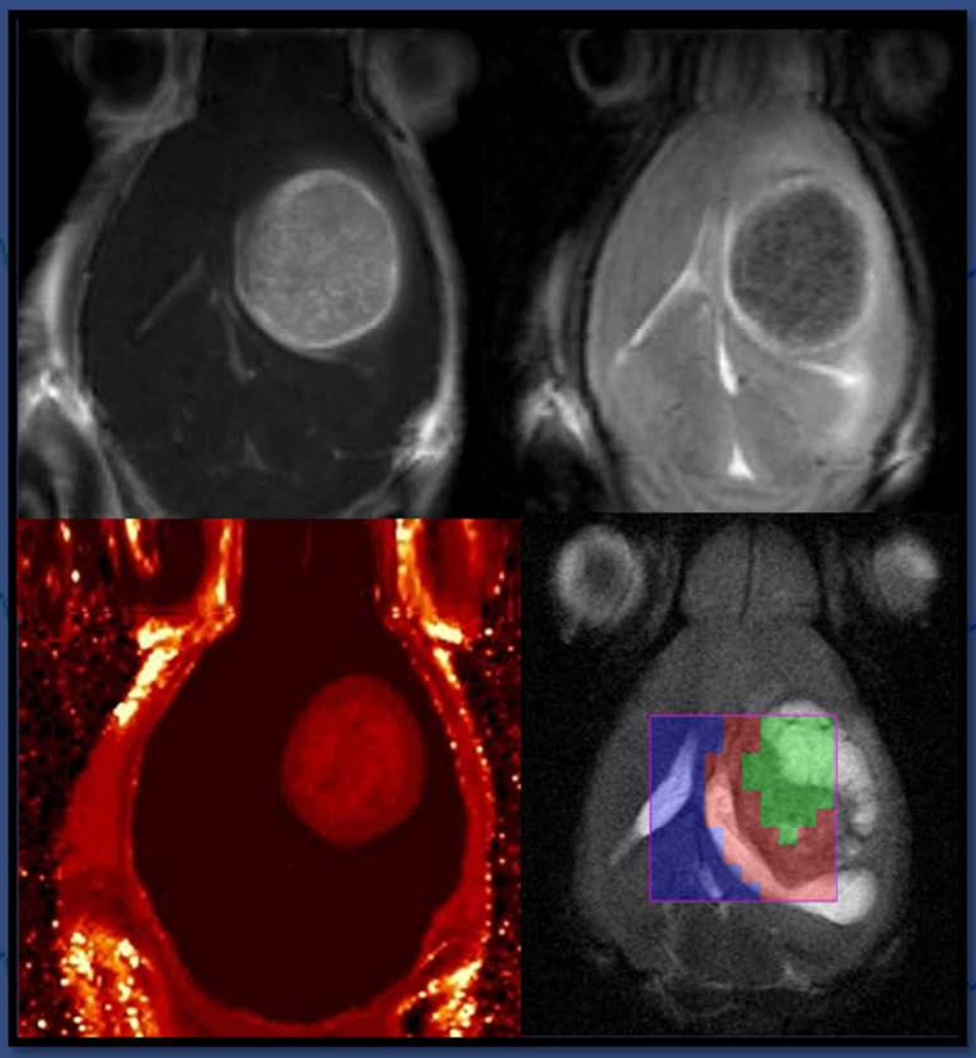

Nuria Arias Ramos

Ph.D. Thesis 2019

Universitat Autònoma de Barcelona

Universitat Autònoma de Barcelona

Departament de Bioquímica i Biologia Molecular

Towards Improvement of Preclinical Glioblastoma Management: Detection, Therapy and Assessment of Response Using Magnetic Resonance Techniques

Nuria Arias Ramos

PhD Thesis 2019

Dissertation presented by

Nuria Arias Ramos

Submitted for the PhD Degree in Biochemistry, Molecular Biology and Biomedicine at the

Universitat Autònoma de Barcelona

of the Doctoral Program in

Biochemistry, Molecular Biology and Biomedicine

Supervised by

Signature of the Supervisors

_____ _____

Prof. Carles Arús Caraltó **PhD Ana Paula Candiota**

Signature of the PhD Thesis Author

_____

Nuria Arias Ramos

Cerdanyola del Vallès, March 29th 2019

Table of contents

Index of Figures IX

Index of Tables XV

Abbreviations XVII

1. Introduction 1

1.1 Brain tumours 1

1.1.1 Epidemiology and classification 1

1.1.2 Grading and Incidence 2

1.1.3 Glioblastoma (GB) 4

1.1.4 Brain tumour diagnosis 5

1.1.5 Therapy for Glioblastoma 6

1.1.5.1 Surgical resection 6

1.1.5.2 Radiotherapy 6

1.1.5.3 Chemotherapy 7

Temozolomide 7

Other chemotherapeutic approaches 8

1.1.6 Role of the immune system in brain tumours 9

1.1.7 Brain tumour follow-up 11

1.1.8 Preclinical models of human glioma 13

1.1.9 The GL261 murine model 14

1.2 Nuclear Magnetic Resonance (NMR) 15

1.2.1 Biomedical applications of MR: Magnetic Resonance Imaging (MRI) and Magnetic Resonance Spectroscopy /Spectroscopic Imaging (MRS/MRSI) 15

1.2.1.1 Magnetic Resonance Imaging (MRI) 15

Relaxation times 16

T_1 relaxation 16

T_2 relaxation 16

Repetition time (TR) and echo time (TE) in image acquisition 17

Exogenous contrast agents 20

1.2.1.2 Magnetic Resonance Spectroscopy (MRS) 21

Chemical shift 21

1.2.1.3 Magnetic Resonance Spectroscopic Imaging (MRSI) 23

Brain tumour metabolites and their biological significance 24
1.3 Pattern recognition (PR) analysis 27
1.3.1 Supervised PR analysis 28
1.3.2 Unsupervised PR analysis 28
1.3.2.1 NMF (& Convex-NMF) methods 29
1.3.3 Semi-supervised PR analysis 29
1.3.1.2 Nosological imaging of the response to therapy 30
1.4 Nanoparticles and its potential to improve GB diagnosis and therapy 31
1.4.1 Nanoparticle characterization 32
1.4.2 Types of Nanoparticles 34
1.4.3 Hyperthermia for cancer therapy using Gold Nanoparticles 35
1.4.4 Nanoparticles as brain tumour contrast agents 36
1.4.5 Nanoparticle distribution – EPR and other effects 37
1.4.6 Nanoparticle toxicology 38
1.4.6.1 Endotoxin contamination 39
2. General Objectives 41
3. General materials and methods 42
3.1 Cell culture 42
3.1.2 Cell counting 42
3.2 Animal model 42
3.2.1 Wild type C57BL/6J mice 43
3.2.2 Generation of GL261 tumours by stereotactic injection of cells 43
3.2.3 Stereotactic injection of nanoparticles in mice 45
3.3 Tissue preservation for post-mortem procedures 45
3.4 Temozolomide therapy 45
3.5 *In vivo* MRI/MRSI 45
3.5.1 MRI acquisition for tumour volume calculations 46
3.5.2 MRSI acquisitions 46
3.6 MR data processing and post-processing 47
3.6.1 Tumour volume calculation from MRI acquisitions 47
3.6.2 MRSI data processing and postprocessing 47
3.7 Pattern recognition with source analysis and nosological imaging generation 48
3.7.1 Unsupervised source analysis 48
3.7.2 Semi-supervised source analysis 48

3.8 Statistical analysis 49

4. Study of Nanostructured coordination polymers with potential dual T_1/T_2 contrast enhancement properties: novel MR contrast agents 50

4.1 Specific objectives 50

4.2 Results originating from preliminary characterization of the nanoparticles performed by the *NanoSFun group* 50

4.2.1 Structure and synthesis 50

4.2.2 Particle size, stability, biocompatibility and *in vitro* MR properties 51

4.3 Specific materials and methods 52

4.3.1 *Ex vivo* postmortem contrast enhancement assessment 52

4.3.1.1 Animals and contrast injection procedures 52

4.3.1.2 MRI acquisitions 53

T_1 and T_2 weighted MRI 53

T_1 and T_2 maps 53

4.3.1.3 Ex vivo data processing and postprocessing 53

4.3.2 *In vivo* experiments 55

4.3.2.1 Tolerability studies 55

4.3.2.2 MRI in vivo contrast enhancement studies 56

DCE-T_{1w} MRI study using vehicle (PBS+MSA) 56

DCE-T_{1w} and T_{2w} MRI study with Gd-DTPA and Fe-NCP 56

4.3.2.3 Data processing and postprocessing 57

4.3.3. Animal euthanasia and organ storage 57

4.4 Results and discussion 57

4.4.1 *Ex vivo* experiments 57

4.4.2 *In vivo* experiments 61

4.4.2.1 Tolerability experiments 61

4.4.2.2 MRI experiments 62

Alternated T_1-T_{2w} images with Gd-DTPA (0.4 mmol Gd/kg) and Fe-NCP (0.4mmol Fe/kg) studies 62

T_{1w} DCE-MRI with vehicle injection 67

4.5 Discussion 68

4.6 Conclusions 71

5. Optimization of a MRSI multi-slice protocol for volumetric analysis of mouse brain tumour 72

5.1 Specific objectives 72

5.2 Specific material and methods 72

5.2.1 Initial set up of MRSI grid size and position with wt mice 72
5.2.1.1 MRSI grid size: 10 x10 vs 12 x 12 72
5.2.2 Combination of MRSI grid size and position in tumour-bearing mice 73
5.2.3 Spectral quality assessment of MRSI grids 74
Signal to noise ratio 74
Spectral pattern inspection and presence of artefacts 75
5.3 Results and discussion 75
5.3.1 Assessment of Spectral Quality in MRSI grids of wt mice. 75
5.3.1.1 Consecutive grids with the same matrix size (10x10) 75
SNR, mean spectra and artifact analysis 75
Unsupervised source analysis 78
5.3.1.2 Consecutive grids with different matrix size (10x10 and 12x12) 80
SNR, mean spectra and artefact analysis 80
Unsupervised source analysis 82
5.3.2 Preliminary experiments with GL261 tumour-bearing mice. Assessment of Spectral Quality 84
5.3.2.1 SNR, mean spectra and artifact analysis 84
5.3.2.2 Unsupervised source analysis 89
5.3.2.3 Semi-supervised source analysis 91
5.4 General discussion for this section 94
5.4.1 Acquisition of MRSI multi-slice grids in wt and GL261 tumour-bearing mice 94
5.4.1.1 SNR results 94
SNR from edges and centre of the grids 94
Studies with wt mice 94
Studies with GL261 tumour-bearing animals 95
Comparisons between multi-slice and single-slice MRSI results from previous studies 96
5.4.1.2 Presence of artefacts 97
5.4.1.3 Semi-supervised analysis 98
5.5 Conclusions 99
6. Unraveling therapy response heterogeneity in preclinical GL261 tumour-bearing mice with a multi-slice MRSI approach 101
6.1 Specific objectives 101
6.2 Specific material and methods 101
6.2.1 Animals 101

6.2.2 Animal treatment with Temozolomide 102
6.2.3 In vivo MRI and MRSI studies and nosological images generation 102
6.2.4 Tumour Responding Index (TRI) calculations 103
6.2.5 Animal euthanasia and sample storage 104
6.2.6 Histopathology studies 104
6.2.7 Volumetric representation of the multi-slice nosological images 105
6.3 Results 105
6.3.1 MRSI Multi-slice protocol applied to TMZ-treated GL261 tumour-bearing mice 105
6.3.1.1 Group A: Cases starting therapy at day 11 p.i.: inclusion into different groups of response level 106
TRI and nosological images evolution vs tumour volume evolution 108
6.3.1.2 Group B: Therapy response in cases starting therapy with tumour volume 2.5-5.5 mm^3: Finding high response (HR) cases 113
6.3.2 Metabolic Pattern Contributing to Responding and Non-Responding (Red and Green) Areas Detected in MRSI Studies of the Investigated Mice 115
6.3.3 Histopathology validation 118
6.3.3.1 Haematoxylin/Eosin morphology analysis 118
6.3.3.2 Ki67 analysis 120
Comparison of responding and non-responding zones 120
6.3.4 TRI calculation in retrospective TMZ-treated mice: 123
6.3.5 Preliminary volumetric-rendering of nosological data 126
6.4 General discussion for this section 127
6.4.1 Multi-slice MRSI and TRI for therapy response level evaluation 127
6.4.2 Classification of TMZ-treated mice after TRI calculation and evolution of TRI values 128
6.4.3 Histopathology results 131
6.4.4 A possible explanation for the oscillatory TRI behaviour: TMZ therapy triggering immune response in host 135
6.5 Conclusions 139
7. Development of a system for Hyperthermia with Gold nanoparticles for preclinical GB therapy 141
7.1 Specific objectives 141
7.2 Specific materials and methods 141
7.2.1 Preliminary studies: performed before the starting of this thesis 141
7.2.1.1 Nanoparticles studied 141

7.2.1.2 Set up of NIR (808 nm) laser device for irradiation inside the MR scanner..... 142
7.2.1.3 In vitro and in vivo temperature measurement by MRS (I) 143
7.2.1.4 Hyperthermia experiments in vitro..... 144
Laser irradiation protocol and temperature control..... 144
Phantom irradiation (preliminary studies)..... 144
Temperature evolution of a HGNPs phantom along an irradiation experiment .. 145
7.2.1.5 Hyperthermia experiments ex vivo..... 145
Laser irradiation protocol and temperature follow-up during the *ex vivo* experiment 145
7.2.1.6 Hyperthermia experiments in vivo..... 146
7.2.1.6.1 Continuous laser irradiation – single laser power..... 146
wt mice - normothermia 146
7.2.1.6.2 Continuous laser irradiation – varying laser powers..... 147
wt mice - mild hypothermia 147
GL261 tumour-bearing mice - mild hypothermia - HGNP injection..... 147
wt and GL261 tumour-bearing mice - normothermia - stepwise power increase approach..... 147
7.2.1.6.3 Pulsed laser protocol..... 148
wt mice -normothermia 148
7.2.1.6.4 Specific hyperthermia studies using Nanorods (Batch 3) 148
wt mice – stereotactic injection 149
Preliminary studies with GL261 tumour-bearing mice – i.v. injection..... 149
Tolerability assessment in wt mice 149
Hyperthermia experiment after i.v. injection 149
MRSI temperature maps and temperature control during pulsed laser protocol 149
7.2.2 Studies performed in this thesis..... 149
7.2.2.1 Endotoxin assay of PEGylated HGNPs (Batch 4) 149
7.2.2.2 Confocal microscopy studies: nanoparticle internalization 150
GL261 cells exposed to PEG-HGNPs..... 150
7.2.2.3 Influence of PEG-HGNPs in GL261 cell viability..... 150
7.2.2.4 PEG-HGNPs in vivo tolerability studies 151
7.2.2.4.1 Dose calculation 151
7.2.2.4.2 Dose fractioning and protocol design 151
7.3 Results and discussion..... 151
7.3.1 Preliminary set-up of protocols and choosing the best NP..... 151

7.3.1.1 In vitro studies: which was the most promising NP for in vivo use? 151
7.3.1.2 Ex vivo studies with non-PEGylated HGNPs (Batch 1) 153
7.3.1.3 In vivo experiments: choosing laser protocol and power; checking for differential heating 154
7.3.1.3.1 Studies with continuous laser irradiation using different laser powers in mild hypothermia 155
Tumour-bearing mice with i.v. injection of non-pegylated HGNPs (Batch 1) 155
7.3.1.3.2 Sequential increase of laser powers in normothermia 157
wt and GL261 tumour-bearing animals without HGNPs injection 157
7.3.1.3.3 Hyperthermia experiments using PEGylated NPs with stepwise power increase approach 158
Stereotactic injection of PEG-HGNPs (Batch 2) in wt mice 158
7.3.1.3.4 Pulsed laser protocol in normothermia: pursuing better temperature stabilization 160
7.3.1.3.5 Application of pulsed laser protocol to wt mice injected with PEGylated Nanorods (Batch 3) 162
Stereotactic injection and PEG signal detection 162
Intravenous injection of NRs in GL261 mice 162
Tolerability experiment using Nanorods 163
Hyperthermia experiment with NRs in a GL261 tumour-bearing mouse 163
MRSI temperature maps in a GL261 mouse administered with NRs: 165
7.3.2 Experiments performed during this thesis: PEG-HGNPs 167
7.3.2.1 Studies with the new batch of HGNPs (PEG-HGNPs) (Batch 4) 167
7.3.2.1.1 Confocal microscopy results 167
Assessment of PEG-HGNPs internalization by GL261 cells at different cell-culture time points 167
7.3.2.1.2 Effects of PEG-HGNPs over GL261 viability after addition 169
7.3.2.2 Tolerability studies of PEG-HGNPs in C57BL/6J mice 170
7.3.2.2.1 Endotoxin assay 171
7.3.2.3 Security issues in hyperthermia studies: lessons learned 172
7.3.2.3.1 Implementation of safety measures for hyperthermia studies 173
Use of extra temperature sensors 173
Use of air as anaesthesia carrier instead of oxygen during MR experiments 173
7.4 General discussion for this section 176
7.4.1 NIR hyperthermia inside the MR scanner: Real time temperature monitoring and animal irradiation conditions 176

7.4.2 Effect of the studied Nanoparticles in brain and tumour heating 178

7.4.3 Characterization of a new batch of PEG-HGNPs (batch 3): NP stability, cell uptake and *in vivo* tolerability studies 180

7.4.4 Safety actions for future hyperthermia studies 181

7.5 Conclusions 182

8. General Discussion 184

8.1 Studies with novel dual contrast agents 185

8.2 Non-invasive assessment of therapy response: what are we sampling? 186

8.3 Hyperthermia generation for GB: lessons learned 189

8.4 Interweaving of different issues studied in this thesis 191

9. General Conclusions 193

10. References 195

11. ANNEXES 218

Index of Figures

Figure 1.1: Incidence age-standardised rate (ASR) of brain and central nervous system tumours per 100,000 inhabitants in both sexes worldwide estimated by the GLOBOCAN report. 1

Figure 1.2: Distribution of Primary Brain and CNS Tumours by behaviour (malignant vs benign) and distribution of malignant primary brain and CNS tumours by histology subtypes. 3

Figure 1.3: Common progenitor cells are thought to produce neuronal and glial progenitors that eventually differentiate into mature neurons, astrocytes and oligodendrocytes. 4

Figure 1.4: TMZ activation and resistance pathways scheme. 8

Figure 1.5: Scheme of the cycle for immune response against a tumour. 10

Figure 1.6: Human GB therapy and follow-up current scheme. 12

Figure 1.7: Preclinical cancer model scheme. 13

Figure 1.8: T_1 relaxation time constant. 16

Figure 1.9: T_2 relaxation time constant. 17

Figure 1.10: Scheme of the parameters TR and TE. 18

Figure 1.11: Different image contrast obtained with combination of short or long TR and short or long TE values. 19

Figure 1.12: T_{2w} image and T_{1w} image after contrast agent administration of a human GB. 20

Figure 1.13: Example of a single voxel spectrum of a healthy human brain. 22

Figure 1.14: Spectral patterns of GL261 tumours at TE= 12 ms and TE= 136 ms obtained from MRS explorations of C57BL/6J tumour bearing mice. 23

Figure 1.15: MRSI acquisition from a mouse bearing a GL261 tumour *in vivo* at 7T. 24

Figure 1.16: Main differences between the responsive (green) and unresponsive (red) spectral patterns of GL261 GB and their peak assignments. 26

Figure 1.17: Decomposition of the data matrix V in two matrix components, the matrix of sources or data basis W and the mixing matrix H. The product of the matrix W and H provides a good approximation to the original data matrix (V). 29

Figure 1.18: Examples of nosological semi-supervised maps corresponding to mice C971 (GL261 GB responding to TMZ) and C1111 (control GL261 GB) 31

Figure 1.19: Figure showing the EDL on a negatively charged particle. 33

Figure 1.20: Representative examples of nanoparticles frequently used for diagnosis and therapy of gliomas and their relative sizes. 34

Figure 1.21: Mechanisms of transportation of multifunctional nanoparticles into a brain tumour. 38

Figure 3.1: Scheme for marking mice by ear punching. 43

Figure 3.2: An anaesthetized C57BL/6J mouse immobilized in a stereotactic holder. 44

Figure 3.3: TMZ administration schema with 3 therapy cycles with a 3-day interleave. 45

Figure 3.4: Scheme of the volume measurement carried out in mice. 47

Figure 4.1: Basic structure of the nanoparticles studied in this section (reproduced with permission of providers). 51

Figure 4.2: T_1 weighted MRI and T_2 weighted MRI after stereotactic injection of CA Fe-NCP and examples of ROIs drawn for *ex vivo* postmortem RCE studies and postprocessing of T_{1w} and T_{2w} MRI with an algebra algorithm of imaging division. 55

Figure 4.3: MRI acquisition scheme used in the experiment with i.v. injection of 0.4 mmol/kg of Gd-DTPA and 0.4 mmol/kg of Fe-NCP. 57

Figure 4.4: Postprocessing of T_{1w} and T_{2w} MRI with an algebra algorithm of imaging division (T_{1w}MRI/T_{2w}MRI), to highlight double enhancement potential in the studied CA..... 59

Figure 4.5: Percentage of body weight variation of animals injected with Fe-NCP, animals injected with vehicle and body weight variation data from *The Jackson laboratory body weight chart for C57BL/6J mice*. 61

Figure 4.6: A. Mean kinetics of RCE T_{1w} images in 3 GL261 mice, during 30 minutes after intravenous injection of a dose of 0.4 mmol/kg of Gd-DTPA and after intravenous injection of a dose of 0.4 mmol/kg of Fe-NCP. **B.** Mean kinetics of RCE T_{1w} images in the same mice, during 30 minutes, 2 hours and 24 hours after intravenous injection of a dose of 0.4 mmol/kg of Gd-DTPA and after intravenous injection of a dose of 0.4 mmol/kg of Fe-NCP. 63

Figure 4.7: A. Mean kinetics of RCE T_{2w} images in 3 GL261 mice, during 30 minutes after intravenous injection of a dose of 0.4 mmol/kg of Gd-DTPA and after intravenous injection of a dose of 0.4 mmol/kg of Fe-NCP. **B.** Mean kinetics of RCE T_{1w} images in the same mice, during 30 minutes 2 hours and 24 hours after intravenous injection of a dose of 0.4 mmol/kg of Gd-DTPA and after intravenous injection of a dose of 0.4 mmol/kg of CPP-Fe. 66

Figure 4.8: T_{1w} and T_{2w} images acquired before Fe-NCP injection and 24 hours after injection in the 3 studied animals. 66

Figure 4.9: Example of a case (C1209) studied with i.v. injection of 0.4 mmol/kg of Gd-DTPA and 24 hours later, with i.v. injection of Fe-NCP for T_1 and T_2 contrast. 67

Figure 4.10: Mean of T_1 RCE from T_{1w} images in 3 GL261 mice, during 60 minutes after intravenous injection of vehicle (PBS+MSA). 68

Figure 5.1: Different views of T_{2w} images from a wt mouse with consecutive MRSI grid positions. 73

Figure 5.2: T_{2w} MRI of mouse C894 brain, with the position of the four MRSI slices in sagittal and coronal planes. 74

Figure 5.3: Schemes of MRSI grids of 10x10 voxels dimension and 12x12 voxels dimension. The blue area was considered the edge and the orange area was considered the centre of the grids. The yellow area corresponds to the tumour injection point and the green area indicates the normal brain parenchyma region in a GL261 tumour-bearing animal..... 74

Figure 5.4: SNR maps calculated for each MRSI grid tested in this multi-slice experiment, superimposed to the T_{2w} images. The grids dimension was 10x10. 76

Figure 5.5: Mean spectra calculated in area corresponding to usual tumour injection point (yellow) and normal brain (green) areas selected in MRSI grids for this multi-slice experiment. The grids dimension was 10x10..... 77

Figure 5.6: Results of the unsupervised analysis of the three grids of the 10x10-combination matrix 79

Figure 5.7: SNR maps calculated for each MRSI grid tested in this multi-slice experiment using different dimensions, superimposed to the T_{2w} images. (Grid 1 with 10x10 voxels, Grid 2 with 12x12 voxels and Grid 3 with 10x10 voxels). 80

Figure 5.8: Mean spectra calculated in area corresponding to tumour injection point (yellow) and normal brain (green) areas selected in MRSI grids for this multi-slice experiment. (Grid 1 with 10x10 voxels, Grid 2 with 12x12 voxels and Grid 3 with 10x10 voxels)..... 81

Figure 5.9: Results of the unsupervised analysis of the three grids of the 10x10 and 12x12 combination matrixes. 83

Figure 5.10: SNR maps calculated for each MRSI grid tested in this multi-slice experiment, superimposed to the T2w images in the representative case C894. 85

Figure 5.11: Mean spectra calculated for case C894 from tumour area (yellow) and contralateral area (green) in the four grids. 88

Figure 5.12: Calculated sources, intensity maps of each source and nosological images obtained from an unsupervised analysis for case C894, superimposed to the corresponding T_{2w} image. 90

Figure 5.13: Nosological images obtained from semisupervised source analysis for case C894, superimposed to the correspondent T_{2w} images. 93

Figure 5.14: Calculated sources, intensity maps of the sources and nosological images obtained from an unsupervised analysis superimposed to the corresponding T_{2w} image in the case C583 (untreated tumour-bearing mice studied with single-slice MRSI approach) from [117]. 98

Figure 6.1: Coronal T_{2w} MRI of mouse C971 brain, with the position of the four MRSI slices. 102

Figure 6.2: Mean tumour volume evolution of different cases studied in this thesis and previous work from the GABRMN group. 107

Figure 6.3: Mean evolution of body weight of mice studied by multi-slice MRSI. 108

Figure 6.4: Graphical representation of the tumour volume evolution and the percentage of responding “green” pixels obtained after application of source analysis to MRSI data acquired in the multislice sets for IR cases C971 and C1022; and LR cases C979 and C981. 110

Figure 6.5: Graphical representation of the tumour volume evolution and the percentage of responding “green” pixels obtained after source analysis of MRSI data acquired in the multi-slice set for case C974 (IR case)..... 112

Figure 6.6: Tumour volume evolution (in mm3, black line) of untreated, control cases (C1109, C1110, C1111 and C1112). 113

Figure 6.7: Graphical representation of the tumour volume evolution and the percentage of responding "green" pixels obtained after source analysis of MRSI data acquired in the multi-slice set of HR cases (C1100 and C1108). 115

Figure 6.8: Example of mean spectra extracted from the MRSI grid of a treated case (HR case C971: Grid 1, day 34 pi). 117

Figure 6.9: Ki67 immunostainings (40x magnification) in histological areas corresponding to red or green regions in nosological images, from different grids of the control case C1110, the LR case C979, the IR case C971 and the HR case C1108. 119

Figure 6.10: Graph bar of mean of Ki67% values found in green and red areas from nosological images of all studied cases. 120

Figure 6.11: Example of the histopathological validation of a nosological image of Grid 2 of the case C1022 (IR case). 121

Figure 6.12: Graph bars representing global Ki67% values (mean ± SD). 122

Figure 6.13: Boxplot of global percentage of Ki67 (white boxes) and percentage of TRI values (striped boxes) of each MRSI grid of different groups of cases classified by TRI response and analyzed by histopathology 123

Figure 6.14: Evolution of tumour volume and evolution of TRI along time in the retrospective case C817 125

Figure 6.15: Volumetric 3D representation of nosological images obtained from case C971 at day 34 p.i. 127

Figure 6.16: Boxplot of global number of Ki67 positive cells/mm^2 of different groups of cases classified by TRI response 132

Figure 6.17: Boxplot of volume of Ki67 positive cells in each TRI group and representation of percentage of acellular spaces observed in different TRI groups. 133

Figure 6.18: Histopathological regions (20x magnification) from representative fields of control, LR, IR and HR cases. 134

Figure 6.19: Scheme of the cycle for immune response against a brain tumour. 136

Figure 7.1: Hyperthermia laser set-up (continuous and pulsed modes). 143

Figure 7.2: Design of a continuous NIR laser irradiation protocol for NP-phantom studies. ... 145

Figure 7.3: Example of voxel position in SV MRS hyperthermia experiments in a GL261-bearing mouse and a wt mouse. 146

Figure 7.4: Scheme of a preliminary experiment with GL261 tumour-bearing mice using continuous NIR laser irradiation with different laser powers. 147

Figure 7.5: Design of pulsed protocol for laser increasing power applied to wt mice. Percentages indicate the percentage of duty cycle used in each step. 148

Figure 7.6: Temperature curve increase (measured by SV MRS) obtained with a 5 ml phantom with non-PEGylated HGNPs after continuous laser exposition at 1.3 W. 153

Figure 7.7: Temperature curves evolution (measured by SV MRS) (mean±SD) of injection area and contralateral area in *ex vivo* brain HGNPs or PBS injections. 154

Figure 7.8: Mean temperature increase curves measured by SV MRS for two GL261 tumour-bearing mice (C742 and C743) irradiated after one injection of non-PEGylated HGNPs. Laser power was 0.07W and 0.28W in continuous laser protocol. 156

Figure 7.9: Mean temperature increase curves (measured by SV MRS) for two GL261 tumour-bearing mice (C744 and C745) irradiated after 2 injections of HGNPs; 0.07W and 0.28W laser irradiation in continuous laser protocol. 157

Figure 7.10: Evolution of brain temperature increase (mean ± SD) in animals irradiated by continuous laser irradiation combining 3 laser powers in the same irradiation: 0.07; 0.14 and 0.21W in control wt and GL261 mice. 158

Figure 7.11: Evolution of brain temperature increase in mice brain of two wt animals (wt35 and wt36) after stereotactically injection of PEG-HGNPs in the brain with a dose of 20 mg Au/kg. 159

Figure 7.12: Example of SV spectra (TE=136 ms) acquired *in vivo* from the brain parenchyma of control mice injected stereotactically with 20 mg Au/Kg of PEG-HGNPs (**A**: wt 35. **B**: wt 36). PEG resonance peak at 3.71 ppm was observed in both spectra. 160

Figure 7.13: Temperature evolution (mean±SD) in 3 wt animals irradiated with a pulsed laser protocol. 161

Figure 7.14: Temperature evolution (mean±SD) in the animals studied by continuous laser protocol irradiation: 3 wt animals, 3 GL261 tumour-bearing mice and in the 3 wt animals studied by pulsed laser irradiation protocol. 161

Figure 7.15: SV MRS (TE=136 ms) spectra acquired *in vivo* from brain parenchyma in control wt mice injected stereotactically with 20 mg Au/Kg of Nanorods. PEG resonance signal at 3.71 ppm was clearly observed in the three recorded spectra. 162

Figure 7.16: Evolution of percentage weight variation (mean±SD) of animals i.v. injected with a single dose of Nanorods, 10 mg Au/kg and animals injected with a single dose of 20 mg Au/kg. 163

Figure 7.17: Temperature evolution of the brain and body temperature of the animal C787 after i.v injection of 20 mg Au/kg of Nanorods followed by pulsed laser irradiation. 164

Figure 7.18: **A.** SV spectrum (TE= 136 ms) of the animal wt35, injected sterotactically with a dose of 20 mg Au/kg of PEG-HGNPs. **B.** Mean spectra of all the SV acquisitions (TE= 136 ms) during the hyperthermia experiment of the mouse C787, injected i.v. with a dose of 20 mg Au/Kg of NRs. **C.** Mean spectra of all the SV acquisitions (TE= 136 ms) during the hyperthermia experiment of the mouse C749 which was not injected with nanoparticles. 164

Figure 7.19: Temperature evolution registered during the pulsed laser protocol in mouse C789, 72 hours after being injected with 2 sequential doses of 10 mg Au/kg of NRs. 165

Figure 7.20: Temperature maps acquired in normothermia and post-laser irradiation of the GL261 tumour-bearing mouse C789 administered with 2 sequential doses of 10mg Au/kg of NRs. 166

Figure 7.21: Confocal microscopy studies of internalization of PEG-HGNPs by GL261 cells: First row corresponds to GL261 cells without nanoparticles and the second row corresponds to GL261 cells with prior nanoparticles addition. First column indicates fields acquired 24 hours after cell seeding and/or nanoparticle addition, the second column correspond to 48 hours later and the third column to 72 hours after cell seeding and/or nanoparticle addition. 168

Figure 7.22: Percentage of body weight variation (mean±SD) of mice injected with 12 injections of 33.8 mg Au/kg PEG-HGNPs. 171

Figure 7.23: C57BL/6J mouse after hair depilation in legs and abdomen and the plethysmogram from pulseoximeter measurements: pO2 display while breathing oxygen (100%) and the waveform signal which indicates the cardiac cycle. 175

Figure 7.24: Evolution of pO2 and temperature of a GL261-bearing mouse along experimental time and while breathing oxygen or air in hyporthermia conditions and normothermia conditions. 176

Index of Tables

Table 1.1: Signal intensities of different tissues on T_1 and T_2-weighted images..... 19

Table 1.2: Resonance assignments corresponding to each metabolite resonances that can be found in human brain *in vivo* 1H spectra at 1.5T in human brain..... 27

Table 1.3: NPs stability according to ZP values..... 33

Table 4.1: List of CAs studied in this chapter. 52

Table 4.2: Increasing doses of NCP injected in mice in different days 55

Table 4.3: RCE% calculated (mean±SD) in T_{1w} and T_{2w} *ex vivo postmortem* MRI, as well as RCE%T_{1w}/RCE%T_{2w} ratio. 58

Table 4.4: Relaxation times calculated from T_1 and T_2 map acquisitions and "fold change" values. 60

Table 4.5: Mean ± SD for RCE calculated in T_{1w} and T_{2w} *in vivo* MRI studies for Gd-DTPA, Fe-NCP and vehicle. 64

Table 5.1: Acquisition parameters of different MRSI grids used in the set-up experiments for the multi-slice protocol. 72

Table 5.2: SNR data from the grids of the multi-slice combination of 10x10 voxels: Percentage of voxels with SNR<10, SNR of the edges and centre of the grids 76

Table 5.3: SNR data from the grids of the multi-slice combination of 10x10 and 12x12 voxels: Percentage of voxels with SNR<10, SNR of the edges and centre of the grids..... 80

Table 5.4: SNR data from edges and centre voxels of the grids of tumour-bearing mice, as well as SNR from tumour and normal brain parenchyma zones. 86

Table 5.5: Assignment of the predominant tissue pattern contributing to each source calculated in the unsupervised analysis of case C894. 91

Table 5.6: SNR data from edges, centre, tumour and normal parenchyma voxels and percentage of voxels with SNR<10 of 6 previous cases studied with MRSI single-slice from GABRMN compared to the 3 mice studied using the MRSI multi-slice approach in this thesis. 97

Table 6.1: Data summary of tumour volume the day before starting therapy administration and the day in which euthanasia was carried out. Classification with RECIST and TRI criteria the day of euthanasia. 106

Table 6.2: List of the main metabolites contributing to the spectral pattern recorded in tumour/peritumoural MRSI of responding and non-responding mice, with the corresponding approximate ppm position..... 116

Table 6.3: Results of Ki67 percentage ±SD of fields corresponding to green and red pixels in nosological images, as well as the global percentage of Ki67 for the studied cases. Percentage of TRI and its classification by TRI criteria are also shown. 122

Table 7.1: Different groups of animals injected with non-pegylated HGNPs *ex vivo*. 145

Table 7.2: Temperatures obtained with the different NP phantoms in *in vitro* hyperthermia studies. 152

Table 7.3: Results obtained with cell counting and viability assessment of control and GL261 cells with PEG-HGNPs. 169

Abbreviations

3DiCSI	3D interactive chemical shift imaging
AICD	Activation-Induced Cell Death
Ala	Alanine
APC	Antigen presenting cell
ASR	Incidence age-standardised rate
B_0	Main magnetic field
BBB	Blood-brain barrier
BCNU	bis-chloroethylnitrosourea (carmustine)
BER	Base Excision Repair
Bix	1,4-bis(imidazol-1-ylmethyl)benzene
BSA	Bovine serum albumin
CA	Contrast agent
CBTRUS	Central Brain Tumour Registry of the United States
Cho	Choline
CNI	Choline-NAA index
CNS	Central Nervous System
CNTs	Carbon nanotubes
Contra	Contralateral
CPA	Cyclophosphamide
Cr	Creatine
CSC	Cancer stem cells
CT	Computed Tomography
CTAB	Cetyltrimethylammonium Bromide
CTLs	Cytotoxic T lymphocytes

DCE	Dynamic contrast enhancement
DCs	Dendritic cells
DLS	Dynamic light scattering
DMPM	Dynamic MRSI processing Module
DMSO	Dimethyl sulfoxide
DSBs	Double strand breaks
DWI	Diffusion Weighted Imaging
EDL	Electric double layer
EGF	Endothelial growth factor
EGFR	Endothelial growth factor receptor
EPR	Enhanced permeability and retention effect
ETL	Echo train length
EU	Endotoxin units
f_0	Scalar Larmor frequency
FASL	FAS ligand
FDA	US Food and Drug Administration
FI	Fisher Information
FID	Free induction decay
FOV	Field of view
fps	frames per second
GB	Glioblastoma
Gd^{3+}	Gadolinium
Gd-DTPA	Gadopentetate dimeglumine
GEM	Genetically engineered mouse
GIC	Glioma-initiating cells
Glx	Glutamine and glutamate

Gly	Glycine
Gy	Gray
HE	Hematoxylin-eosin
HGNPs	Hollow Gold Nanospheres
HR	High response
ICMAB	*Institut de Ciència de Materials de Barcelona*
ICP	Inductively coupled plasma mass spectrometry
IDH	Isocitrate Dehydrogenase
INA	*Instituto de Nanociencia de Aragón*
Inter-ST	Inter-slice thickness
Ipsi	Ipsilateral
IQR	Interquartile range
IR	Intermediate response
ISA	Image sequence analysis
Lac	Lactate
LAL	*Limulus amoebocyte* lysate
LD 50	Lethal dose 50%
LDA	Linear Discriminant Analysis
LN	Lymph nodes
LR	Low response
MGMT	O6-meG-DNA methyltransferase
MHC	Major Histocompatibility Complex
MHz	Megahertz
mI + Gly	Myo-inositol + Glycine
mI	Myoinositol

ML	Mobile Lipids
MLP	Multi-Layer Perceptron
MM	Macromolecules
MMR	Mismatch repair
MnDPDP	Mangafodipir trisodium
MPIOs	Magnetic iron oxide nanoparticles
MR	Magnetic Resonance
MRI	Magnetic Resonance Imaging
MRS	Magnetic Resonance Spectroscopy
MRSI	Magnetic Resonance Spectroscopy Imaging
MSA	Mouse Serum Albumin
MSME	Multi-Slice Multiecho
MTD	Maximum tolerated dose
MTIC	Methyl-triazeno imidazole-carboxamide
MTX	Matrix size
M_z	Net magnetization
N3- meA	N^3-methyl-adenine
N7-MeG	N^7-methyl-guanine
NA	Number of averages
NAA	N-acetyl-aspartate
NAc	N-acetyl group containing compounds
NCPs	Nanostructured coordination particles
NIR	Near Infrared Radiation
NK	Natural killer cells
NMF	Non-negative matrix factorization
NMR	Nuclear Magnetic Resonance

NPs	Nanoparticles
NRs	Gold Nanorods
NS	Number of slices
NTA	Nanoparticle Tracking Analysis
O6-meG	O6-methyl-guanine
ODG	Oligodendroglioma
p.i.	Post-inoculation
PAMPs	Pathogen-associated molecular patterns
PBS	Phosphate-buffered saline
PCA	Principal Component Analysis
PEG	Polyethyleneglycol
PEG-HGNPs	Pegylated Hollow Gold Nanospheres
PEG-NRs	Pegylated Nanorods
PE-MRSI	Perturbation-enhanced MRSI
PET	Positron Emission Tomography
ppm	parts per million
PR	Pattern recognition
PRESS	Pointed-resolved spectroscopy
PTEN	Phosphatase and Tensin homolog
PUFA	Polyunsaturated fatty acids
RANO	Response assessment in neuro-oncology
RARE	Rapid acquisition with relaxation enhancement
RCE	Relative contrast enhancement
RECIST	Response Evaluation Criteria in Solid Tumours
RES	Reticuloendothelial system

RF	Radiofrequency
RGB	Red-Green-Blue colour moldel
Rh	Hydrodynamic radius
ROIs	Regions of interest
ROS	Reactive oxygen species
RPMI	*Roswell Park Memorial Institute*
SCID	Severe combined immunodeficiency
SEM	Scanning Electron Microscopy
SNR	Signal to noise ratio
SPIO	Superparamagnetic iron oxide nanoparticles
SPR	Surface plasmon resonance
spv	Spectral vector
SSBs	Single-strand breaks
ST	Slice thickness
STEAM	Stimulated echo acquisition mode
SV	Single voxel
SVZ	Subventricular zone
SW	Spectral width
T	Tesla
T_{1w}	T1 weighted image
T_{2w}	T2 weighted image
TAT	Total acquisition time
Tau	Taurine
TCR	T-cell receptor
TE	Echo time
TE_{eff}	Effective echo time

TEM	Transmission electron microscopy
TF	Fourier Transform
TGF-β	Transforming growth factor beta
TMS	Tetramethylsilane
TMZ	Temozolomide
TR	Repetition time
Treg	T regulatory Lymphocyte
TRI	Tumour responding index
TV	Tumour volume
UL	Unit length
VAPOR	Variable Pulse Power and Optimized Relaxation Delays
VEGF	Vascular endothelial growth factor
VOI	Volume of interest
WHO	World Health Organization
wt	Wild type
YPLL	Years of Potential Life Lost
ZP	Zeta potential
γ_0	Gyromagnetic ratio
δ	Chemical shift

1. Introduction

1.1 Brain tumours

1.1.1 Epidemiology and classification

From all the cancer cases diagnosed each year in the world, less than 2% correspond to Central Nervous System (CNS) tumours, which are responsible for a mortality rate of 2.3% of all cancer patients [1]. However, this scenario changes when considering children or young adults, for whom higher mortality values can be observed [2].

Incidence rates of CNS tumours in 2012 (GLOBOCAN-IARC data available online [1]) were lower in less developed countries (3 per 100,000) than in more developed countries (5.1 per 100,000) (Figure 1.1). This lower incidence in less developed countries is probably related to the limited access to diagnostic techniques currently used to identify and follow up these tumours, with low availability in these countries.

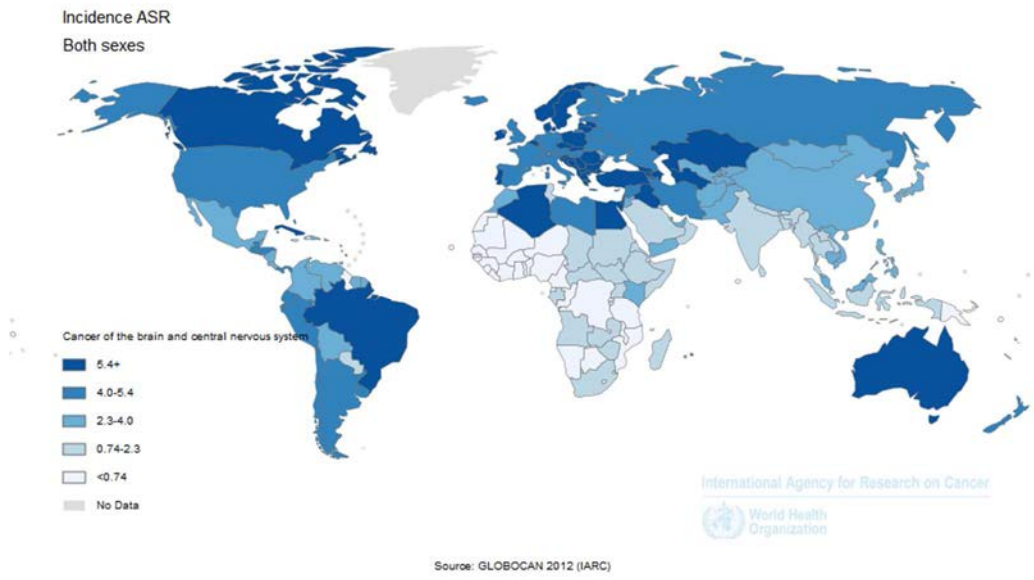

Figure 1.1: Incidence age-standardised rate (ASR) of brain and central nervous system tumours per 100,000 inhabitants in both sexes worldwide estimated by the GLOBOCAN report [1].

Brain tumours are a designation for CNS tumours emerging in intracranial regions: in brain itself, cranial nerves, meninges, skull, pituitary and pineal gland. Primary brain tumours originate in the brain, whereas secondary brain tumours have a metastatic origin, resulting from cancers which origin is located in other organs. Tumours that can metastasize to the brain are mainly from lung (40-50%), breast (15-25%) and melanoma (5-20%), with a median survival from 2 to 16 months [3].

1.1.2 Grading and Incidence

Brain tumours are categorized according to the World Health Organization (WHO) Classification of Tumours of the Central Nervous System [4, 5] which classifies them based on the type and location of originating cells, and a grade is assigned (grade I - grade IV) based on predicted clinical behaviour [4]. However, new updates are changing the paradigm of classification, introducing new entities that are defined by both histology and molecular features [5].

The degree of malignancy is based on histopathological criteria: nuclear atypia, mitotic activity, endothelial hyperplasia and necrosis, which indicate tumour growth and spreading, and predicting patient survival. Combining all these characteristics, a scale of four grades of malignancy of tumours was stablished [4]:

> **Grade I**: Low proliferative potential, diffused nature. The tumour may be cured by surgery (e.g. pilocytic astrocytoma, meningioma).
>
> **Grade II**: Infiltrating tumours with low proliferative activity and potential of recurrence after surgery. Most of them tend to progress to high grade lesions (e.g. diffuse astrocytomas and oligodendrogliomas).
>
> **Grade III**: Histological evidence of malignancy: nuclear atypia, elevated mitotic activity, clearly expressed infiltrative capabilities and anaplasia (e.g. anaplastic oligodendroglioma).
>
> **Grade IV**: Mitotically active with vascular proliferation, necrosis and generally associated with a rapid preoperative and postoperative progression of disease and fatal outcome (e.g. glioblastoma (GB), medulloblastoma).

According to the Central Brain Tumour Registry of the United States (CBTRUS) Statistical Report (Primary Brain and Central Nervous System Tumours Diagnosed in the United States) [6], non-malignant brain tumours (grade I) represent a 67.2% of incidence whereas malignant brain tumours (grades II to IV) represent 32.8% (Figure 1.2.A).

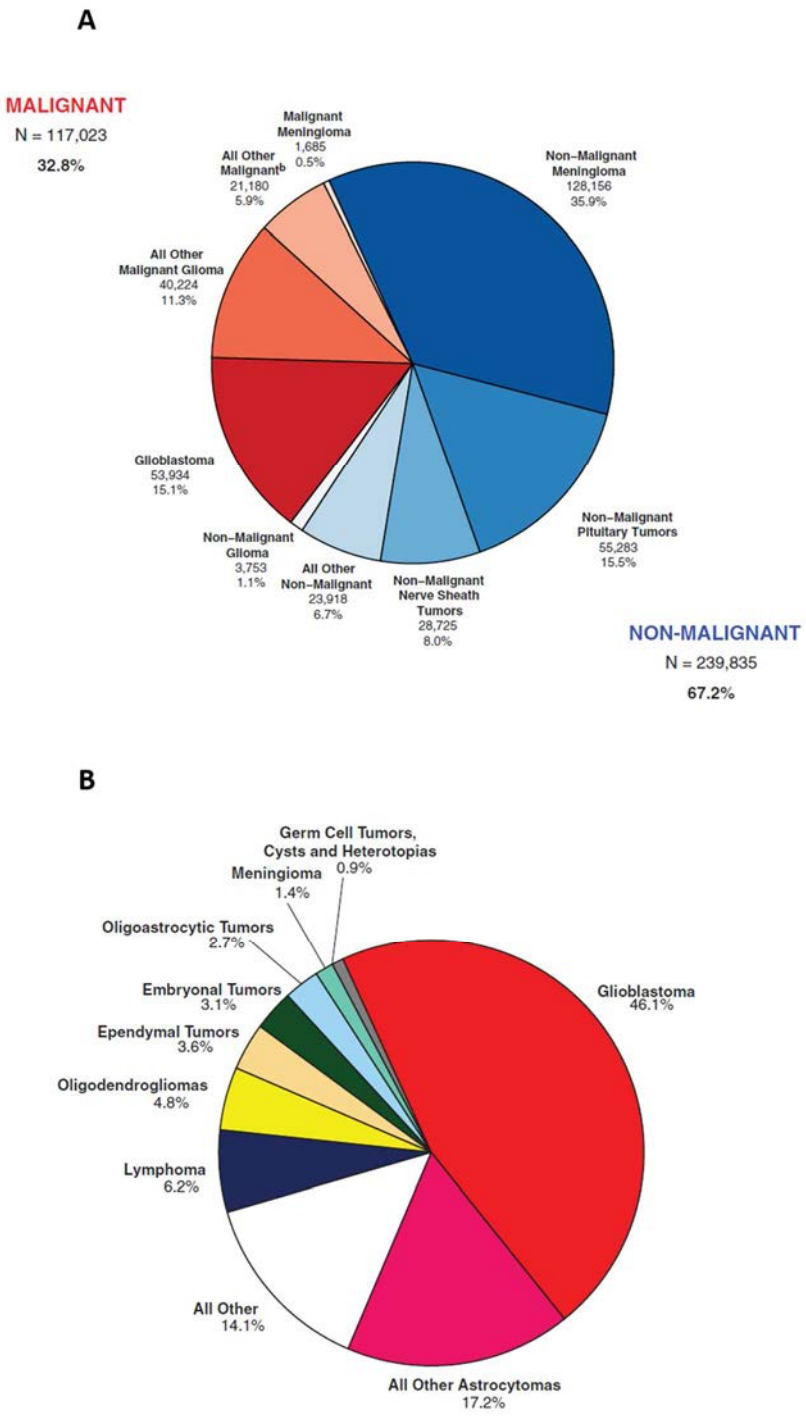

Figure 1.2: Distribution of A. Primary Brain and CNS Tumours by behaviour (malignant vs benign). B. Distribution of malignant primary brain and CNS tumours by histology subtypes (Adapted from [6]).

The most common primary malignant brain tumours are gliomas, mostly GB and other astrocytoma types (Figure 1.2.B). Gliomas are tumours which originate from glial cells or their less differentiated precursors that infiltrate the surrounding brain tissue. They are classified in different groups taking into account the cell type they originate from (Figure 1.3) [7], their location (supra/infratentorial) and their grade.

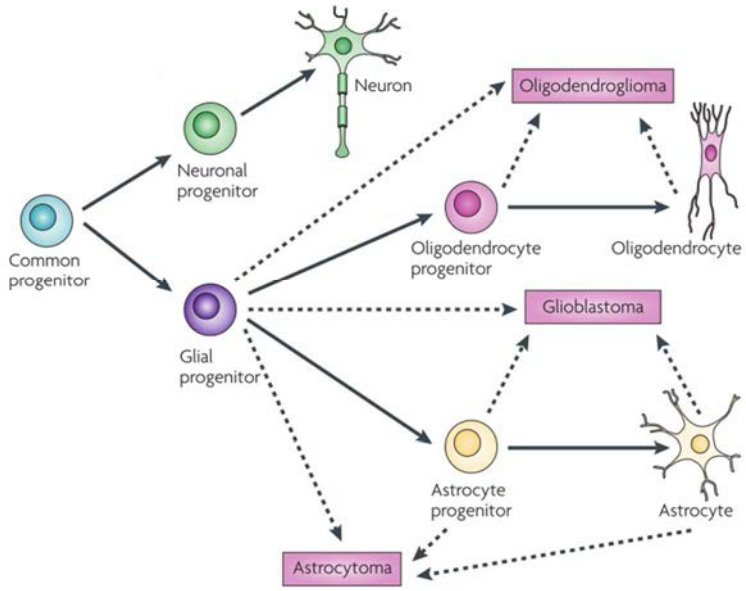

Figure 1.3: Common progenitor cells are thought to produce neuronal and glial progenitors that eventually differentiate into mature neurons, astrocytes and oligodendrocytes. A selection of likely candidates for each tumour type (dashed arrows) is indicated (figure adapted from [7]).

1.1.3 Glioblastoma (GB)

Glioblastomas account for 46.1% from all malignant primary brain tumours (Figure 1.2.B) [6]. The survival rates for glioblastoma are low, with a median survival of 14.6 months even when aggressive therapy is applied [8], and only 5.1% of patients survive 5 years post diagnosis [6, 9]. In addition, malignant brain tumours such as GB present one of the highest average of years of potential life lost (YPLL) reaching 19.93 years [10], which inevitably implies a problem with high social impact. Due to the poor prognosis and such high social impact, there is an urgent need of methods to improve patient management. Improving aspects of detection, diagnosis, treatment and especially the therapy response follow-up enlarging the corresponding decision-making frame would be useful in this context.

Glioblastomas are heterogeneous tumours. This heterogeneity can be observed inter-tumour by identification of different somatic mutations and copy number alterations, differences in the expression profiling, differences in epigenetics and in histopathological studies, the number of mitosis and the distributions of cell density, calcification, vascularization and necrosis, heterogeneity of cancer stem cells (CSC) and in the microenvironment [11]. However, tumour heterogeneity is also observed within each tumour. Intra-tumour heterogeneity in molecular profiles have been observed, such as described in [11] revealing that a single tumour mass

analysed by transcriptomics can be classified into at least two different GB subgroups. Still, different subclones of CSC of the same tumour mass could develop different phenotypes and proliferative potentials when implanted in NOD-SCID mice [12, 13]. This intra-tumour heterogeneity in glioblastoma could explain the difficulties observed in the validation of oncologic biomarkers, the selection of patients for single target therapies, treatment failure or drug resistance [14, 15]. The other important point related to treatment failure is the immunosuppressive environments which have long been recognized for GB [16], which is also able to reprogram glioma-associated microglia/macrophages, evading drug effects [17]. As it has been mentioned, CSC are highly related with the intra-tumour heterogeneity. The *CSC hypothesis* proposes that neoplastic processes are heavily dependent on a small CSC population which are characterized for having self-renewal and multipotency properties and for being resistant to conventional therapy [18]. Related to this hypothesis, there is some evidence that also the specialized microenvironment (niches) of this CSCs is crucial for maintaining their cellular characteristics, especially the vascular area of the subventricular zone (SVZ) where normal neural stem cells are located [19].

1.1.4 Brain tumour diagnosis

Until evident clinical symptoms occur in patients, brain tumours are not usually diagnosed and that is why their detection corresponds to a late stage. This late detection occurs mainly because the absence of pain receptors in the brain allowing the tumour to grow “silently”. Common symptoms of brain tumours are: headache, nausea, vomiting, seizures, memory loss and altered mental functions (personality changes, respiratory arrest or even coma episodes). These are common signs that can manifest when intracranial pressure rises due to mass effect of the lesion [20]. For a confident diagnostic, appropriate brain imaging is needed. Computed Tomography (CT), Positron Emission Tomography (PET), Magnetic Resonance Imaging (MRI) could be used, although the technique of choice is usually MRI due to the high level of anatomical detail provided. In addition, acquisitions with exogenous contrast administration can be performed to assess contrast uptake by tumours and estimate the grade of the lesion (see section 1.2.1.1). Magnetic Resonance Spectroscopy (MRS) can provide metabolic information of tumour environment but it is not included in the diagnostic pipeline of most clinical centres, as most radiologists are not properly trained to process/interpret MRS data (see section 1.2.1.2 for a more comprehensive description of NMR and its biomedical applications as MRS/MRSI). However, apart from the non-invasive diagnostic, a histopathological analysis from a tumour biopsy or surgical sample (the gold standard method yet) is needed to evaluate the tumour grade and classification.

1.1.5 Therapy for Glioblastoma

The standard clinical treatment for GB is surgical resection followed by combined radiotherapy/ temozolomide (TMZ) chemotherapy, plus several adjuvant TMZ chemotherapy cycles, as described by [8] and which provides the best survival rate in clinical patients. Unfortunately, tumours become rapidly resistant to the applied therapy [12] and relapse is the norm.

1.1.5.1 Surgical resection

The current standard of care for newly diagnosed GB is surgical resection to the extent feasible. Its principal objective is to remove as much tumour mass as possible to get a better survival [21]. In addition, a complete removal of the tumour mass without compromising neurological functions would be the ideal situation. In case of high grade gliomas, surgery may be insufficient, mainly due to tumour infiltration. Advances in neurosurgery such as minimally invasive neurosurgery [22], brain mapping [23], intraoperative MRI [24] and labelling tumour cells with special agents as 5-aminolevulinic acid [25] have helped to improve tumour resection effectiveness and safety. However, despite these achievements, complete resection in a high grade glioma is almost impossible due to its highly infiltrative pattern. For this reason, after surgery, adjuvant radiotherapy and/or chemotherapy must be administered.

1.1.5.2 Radiotherapy

Radiotherapy is an important tool in the treatment for survival improvement of patients. The effects of the irradiation of the cells structures, especially DNA, are cell death, chromosomal aberration and DNA damage, which could result either from the direct ionization, or indirectly, through the generation of reactive oxygen species produced by radiolysis of water, breaking the DNA covalent bonds. In addition, its effects over the immune system and impact in therapy response are also being studied nowadays [26]. The handicap of radiotherapy is that apart from damaging tumour cells, also healthy cells are affected [27]. Healthy cells can repair themselves efficiently, keeping their normal function, whereas tumour cells in general are not as efficient as normal cells repairing the damage caused by radiation, and this results in a differential cell killing [28]. The delineation of the irradiation zone, avoiding the normal brain tissue is an important aim that has been improved with the help of stereotactic radiosurgery and computerized systems [29]. Apart from MRI, other non-invasive techniques as MRS, MRSI, perfusion or diffusion MRI are useful to help discriminating between tumour and healthy brain and can also help in delineation [30, 31]. However, GBs often reappear after radiotherapy treatment as focal masses [32] probably due to a subset of resistant CSC leading to regrowth and relapse. In this sense, it has been reported that some CSC of GBs develop radio-resistance by activation of DNA

damage response [14] and also by hypoxia and inflammatory processes generated when the tumour microenvironment is irradiated, also leading to radiotherapy resistance [28].

1.1.5.3 Chemotherapy

The objective of the chemotherapeutic agents is to eliminate the tumour or at least to stabilize the disease controlling the tumour growth and improving patients' quality of life. Nevertheless, the major problem with chemotherapy for brain tumours is reaching an effective dose within the tumour due, for example, to bad perfusion or collapsed and aberrant blood vessels [33], as well as the challenge of crossing the blood-brain barrier (BBB).

Temozolomide

Standard chemotherapy for brain tumours is based mainly on alkylating agents, such as temozolomide (TMZ), which is at present the most effective drug for the treatment of human GB [8, 34]. Other authors have also reported its effectiveness in preclinical models [35] being usually dissolved in dimethyl sulfoxide (DMSO), before being administered intragastrically [36], as opposed to patients in which capsules or powdered form for dissolution are available. This group of medications is also one of the few with the ability to penetrate the BBB, achieving therapeutic concentrations in cerebrospinal fluid and brain parenchyma, although in case of GB the BBB is disrupted [37].

The TMZ itself is not responsible for the therapeutic effect. After oral uptake, TMZ is spontaneously hydrolysed to its active form, 5-(3-methyl-triazen-1-yl)imidazole-4-carboxamide (MTIC). In turn, MTIC is rapidly converted to the inactive 5-aminoimidazole-4-carboxamide (AIC) and to the electrophilic alkylating methyldiazonium cation that may transfer a methyl group to DNA and these DNA-methyl adducts are responsible for its therapeutic effect. The primary responsible for the therapeutic effect of TMZ is the O6-methyl-guanine (O6-meG), although it only accounts for 5% of DNA adducts [38]. The O6-meG lesion may lead to DNA double strand breaks (DSBs) and subsequent cell death via apoptosis and/or autophagy [38], although unpublished data from our group and recent data regarding calreticulin exposure [39] (see also section 1.1.6) would point to that other effects apart from direct cell killing are responsible for TMZ effects over tumour response.

The resistance to alkylating agents such as TMZ observed in some GBs could be at least partially due to MGMT (O6-meG-DNA methyltransferase) overexpression. MGMT repairs the O6-meG lesion by transferring the methyl group from the adduct to its own cysteine residue and then, methylated MGMT is degraded and new MGMT protein must be synthesized in order to continue repairing DNA. In the same line, better response to therapy with TMZ has been

reported in patients who presented the MGMT promoter silenced by methylation [40]. If not repaired, alkylated bases cause replication interruption and collapsing of the replication fork, generating single-strand breaks (SSBs), which ultimately would induce double-strand breaks (DSBs) (see scheme in Figure 1.4). It is possible that the activation of SSB and DSB repair pathways also decrease the cytotoxic effect of TMZ [41].

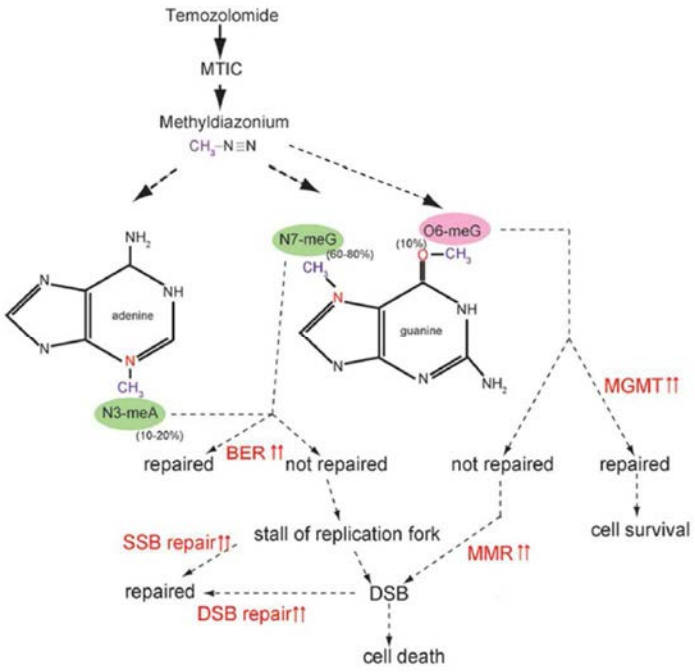

Figure 1.4: TMZ activation and resistance pathways scheme. O6-meG DNA adducts account for only 5 of TMZ-induced DNA lesions, but they are thought to be responsible for its cytotoxic effect. MGMT repairs the lesions, resulting in resistance to TMZ. If MGMT is depleted or suppressed by methylation of its gene promoter, cytotoxicity of TMZ is enhanced. MMR recognizes the abnormal base pairs containing O6-meG, eventually leading to DNA DSB and cell death. N3-meA and N7-meG adducts are also cytotoxic, but are usually repaired by the BER system. It is possible that SSB and DSB repair pathways are activated and diminish the cytotoxic effects of TMZ. BER: base excision repair, DSB: double-strand break, MGMT: O6-methylguanine-DNA-methyltransferase, MMR: mismatch repair, N3-meA:N3-methyl-adenine, N7-meG:N7-methyl-guanine, O6-meG:O6-methyl-guanine and SSB: single-strand break. Adapted from [41].

Other chemotherapeutic approaches

Besides TMZ therapy, there are other therapeutic strategies that target intracellular signalling pathways determining the key functions of tumour biology, such as proliferation and apoptosis or angiogenesis. Those are considered after failure of standard treatment. Two main pathways that are targeted are the vascular endothelial growth factor (VEGF) or the endothelial growth factor (EGF) and its receptor (EGFR), which is a promoter of numerous effects at cell proliferation, invasion and angiogenesis levels [42]. Among the developed drugs to act on these signalling pathways, Bevacizumab (monoclonal antibody against VEGF, that targets

angiogenesis) added to chemo-radiotherapy with temozolomide is under study in first-line glioblastoma treatment. Results demonstrated an increase in progression-free survival, but not in overall survival with the addition of Bevacizumab [43, 44].

Alternative treatment with BCNU (bis-chloroethylnitrosourea, o carmustine), which is also a DNA alkylating agent [45] is applied in some cases, although inconclusive trials give it a lower level of evidence, which in addition to considerable toxicity described, discourage the massive application of this treatment [46].

1.1.6 Role of the immune system in brain tumours

Research over the past decades have demonstrated that immune system not only interacts with developing neoplasms, but it is also able to eliminate damaged cells which are more prone to become malignant (which is known as anticancer immunosurveillance) [47] and it has been observed that the immune system also plays an important role in the response to treatment in several malignancies [48]. The development of effective antitumour immune response relies on coordinated interactions of host immunocompetent cells and generation of tumour antigen-specific cytotoxic T lymphocytes (CTLs), which play a relevant role in the defence against cancer recognising specific antigens presented on the surface of transformed cells. To become competent killer cells, naïve lymphocytes require priming by dendritic cells (DCs), which are antigen-presenting cells (APCs), as well as support from CD4+ T-cells (helper).

Malignant cells express pathogen-associated molecular patterns (PAMPs) that can be recognized by DCs precursors, triggering the local release of cytokines and chemokines which result in the recruitment and activation of innate immunity effector cells. On the other hand, DCs engulf dying tumour cells and develop a maturation process, then they migrate to regional lymph nodes (LN) where they present the processed tumour-derived peptides to naïve T and B lymphocites, which are activated in case of antigen match (CD4+ helper T lymphocytes or CD8+ T lymphocytes). Then, activated clones of T lymphocytes expand and leave LNs infiltrating tumour tissues and eventually getting activated to mediate effector functions (scheme in Figure 1.5) [49].

Still regarding immune system in response to therapy, it should not be neglected that the percentage of tumour-associated macrophages can be as high as 30% of the abnormal mass [50], constituting a cell population with high plasticity. In response to various signals, macrophages undergo M1 (anti-tumour) or M2 (pro-tumour) polarisation, which in fact represents extreme situations of a continuum of activation states having relevant roles in response to therapy.

Finally, it is worth remembering that the process called "immunogenic death" could be also relevant in the recruitment of immunological response against the tumour [51, 52]. TMZ has been suggested as one of the chemotherapeutic agents which trigger immunogenic death after its administration [39].

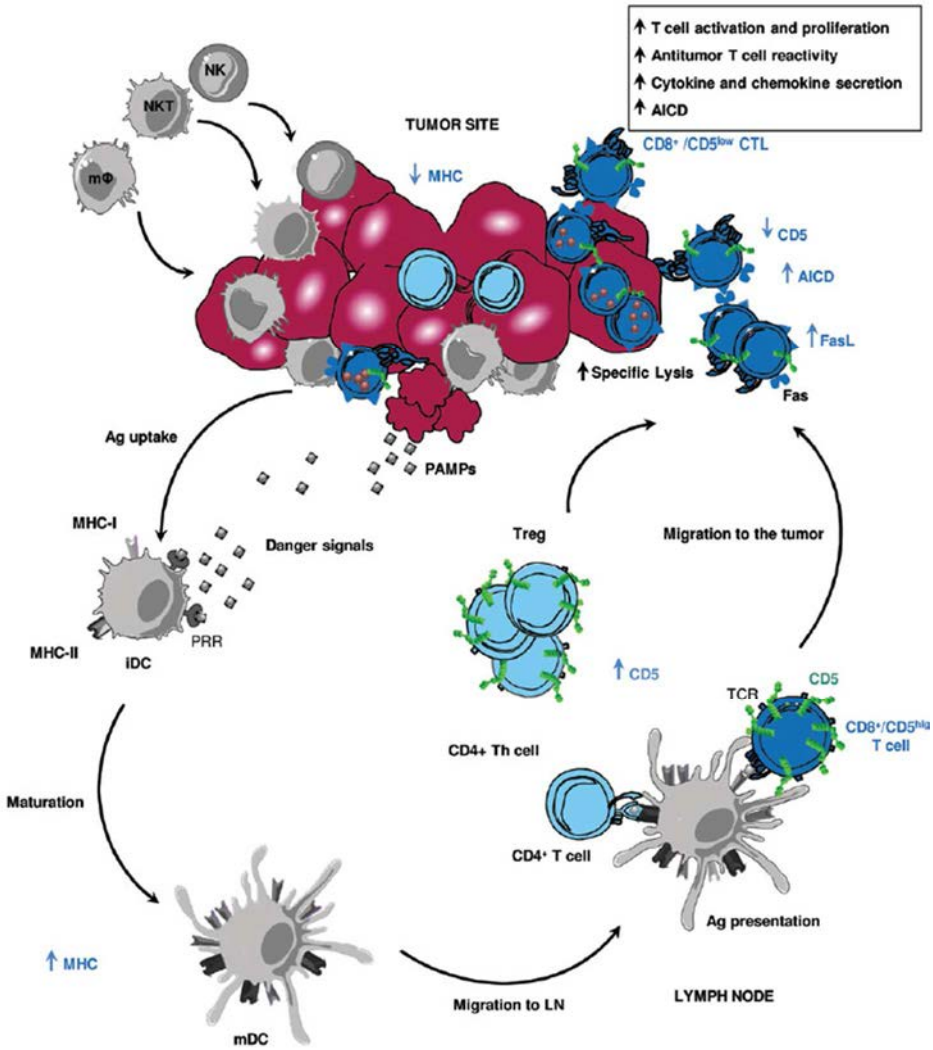

Figure 1.5: Scheme of the cycle for immune response against a tumour. The malignant cells may express pathogen-associated molecular patterns (PAMPs) that can be recognized by pattern recognition receptors (PRRs) on dendritic cells (DCs) precursors, triggering the local release of cytokines and chemokines. Then, DCs migrate to local lymph nodes (LN) and present processed tumour-derived peptides to naïve T and B-lymphocytes, which are then activated in case of Antigen (Ag) match to become plasma cells producing antibodies and CD4+ helper T lymphocytes or CD8+ T lymphocytes. CD8+ T lymphocytes leave LN to infiltrate tumour tissues and exert effector functions once activated to cytotoxic T lymphocytes (CTLs) by encounter with target cells. Immunotolerance may be induced by downregulation of cluster of differentiation 5 (CD5) in CTLs infiltrating the tumour causing activation-induced cell death (AICD). FASL: FAS ligand, MHC: Major histocompatibility complex, Mϕ: macrophages, NK: natural killer, NKT: natural killer T, TCR: T-cell receptor, and Treg: Lymphocyte T regulatory. Taken from [49].

Nevertheless, multiple immune suppressive mechanisms which may inhibit T cell function in cancer have been described [53]. For instance, GB tumours secrete immunosuppressive factors which accumulate in the tumour microenvironment [54], as transforming growth factor beta (TGF-β) and VEGF (which suppress T cell proliferation and cytotoxic function) [55]. In addition, it is known that T cell unresponsiveness occurs during the growth of hematologic and solid tumours in complex microenvironments which can strongly influence the growth and progression of the tumour cells and can act as a barrier, limiting the efficacy of cancer immunotherapy [56]. Moreover, most of the antigens expressed by tumour cells are also expressed in normal cells resulting in immunotolerance and failure of the immune system, allowing the development of solid tumours [56] and various immune escape mechanisms have been described for some tumour types [57].

Accordingly, efforts have been made to use the immune system as therapy against cancer, improving the patient immune response to a tumour. In the case of GB, immunotherapy approaches are being tested in early-stage clinical trials using different strategies such as cancer vaccines, oncolytic virus therapy, adoptive cell therapy, monoclonal antibodies, amongst others [58–63]. Another approach is the "metronomic therapy" based on equally spaced, low, minimally toxic doses of chemotherapeutic drugs without extended rest periods which effectivity is related with the immune system activation that enhance tumour regression and prevent tumour regrowth [64, 65].

Studies carried out in preclinical GL261 GB tumours growing subcutaneously in immunocompetent mice, showed that metronomic therapy with cyclophosphamide (CPA) was able not only to activate antitumour CD8+ T cell response, but also to induce long-term, specific T-cell tumour memory [66]. Regarding clinical patients, CPA and also TMZ metronomic low dose schedules have demonstrated satisfactory results [67–69].This complex interplay between immune system recruitment and modulation should not be neglected during treatment, and it would be useful to develop a tool for therapy response monitoring that could provide information about proper immune system elicitation and action.

1.1.7 Brain tumour follow-up

Radiological and clinical guidelines are used to evaluate brain tumours response to therapy, especially through the application of the Response Assessment in Neuro-oncology (RANO) criteria [70] and Response Evaluation Criteria in Solid Tumours (RECIST) criteria [71].

In the case of GB, follow-up is usually performed through MRI (see section 1.2.1 for biomedical applications of MR) exploration after the first round of therapy is applied (Figure 1.6). Normally,

the first follow-up study is carried out around 21-28 days after finishing the radiotherapy and then, every three months [72]. Therefore, large frames of time are needed to assess patient response to therapy, with the consequent delay in clinical decisions related to patient management, e.g. application of a second line therapy. In addition, MRI information is not always precise enough and sometimes it could lead to misunderstandings due to pseudoresponse and pseudoprogression appearance [73]. In this case, further periods of time are needed for confirmation. However, it is widely accepted that changes in metabolite pattern (MRSI-detectable) should precede morphological changes (MRI-detectable). Accordingly, integrating the metabolite pattern information in the GB assessment pipeline could produce early warning of therapy response related changes relevant for patient management. Early detection of surrogate biomarker/s of therapy response should allow a proper evaluation of therapy response and, in some cases, lead to a change in the therapeutic strategy in order to combat regrowth/relapse. Improving such techniques for patient management would be of great interest for the clinical practice and probably would improve patient outcome.

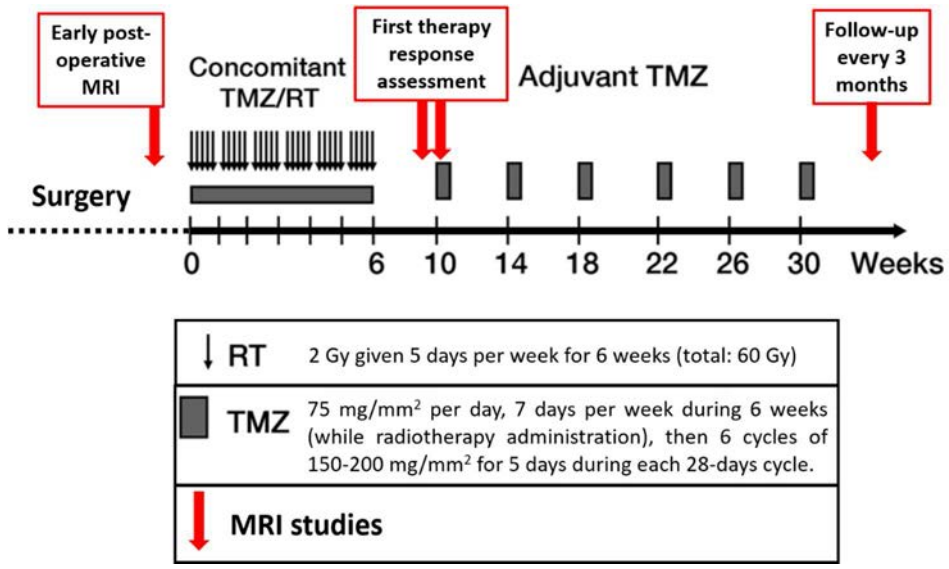

Figure 1.6: Human GB therapy and follow-up current scheme [8]. Fractionated focal irradiation in daily fractions of 2 Gy given 5 days per week for 6 weeks, for a total of 60 Gy plus continuous daily temozolomide (75 mg/mm^2) per day, 7 days per week from the first to the last day of radiotherapy), followed by six cycles of adjuvant temozolomide (150 to 200 mg/mm^2 for 5 days during each 28-day cycle). MRI studies are indicated by red arrows, a first MRI study is carried out after tumour surgical resection and before starting further treatment. Then, the follow-up studies are performed first, around 21 to 28 days after the completion of radiotherapy and every 3 months thereafter. (Adapted from [74]).

1.1.8 Preclinical models of human glioma

Due to evident ethical restrictions, it is not possible to perform repeated exams in patients with a brain tumour or to repeatedly collect biopsy samples at given time points of tumour growth/ progression for research purposes, especially if surgical resections or chemotherapy are feasible. For this reason, animal models of human brain tumours have been developed to facilitate the studies of tumour characterization, progression and response to therapy. There are several types of preclinical models of brain tumours (Figure 1.7) but the utility of any preclinical model depends on how closely it replicates the original human disease. Animal models of human glioma should be ideally orthotopic and reproduce characteristics such as infiltration in the cerebral parenchyma that characterizes their aggressiveness. Subcutaneous models are known to provide over-optimistic therapy response results with respect to intracerebral models [75] due to different micro-environment and are not always able to recapitulate the originating phenotype. In this sense, the use of ortothopic models should provide more realistic results.

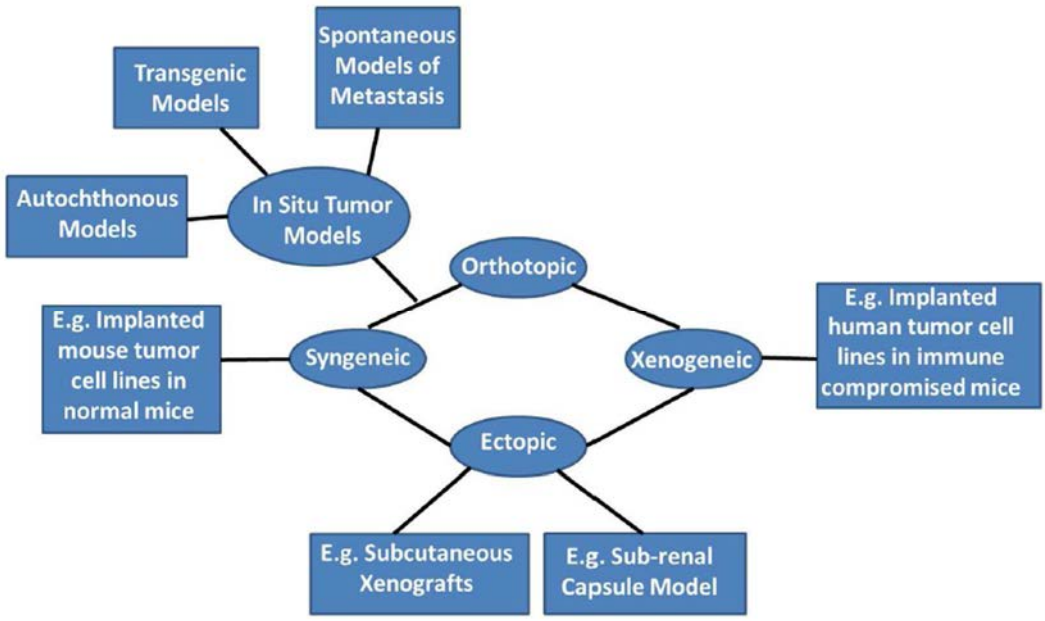

Figure 1.7: Preclinical cancer model scheme (obtained from [76]). The model studied in this thesis belongs to an implanted, orthotopic model from glioblastoma murine cells in C57BL/6J mice.

For GB, the most widely used preclinical murine models are those induced by stereotactic injection of glioma cells into the brain parenchyma (orthotopic), either with cell lines from the same species (syngeneic or isogeneic in some cases) or samples obtained from human tumour biopsies (xenogeneic, implanted in immune-deprived mice models). These immune-deprived mice models are used to evade immune response effects against the human implanted cells (as for example in [77]). However, the use of these models prevents the correct evaluation of the role of the immune system in either tumour progression or response to therapy. For example,

Nude mice are unable to generate T lymphocytes [78], whereas severe combined immunodeficient (SCID) mice possess a completely intact innate immune system but lack functional adaptive immunity (T and B cells) [79], and T cells have proven to be relevant in tumour therapy response [51] (see also section 1.1.6). Thus, it becomes clear that the use of immunologically intact mice is needed for a correct evaluation of the immune system participation in tumour response [80, 81]. Moreover, an increased understanding of genomic alterations in primary brain tumours has led to the development of highly characterized genetically engineered mouse (GEM) models based on specific genetic alterations observed in human tumours and preclinical models of GB have been reported to reflect the histology and biology of human GB. These models arise spontaneously along animal's life, but the lack of standardization in these tumours (especially in relation to the time point of tumour initiation), make it difficult to achieve a homogeneous group of tumour-bearing mice to control therapy response effects [82].

1.1.9 The GL261 murine model

The immunocompetent GL261 mouse glioma line is one of the most widely used to study GB and is usually inoculated into the C57BL/6 strain, resulting in tumours with invasive and infiltrative characteristics similar to those of human GB [83]. The C57BL/6J sub-strain is the "original'' Jax mouse strain [84], which was initially derived as C57BL in 1921 by Dr. CC Little, although it first appeared described in literature around 1935 [85].

The GL261 model is one of the best characterised orthotopic allograft mouse models of human malignant glioma: it was generated first in the early 40's [86, 87] and it would probably belong to the "venerable" (i.e. any long-transplanted tumour) tumour classes [88] where no or few immunological effects are expected against the tumour when inoculating these cells in immunocompetent mice. These tumours grow exponentially for about three/four weeks, killing the animals due to mass effect at the end on this period [83, 89]. Studies on gene alterations, immunological characteristics and radiation sensitivity demonstrate the utility of the GL261 model to investigate the anti-tumour effect of various treatment strategies: immunotherapy, gene therapy, chemotherapy, radiotherapy or antiangiogenic therapy [83, 89, 90].

1.2 Nuclear Magnetic Resonance (NMR)

NMR was first described in 1946 by Edward Purcell and Felix Bloch, but it was in the middle of the decade of 1970's when NMR started to be used *in vivo*, after gradient introduction into the magnetic field experiment, allowing to determine the location of the emitted signal and to reproduce it in an image. During the decade of 1980's, the first MR medical scanners became available for clinical use and since then, extensive MR-based applications have been developed (the word "nuclear" is usually omitted in clinical environments due to its negative and erroneous association with nuclear medicine and, therefore, ionizing radiation). An extensive description of the physics behind the NMR phenomena is beyond the scope of this thesis and can be found in different sources such as [91].

1.2.1 Biomedical applications of MR: Magnetic Resonance Imaging (MRI) and Magnetic Resonance Spectroscopy /Spectroscopic Imaging (MRS/MRSI)

1.2.1.1 Magnetic Resonance Imaging (MRI)

The signal from the nuclei of hydrogen atoms (^{1}H), which is abundant in the human body and has a single proton with a large magnetic moment, is used for image generation. In this sense, images are obtained from the body ^{1}H signal present in the tissue (mostly water and in a lesser extent, fat).

Three intrinsic features of a biological tissue, which contribute to signal contrast in MRI, are:

A) The proton density, i.e. the number of excitable spins per unit volume in a given tissue, determines the maximum signal that can be obtained from a tissue.
B) The T_1 relaxation time constant of a given tissue, which is related to how fast the excited spins recover the original state and are available for the following excitation (related to spin-lattice relaxation, see next subsection).
C) The T_2 relaxation time constant of a given tissue, which mostly determines how quickly an MR signal fades after excitation (related to spin-spin relaxation, see next subsection).

Proton density, T_1 and T_2 times are intrinsic features of biological tissues and may vary widely from one tissue to the next. Depending on which of these parameters is emphasized in an MR sequence, the resulting images differ in their tissues contrasts. This fact provides the basis of soft tissue discrimination in MR imaging (see examples in the subsection *Repetition time (TR) and echo time (TE) in image acquisition*).

Relaxation times

T_1 relaxation

As transverse magnetization decays after an excitation, the longitudinal magnetization, Mz, is slowly restored. This process is known as longitudinal relaxation or T_1 recovery (Figure 1.8). The nuclei can return to the equilibrium state only by dissipating their excess energy to their surroundings ("lattice"). The time constant for this recovery is T_1 and it is dependent on the strength of the external magnetic field, $\beta_{0,}$ and the internal motion of the molecules (Brownian motion). Biological tissues have T_1 values ranging from half a second to several seconds at 1.5 T.

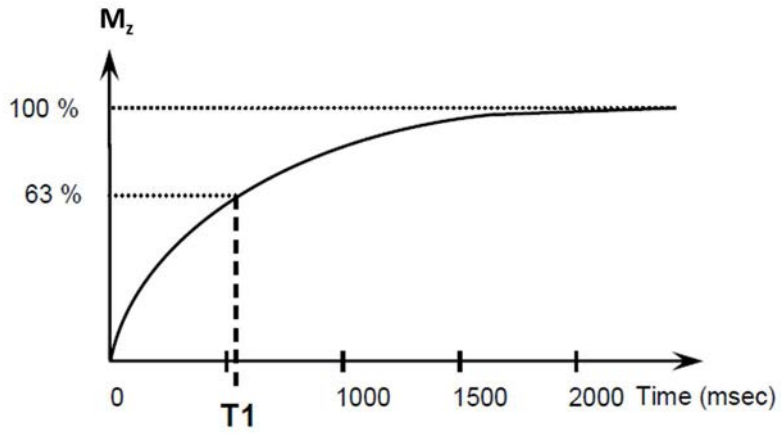

Figure 1.8: T_1 relaxation time constant is defined as the time it takes for the longitudinal magnetization (M_z) to recover 63 % of the original magnetization after an excitation pulse. (Taken from [92]).

T_2 relaxation

The T_2 relaxation is the decay of transverse magnetization due to spin loss of coherence (dephasing). "Phase" refers to the position of a magnetic moment on its circular precessional path and it is expressed as an angle. Immediately after the excitation, the spins precess synchronously and are said to "be in phase". This phase is gradually lost because some spins advance while others fall behind on their precessional paths. The individual magnetization vectors begin to cancel each other out instead of adding together, the resulting vector sum (the transverse magnetization) becomes smaller and finally disappears, and with it, the MR signal (Figure 1.9). Transverse relaxation differs from longitudinal relaxation in that the spins do not dissipate energy to their surroundings but instead, exchange energy with each other (interaction spin-spin). The coherence of spins is lost in two ways:

A) Due to energy transfer between spins as a result of local fluctuations in the magnetic field. These fluctuations happen because spins randomly interact with each other (spin-spin interaction) and they precess faster or slower according to these magnetic field fluctuations. The final result is the loss of phase.

B) Due to inhomogeneities of the external magnetic field β_0. These are intrinsic inhomogeneities that are caused by the magnetic field generator itself and by the sample being studied. These contributions induce to dephasing, resulting in a signal decay that is even faster than described by T_2. This type of decay occurs with the time constant T_2*, which is typically shorter than T_2. Most of the inhomogeneities that produce the T_2* effect occur at tissue borders, particularly at air/tissue interferences or are induced by local magnetic field inhomogeneities.

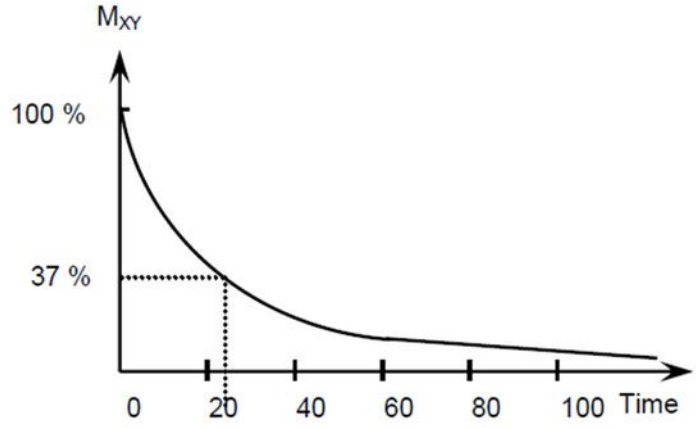

Figure 1.9: T_2 relaxation time constant is defined as the time that takes for the spins to de-phase to 37% of the original value (Mxy for time=0). Taken from [92].

The T_1 and T_2 relaxation times are completely independent of each other but occur more or less simultaneously, being T_2 values always shorter than T_1 (about a tenth of T_1) in biological samples.

Repetition time (TR) and echo time (TE) in image acquisition

Choosing the correct parameters in the MRI acquisition is fundamental to interpret the intrinsic contrast produced. The parameter that influences most the contrast in T_1 weighted MRI is the repetition time (TR), which is the length of the period between two excitation pulses. On the other hand, the parameter that determines the influence of T_2 on image contrast is the echo time (TE) that is the interval between application of the excitation pulse and collection of the MR signal (Figure 1.10).

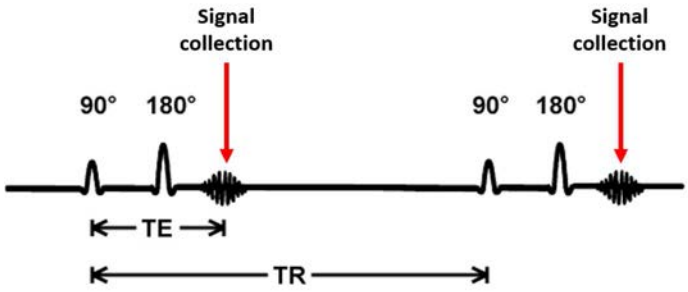

Figure 1.10: Scheme of the parameters TR and TE. TR is the period of time between two excitation pulses (in the figure, between two pulses of 90°) and TR is the period of time between a pulse application and the collection of the MR signal. (Adapted from [93]).

Accordingly, different types of images can be obtained, depending on the predominant weighting given by different parameters in the acquisition sequence: e.g. proton density weighted images, T_1-weighted (T_{1w}) images, and T_2-weighted (T_{2w}) images, although a mixed contribution is always expected to the final signal as shown in Equation 1.1, where *S* is the signal and *N* is the Proton density.

$$S = N\,x\,\underbrace{(1 - e^{-TR/T1})}_{\text{T1 effect}}\,x\,\underbrace{(1 - e^{-TE/T2})}_{\text{T2 effect}}$$

Equation 1.1

In summary, the proper selection of acquisition parameters can emphasize one of the effects and diminish the others, as it can be seen in Figure 1.11. For example, a short TR will highlight differences between tissues with different T_1 (tissues with short T_1 would recover most of their signal appearing as hyperintense components in the image, and the other way round) in T_{1w} images. Regarding TE, a large value will highlight differences between tissues with different T_2 in T_{2w} images: tissues with a large T_2 will have spins still on phase after TE, and will appear hyperintense in the corresponding image, while tissues with short T_2 will appear as hypointense zones. Examples of different tissues' appearance in T_{1w} and T_{2w} images (hyperintense or hypointense) are shown in Table 1.1.

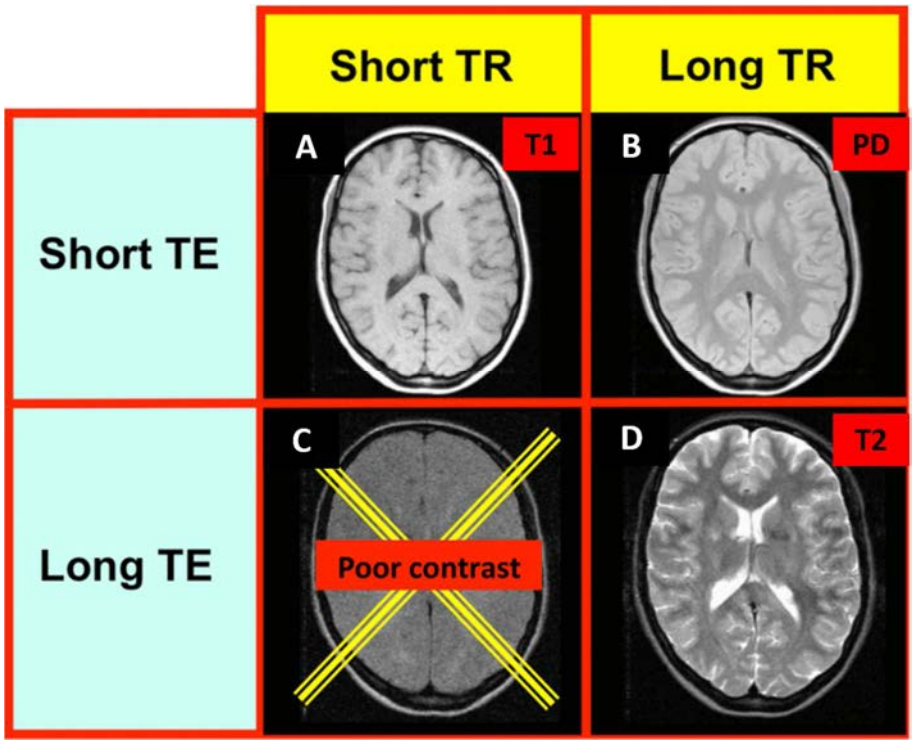

Figure 1.11: Different image contrast obtained with combination of short or long TR and short or long TE values. **A.** T_{1w} images use short TR and TE values. **B.** Proton density images use long TR and short TE values. **C.** Poor contrast is observed using short TR and long TE values. **D.** T_{2w} images use long TR and long TE values. (Adapted from [93]).

Table 1.1: Signal intensities of different tissues on T_1 and T_2-weighted images (adapted from [94]).

Tissue	T_1- weighted image	T_2- weighted image
Fat	Hyperintense	Hyperintense
Aqueous liquid	Hypointense	Hyperintense
Tumour	Hypointense	Hyperintense
Inflammatory tissue	Hypointense	Hyperintense
Muscle	Hypointense	Hypointense
Connective tissue	Hypointense	Hypointense
Hematoma, acute	Hypointense	Hypointense
Hematoma, subacute	Hyperintense	Hyperintense
Compact bone	Hypointense	Hypointense

Exogenous contrast agents

The contrast observed in MRI is the result of the differences in the signal intensity between tissues and it is determined basically by intrinsic and extrinsic factors. These are, respectively, properties of the different tissues and properties of the MR scanner and acquisition parameters chosen. Nevertheless, sometimes the intrinsic tissue contrast is not enough to detect different pathological situations (e.g. tumours). For this, exogenous contrast agents (CA) can be administered in MR imaging to further enhance the natural contrast and additionally to obtain dynamic (pharmacokinetic) information. CAs basically interact with the surrounding hydrogen nuclei of the water or fat molecules in the tissue and alter their relaxation properties by shortening T_1 and T_2.

A CA that accelerates the relaxation of nearby protons by withdrawing the excess of energy previously absorbed lead to a faster recovery of longitudinal magnetization. Accordingly, a hyperintense signal in seen in T_{1w} images and it is called "positive CA". Gadolinium-based CAs are examples of positive CAs [95] (Figure 1.12).

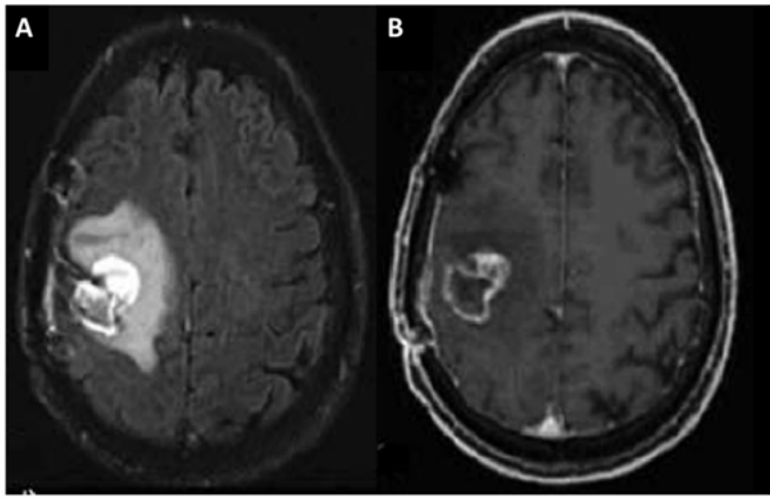

Figure 1.12: A. T_{2w} image and **B**. T_{1w} image after Gadovist (Gadolinium based contrast agent) administration of a human GB (obtained from [96]). In T_{2w} image, the hyperintensity area defines tumour and oedema. Meanwhile in T_{1w} image after CA administration, the tumour area is better delimited.

Contrast agents having high magnetic moment can lead to local field inhomogeneities and fast dephasing of the protons thus shortening T_2. This phenomenon is known as magnetic susceptibility and becomes manifest as a pronounced signal loss that is best appreciated on T_{2w} images. The CAs mostly producing signal loss are named negative CAs, such as iron oxide (SPIO) nanoparticles [97, 98] (see section 1.4).

Most of the clinically available CAs are not able to cross the intact blood brain barrier (BBB) but they can reach a lesion if BBB is disrupted as in GB tumours [37]. Gadolinium (Gd^{3+}) is a trivalent lanthanide with paramagnetic properties and is one of the examples of CA that is widely used in the clinical practice. Most CAs used in patients are based on this metal, which is a CA used at small concentrations (0.1- 0.2 mmol Gd^{3+}/kg). However, due to its elevated toxicity in free form [99], it is normally administered during MRI exams in the form of chelated compounds [95, 100, 101], although even the chelated forms can lead to problems in renal failure patients [102]. For this reason, the use of non-toxic CAs is necessary and recently, this constitutes an important research field [103]. In addition, there are several studies about potentially non-toxic nanoparticles which can behave as dual CAs (i.e. positive and negative contrast behaviour) [104–107] (see section 1.4).

Finally, some approaches describe CAs which are able to target some tissue or cell receptors/structures apart from increasing the contrast. This could be useful for the simultaneous delivery of therapeutic agents to the tumour area and real-time tracking of their *in vivo* biodistribution [108–110] (see section 1.4).

1.2.1.2 Magnetic Resonance Spectroscopy (MRS)

MRS is an analytical method that enables the identification and quantification of metabolites and macromolecules and allows the biochemical characterization of tissues *in vivo*. It differs from conventional MRI in that the MR spectra provides information of the biochemical environment, instead of anatomical information.

Chemical shift

When a tissue is exposed to an external magnetic field, its nuclei will resonate at a given frequency called Larmor frequency. This frequency can be affected by the chemical environment of the nuclei, resulting in a "shift" (slightly different resonance frequencies) expressed in parts per million (ppm) in comparison with a known reference. The expression of chemical shift position in ppm is independent of the field strength, making it easier for comparisons between different magnetic fields and it is expressed by the Equation 1.2:

$$\delta = \frac{\nu\ sample - \nu\ reference}{spectrometer\ frequency} \qquad \textbf{Equation 1.2}$$

Where δ is the chemical shift, *ν sample* is the resonant frequency of the unknown sample and *ν* reference is the reference frequency of a standard compound, measured in the same applied

field (B_0). Conventionally, tetramethylsilane (TMS) dissolved in organic sample is used as a standard signal for this reference, which will have a chemical shift of zero.

The MR spectrum is represented by the *x*-axis that corresponds to the frequency in ppm of a certain proton containing chemical group of a metabolite according to its chemical shift and the *y*-axis that corresponds to the peak amplitude (Figure 1.13).

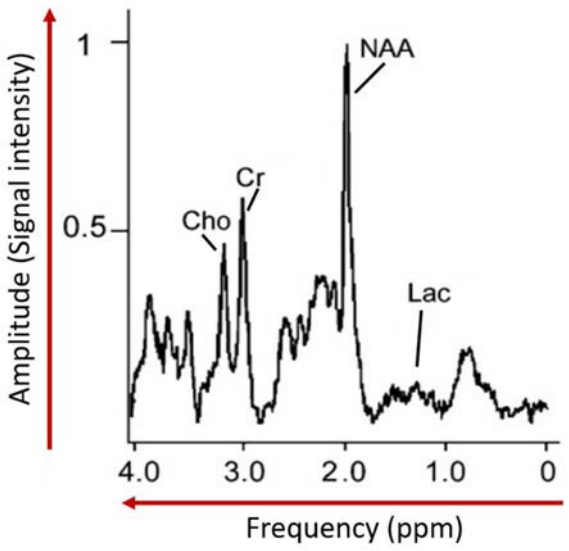

Figure 1.13: Example of a single voxel spectrum of a healthy human brain, *y*-axis correspond to amplitude and-*x* axis to the metabolites frequency. Major labelled resonances are indicated: Cr, total creatine (3.03 ppm); Cho, choline (3.21 ppm); NAA, N-acetyl aspartate (2.01 ppm); Lac, lactate (1.31 ppm). Adapted from [111].

For *in vivo* ^{1}H MRS acquisition, a volume of interest (VOI, named voxel), from which the spectrum will be acquired, is selected in the MRI acquisition. MRS can be acquired either in a single voxel format, or multivoxel format in which several voxels are selected allowing both metabolic and spatial distribution analysis. Acquisition parameters such as TR and TE can also modify spectral appearance. Short TEs (20-40 ms) present in general higher SNR in comparison with long TE, due to less signal losses in short T_2 metabolites (e.g. lipids, macromolecules). On the other hand, some signals overlap at lower magnetic fields, which can make it difficult metabolite assignment and quantification. The use of long TEs would produce simpler spectra due to the filtering of short T_2 signals, but with a lower SNR. The use of long TEs (135-144ms) will also modify the appearance of some signals, as for example lactate which would be inverted (allowing distinction of lactate and lipid signals which otherwise would overlap in the magnetic field used of *in vivo* acquisitions). See examples of short and long TE spectra in Figure 1.14.

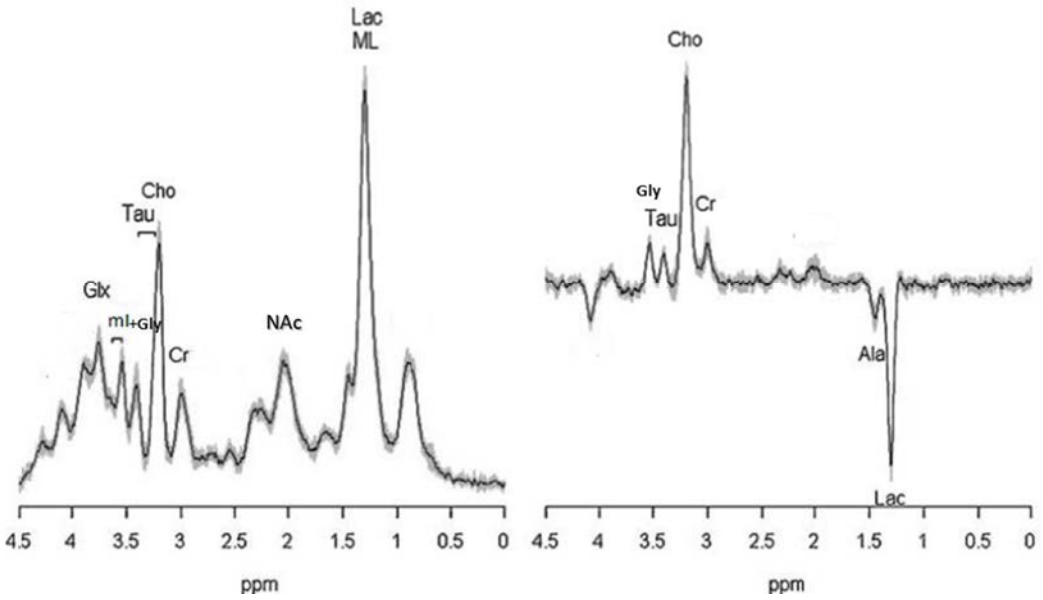

Figure 1.14: Spectral patterns and SD (grey shading) of GL261 tumours at two TEs (12 ms, left, and 136 ms, right) obtained from MRS explorations of C57BL/6J tumour bearing mice (n = 6). Major labelled resonances originate in Ala, alanine (1.45 ppm); Cr, total creatine (3.93 and 3.03 ppm); Cho, choline (3.21 ppm); Glx, glutamine and glutamate (3.77/3.75 ppm); Lac, lactate (1.31 ppm); Lac/ML, lactate and methylene group of fatty acyl chains in ML (1.31 ppm) ; mI+Gly, myo-inositol and glycine (3.55 ppm); NAc, N-acetyl-containing compounds (2.01 ppm); Tau, taurine (3.42 ppm). Modified from [112], (see original work for more detailed assignments).

1.2.1.3 Magnetic Resonance Spectroscopic Imaging (MRSI)

The MRSI acquires simultaneously multiple signals from a grid of voxels, being able to provide metabolic analysis from different regions of the studied tissue and adding spatial information [113] (Figure 1.15) Usually this technique is applied using 2D sequences in clinical [114, 115] and preclinical studies [116, 117]. The 3D-MRSI is also possible but these sequences are not yet implemented in most clinical scanners and their processing pipeline is not so straightforward. Also, the cubic shape of the VOI makes difficult the coverage of the edges of the brain [118], as well as it makes difficult to avoid the interface area among tissues which may decrease the spectral quality due to subcutaneous fat contamination [119]. Despite of these issues, 3D-MRSI clinical studies have been carried out in patients with GB in order to study the tumour or the treatment planning [30, 120–123].

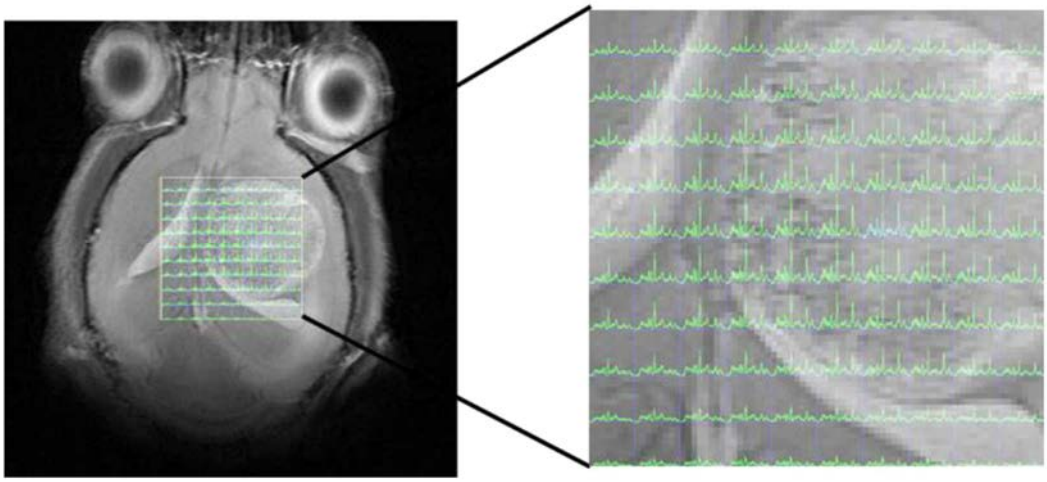

Figure 1.15: MRSI acquisition from a mouse bearing a GL261 tumour *in vivo* at 7T. On the left, MRSI grid superimposed to the correspondent T_{2w} image. On the right, magnification of the grid in which individual spectra can be seen. (Taken from [124]).

MRS and MRSI are important tools for studying brain tumours [125, 126]. It has been also shown that the basal changes observed with MRS or MRSI can be enhanced through perturbation of the basal pattern (perturbation enhanced MRSI, PE-MRSI) with metabolic challenges which could be relevant in pattern recognition studies for improving mouse brain tumour discrimination using acute hyperglycemia [127]. Apart from hyperglycemia PE-MRSI studies, our group has also suggested that DMSO (used to dissolve TMZ in preclinical studies and detected in MRS and MRSI in the brain of treated mice) could also have a potential interest in PE-MRSI studies. It has been proven to present differential retention in untreated GB, GB responding to treatment or relapsing [90] and this could be of great interest for non-invasive assessment of therapy response, although it has not been fully exploited in pattern recognition studies. Also, our group has employed the MRSI technique to acquire MRSI temperature maps of the mouse brain [116, 128] (see also chapter 7).

Brain tumour metabolites and their biological significance

The main brain tumour metabolites and their most detectable NMR signals are described below and Table 1.2 describes the major and minor resonance assignments of these metabolites.

N-acetylaspartate (NAA)

NAA peak is observed at 2.01 ppm, it is one of the most abundant aminoacids in human brain and it is often referred to as a "neuronal marker" related to neural health. NAA concentration is markedly reduced or even absent in pathologies causing axonal loss including malignant or benign tumours, [118, 129]. NAA also serves as a source of metabolic acetate for oligodendrocyte myelination.

Creatine (Cr)

Cr peak is observed at 3.03 ppm with a second signal at 3.9 ppm. Actually, it represents a group of molecules containing both creatine and phosphocreatine and it is involved in cellular metabolism and energy. Cr concentration is relatively constant and it is considered a stable cerebral metabolite, for this reason it is often used as an internal reference for calculating metabolite ratios [130]. However, decreased Cr levels have been reported in hypoxic tumours and stroke [131, 132].

Choline (Cho)

Cho peak is seen at 3.21 ppm, but it represents a set of choline and choline-containing compounds (e.g. phosphocholine, glycerophosphocoline). Cho is a cell membrane turnover marker which reflects cellular proliferation [118]. In tumours, high Cho levels are related to malignancy degree [133].

Lactate (Lac)

Lac peak is a doublet which can be found at 1.33 ppm (also having a signal at ca. 4.1 ppm) which projects above the baseline on short TE acquisitions and inverts below the baseline at long TE. It is a product of anaerobic glycolysis, so its concentration increases under anaerobic metabolism, as hypoxia, ischemia or necrotic tissue. Increased rates of lactate production are associated with a range of tumours and usually points to higher tumour grade but also correlates with tumour metabolic activity [129]. Nevertheless, it has been also described that increased levels of lactate could have important role as neuroprotector in cerebral ischemia [134, 135].

Myoinositol (mI)

Myo-inositol (mI), with a major signal around 3.56 ppm and other signals at 3.26, 3.61 and 4.04 ppm, is considered a glial marker and mI levels have been shown to inversely correlate with astrocytic grade *in vivo*, being lower in high grade tumours [136]. On the other hand, high levels of mI have been reported in gliosis, astrocytosis and in Alzheimer's disease [137].

Glutamate and Glutamine (Glx)

Glutamate (Glu) with major resonance signals in the region 2.04-2.35 ppm acts as the major excitatory neurotransmitter in the brain. Glutamine (Gln) with major signals in the region 2.11-2.46, is a precursor and storage form of Glu located in astrocytes. Glu and Gln play a role in detoxification and regulation of neurotransmitters [137].

Glycine (Gly)

Gly resonates as a single signal at 3.55 ppm, found in elevated concentration in high grade gliomas [138]. It overlaps with MI signal *in vivo* and they cannot be distinguished unless specific

acquisition strategies are used (e.g. acquisition with two different echo times as described in [136]).

Mobile Lipids (ML) and Macromolecules (MM)

ML and MM resonances occur at various regions of the spectrum: around 0.9, 1.3 - 1.4 and 2.0 -2.6 ppm. ML peaks are not observed in normal brain, although artifactual presence, resulting from voxel contamination of lipids from subcutaneous tissue close to the scalp, is not uncommon [119]. Furthermore, they are components of cell membranes, and they are observed when there is cellular membrane breakdown [139]. Therefore, they are all known to be significant markers of tumour malignancy and high lipid signals correlate with necrosis which is a histopathological characteristic of high grade gliomas, caused by hypoxic stress [140].

Polyunsaturated fatty acids (PUFA)

The PUFA, with a peak at 2.8 ppm, are primarily constituents of cellular membranes and in normal brain conditions, its NMR-detectable content is very low. However, it has been observed by MRS that PUFA levels increase in brain tumours after therapy with ganciclovir in BT4C gliomas is administered, which is related to cell apoptosis [141, 142]. Moreover, it has been described by our group that an increase in PUFA levels are observed in spectra of GL261 tumour-bearing mice after the treatment with TMZ [90, 117] in comparison with spectral patterns of non-responding to therapy mice (Figure 1.16).

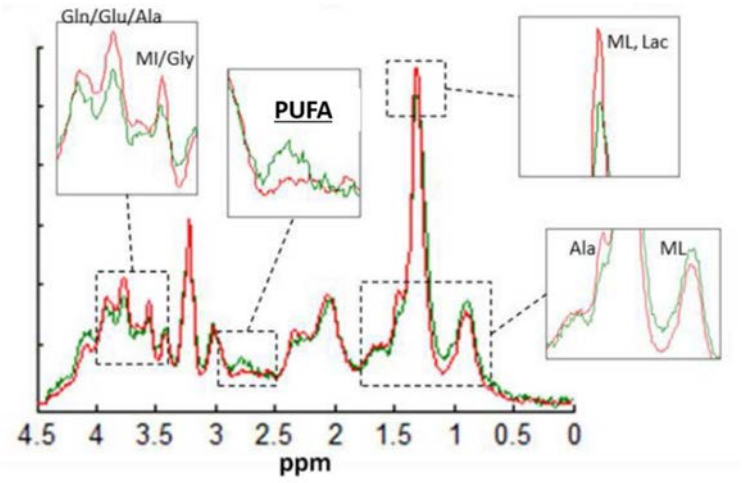

Figure 1.16: Main differences between the responsive (green) and unresponsive (red) spectral patterns of GL261 GB and their peak assignments: higher lactate (4.1 ppm) intensity, combined with lower saturated fatty acid MLs (1.3 ppm), higher total ML (0.9 ppm) and PUFA (2.8 ppm) resonances and a lower myo-inositol/glycine signal (3.55 ppm) are characteristic of cases responding to TMZ. Adapted from [117].

Different metabolites can be seen in spectra from normal-appearing parenchyma or brain tumour masses. The brief description shown above was focused on metabolites presenting special interest for this work. However, it is worth noting that other minority metabolites such as 2 hydroxyglutarate or fumarate (also known as oncometabolites, [143, 144]) are currently being studied and should not be neglected.

The information contained in MRS/MRSI can be analysed using different strategies. Most studies rely on single metabolite study (Cho, 2HG) or particular metabolite ratios (NAA/Cho, NAA/Cr, [145]) or indexes such as the Choline-NAA index (CNI) [146]. However, these type of approaches neglect the rest of the information contained in the whole spectral vector, which can improve or refine MRS/MRSI based studies, either for diagnosis or for tumour follow-up during therapy. Pattern recognition studies can embrace the rich information contained in spectral patterns and integrate it in a supervised or semi-supervised way (see section 1.3 below).

Table 1.2: Resonance assignments corresponding to each metabolite resonances that can be found in human brain *in vivo* 1H spectra at 1.5T in human brain (adapted from [147]).

Metabolite	ppm
N-acetylaspartate (NAA)	2.01, 2.49, 2.67, 4.38 and 6.13
Creatine (Cr)	3.03 and 3.91
Choline (Cho)	3.19, 3.50 and 4.05
Lactate (Lac)	1.31 and 4.10
Myoinositol (mI)	3.26, 3.52, 3.61 and 4.05
Glutamate (Glu)	2.04, 2.12, 2.34, 2.35 and 3.74
Glutamine (Gln)	2.11, 2.13, 2.43, 2.45 and 3.75
Glycine (Gly)	3.55
Mobile Lipids (ML) and/or macromolecules (MM)	0.9, 1.3-1.4 and 2.0-2.9

1.3 Pattern recognition (PR) analysis

MRS allows obtaining information about the biochemical environment of a given tissue, and different situations (e.g. grading, treated vs untreated tumour) can produce metabolic changes of variable magnitude. However, the richness of information contained in the spectra could represent a challenge for its interpretation, especially when changes are observed in several metabolites at once. Combining MRS techniques with reliable algorithms of pattern recognition (PR) analysis has the potential to identify relationships between the quantitative changes of different metabolites simultaneously and detect subtle differences in metabolic profiles. The PR is defined as the process of the classification from a given collection of measurements (input

data, e.g. spectral vectors) into different categories based on key features contained in it (e.g. treated vs untreated tumour) using automated decision-making processes. There are three major classification strategies used in PR: supervised, unsupervised and semi-supervised classification.

1.3.1 Supervised PR analysis

In the supervised PR methods, a mathematical model is developed using a given collection of cases named "training set". Data vectors are assigned to different classes based on a previous classification – normally histopathological analysis in case of brain tumours [148]. Once the system is trained, the classifier and mathematical algorithms extracted can be applied to a different set of cases ("test set"). Thus, the robustness of the classifier is assessed by comparing the assignment of the input data to the appropriate class labels [149].

Supervised classification basically consists in three steps:

1. Dimensionality reduction of the data, allowing the detection of the relevant characteristics of spectra that may better represent one class.
2. Learning phase on training set and classification of the spectra in different classes based on the differential descriptive characteristics.
3. Predictive (allowing to assign a new spectrum to one of the previously established classes) and evaluation of the robustness of the classification in terms of their descriptive characteristics (which allows discrimination of differences between groups) [127].

There are several types of supervised techniques that can be applied to MR data, but the most classical one is Linear Discriminant Analysis (LDA) [150].

1.3.2 Unsupervised PR analysis

As opposed to the supervised methodology, in the unsupervised classification, the user does not assign the initial cases to a particular class. Unsupervised techniques try to group cases based on their similarities, without a previous knowledge of the exact grouping. The similarity measurement is based on the distance of the samples in the multi-dimensional feature space constructed by the observed data features. Clustering technique, Principal Component Analysis (PCA) or non-negative matrix factorization (NMF) [151, 152] are examples of common unsupervised techniques.

Such techniques have the advantage that each class is represented by a spectroscopic characteristic pattern of a given "metabolic state", also called source, instead of being

represented by a given number of features. From the biochemical point of view, the source extraction technique for MRS data classification assumes that in each voxel there is a mixture of heterogeneous tissues pattern and contribution of each source can be presented [153]. The obvious advantage of this approach lies in the fact that the labelling procedure becomes independent of the availability of labelled MRSI datasets and the negative effect of mislabelled cases on the generalization capabilities of the model will be prevented.

1.3.2.1 NMF (& Convex-NMF) methods

NMF methods are a group of multivariate data analysis techniques aimed to estimate meaningful latent components, also known as sources, from non-negative data. In standard NMF methods [152], the data matrix V (of dimensions *d* x *n*, where *d* is the data dimensionality and *n* is the number of observations) is approximately factorized into two non-negative matrices, the matrix of sources W (of dimensions *d* x *k*, where *k* is the number of sources, and *k*< *d*) and the mixing matrix H (of dimensions *k* x *n*, each of whose columns provides the encoding of a data point from the spectrum of a voxel). The product of these two matrices provides a good approximation to the original data matrix (Figure 1.17).

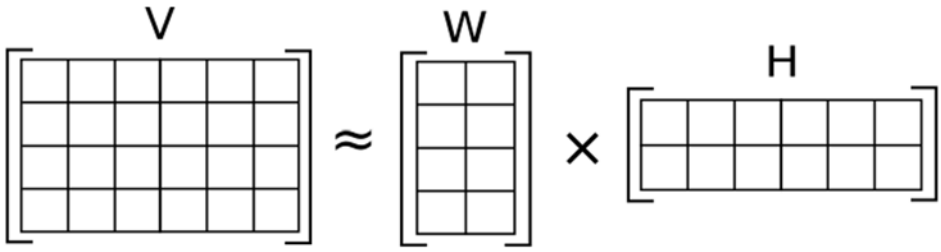

Figure 1.17: Data matrix V could be decomposed in two matrix components, the matrix of sources (2 in this example) or data basis W and the mixing matrix H. The product of the matrix W and H provides a good approximation to the original data matrix (V).

A variant of NMF is Convex-NMF [153, 154], unlike the other variants of NMF methods, this one applies to both nonnegative and mixed-sign data matrices. It allows also the sources in W to be of mixed-sign, while the mixing coefficients in H are non-negative.

In [153], robust delimitation between tumour and normal brain in individual cases was achieved applying an unsupervised methodology using Convex-NMF source extraction in preclinical MRSI data.

1.3.3 Semi-supervised PR analysis

The semi-supervised PR methodology is based on the fact that Convex-NMF is able to generate sparse mixing matrices H, which are practical as cluster indicators. Therefore, the sources obtained by Convex-NMF are likely to be interpretable and similar to data group centroids [153].

The semi-supervised system described in [155] makes use of both labelled and unlabelled data for training and proposes to take benefit from the use of prior knowledge derived from class membership of the spectra to guide the source extraction. The first stage is the definition of a Fisher Information (FI) metric [156] to model pairwise similarities and dissimilarities between data points, using a Multi-Layer Perceptron (MLP) classifier to estimate the conditional probabilities of class membership. The second part consists on the approximation of the empirical data distribution in a Euclidean projective space in which NMF-based techniques can be applied (this was done in [155] with Multidimensional Scaling methods, specifically with the iterative majorization algorithm). The last part involves the application of Convex-NMF for the source decomposition of the data.

1.3.1.2 Nosological imaging of the response to therapy

The potential of classifying different tissue types in brain tumours applying PR recognition techniques to MRSI datasets leads to the possibility of representing the different output classes (tissues) as nosological images [90]. This approach is not new and was first proposed several years ago by researchers from Grenoble [114]. The representation of the MRSI data classification as images may help radiologists in the clinical management of brain tumours, for instance in the appropriate delimitation of the pathological area. The PR analysis of different spectra of treated and untreated animals can be used to classify which voxels from MRSI matrices correspond to each class, namely normal brain tissue, treated/responding and untreated/unresponsive tumour as described in [117], in which each individual voxel in the MRSI grid is referred to as spectral vector (spv) and considered as an individual case. Then, after the PR studies, the classification result obtained for each voxel is colour-coded being assigned the colour corresponding to the source most contributing to each voxel, either responding or untreated/unresponsive/relapsing or normal brain. An example of therapy follow-up study obtained during this thesis work using this approach is shown in Figure 1.18.

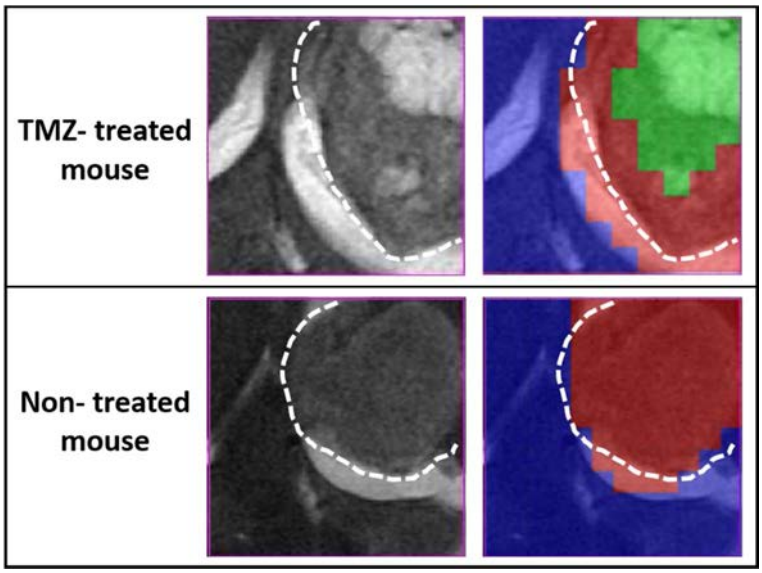

Figure 1.18: Examples of nosological semi-supervised maps corresponding to mice C971 (GL261 GB responding to TMZ, top) and C1111 (control GL261 GB, bottom). The Cxxx notation corresponds to the internal GABRMN research group unique mouse identifier code. The boundaries of the T_{2w} abnormal masses are marked with a white discontinuous line. On the left of each map, the high resolution T_{2w} images used as references for MRSI studies are shown. For each map, colour coding is as follows: blue represents normal tissue, red is actively proliferating tumour and green is tumour responding to therapy.

1.4 Nanoparticles and its potential to improve GB diagnosis and therapy

Nanoparticles (NPs) are defined as particulate dispersions or solid "nanoscale" particles with a size usually in the range of 10-1000 nm which show properties than can be exploited for the design of therapeutic effects and diagnostics [157]. NPs can be made from a variety of materials such as polymers, lipids, proteins, metals, or semiconductors. They can be synthesized with a variety of shapes as solid spheres, rods, tubes, and other complex shapes.

In general, NPs have larger surface to volume ratios when compared to the same volume of material made up of bigger particles, and this feature contributes to their high loading capacity. As drug delivery systems, nanoparticles have been shown to improve drug solubility, prolong blood circulation half-life, and control drug release [158]. Many nanoparticle delivery systems are designed to respond to various environmental stimuli such as pH, allowing a controlled therapeutic release [159]. Regarding NPs in brain tumour research, they can be classified into three categories: organic- based (liposomes, polymeric nanoparticles, micelles, dendrimers, and solid lipid nanoparticles), inorganic-based (such as iron oxide nanoparticles, gold nanoparticles, carbon nanotubes) and hybrid nanoparticles (synthesized from two or more types of nanomaterials [160]). The ability of crossing the BBB and acting as CA or drug-carriers, and also

the possibility of generating local hyperthermia, makes them an interesting field to be studied, which also opens the possibility of creating multifunctional NPs.

1.4.1 Nanoparticle characterization

Proper characterization of nanoparticles is crucial because aspects such as particle size, shape or charge can determine the *in vivo* distribution, biological fate, toxicity and the targeting ability of nanoparticle systems. In addition, they can also influence the drug loading, drug release and stability of nanoparticles [161]. Indeed, particle size and surface charge are the two most commonly mentioned factors that are responsible for a range of biological effects of NPs including cellular uptake, toxicity and solubility properties [162].

Particle size can be determined by Dynamic light scattering (DLS), Nanoparticle Tracking Analysis (NTA) or electron microscopy (SEM or TEM). The hydrodynamic radius (Rh) is defined as the radius of the hypothetical hard sphere that diffuses with the same speed as the particles assayed. Often the dispersed particles are hydrated/solvated and surrounded by a corona which composition depends on the ionic strength, molecules present in the environment and nature of solvents [163].

Particle charge (zeta potential, ZP) reflects its surface electrical potential, and it is influenced by the composition of the particle and the medium in which it is dispersed. When a charged particle is dispersed, an electric double layer (EDL) develops on its surface [164] (Figure 1.19). When an electric field is applied to the dispersion, the charged particles move towards the opposite electrode and there is a hypothetical plane acting as the interface between moving particles and the dispersant. This plane is the Slipping/Shear plane and ZP reflects the potential difference between the electrophoretically mobile particles and the layer of dispersant around them at the slipping plane. Some factors can influence ZP [162], such as pH changes, ionic strength, concentration of NPs or the of cell culture medium.

Zeta potential is related to the colloidal stability prediction. Orientative guidelines were established in order to classify the stability of a dispersion of NPs according to the ZP, as it shown in Table 1.3:

Table 1.3: NPs stability according to ZP values [162]:

ZP value	Stability
± 0 – 10 mV	Highly unstable
± 10 – 20 mV	Relatively stable
± 20 – 30 mV	Moderately stable
± 30 mV	Highly stable

Those are only indicative values, being real situations more complex because ZP does not provide any insight on the attractive van der Walls forces. Therefore, is not uncommon to find stable NPs dispersions with low ZP and viceversa. Also, it should be noted that steric interactions and addition of polyethylene glycol (PEG, see also section 1.4.5) to nanoparticles can stabilize NPs while decreasing ZP value [165].

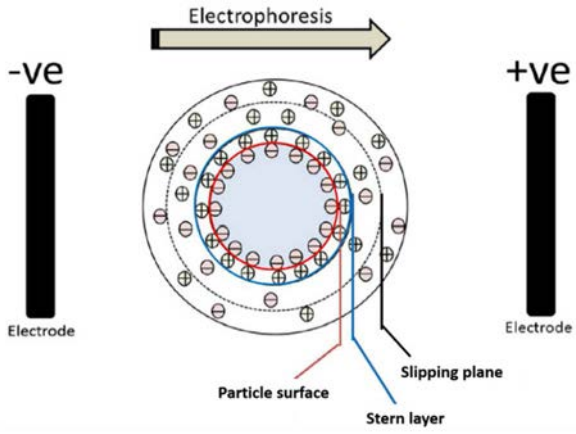

Figure 1.19: Figure showing the EDL on a negatively charged particle. Immediately on top of the particle surface there is a strongly adhered layer (Stern layer) comprising of ions of opposite charge i.e. positive ions in this case. Beyond Stern layer a diffuse layer develops consisting of both negative and positive charges. During electrophoresis the particle with adsorbed EDL moves towards the electrodes (positive electrode in this case) with the slipping plane becoming the interface between the mobile particles and dispersant. The ZP is the electrokinetic potential at this slipping plane. Obtained from [162].

1.4.2 Types of Nanoparticles

Some of the most representative types of nanoparticles studied for glioma diagnosis and therapy applications are shown in Figure 1.20.

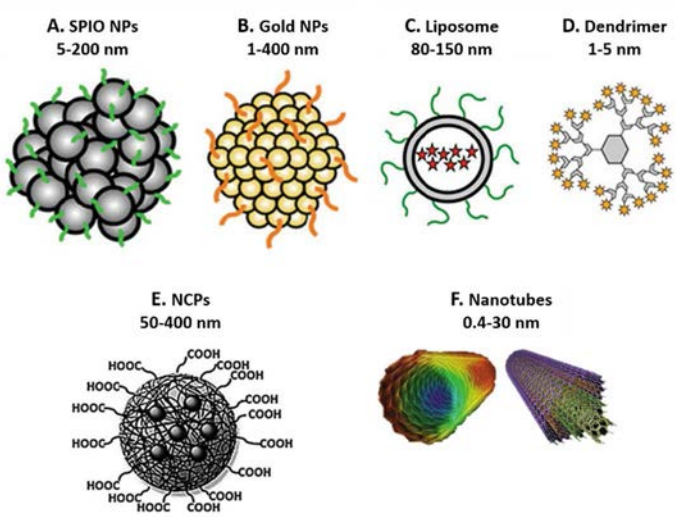

Figure 1.20: Representative examples of nanoparticles frequently used for diagnosis and therapy of gliomas and their relative sizes. (A, B, C and D adapted from [166]; E adapted from [104]; F adapted from [167] and [168]).

Although there is a high number of studies involving nanoparticles, very few of them reach clinical trials and in fact most of the currently approved nanoparticles for cancer treatment such as Abraxane® and Doxil®, are based in liposomes. **Liposomes** are self-assembled spherical phospholipid bilayers with easy surface modification, encapsulation capacity and good biocompatibility. Major advantages of liposomes include selective accumulation in brain tumours by passive and active targeting and improved pharmacokinectic effect [110]. Some examples of liposome-based drugs delivery systems to target gliomas are described in [169–171].

Other nanoparticle types currently being studies are **dendrimers**, polymer-based structures which are highly branched, giving rise to multigenerational nanoparticles with external end groups that can be functionalized. Dendrimers have been proven to be successful carriers for drugs and contrast agents in preclinical studies [172–174].

Nanotubes, which are self-assembling sheets of graphite-like carbon atoms arranged in tube forms, have been studied in combination with TMZ metronomic therapy with good results in GL261 tumour-bearing mice [175].

Regarding **Inorganic Nanoparticles,** they consist of a solid core material that can be either a semiconductor framework, metal or magnetic and some of them have been developed as

therapeutic agents for light-mediated glioma treatment [176]. Particularly, within metal nanoparticles, Gold NPs have been of high interest because of their relative low toxicity, dynamic surface chemistry, size, and shape. Nanorod or Nanoshell nanoparticles can strongly absorb light in the near-infrared (NIR) range due to surface plasmon resonance (SPR) properties and to efficiently convert this energy into heat for photothermal therapy or hyperthermia [177–180] (see section 1.4.3). Still, novel developments such as gold nanoprisms are also being evaluated [181]. On the other hand, regarding magnetic nanoparticles, iron oxide-based nanoparticles as SPIO (small iron oxide particles) can be used as contrast agents to produce hypointense regions on T_2/T_2*-weighted MR images (see section 1.2.1.1 and section 1.4.4). They can be also used as therapeutic agents by drug conjugation or for hyperthermia treatment through application of magnetic fields [182–185].

Finally, a novel and promising group of nanoparticles are the **nanostructured coordination particles** (NCP) which consists of a family of metal-organic nanoparticles formed by the assembly of metal ions and organic polymers [186] showing relevant potential applications in the Biomedicine field as contrast agents or drug-delivery systems [104, 187, 188].

An exhaustive description of all nanoparticle types and applications is beyond the scope of this thesis. Studies described here will be focused into preclinical glioblastoma therapy and diagnosis using respectively Gold and NCP nanoparticles (sections 1.4.3 and 1.4.4).

1.4.3 Hyperthermia for cancer therapy using Gold Nanoparticles

In cancer therapy, hyperthermia consists in heating a chosen tumour area in order to eradicate tumour cells or make them more sensitive to the effects of radiation and chemotherapeutic drugs. For humans, temperatures between 40 and 44 °C are enough to act as cytotoxic death-inducers for cells in an environment with a low pO_2 and low pH, conditions that are found specifically in tumour tissue [189]. In this sense, the progress in nanomedical research offers the potential to specifically target metal NPs into tumour cells, with a special interest in gold NPs. Then, when an energy source such NIR laser is applied, local heating is produced, leading to tumour cell death [177]. It is worth mentioning that hyperthermia was also described to elicit immunogenic cell death/damage [190] which could offer a potential added interest for therapy.

Furthermore, lasers can be specifically tuned to the SPR frequency of nanoparticles, which varies with their size, shape and composition. Gold nanoshells and nanorods were proven useful in several preclinical model applications [191]. Regarding hyperthermia, gold nanoshell potential has been previously described in breast tumour xenografts [178, 192], subcutaneous models of

both murine colon carcinoma and brain tumours [193, 194] and intracranial tumours [195]. The use of hyperthermia as an alternative therapeutic strategy for preclinical glioblastoma would be of great interest, given that these tumours only present a transient response to TMZ therapy in the classical described schedule, and hyperthermia could be a possible "second line" treatment whenever a tumour becomes resistant.

1.4.4 Nanoparticles as brain tumour contrast agents

Nanoparticles have been used in brain tumours with different applications in clinical studies and in preclinical models, including tumour diagnosis improvement and therapy [168, 180, 196, 197]. Nevertheless, most NPs are unable to cross the BBB [198, 199] unless specific peptides for barrier crossing are attached to NPs [200], and this is relevant in case of early brain tumour stages, or low grade tumours. In the case of GB, the BBB is compromised, being permeable to different molecules. This BBB disruption in GB is due to disorganisation of vessel structures produced by migration of endothelial cells to participate in new angiogenic processes closely associated with the tumour. Moreover, as the tumour secretes different molecules that alter the normal microenvironment, cell migration is not controlled and it is reflected in resulting abnormal vascular architecture [37]. For this reason, contrast agents are able to cross the disrupted BBB and whenever this takes place, contrast enhancement is observed in affected regions.

Different NP systems are able to behave as T_1 or T_2 contrast agents (reviewed in [166]). However, regarding T_2 contrast agents, only ultra-small superparamagnetic iron oxide (USPIO) reached the clinic, mostly for imaging liver, spleen and lymph nodes, but not brain tumours [98, 166]. At present, no T_2 agent is used in clinics in Europe (e.g. *Sinerem*, withdrawn since 2007 [166, 201] or *Endorem* which had its synthesis discontinued by manufacturers since 2008). It is worth noting that preclinical research is still carried out in order to search for improvement in this type of contrasts agents [202].

More recently, synthesis of dual contrast agents (able to produce contrast in both T_1 and T_2 weighted images) is being explored by several groups [104, 107, 203, 204]. This dual modality would allow obtaining information of T_{1w} and T_{2w} images in the same exploration with the same contrast agent. Some of the dual agents developed are gadolinium-based [106, 204, 205] but others are exploring less toxic or non-toxic approaches such as iron [104] which could represent an advantage over gadolinium-based systems. In case of brain tumours, the information provided by a T_2 (or dual) contrast agent in diagnosis or follow-up is not fully evaluated yet.

Whether this information could offer an added value in addition to evaluation with RECIST [71] or RANO [70] MRI criteria or metabolomic information is still to be investigated.

1.4.5 Nanoparticle distribution – EPR and other effects

The size of a NP is a fundamental parameter which determines its passive targeting and biodistribution in brain tumours. NPs with a size range between 10 and 100 nm are able to go through the leaky vessels of tumours to passively enter the intratumoural space, but not accumulating in healthy brain tissue. This phenomenon of accumulation in the tumour due to the permeability of the vessels is named enhanced permeability and retention (EPR) effect [206]. Nevertheless, despite the EPR effect seems to be an advantage for the GB evaluation with NPs, care should be taken to avoid NP removal by cells of the reticuloendothelial system (RES) once injected. When NPs are intravenously injected, opsonisation and removal by RES can take place and NPs found trapped in the liver, spleen, lung, kidney and bone marrow [207]. In order to achieve an optimal EPR effect, NPs size should present a diameter smaller than 100 nm and present biocompatible surfaces (neutral electric charge).

This means that, in addition to the size, the functionalization of NP surface is an important factor which can determine their behaviour and applications [208]. One of the most used methods of functionalization is the use of hydrophilic polymers such as PEG for surface coating which would make NPs more resistant to protein adsorption [209] and RES uptake [210]). The functionalization with PEG extends the circulating half-life of NPs, which in turn increases the chance of reaching the tumour. However, a number of limitations and challenges still hamper complete deployment of PEG-coated NPs. Although its toxicity is low (inversely proportional to molecular weight, especially after oral ingestion), PEG immunogenicity has been reported, but generally less than the immunogenicity of the naked NPs [211]. A final challenge of PEG-coating is its degradation by light, heat or sheer stress, which can result in fragmentation of the PEG cover and diminish cloaking ability [212]. Last, but not least, the PEG signal could be detected by MRS and could work as a “reporter” of the NP presence inside the tumour, provided a minimum concentration which reaches the tumoural tissue.

Targeting the receptors normally expressed on the brain capillary endothelial cells, such as transferrin transporters, is another way of directing NPs to tumours and enhance their delivery [172, 183, 213]. As more glioma-specific receptors are identified, nanoparticles may be able to integrate multiple moieties providing a dynamic platform for targeting heterogeneous brain tumours. Figure 1.21 summarizes the variety of mechanisms nanoparticles can use to reach a

brain tumour including the EPR effect, carrier-mediated transportation, receptor-mediated endocytosis, and adsorptive-mediated endocytosis. However, even in most favourable conditions, the overall percentage of systemically injected nanoparticles found in a solid tumour is only 0.7% of the total injected [214].

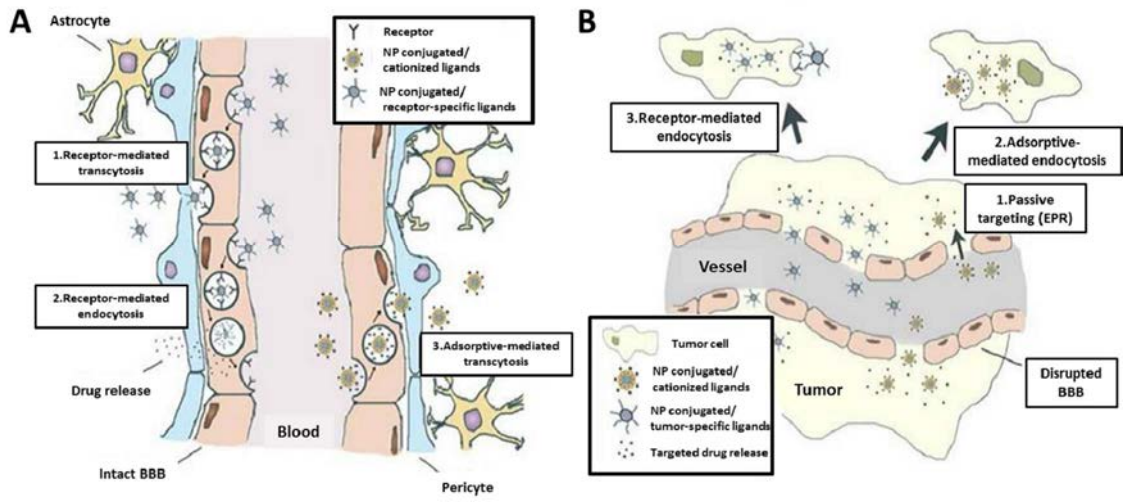

Figure 1.21: Mechanisms of transportation of multifunctional nanoparticles into a brain tumour. A. Transport of multifunctional nanoparticles across the BBB: 1) receptor-mediated transcytosis, 2) receptor-mediated endocytosis, 3) adsorptive-mediated transcytosis of nanoparticles. B. Mechanisms of transportation across the disrupted BBB and selective targeting of brain tumour cells: 1) passive targeting via the EPR effect, 2) adsorptive-mediated endocytosis or 3) receptor-mediated endocytosis. Obtained from [110].

1.4.6 Nanoparticle toxicology

Investigating the potential toxicity of nanoparticles and their impact in health is essential before the use of these nanomaterials reaches preclinical or clinical applications. Long-term effects of nanomaterials are not enough studied and still have to be addressed.

Although inorganic NPs are being used in research approaches, their safety is not clear in some cases. While several studies with metallic particles have shown no apparent toxicity at short term time frames, there is still concern about potential adverse side effects *in vivo*, particularly due to non-specific accumulation in non-target tissues [215–217] or generation of reactive oxygen species (ROS) due to exposition to magnetic iron oxide NP as described in [218]. Regarding gold nanoparticles, toxicity could arise from any of the components of the NPs, as well as from residual surfactants such as Cetyltrimethylammonium Bromide (CTAB) or other synthesis adjuvants which could contribute to the potential toxicity [219]. More insight in the toxicological aspects of NPs will be described in chapter 7.

Although there are several toxicological studies to assess the safety of nanoparticles [220], there is still room for improvement, taking into account that a whole organism is far more complex than a cell culture. More comprehensive toxicological studies should include assessment of abnormality in animal behaviour, weight loss, mortality percentage and life span which cannot be properly addressed in short term studies. In addition, specific studies at tissue-level are needed to assess hepatotoxicity, nephrotoxicity, haematological toxicity and immunogenicity and inflammatory responses due to nanoparticles [207, 215, 221].

Nanoparticle size can also be determinant in its toxicity in preclinical models and it should be taken into account when using NP for diagnosis or therapy. Sizes ranging 5-50nm seem to produce more evident toxicological effects in comparison with larger sizes [222, 223]. This should not be neglected in studies with whole organisms, although some of the toxicological effects related to accumulation in non-target organs could be simulated *in vitro* [224].

1.4.6.1 Endotoxin contamination

Endotoxin or LPS (lipopolysaccharide) is a large molecule (200–1000 kDa) found on the outer membrane of Gram-negative bacteria and can be a relevant factor in NP toxicology, if the synthesis is not properly done. It consists of a polysaccharide region and a lipid region (lipid A), which is the responsible for inducing toxicity. In humans, endotoxin could cause various life-threatening diseases, such as respiratory symptoms, pulmonary inflammation and asthma, and high levels of endotoxin in blood circulation (called endotoxemia) can occur in some systemic infections or severe trauma, causing a systemic response such as fever, hypotensive shock, impaired organ function and eventually multiple organ failure and death [225]. Mice also present acute inflammatory responses due to endotoxin [226]. In addition, authors from [227] described some additional symptoms for C57BL/6 mice inoculated with LPS, such as hind leg weakness or paralysis, rigidity, jerky rhythmic motions, intention tremor, ataxia, spastic paralysis, convulsions, coma, lethargy, anorexia, dehydration, anuria, body swelling with oedematous pouches, ruffled fur, loss of fur, shivering, tachypnea, restlessness and death.

Endotoxin can attach to nanomaterials, adhering to hydrophobic surfaces through its lipid moiety, while its phosphate group allows it to bind to positively charged surfaces [228]. The biological effects generated by endotoxin contamination of nanoparticles could mask or interfere with the true biological effects of nanomaterials. Hence, reliably discriminating the endotoxin activity from the nanomaterials' intrinsic inflammatory activity is important for nano-safety studies. The *Limulus amoebocyte* lysate (LAL) assay is one endotoxin detection method that is approved by FDA (US Food and Drug Administration). In the LAL assay, an enzyme in the

blood cells (amoebocytes) of the horseshoe crab *Limulus polyphemus* causes protein clotting when activated by endotoxin [229] and it is commonly used for assessment of endotoxin content in NP batches [225, 229].

2. General Objectives

The general objective of this thesis was to improve and refine preclinical glioblastoma detection, treatment and response follow-up using MR-based methods, through the following specific sub-objectives:

A. Detection and diagnosis: characterization of novel nanostructured coordination particles with potential dual T_1/T_2 MRI contrast enhancement in a preclinical GL261 GB model (chapter 4).

B. Non-invasive therapy response assessment:

B.1 Development of a multi-slice MRSI approach for non-invasive therapy response monitoring in a volumetric approach (chapter 5).

B.2 Longitudinal evaluation of the developed multi-slice MRSI method in preclinical GL261 GB under TMZ treatment using semi-supervised source analysis and its correlation with histopathology analysis (chapter 6).

C. ***Preliminary unfinished work:***

Set-up and development of a gold nanoparticle-based hyperthermia therapeutic strategy for preclinical GL261 GB treatment (chapter 7).

3. General materials and methods

3.1 Cell culture

Glioma GL261 mouse cells were obtained from the Tumour Bank Repository in the National Cancer Institute (Frederick/MD, USA) in a passage 8, and cultured as described in [112]. Essentially, cells were cultured in 75 cm^2 flasks (Nunc, LabClinics SA, Barcelona), using culture medium RPMI-1640 (Roswell Park Memorial Institute, Sigma-Aldrich, Madrid), supplemented with 2.0 g/L sodium bicarbonate, 0.285 g/L glutamine, 1% penicillin-streptomycin (Sigma-Aldrich, Madrid) and 10% of foetal bovine serum (Gibco, Invitrogen, UK). Flasks were maintained at 37 ˚C, 5% CO_2 and 95% humidity in a sterile cell-incubator (HERAcell 150i, Thermo Scientific).

Cells were subcultured when 75-85% of confluence was reached (ca. at day 7 post-cell culture) and culture medium change was performed at days 3 and 5 post-cell culture. For subculturing, the culture medium was aspirated using a vacuum pump and the flask washed with 10 ml of sterile PBS. The PBS was removed and 2 ml of trypsin-EDTA (0.5 g/L and 0.2 g/L respectively, Sigma-Aldrich, Madrid) were added in order to detach the cells. RPMI medium (8 ml) was added until 10 ml of total volume and cells were resuspended. New flasks with 25 ml of culture medium were seeded with ~$7x10^5$ cells from this suspension. Cells were maintained in culture up to passage 30-35, when the cells were discarded to avoid genetic drift or unexpected mutations.

3.1.2 Cell counting

The cellular resuspension obtained in section 3.1 was centrifuged at 1,400 x g during 1.5 minutes. The obtained supernatant was aspirated and the pellet was resuspended in 10 ml of culture medium. From this cell resuspension, an aliquot of 10 µl was added to 10 µl of Trypan Blue (0.4 % solution prepared in 0.81% of sodium chloride and 0.06% of potassium phosphate, Sigma Aldrich). Trypan Blue exclusion test differentially stains living and dead cells, as the latter are unable to extrude the dye. Cell counting was performed in duplicate with the TC20™ automated cell counter system (BioRad, Madrid)[1].

3.2 Animal model

All animals studied in this thesis were assigned an alphanumeric individual identifier corresponding to CXXX or wtXXX (depending on whether they were tumour-bearing animals or

[1] The counting mechanism of this equipment is based on a microscope with an automatic focus mode that analyses multiple focal planes to identify alive and dead cells (stained with Trypan Blue). The output is the number of total cells per mL of initial cellular resuspension, number of total living cells per mL of cellular resuspension and the percentage of viability (which in our case ranged 95-100%).

wt animals), being "XXX" a correlative increasing number. Animals were housed in *Servei d'Estabulari* of *Universidad Autònoma de Barcelona*[2]. The supervision protocol for these animals is shown in Annex I and was followed by veterinary staff from *Servei d'Estabulari* to assess the animals' health state and decide about mitigating actions or euthanization. The experiments were conducted according to experimental protocols, previously approved by the local ethics committee (*Comissió d'Ètica en l'Experimentació Animal i Humana*[3], protocol CEEAH 2785/DMAH 8333).

3.2.1 Wild type C57BL/6J mice

Female C57BL/6J mice of 18-23g in weight and 14-16 weeks of age were obtained from Charles River Laboratories (Charles River Laboratories International, L'Arbresle, France). These mice were used either to generate the stereoactically induced GL261 tumour as described in Section 3.2.2, or as control animals in therapy studies. In order to distinguish animals housed in the same cage, unique ear notches were made by an ear punch device; 1, 2 or 3 notches and their combinations in both ears, as shown in Figure 3.1.

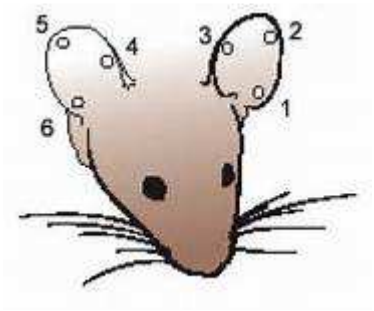

Figure 3.1: Scheme for marking mice by ear punching.

3.2.2 Generation of GL261 tumours by stereotactic injection of cells

The generation of GL261 tumours was performed following protocols previously established in our group [112]. After cell counting (Section 3.1.2), the cell suspension was transferred into a 15 ml Falcon tube (Deltalab SLU, Barcelona, Spain) and centrifuged 1.5 minutes at 1,400 x g (Centrifuge Selecta S-240, ALCO, *Suministres per a Laboratori*, Terrassa, Spain). The supernatant was removed and the pellet resuspended in the RPMI medium, so that each 4 µl contained 10^5 cells, according to the Equation 3.1:

[2] (https://estabulari.uab.cat/#!/home)
[3] http://www.uab.cat/web/comissio-d-etica-en-l-experimentacio-animal-i-humana-1345713724512.html,

$$Vf = \frac{(4\ \mu l\ x\ Cf)}{10^5}$$ **Equation 3.1**

Where Vf is the final volume of the medium for cells resuspension (in µl) and Cf is the total number of cells in the pellet.

Analgesia was administered subcutaneously to each animal 15 minutes prior to anaesthesia and also 24 and 48 hours after surgery (Meloxicam, 1.0 mg/kg, Boehringer Ingelheim, Barcelona). Animals were anesthetized with a mixture of ketamine (Parke-Davis SL, Madrid) and xylazine (Carlier, Barcelona) with doses of 80 mg/kg and 10 mg/kg respectively. This mixture was administered intraperitoneally and the animal was immobilized in a stereotaxic holder (Kopf Instruments, Tujunga/ CA, USA), as shown in Figure 3.2. After shaving the hair of the head area, the incision site was sterilized and 1 cm incision was made exposing the skull, and a 1mm hole was drilled using a microdrill (Fine Science Tools, Heidelberg, Germany) in a precise area using these coordinates: 0.1 mm posterior to the *Bregma* and 2.32 mm lateral (right) to the midline.

A 26 G Hamilton syringe (Reno/NV, USA), positioned on a digital push-pull microinjector (Harvard Apparatus, Holliston/MA, USA) was then used for injection of 4 µl RPMI medium containing 10^5 GL261 cells at a depth of 3.35 mm from the skull surface at a rate of 2 µl/min. Once the injection was completed, the syringe was left for two minutes before the removal to allow the cells to settle and to prevent them from leaking outside the skull. Then the Hamilton syringe was gently taken out, the scission site closed with suture silk 5.0 (Braun, Barcelona) and the animal was allowed to recover form anaesthesia in cage racks in the animal facility in a warm environment (~25°C).

Figure 3.2: An anaesthetized C57BL/6J mouse immobilized in a stereotactic holder.

3.2.3 Stereotactic injection of nanoparticles in mice

The stereotactical injection of nanoparticles performed in chapters 4 and 7 used the same protocol described in the section 3.2.2, replacing tumour cell suspension by NP solution.

3.3 Tissue preservation for post-mortem procedures

Whole brains were excised and fixed (preserved in 4% paraformaldehyde) for histopathological analysis or stored frozen in liquid nitrogen for further analysis with inductively coupled plasma mass spectrometry (ICP-MS) studies. Animal euthanization was performed either for validation purposes or due to endpoint criteria. The criteria used to decide about animal euthanization due to welfare parameters are shown in Annex I.

3.4 Temozolomide therapy

TMZ (Sigma-Aldrich, Madrid, Spain) was dissolved in 10% DMSO in saline solution (0.9% NaCl) for *in vivo* experiments and it was administered using an oral gavage at a dose of 60 mg/kg as in [90]. The standard administration consisted in 3 therapy cycles with a 3-day interleave, the duration of each cycle is 5 days for the first cycle and 2 days for second and third cycle. A scheme of standard TMZ administration is shown in Figure 3.3.

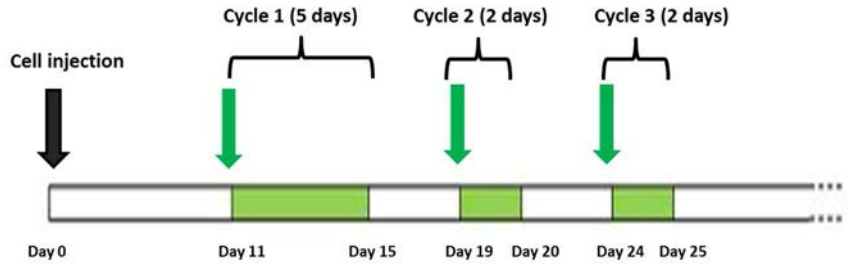

Figure 3.3: TMZ administration schema with 3 therapy cycles with a 3-day interleave, as described previously by us [90]. The starting day of each cycle is marked with green arrows.

3.5 *In vivo* MRI/MRSI

MR studies were carried out at the joint NMR facility of the Universitat Autònoma de Barcelona and CIBER-BBN (Cerdanyola del Vallès, Spain), unit 25 of NANBIOSIS ICTS (http://www.nanbiosis.es/portfolio/u25-nmr-biomedical-application-i/) with a 7T horizontal magnet (Biospec 70/30, Bruker BioSpin, Ettlingen, Germany) equipped with actively shielded gradients (B-GA12 gradient coil inserted into a B-GA20S gradient system) and a quadrature receive surface coil, actively decoupled from a volume resonator with 72 mm inner diameter.

Mice were placed in the scanner bed and anaesthesia was maintained with 0.5-2.0% isoflurane in O_2, keeping the breathing frequency at 60-80 breaths/min. The body temperature was controlled using a recirculating water system incorporated to the animal bed and measured by a rectal probe and maintained at ~37°C. Both temperature and breathing rhythm were monitored by a control/gating module from SA Instruments Inc. (Stone Brook, NY, USA). Data gathered by the module was transferred to a personal PC (Dell Inspiron 510m) and monitored with the PCSAM 32 software (version 6.26, Small Animal Instruments, Incorporated). Only the general procedures which are common to several chapters will be described in this section. Specific MRI/MRS/MRSI acquisitions or optimizations will be detailed in the corresponding chapters.

3.5.1 MRI acquisition for tumour volume calculations

Animals were screened by acquiring high resolution coronal T_{2w} images (TR/TEeff= 4200/36 ms) using a Rapid Acquisition with Relaxation Enhancement (RARE) sequence to detect brain tumour presence and monitor its evolution stage. The acquisition parameters were as following: turbo factor, 8; field of view (FOV), 19.2x19.2 mm; matrix size, 256x256 (75x75 µm/pixel); number of slices, 10; slice thickness (ST), 0.5 mm; inter-slice thickness (inter-ST), 0.1 mm; number of averages (NA), 4; total acquisition time (TAT), 6 min and 43 s.

3.5.2 MRSI acquisitions

Mice were studied by MRSI in order to obtain metabolomic information from different parts of a tumour, revealing its heterogeneity, and also from the surrounding tissue. Healthy brain was explored in control animals in order to set-up the 3D-like MRSI protocol. Standard MRSI experiments were performed using a 2D CSI sequence with PRESS localization, where: FOV, 17.6x17.6 mm; ST, 1 mm; volume of interest (VOI), 5.5x5.5x1.0 mm. TE, 14 ms; TR, 2500 ms; sweep width (SW), 4006.41 Hz; NA, 512; TAT, 21 m 30 s.

Water suppression was performed with variable power and optimized relaxation delays (VAPOR), using 300 Hz bandwidth. Linear and second order shims were automatically adjusted with Fast Automatic Shimming Technique by Mapping Along Projections (FASTMAP) in a 5.8x5.8x5.8 mm volume which contained the VOI region. Six saturation slices (ST, 10 mm; sech-shaped pulses: 1.0 ms/20250 Hz) were positioned around the VOI to minimize outer volume contamination in the signals obtained. Spatial resolution was defined by a 8x8 voxel matrix over the FOV (4.84 µl nominal resolution) reconstructed after Fourier interpolation to a 32x32 matrix, as described in [116]. The selected VOI (10x10 voxels) was interpolated in this matrix. Any variations in matrix size for MRSI will be explained in the respective sections of this thesis.

3.6 MR data processing and post-processing

3.6.1 Tumour volume calculation from MRI acquisitions

Tumour volumes in evaluated mice were calculated from T_{2w} HR coronal images using the Equation 3.2:

$$TV\ (mm)^3 = \left[(AS_1\ x\ ST) + \left[(AS_2 + (\dots) + AS_{10})x\ (ST + IT)\right]\right]x\ 0.075^2 \quad \textbf{Equation 3.2}$$

Where TV is the tumour volume, AS is the number of pixels contained in the region of interest (ROI) delimited by the tumour boundaries in each slice of the MRI sequence, ST is 0.5 mm, IT is 0.1 mm, and 0.075^2 mm^2 the individual pixel surface area.

The tumour area was calculated in pixels in each slice, using an automated system for generating ROIs available in the Paravision 5.0 software (Bruker BioSpin, Ettlingen, Germany). The inter-slice volume was not registered and it was estimated adding the inter-ST to the corresponding ST in Equation 3.2 (Figure 3.4).

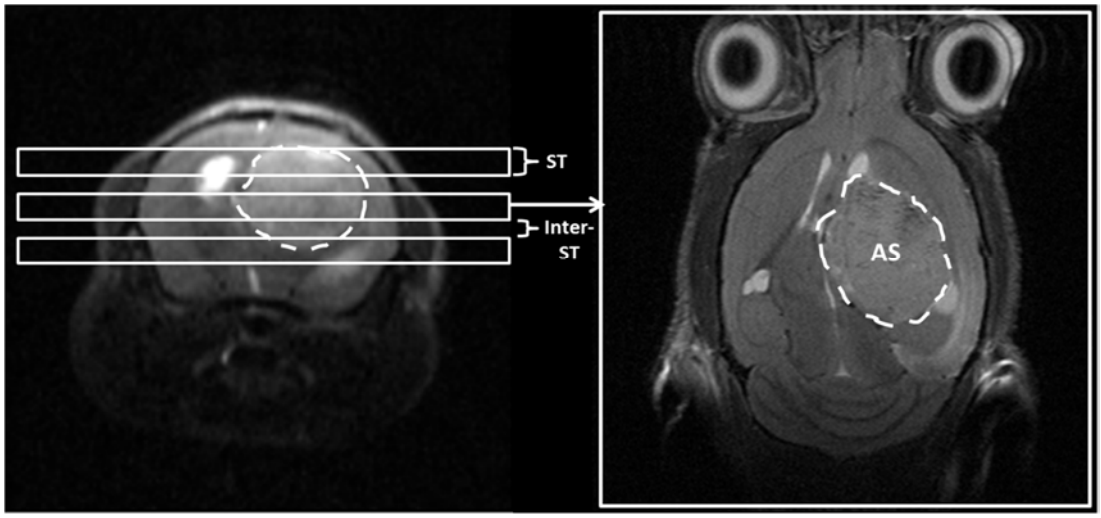

Figure 3.4: Scheme of the volume measurement carried out in mice. High-resolution coronal T_{2w} images were acquired for this purpose (image on the right). The surface area AS of the tumour (white dashed line contour) was measured in each slice of the axial sequence, and the ST and the inter-ST (represented by horizontal slices over a coronal image on the left) were taken into account for final volume calculation.

3.6.2 MRSI data processing and postprocessing

MRSI data processing and postprocessing steps were performed essentially as described in [116]. In summary, data was initially processed with Paravision 5.0 (Bruker BioSpin, Ettlingen, Germany). Then, post-processing with 3D Interactive Chemical Shift Imaging v1.9.10 (3DiCSI) software package (courtesy of Truman Brown, Ph.D., Columbia University) was performed for line broadening adjustment with a Lorentzian filter of 4 Hz, zero-order phase correction and exporting the data from individual voxels in ASCII format.

The dynamic MRSI processing module (DMPM) [230]) running over Matlab (The MathWorks Inc., Natick, MA, USA) and developed by the GABRMN group was used to align all spectra within each MRSI matrix using the choline peak as reference, 3.21 ppm. Then, depending on the objective of the study, spectra were used to Signal to noise Ratio (SNR) calculation or UL normalized and used for PR:

- For SNR calculation purposes, SNR values were obtained for each voxel of the MRSI grid (calculated as in [126], see also Equation 3.3) and coloured maps were generated.

$$SNR = \frac{maximum\ metabolite\ signal\ in\ range\ 0{-}3.4\ ppm}{standard\ deviation\ of\ noise\ in\ range\ 9{-}11\ ppm} \qquad \textbf{Equation 3.3}$$

- For pattern recognition purposes, the 0 – 4.5 ppm region of each spectrum in the MRSI matrix was individually normalized to UL2 and the normalized matrix was exported in ASCII format. These ASCII files were the input for pattern recognition analysis described in section 3.7.

3.7 Pattern recognition with source analysis and nosological imaging generation

Pattern recognition (PR) analysis of different spectra in MRSI grids was applied in order to classify voxels from MRSI matrices in an automated, user-independent way. Two approaches based in Non-negative Matrix Factorization (NMF) were used in this thesis: unsupervised and semi-supervised source analysis.

3.7.1 Unsupervised source analysis

This analysis was implemented in Matlab using a script developed by Dr Sandra Ortega-Martorell and further modified by Dr Victor Mociou, in order to accept as input MRSI grids with different matrixes size (10x10, 12x12). A defined number of sources were extracted from different grids and individual maps were generated to reflect the contribution of each source for every voxel. Finally, a nosological image was obtained where the colour assigned to each voxel is the colour assigned to the source most contributing to it. An additional script was developed by Dr. Victor Mocioiu, allowing generation of nosological images in RGB code (see chapter 8).

3.7.2 Semi-supervised source analysis

The semi-supervised system using NMF methods for source analysis was performed applying sources which were extracted from a training set of a labelled set of cases (control/untreated and TMZ-treated cases), as described in [117].

From the biochemical viewpoint, the source extraction technique to classify MRS data assumes that in each voxel there is a mixture of heterogeneous tissues, from which the contribution of

each source can be obtained. The fixed sources used for this study corresponded to a) normal brain parenchyma pattern, b) non-treated/unresponsive tumour pattern and c) responding tumour pattern. MRSI grids of new cases were thus analysed using this system and colour-coded nosological images were generated reflecting, for each voxel, the source with the highest contribution to it. For this semisupervised analysis, voxels which had major correlation with the normal brain source were coloured in blue, non-treated/non-response tumour coloured in red, and responding tumour coloured in green. Finally, undetermined tissue voxels were coloured in black (when the correlation between the spectrum of a voxel and each of the sources was below a threshold of 50% [117]).

3.8 Statistical analysis

The statistical analysis was carried out using IBM SPSS Statistics v.20 software. Data was evaluated for compliance with the normal distribution using the Shapiro–Wilk and Kolmogorov–Smirnov tests. Variance homogeneity was evaluated with the Levene's test. A two-tailed Student's t-test for independent measurements was used for comparisons in case of samples following a normal distribution. For non-normal distribution samples, non-parametric Mann-Whitney's U-test was applied. The global evolution of measurements along time was evaluated with the UNIANOVA test. The significance level for all tests was $p<0.05$

4. Study of Nanostructured coordination polymers with potential dual T_1/T_2 contrast enhancement properties: novel MR contrast agents

4.1 Specific objectives

Most clinically available MRI contrast agents are T_1 contrast agents using paramagnetic gadolinium complexes, but due to the complication related to Gd-CAs administration to patients with renal failure, CA complexation with other metals such as manganese or iron is being studied. Accordingly, the aim of this section was to apply MR techniques for evaluating the potential of a group of nanostructured coordination polymers (NCPs) as dual mode T_1/T_2 MRI contrast agents, following a strategy previously developed by our group [231] in which candidate nanoparticles are evaluated in a stepwise *ex vivo* procedure. The NCPs have emerged as an alternative platform to provide new opportunities for engineering multifunctional systems. The flexibility of their coordination chemistry allows the use of metal ions which are active in MRI pointing to their potential as contrast agents for biomedical imaging. Our final objective was to select the best nanoparticle which would be tested in a preclinical *in vivo* study and compare its performance with commercially available CAs. Most of the work described in this chapter was published in ACS Applied Materials & Interfaces (Suárez-García S, Arias-Ramos N et al, 2018 [232]).

4.2 Results originating from preliminary characterization of the nanoparticles performed by the *NanoSFun group*

The candidate nanoparticles have been synthesized and characterized by the research group of *Nanostructured Functional Materials* (NanoSFun), from the *Institut Català de Nanociència i Nanotecnologia* (http://nanosfun.icn2.cat/), and this chapter is the result of the collaboration with Dr Daniel Ruiz-Molina, Dr Fernando Novio and Salvio Suárez from this group.

4.2.1 Structure and synthesis

The general structure of the NCPs used in this chapter is shown in Figure 4.1. Briefly, two co-ligands were used, mostly the 1,4-bis(imidazol-1-ylmethyl)benzene (Bix) and the 3,4-dihydroxycinnamic acid (caffeic acid). Then, different metals were added through the use of the corresponding acetate salt. In addition, in the first part of this study two nanoparticles which present a variation in the aforementioned structure were analysed (MnPtha-NCP and Dopa-NCP, see Table 4.1). The nanoparticles were functionalized with BSA (bovine serum albumin) for *in vitro* and *ex vivo* studies, and with MSA (mouse serum albumin) for *in vivo* studies, in order to

obtain better dispersion in biological dissolvent. The use of serum albumin also brings some benefits such as increased solubility, stability in solution, long circulation half-life, biocompatibility and biodegradability [233, 234].

This synthesis was essentially performed as described in [104, 187] and is currently patented under the registry number **ES2541501 A1**[4]**.**

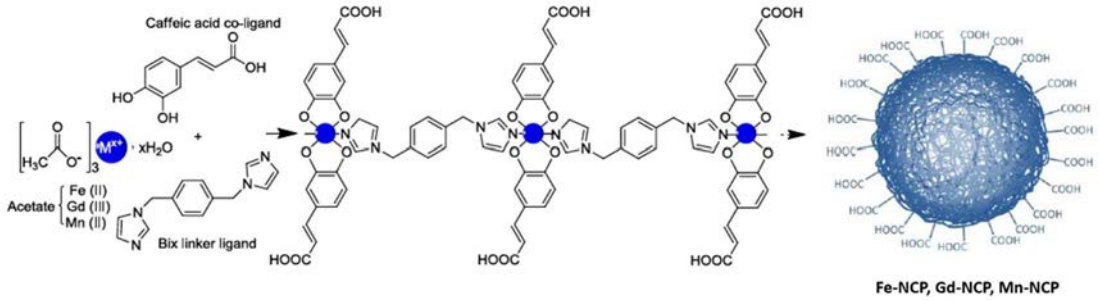

Figure 4.1: Basic structure of the nanoparticles studied in this section (reproduced with permission of providers). See [235] for further details.

4.2.2 Particle size, stability, biocompatibility and *in vitro* MR properties

Under scanning electron microscope (SEM), all nanoparticles showed spherical shape, which variable diameter depending on the nanoparticle being studied, ranging from 45±5 nm (Fe-NCP) to 161±13 nm (Mn-Phthalocyanine-NCP (MnPtha-NCP)), see table 4.1 for a complete list of the studied nanoparticles. Particle size was also measured using DLS and dissolving the NPs in PBS+BSA at pH 7.4, which is close to biological environment values. Slightly higher values were obtained with DLS: the average measured size was 56± 21 mm for Fe-NCP, 73±18 mm for Gd-NCP, 151± 23 mm for Mn-NCP, 80 ±15 nm for GdDTPA-NCP, 142±37 nm for MnPtha-NCP and 112±8 nm for Dopa-NCP, in comparison with SEM measurements for the same NCPs: 45±5 nm, 70±3nm and 130±7nm, 75±8 nm, 130±27 nm and 92±17 nm, respectively.

Colloidal stability was also assessed through zeta-potential measurements in the same environment. Results showed that at pH 7.4, zeta-potential was -19.1 mV for Fe-NCP, -14.7 mV for Gd-NCP, -2.2 mV for Mn-NCP, -11.9 mV for GdDTPA-NCP, -7 mV for MnPhta-NCP and -18 mV for Dopa-NCP. These data suggested that Mn-NCP would probably be more unstable in solution than the other ones.

Satisfactory results have been reported with Fe-NCP regarding cell viability effects over HeLa cultured cells at 24h and 72h after incubation and also for *in vitro* T_1 and T_2 relaxivity measurements in agarose phantoms [104], reinforcing the compatibility of the NCP system with

[4] http://www.oepm.es/pdf/ES/0000/000/02/54/15/ES-2541501_A1.pdf

biological systems. The dual T_1-T_2 contrast enhancement potential is suggested by the r2/r1 measured ratio of 2.06 for Fe-NCP in comparison with 1.05 for the commercial gadoterate meglumine (Gd-DTPA), whereas Mn-NCP exhibits a r2/r1 ratio of 0.6. Taken together, *in vitro* results suggested that NCPs could have potential interest as contrast agents to be tested *in vivo*. However, *in vitro* approaches cannot accurately reproduce the *in vivo* environment [236]. Factors such as the interaction with extracellular macromolecules may change the overall NCP mobility, leading to changes in its relaxivity. In this sense, ex vivo experiments such as the ones described by our group [231] are an intermediate step which could provide more reliable results.

4.3 Specific materials and methods

The list of the nanoparticles and contrast agents tested in this experiment is shown in Table 4.1

Table 4.1: List of CAs studied in this chapter. Apart from nanoparticles, commercial agents were included for comparisons: gadopentetate dimeglumine (from Guerbet, Roissy, France) and mangafodipir trisodium (from Bayer Healthcare).

Experimental CA	
NCP	**Fe-NCP**: NCP containing Fe^{3+} ions
	Gd-NCP: NCP containing Gd^{3+} ions
	Mn-NCP: NCP containing Mn^{2+} ions
	GdDTPA-NCP: NCP containing Gd^{3} ions and DTPA
	MnPhta-NCP: NCP containing Mn^{2+} ions and Phthalocyanine + Ligand L2 [237] (instead of Bix)
	Dopa-NCP: NCP containing Fe^{3+} ions, Bix and Dopamine (instead of caffeic acid)
Commercial CA	
Mangafodipir trisodium, **MnDPDP** (based in Mn)	Teslascan ®
Gadopentetate dimeglumine, **Gd-DTPA** (based in Gd)	Magnevist ®
Vehicle	Phosphate buffered saline (PBS) and Bovine Serum Albumin (BSA)

4.3.1 *Ex vivo* postmortem contrast enhancement assessment

4.3.1.1 Animals and contrast injection procedures

A total of 18 C57BL/6J wt female mice of 12 weeks of age, weighing 21.3±1.3 g were used in this *ex vivo* study. Experiments were performed essentially as described in [231]. The CAs (Table 4.1) were dissolved in Phosphate buffered saline (PBS)-BSA solution (10mM PBS with 0.5mM BSA) taking into account the estimation of Gd, Mn or Fe content measured from providers in order

to achieve solutions of comparable concentration of the desired metal. The amount of NCP used for each animal was 5 nmol of metal dissolved in 4 µl of PBS-BSA. A total of n=2 animals for NCP were explored to ensure sufficient measurements for statistical signification, however not all slices were suitable for measurements (see sub-section 4.3.1.2). The whole process of NCP *ex vivo* injection took ca. 20 minutes. Animals were euthanized with an overdose of intraperitoneal sodium pentobarbital (200 mg/kg, Vetoquinol, Madrid, Spain) and then immobilized in a stereotactic holder. The contrast administration was carried out as described for tumour generation (see materials and methods, section 3.2.3) except that the cell suspension was replaced with the contrast agent solution. Three different locations were used for NCP injection, which coordinates were (distance in mm from Bregma):

a) **X**: -2.32 mm; **Y**: -0.1 mm; **Z**: -3.35 mm

b) **X**: -2.32mm; **Y**: -1.50 mm; **Z**: -3.35 mm

c) **X**: -2.00 mm; **Y**: -3.9 mm; **Z**: -3.35 mm

4.3.1.2 MRI acquisitions

T_1 and T_2 weighted MRI

High-resolution axial T_2-weighted images (TR/TE =4200/12ms) were acquired using a RARE sequence for a morphological characterization of the investigated tissue. The parameters were: RARE factor=8; FOV 19.2×19.2 mm; MTX, 256×256 matrix (75×75 µm/pixel); NA, 4; number of repetitions (NR), 1; TAT, 6 min 43 sec. After this, a T_1-weighted image (TR/TE, 350/10 ms) was acquired with a Multi-Slice Multiecho (MSME) sequence with: FOV 19.2 x 19.2 mm; MTX, 256×256 matrix (75×75 µm/pixel); NA, 8; number of repetitions (NR), 1; TAT, 11 min 56 sec.

T_1 and T_2 maps

For T_1 maps acquisition, a RARE-VTR sequence was chosen with RARE factor, 2; FOV, 17.6 x 19.2 mm; MTX, 128×128 (138×151 µm/pixel); NS, 3; ST, 1 mm; TEeff, 7.5 ms; TRs were according to the following list: 100, 400, 700, 1000, 1300, 1700, 2000, 2600, 3500 and 5000 ms; NA, 1; TAT, 19 min 31 sec. For T_2 maps acquisition, a Multi-Slice-Multi-Echo (MSME) sequence was used; FOV, 17.6 x 19.2 mm; MTX, 128×128 (138×151 µm/pixel); NS, 3; ST, 1 mm; TR, 3000 ms; TEs were according to the following list: 10, 20, 30, 40, 50, 60, 70, 80, 90, 100, 110, 120, 130, 140, 150, 160, 170, 180, 190 and 200 ms; NA, 4; TAT, 6 min 24 sec.

4.3.1.3 Ex vivo data processing and postprocessing

T_{1w} and T_{2w} images were analyzed with ImageJ 1.49V (National Institutes of Health, USA). Acquired T_1 and T_2 maps were analysed using Bruker software Paravision 5.1 by using the image sequence analysis (ISA) tool package.

Signal intensity was measured in regions of interest (ROIs) from each coordinate (n=3) which were manually delimited after visual inspection both in the area of maximum enhancement and in the equivalent area of the contralateral parenchyma (Figure 4.2). The relative contrast enhancement (RCE) (injection site ROI vs. contralateral parenchyma) was then calculated using Equation 5.1 (see also [231]). Only the slice with the best defined contrast-enhanced region was used for measurements. Similar slices were used for T_1 and T_2 RCE measures.

$$RCE(\%)_{exvivo} = \left(\frac{S(i)}{S(c)}\right) \times 100 \qquad \textbf{Equation 5.1}$$

Where *S(i)* is the signal obtained from ROIs from any of the 3 coordinates injected with contrast agent and *S(c*) is the signal obtained from the ROI in the contralateral area (defined as the 100% of the signal).

T_1 and T_2 values were estimated through different adjustments to map parameters:

$$y = A + C * \left(1 - \exp^{(-t/T1)}\right) \qquad \textbf{Equation 5.2}$$

Where *y* is the image signal intensity after *t*, *A* is the absolute bias, *C* is the estimated image signal intensity at t = 0 sec, and *t* stands for the different TR used in the sequence.

$$y = A + C * \exp^{(-t/T2)} \qquad \textbf{Equation 5.3}$$

Where *y* is the image signal intensity after *t*, *A* is the absolute bias, *C* is the estimated image signal intensity at t = 0 sec, and *t* stands for the different TE used in the sequence.

Finally, dual images reflecting both T_1 and T_2 RCE changes were generated with a postprocessing algorithm of imaging division (T_{1w} image / T_{2w} image) producing a coloured image highlighting dual RCE, as shown in Figure 4.2.

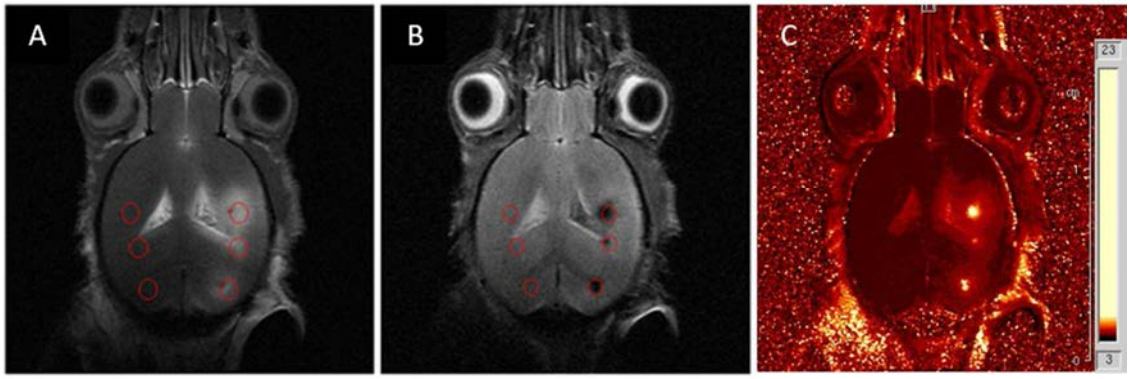

Figure 4.2: A. T_1 weighted MRI and **B.** T_2 weighted MRI after stereotactic injection of CA Fe-NCP and examples of ROIs drawn for *ex vivo* postmortem RCE studies. **C.** Postprocessing of T_{1w} and T_{2w} MRI with an algebra algorithm of imaging division (T_{1w}MRI/T_{2w}MRI), to highlight double enhancement potential in the studied region (dual enhancement image). Scale indicates colour intensity.

4.3.2 *In vivo* experiments

4.3.2.1 Tolerability studies

The tolerability protocol was based in the approach described in [238]. A total of 6 female C57BL/6J wt mice of 12 weeks of age weighing 21.3±1.3 g were i.v. injected with different doses of Fe-NCP nanoparticles (calculated as the equivalent of metal/kg) in order to estimate the maximum tolerated dose to be used in a future MRI *in vivo* study.

Increasing amounts of Fe-NCP were i.v. administered to n=3 mice (Table 4.2) with a 2-day rest period between injections in order to permit tail vein regeneration. An additional group of 3 mice was injected with the vehicle (10mM PBS with 0.5 mM Mouse Serum Albumin (MSA)). The maximum dose (0.4 mmol Fe/kg) is in the range of doses that have been proved safe for Fe-based nanoparticles, which can be up to 0.6 mmol/kg [239, 240].

Table 4.2: Increasing doses of NCP injected in mice in different days

Day of injection	1	4	7	10	13	16	19	22
Dose (mmol Fe/kg)	0.003	0.006	0.0125	0.025	0.05	0.1	0.2	0.4

During the following hour after NCP injection, animals were observed in order to check for immediate symptoms of suffering or acute toxicity such as described in [241] (weight loss up to 20%, piloerection, convulsions, tremors, ataxia). Mice body weight was followed up during 30 days after the last administration. In case of toxicity symptoms detection or animal death, the whole body was preserved in paraformaldehyde 4% for further necropsy studies. In case a dose

tested was consider as toxic, 3 new animals would be injected with a dose concentration immediately lower to the dose that caused the toxic symptoms.

4.3.2.2 MRI in vivo contrast enhancement studies

A total of 12 female C57BL/6J mice weighing 21.4±1.2 g were used for tumour generation as described in materials and methods section 3.2.2. Tumour generation took place in 2 rounds of 6 animals. Then, 3 animals with the most similar tumour volumes were chosen for each experimental condition (vehicle or CAs). The average volume i.v. injected was 107.1±6.4 µl and CAs were finally administered with a dose of 0.4 mmol metal/kg.

DCE-T_{1w} MRI study using vehicle (PBS+MSA)

T_{1w} Dynamic contrast enhancement (DCE) studies were performed in 3 GL261 tumour-bearing animals. After acquiring three pre-contrast standard T_{1w} images, vehicle was injected intravenously and a series of 70 dynamic images was acquired with temporal resolution of 51.2 s per frame to account for any contrast enhancement produced for vehicle injection. For this, a MSME sequence was used with: FOV; 17.6×17.6 mm_2; matrix, 128x128 (138×138µm/pixel); TR/TE, 200/8.5 ms; NA, 2; ST, 1 mm; TAT, 59 min 44 sec.

DCE-T_{1w} and T_{2w} MRI study with Gd-DTPA and Fe-NCP

The DCE-T_{1w} MRI experiments were designed to use both CA in the same experimental mice. For this, a first experiment with i.v. administration of Gd-DTPA was carried out in 3 GL261 tumour-bearing mice at day 13 p.i. Then, 24 hours after the first administration and after complete washout of Gd-DTPA, a second experiment with administration of Fe-NCP was performed in the same 3 mice. For this experiment, T_1- and T_2-weighted images (TR/TE = 200/8.5 ms and 4200/12 ms) were acquired before and immediately after i.v. injection of CA. The acquisition parameters for T_{1w} images were: MSME sequence, FOV: 17.6x17.6 mm^3, Matrix: 128x128 (138x138 µm/pixel), NA: 2, ST: 1 mm, IST: 0.1 mm, Time resolution: 51.2 s/ frame. For T_{2w} images, a RARE sequence was used with RARE factor=8; FOV: 17.6x17.6 mm^3, Matrix: 128x128 (138x138 µm/pixel), NA: 1mm, ST: 1 mm, IST: 0.1 mm, Time resolution: 1 min 7s 200 ms/ frame. In this experiment, alternating T_{1w} and T_{2w} MRI were acquired continuously during 30 minutes after CA administration, resulting in a total of 15 frames each, with a temporal resolution of 2 minutes. In addition, T_{1w} and T_{2w} additional acquisitions were also performed at 2 hours and 24 hours after administration (Figure 4.3).

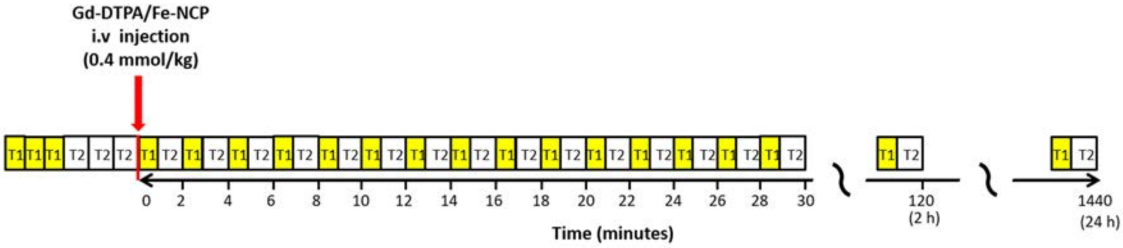

Figure 4.3: MRI acquisition scheme used in the experiment with i.v. injection of 0.4 mmol/kg of Gd-DTPA and 0.4 mmol/kg of Fe-NCP. Three T_{1w} images and 3 T_{2w} basal images were acquired before i.v. injection. Then, alternated T_{1w} and T_{2w} images were acquired after i.v. injection.

4.3.2.3 Data processing and postprocessing

DCE-MRI was acquired in axial orientation with 3 slices and two ROIs were selected in each slice (tumour and contralateral brain). RCE in each slice was calculated as in *ex vivo* studies, and averaged. The mean basal RCE calculated in pre-CA injection images was referred as 100% and post-CA RCE values were estimated accordingly, with respect to basal.

4.3.3. Animal euthanasia and organ storage

After finishing the last MRI experiment, animals were euthanized by cervical dislocation and organs were resected and preserved in liquid nitrogen for further inductive coupled plasma mass spectrometry (ICP-MS) analysis[5]. The preserved organs were brain tumour, contralateral brain, heart, lungs, liver, kidneys, spleen and bladder.

4.4 Results and discussion

4.4.1 *Ex vivo* experiments

The RCE (positive for T_{1w} MRI, or negative for T_{2w} MRI) was measured for all CAs studied in the injection site (Table 4.3) and T_1 and T_2 values variations in brain parenchyma were also estimated (Table 4.4). The fact that not all experimental CA produced similar spots of RCE to be measured, being some of them slightly more dispersed in tissue than commercial CA, made it more difficult to assign measurement ROIs. Also, the ROI drawn to perform RCE measurements in T_{2w} MRI were smaller than ROIs used in T_{1w} measurements due to different effects observed in each image modality (see Figure 4.2).

[5] ICP analysis was performed by NanoSFun and was not part of the experimental work carried out in this thesis.

Table 4.3: RCE% calculated (mean±SD) in T_{1w} and T_{2w} *ex vivo postmortem* MRI, as well as RCE%T_{1w}/RCE%T_{2w} ratio.

CA	*RCE% (T_{1w})*	*RCE% (T_{2w}) [decrease]*	*Ratio RCE%T_{1w}/RCE%T_{2w}*
Gd-DTPA (n=3)	253.1±32.8	74.9±17.6 [-25.1]	3.6±1.4
MnDPDP (n=3)	300.9±47.7	97.4±14.5 [-2.6]	3.2±1.1
Fe-NCP (n=3)	269.0±28.0	44.9±26.0 [-55.1]**	7.7±4.5
Gd-NCP (n=3)	278.6±56.0	70.1±25.4 [-29.9]	4.2±1.1
GdDTPA-NCP (n=3)	180.0±64.3	78.6±2.8 [-21.4]	2.3±0.8
Mn-NCP (n=3)	177.3±64.4	61.6±33.8 [-38.4]	3.9±3.0
MnPhta-NCP (n=3)	109.3±8.8*	102.8±12.3 [2.8]*** (no decrease)	1.1±0.1¥
Dopa-NCP (n=3)	250.3±6.5	79.7±14.5 [-20.3]	3.2±0.7
Vehicle (PBS-BSA) (n=3)	118.6±8.8*	122.9±11.5 [22.9]£ (no decrease)	0.97±0.07¥

*= p<0.05 in comparison with Gd-DTPA, MnDPDP, Fe-NCP, Gd-NCP and Dopa-NCP.
**= p<0.05 in comparison with MnDPDP.
***= p<0.05 in comparison with Fe-NCP and GdDTPA-NCP.
£= p<0.05 in comparison with Gd-DTPA, MnDPDP, Fe-NCP, Gd-NCP, GdDTPA-NCP, MnPhta-NCP and Dopa-NCP.
¥= p<0.05 in comparison with Gd-DTPA, MnDPDP, Fe-NCP, Gd-NCP, Gd-DTPA-NCP, Mn-NCP, and Dopa-NCP.

The considerable dispersion of the values obtained in this set of *ex vivo* experiments prevented us to reach statistical signification in most cases, although the mean values allowed us to make some considerations about the CAs studied:

The Fe-NCP, Gd-NCP and Dopa-NCP presented a mean T_{1w} RCE comparable with the commercial CA Gd-DTPA or MnDPDP. The slight improvement in comparison with Gd-DTPA was not significant ($p>0.05$). Nevertheless, the RCE obtained was not significantly worse than the one obtained with the commercial agents, and in this sense, they could be equally valuable for preclinical or even clinical studies, in case of a translational approach. In case of T_{2w} RCE (which means signal decrease), the Fe-NCP presented the best result, although not significantly, in comparison with other experimental or commercial CAs, except in case of MnDPDP.

It is worth mentioning that it is the combination of T_{1w} and T_{2w} RCE what makes Fe-NCP an interesting CA to be further evaluated, because none of the other agents presented such good combination (e.g. MnDPDP presented a very good T1w RCE but poor T_{2w} RCE, and Mn-NCP

presented a satisfactory T_{2w} RCE but poor T_{1w} RCE). This can be seen in the last column of Table 4.3, where the Ratio RCE T_{1w}/RCE T_{2w} is also stated. Ideally, a double CA (with positive-negative enhancement) should present high values for T_{1w} RCE and low values for T_{2w} RCE, resulting in a Ratio RCE T_{1w}/RCE T_{2w} as high as possible. For the list of evaluated CA, average values ranged from 1.1 for MnPhta-NCP presenting worst performance, to 7.7 for Fe-NCP with the best dual enhancement performance. This could be visually observed in Figure 4.4 with the postprocessing using a division algebra algorithm. The vehicle solution PBS-BSA did not show either T_1 or T_2 contrast enhancement as expected, with a ratio RCE T_{1w}/ RCE T_{2w} of 0.97.

In previous ex vivo work of our group [231], the highest T_{1w} RCE obtained was 201.9±9.3% for gold glyconanoparticles with gadolinium. Values found for Fe-NCP, Gd-NCP and Dopa-NCP in this study were clearly higher (269.0±28.0%, 278.6±56.0% and 250.3±6.5% respectively).

Regarding T_{2w} RCE, it was calculated for SPION-nanoparticles in [231] and the highest RCE T_{2w} value found was -39.3±11.0%, and Fe-NCP performed better in studies performed during this thesis (-55.6±26.0%).

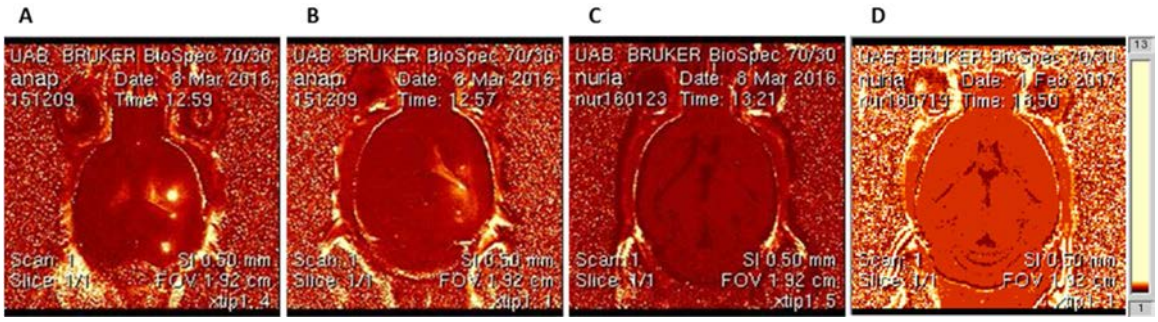

Figure 4.4: Postprocessing of T_{1w} and T_{2w} MRI with an algebra algorithm of imaging division (T_{1w}MRI/T_{2w}MRI), to highlight double enhancement potential in the studied CA. **A.** Fe-NCP, with the higher RCE%T_{1w}/RCE%T_{2w} ratio (Table 4.3), presents high intensity hotspots. **B.** MnDPDP, with good RCE T_{1w} but poor RCE T_{2w} produces less intense hotspots. **C.** MnPhta-NCP, with poor RCE T_{1w} and RCE T_{2w}, produces no noticeable hotspots. **D.** Vehicle, with very poor both RCE T_{1w} and RCE T_{2w}, produces no noticeable hotspots. Images are shown in red-gold colour scale to highlight hotspots. Scale indicates colour intensity.

The calculated T_1 and T_2 water values (1600.0±351.4 ms and 45.7±5.0 ms respectively) in the non-injected parenchyma of all the studied cases is in agreement with values obtained by other authors for the same magnetic field (1939.0±149.0 ms for T_1) in [242] or similar magnetic fields (1927.0±54.7 ms for T_1 and 43.5±2.4 ms for T_2 at 9.4T) [243]. Regarding T_1 and T_2 fold change, it was measured taking into account contralateral and ipsilateral parenchyma (CA injection side). The CA injection area presented lower T_1 and T_2 than the contralateral parenchyma, as expected, except for MnPhta-NCP and vehicle, which is in agreement with RCE values stated in Table 4.3. Taking into account values shown in Table 4.3 and 4.4, MnPhta-NCP was clearly the worst CA of the series. However, the dispersion of the values could also indicate that this agent simply does

not have any relevant effect over T_1 or T_2 when injected in the mouse brain parenchyma. On the other hand, considering changes in T_1 and T_2 shown in Table 4.4, we should expect a similar performance for CPP-Fe and CPP-Gd, which is not confirmed in Table 4.3 for RCE measurements. This could be both due to the dispersion of the values and to the fact that T_1 and T_2 measurements are carried out by mathematical adjustments made through the MRI signal obtained from different brain zones, and this could entail some inaccuracy (especially in tissue measurements, as opposed to *in vitro* studies, performed in a more homogeneous environment). Indeed, the ability of producing a satisfactory RCE would be the final performance measured in the preclinical and clinical practice, and in this sense, the CA with the best overall performance (Fe-NCP) would be the one proposed to proceed with the possible *in vivo* studies.

Table 4.4: Relaxation times calculated from T_1 and T_2 map acquisitions and "fold change" values. The estimated T_1 and T_2 values of the ipsilateral (ipsi) parenchyma were compared with the T_1 and T_2 values from contralateral (contra), non-injected parenchyma in an equal sized ROI. Values are shown as mean ± SD.

CA	T_1 ipsi	T_1 contra	T_1 fold change	T_2 ipsi	T_2 contra	T_2 fold change
GdDTPA (n=3)	463.42± 109.35	1859.31± 111.57	0.25±0.06	40.46± 4.78	46.01± 2.82	0.88±0.05
MnDPDP (n=3)	554.18± 155.70	1840.57± 66.03	0.30±0.08	40.87± 3.46	45.58± 1.61	0.90±0.04
Fe-NCP (n=3)	378.10± 161.62	1678.17± 129.59	0.23±0.11	37.95± 8.95	50.33± 5.12	0.75±0.11
Gd-NCP (n=3)	322.34± 112.76	1389.47± 580.20	0.26±0.14	30.56± 6.10	45.16± 2.47	0.68±0.16
GdDTPA-NCP (n=3)	406.83± 112.13	1317.53± 454.49	0.32±0.07	33.51± 2.49	42.29± 0.85	0.79±0.07
Mn-NCP (n=3)	502.20± 386.01	1253.50± 446.59	0.37±0.16	32.62± 7.23	37.06± 8.07	0.88±0.00
MnPhta-NCP (n=3)	1843.90± 116.75	1987.67± 78.58	0.93±0.08*	53.86± 1.80	45.93± 1.54	1.17±0.00*
Dopa-NCP (n=3)	610.65± 157.29	1579.43± 62.63	0.39±0.11	40.55± 14.29	50.60± 2.79	0.80±0.27
Vehicle (PBS+BSA) (n=3)	1652.48± 46.44	1609.67± 66.33	1.03±0.02*	54.17± 2.66	48.89± 0.46	1.11±0.05**

*= p<0.05 in comparison with Gd-DTPA, MnDPDP, Fe-NCP, Gd-NCP, GdDTPA-NCP, Mn-NCP and Dopa-NCP.

**= p<0.05 in comparison with Gd-DTPA, MnDPDP, Fe-NCP, Gd-NCP, GdDTPA-NCP and Mn-NCP.

4.4.2 *In vivo* experiments

4.4.2.1 Tolerability experiments

The nanoparticle with the best performance in the *ex vivo* experiment was selected to proceed to the *in vivo* experiments. Therefore, Fe-NCP was chosen due to its clear potential for dual-mode T_1-T_2 contrast and tolerability studies were performed to investigate whether this NP would produce harmful effects following injection in mice.

Animals injected with Fe-NCP at different doses did no present any toxicity symptoms, neither during the injections, nor during the rest of the follow-up period (30 days). Animals injected with the vehicle received the same concentration (0.5mM of MSA in 10mM PBS) every injection day, and no toxicity symptoms were observed. Figure 4.5 shows the variation of weight along time, in which no decrease beyond the 20% cut-off set for severe affectation. In fact, an increase in body weight was observed in all studied animals. This is the expected evolution for healthy mice according *to The Jackson laboratory body weight chart* for C57BL/6J mice [244]. According to this database, C57BL/6J wt mice show an increase in body weight from 12 until 20 weeks (also shown in Figure 4.5).

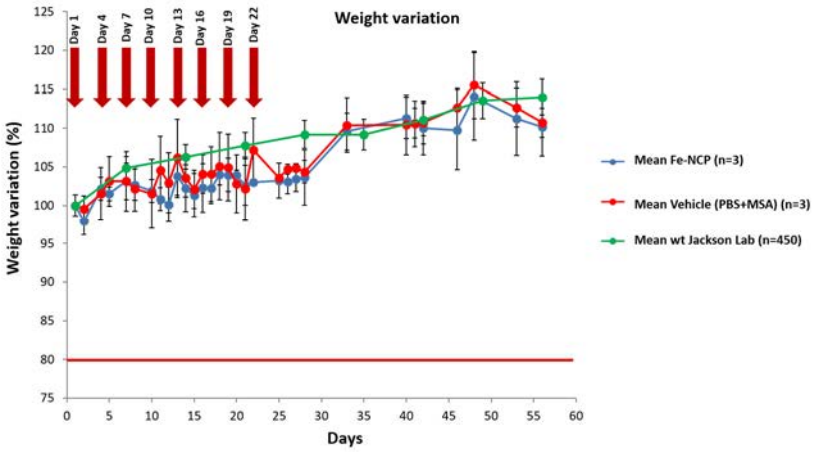

Figure 4.5: Percentage of body weight variation (mean ± SD) of animals injected with Fe-NCP (blue), animals injected with vehicle (red) and body weight variation data from *The Jackson laboratory body weight chart for C57BL/6J mice* (green). Initial mice weight measured the first day of Fe-NCP or vehicle i.v. injection was considered as 100% for injected mice and for *The Jackson laboratory weight data*, the initial measure was considered the weight corresponding to mice of 12 weeks of age. The horizontal red line at the bottom indicates the 20% weight reduction point, not reached by any mice in this preliminary study. Red arrows point to the different days of injection for mice injected with Fe-NCP or vehicle (injection doses were explained in methods section, Table 4.2).

The last value registered for body weight was compared along both groups with Student's t-test and no significant differences ($p>0.05$) were observed. Still, no significant differences ($p>0.05$) using UNIANOVA test were found in the global evolution of body weight measurements between groups of animals injected with Fe-NCP or vehicle. According to these results, the estimated maximum tolerated dose (MTD) for Fe-NCP was equal or higher than 0.4mmol Fe/kg, because no higher doses were tested at this point. Since no harmful effects were detected, this dose could be safely used in *in vivo* studies. However, additional information with higher doses would be needed for estimating the actual MTD in the future.

4.4.2.2 MRI experiments

Alternated T_1-T_{2w} images with Gd-DTPA (0.4 mmol Gd/kg) and Fe-NCP (0.4mmol Fe/kg) studies

As described in section 4.3.2.2, the same tumour bearing mice (C1209, C1210 and C1217) were explored after Gd-DTPA administration and Fe-NCP administration, with an interval of 24h to ensure proper washout. Mean tumour volume at the experiment day (12.6±0.6 p.i.) was 50.3±0.7 mm^3. Mice were first i.v. administered with a dose of 0.4 mmol Gd/kg of Gd-DTPA and alternating T_{1w} and T_{2w} images were acquired. The maximum RCE value found was 250.9±3.1% at 6.1±1.1 minutes (T_{1max}). Then, 2 hours after the injection, the mean RCE value was 111.8±2.7% and 24 hours later, the mean RCE value was 101.0±4.0%, recovering the RCE observed before injection, indicating complete Gd-DTPA washout. A summary of RCE values of the different experiments can be found in Table 4.5. Figures 4.6 and 4.7 show the evolution of mean RCE% T_{1w} and T_{2w} values of both Gd-DTPA and Fe-NCP studies.

Analysis of RCE T_{1w} results

Regarding Gd-DTPA results, Student's t-test was performed in order to compare different RCE values at different time points: pre-injection, T_{1max}, 2 hours and 24 hours post injection. Significant differences ($p<0.05$) were found for RCE between pre injection, T_{1max} (6.1±1.1 min) and 2 hours post-injection. On the other hand, no significant differences were found between pre injection and 24 hours post injection RCE values.

Studies with Fe-NCP 0.4 mmol Fe/kg injection were performed 24 hours later with the same 3 mice and MRI was acquired in the same conditions. The tumour volume was 66.2± 2.5 mm^3 at this time point. As expected, the injection of Fe-NCP showed T_{1w} positive contrast (Figure 4.6). The maximum RCE% value registered was 317.4±14.4% at 9.4±1.1 minutes ($T_{1w\ max}$). Then, 2 hours after the injection, the mean RCE% value was 123.5±4.6% and 24 hours after the injection, the mean RCE value was 88.3±6.7%, even below RCE measured before injection, suggesting the wash out of the nanoparticle from the tumours (Figure 4.6 B; summary of RCE values in table

4.5). Student's t-test was performed as described before, for RCE comparison at different time points: pre-injection, $T_{1w\,max}$, 2 hours and 24 hours post injection. Significant differences ($p<0.05$) were found for RCE between pre-injection and RCE measured at all time points studied.

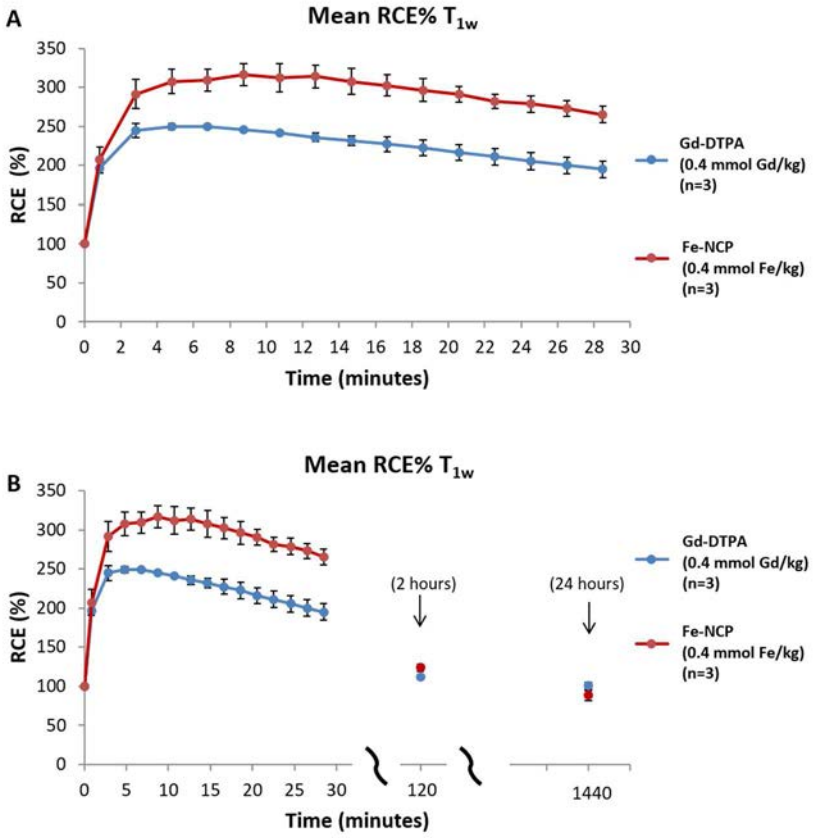

Figure 4.6: A. Mean kinetics ± SD of RCE T_{1w} images in 3 GL261 mice, during 30 minutes after intravenous injection of a dose of 0.4 mmol/kg of Gd-DTPA (in blue); and after intravenous injection of a dose of 0.4 mmol/kg of Fe-NCP (in red). B. Mean kinetics ± SD of RCE T_{1w} images in the same mice, during 30 minutes, 2 hours and 24 hours after intravenous injection of a dose of 0.4 mmol/kg of Gd-DTPA (in blue) and after intravenous injection of a dose of 0.4 mmol/kg of Fe-NCP (in red). Higher T_{1w} RCE was observed with Fe-NCP at T_{1max} and signal recovery was observed 24 hours after injection, for Gd-DTPA and Fe-NCP.

Comparing the evolution of RCE% T_{1w} during the first 30 minutes after injection of Gd-DTPA, Fe-NCP and vehicle, significant differences ($p<0.05$) were observed between the 3 groups using a UNIANOVA test. RCE at T_{1max} also presented significant differences ($p<0.05$) between groups. Regarding 2h and 24h time points, significant differences were found in RCE T_{1w} values of Gd-DTPA and Fe-NCP. Vehicle had no RCE measurements performed at this time point.

Table 4.5: Mean ± SD for RCE calculated in T_{1w} and T_{2w} *in vivo* MRI studies for Gd-DTPA, Fe-NCP and vehicle. For vehicle, no short-term RCE T_{2w} was measured, and no measurements of RCE T_{1w} 2 hours and 24 hours post-injection were acquired.

CA	*RCE% ($T_{1w\ max}$)*	*RCE% (T_{1w} 2 h)*	*RCE% (T_{1w} 24 h)*	*RCE% ($T_{2w\ min}$) [decrease]*	*RCE% (T_{2w} 2 h) [decrease]*	*RCE% (T_{2w} 24 h) [decrease]*
Gd-DTPA (n=3•)	250.9±3.1 *	111.8±2.7 *	101.0±4.0	111.5±2.1 [11.5] (no decrease)**	102.1±7.0 [2.1] (no decrease)	102.3±7.3 [2.3] (no decrease)
Fe-NCP (n=3•)	317.4±9.4 ***	123.5±4.6 ***	88.3±6.7 ***	73.7±14.4 [-26.3] ****	103.1±9.9 [3.1] (no decrease)	79.4±4.2 [-20.6] ****
Vehicle PBS-MSA (n=3)	101.2±1.8					

• The same animals were used for these experiments
*= $p<0.05$ in comparison with Gd-DTPA RCE T_{1w} pre injection
**= $p<0.05$ in comparison with Gd-DTPA RCE T_{2w} pre injection
***= $p<0.05$ in comparison with Fe-NCP T_{1w} pre injection
****= $p<0.05$ in comparison with Fe-NCP T_{2w} pre injection

Analysis of RCE T_{2w} results

No negative enhancement in T_{2w} MRI was observed after Gd-DTPA injections, as expected for the dose administered (Figure 4.7.A, blue line). Gd-DTPA has effects in both T_1 and T_2, but these effects are not enough for it to perform as a T_2 contrast agent [95]. During the first 30 minutes after injection, in fact a slight and significant increase in T_{2w}MRI was observed at the $T_{2w\ min}$ (111.5±2.1%). After 2 and 24 hours after Gd-DTPA injection, measured RCE values were 102.1±7.0% and 102.3±7.3% respectively. No significant differences ($p>0.05$) were observed for measured RCE at 2 and 24 hours post-injection in comparison with pre-injection values.

On the other hand, the administration of Fe-NCP 0.4 mmol Fe/kg showed clear T_{2w} enhancement (i.e., signal decrease, red line in Figure 4.7). The minimum RCE T_{2w} measured value for Fe-NCP was 73.6±14.4% (-26.3% of RCE decrease), reached at $T_{2w\ min}$ (5.3±1.1% minutes). Then, 2 hours after the injection, RCE was of 103.1±9.9% recovering the signal level found before the injection. However, 24 hours after the injection, a further signal decrease was observed with an RCE value of 79.4±4.2%, when a signal recovery was expected. Significant differences were found ($p<0.05$) between pre-injection RCE T_{2w} values in comparison with RCE at $T_{2w\ min}$ and 24h post injection.

One of the hypothesis for explaining the signal decrease observed in T_{2w} MRI 24 hours after Fe-NCP injection (Figure 4.8) could be presence of haemorrhagic zones inside the tumour as suggested in [245], although this was not observed in the first time points. These hypointense areas in the central part of the tumour can affect RCE calculation and care should be taken while interpreting data. Indeed, one of the advantages of a dual mode contrast agent is the inspection of both T_{1w} and T_{2w} images and account for possible situations leading to misinterpretation as the described one. When tumours were resected at the end of the experiment, haemorrhagic zones inside tumours could be visually confirmed. Nevertheless, an additional interpretation of this effect could be the increased Fe-NCP degradation in the tumour, releasing Fe^{3+}, which by itself may produce T_{2w} contrast effect.

The UNIANOVA test was performed for comparison of the evolution of RCE T_{2w} during the first 30 minutes after injection in the Gd-DTPA and Fe-NCP experiments. Significant differences ($p<0.05$) were found between groups. In addition, significant differences ($p<0.05$) were also found in the minimum RCE value in both groups using the Student's t-test. Regarding the last time points measured, the 2h time point did not present significant differences, whereas the 24h time point did, possibly due to interference of haemorrhagic zones in RCE calculation, as previously explained.

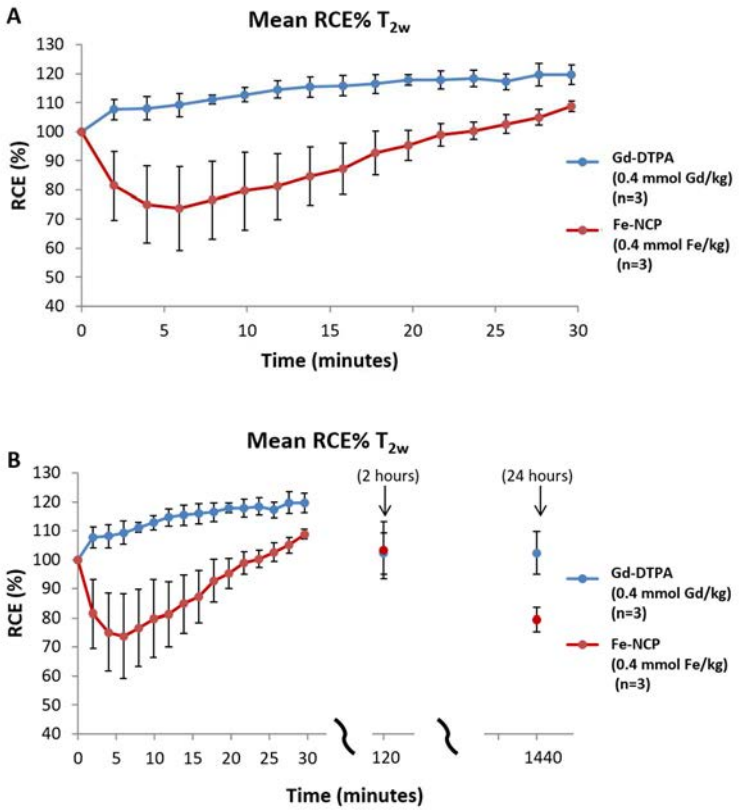

Figure 4.7: A. Mean kinetics ± SD of RCE T_{2w} images in 3 GL261 mice, during 30 minutes after intravenous injection of a dose of 0.4 mmol/kg of Gd-DTPA (in blue) and after intravenous injection of a dose of 0.4 mmol/kg of Fe-NCP (in red). **B.** Mean kinetics ± SD of RCE T_{1w} images in the same mice, during 30 minutes 2 hours and 24 hours after intravenous injection of a dose of 0.4 mmol/kg of Gd-DTPA (in blue) and after intravenous injection of a dose of 0.4 mmol/kg of CPP-Fe (in red). No T_{2w} contrast decrease was observed with Gd-DTPA. Lower T_{2w} RCE was observed with Fe-NCP and T2 signal recovery was observed at 2 hours after injection. However, 24 hours after injection a new decrease in T_{2w} RCE signal was detected.

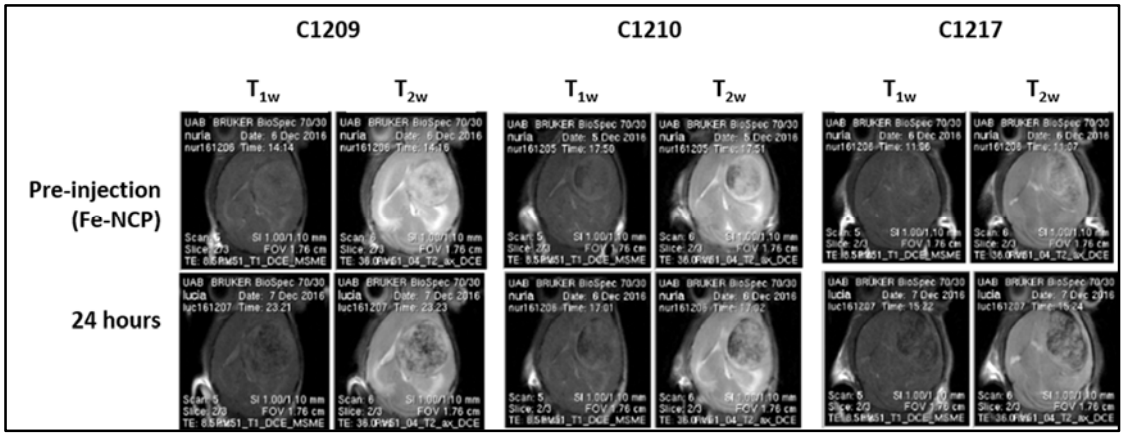

Figure 4.8: T_{1w} and T_{2w} images acquired before Fe-NCP injection and 24 hours after injection in the 3 studied animals. Images acquired 24 hours after injection showed hypointense areas in the tumours suggesting possible haemorrhage presence and/or free Fe^{3+} accumulation in the tissue.

Postprocessing algorithms were applied for generating subtraction images (T_{1w} pre-injection image minus T_{1w} post injection image) and for dual enhancement images (T_{1w} image divided by T_{2w} image) results are shown in Figure 4.9 for case C1209. In the subtraction images, T_1 contrast enhancement could be observed as a low signal zone for both Gd-DTPA and Fe-NCP. For the dual enhancement images, the hotspot produced was clearly more intense with Fe-NCP, confirming its dual enhancement potential, as opposed to Gd-DTPA, which showed high T_1 contrast but poor T_2 contrast, producing a weaker hotspot.

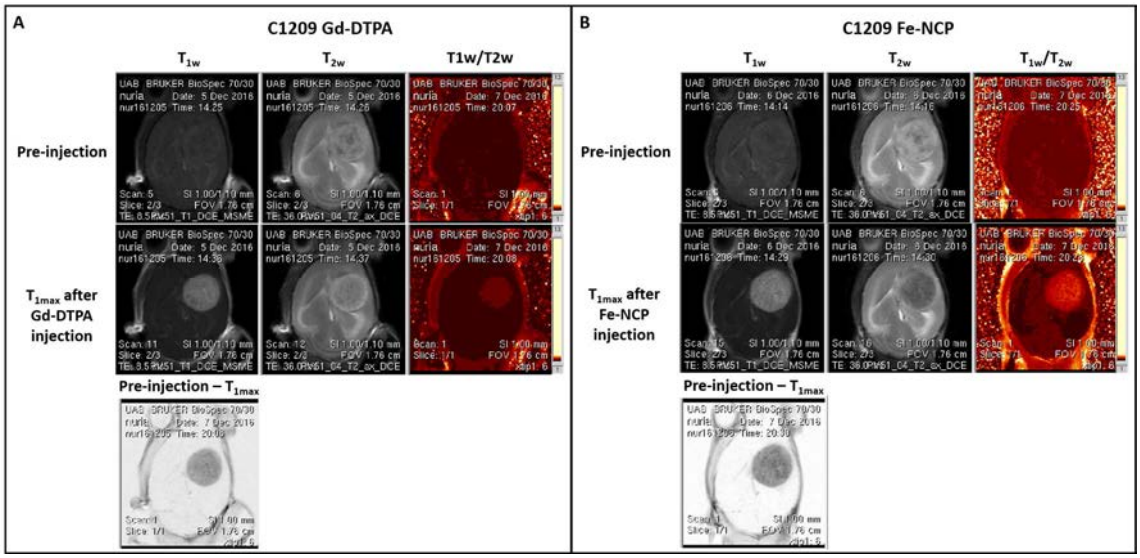

Figure 4.9: Example of a case (C1209) studied with i.v. injection of 0.4 mmol/kg of Gd-DTPA (A) and 24 hours later, with i.v. injection of Fe-NCP (B) for T_1 and T_2 contrast. **A.** T_{1w}, T_{2w} images acquired before Gd-DTPA injection (pre-injection) and at $T_{1\,max}$ (6.1±1.1 min). Processed images: T_{1w}/T_{2w} pre-injection, T_{1w}/T_{2w} at T_{1max} and T_{1w} (pre-injection) - T_{1w} (T_{1max}). **B.** T1w, T2w images acquired before Fe-NCP injection (pre-injection) and at T_{1max} (9.4±1.1 min). Processed images: T_{1w}/T_{2w} pre-injection, T_{1w}/T_{2w} at T_{1max} and T1w (pre-injection) - T_{1w} (T_{1max}). Higher T_1 and T_2 (negative) contrast was observed after Fe-NCP injection. Scale indicates colour intensity.

T_{1w} DCE-MRI with vehicle injection

The three GL261 tumour bearing mice injected with vehicle (C1195, C1197 and C1199) showed a tumour volume of 50.2± 40.7 mm^3 at the day of the experiment (day 20 p.i.). Results are shown in Figure 4.10, in which no T_{1w} enhancement was observed (less than 5% variation respect to pre-injection and they were considered as "no change" respect to preinjection). The maximum average RCE value was 101.2±1.8% at 12.8 min post injection.

Significant differences were found with UNIANOVA test between vehicle, GdDTPA and Fe-NCP evolution along the first 30 min (see data in the section below).

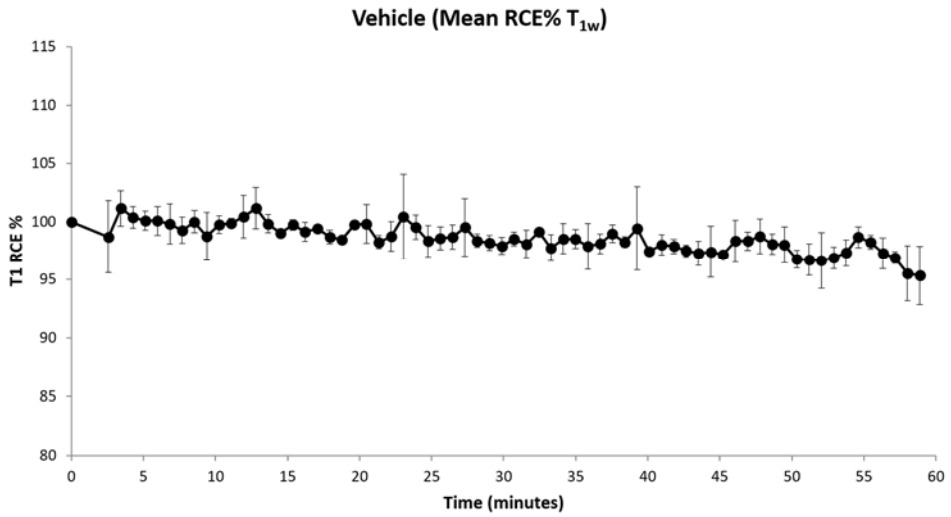

Figure 4.10: Mean ± SD of T_1 RCE from T_{1w} images in 3 GL261 mice, during 60 minutes after intravenous injection of vehicle (PBS+MSA).

4.5 Discussion

The most common contrast agents used in clinics for brain tumour diagnosis and follow-up are based on gadolinium and have effects mostly over T_1 [95] and producing brighter images ("positive contrast agents"). The main disadvantage of Gd-based contrast agents is the toxicity of the metal in its free form, being safe only when administered in a chelated form. Even so, they have been described to be linked to complications in patients with nephrogenic systemic fibrosis [102, 246, 247] and nowadays it is still a problem for patients with renal failure [102]. New approaches have been described for attempting to reduce these harmful effects [95, 100, 101], but there is great interest in developing contrast agents free of Gd and based in other metals, equally able to produce contrast in MRI images, and with less unwanted effects. In the case of T_2 contrast agents, one of the main challenges to be solved is the possible interference of MRI features derived from haemorrhage or air interfaces which could also produce a decrease in T_{2w} RCE and lead to misinterpretation when using this type of CA [248].

In this chapter, NCPs that behave as dual contrast agents for MRI and showed low toxicity *in vitro* were studied, suggesting potential for *in vivo* applications. However, performing an *in vivo* study with every synthesized NCP would demand high amount of NCPs and great efforts in terms of time, animals and resources. Prior selection of the most promising NCP with an *ex vivo* approach acts as a selection filter between *in vitro* and *in vivo* experiments and could be performed with reduced amounts of NCP and animals, mimicking better the "tissue-like" environment to be found *in vivo*. In this case, the *ex vivo* studies confirmed the tendency

described *in vitro* [104, 187] and Fe-NCP was selected to be tested *in vivo* with the well characterized GL261 GB murine model.

The Fe-NCP size described by providers had an average of 56±21 nm, which is comparable with other dual nanoparticle contrast agents described in the literature such as 93 nm in [204] and 73.8±7.6 nm in [205]. Size is a relevant parameter when assessing nanoparticle biodistribution, and it is accepted that sizes between 30-100 nm are small enough to avoid reticuloendotelial opsonisation and clearance, achieving large enough circulatory residence times can be achieved [249]. Biodistribution studies performed by NanoSFun showed that after 24 h of Fe-NCP administration, only spleen showed iron accumulation while lungs, liver and kidneys had negligible amounts of accumulated iron. This suggests minimal tissue accumulation and gradual excretion. The uptake of Fe-NCP observed in spleen suggests their rapid clearance by the mononuclear phagocytic system.

In vivo studies showed double contrast enhancement in T_{1w} and T_{2w} MRI after Fe-NCP injection. Nevertheless, we expected a longer time to maximum RCE detection, as described in [250] for nanoparticles with similar size. In work described by authors in [250], metal-organic nanoparticles of 70 nm of diameter achieved maximum signal in T_{1w} MRI after 24 hours post-i.v. injection in mice with subcutaneous 4T1 tumours. A faster time-to-maximum was observed in our experiments, after only 9.4±1.1 minutes post-injection, with full MR-detectable washout after 24 hours. Authors in [106] described ultra-small dual Gd and Dy-based nanoparticles with a size of 4.1±0.2 nm which were i.v. injected at a dose of 0.05 mmol Gd+Dy/kg. Although DCE-MRI acquisitions were not carried out in [106], T_{1w} enhancement was observed in liver and aorta 5 minutes post-injection and negative T_{2w} enhancement was observed in the liver 32 minutes post-injection. However, it was not clearly indicated by these authors if the previously mentioned times correspond to the maximum detection. In previous work of our group with the same GL261 GB model [231], small size gold nanoparticles ranging 1.8-4.5 nm showed a similar time-to-maximum MRI signal (ca. 8 minutes) as for Fe-NCP (9.4±1.1 minutes) in T_{1w} enhancement. This would suggest that Fe-NCPs could behave as a small size nanomaterial and one hypothesis for explaining this behaviour could be related to deformability, which was also mentioned by authors in [251] for chitosan nanoparticles. In any case, it is remarkable that Fe-NCP nanoparticles are able to produce T_{1w} and T_{2w} enhancement at reasonably short times, being the maximum T_{1w}/T_{2w} effect achieved between 3.95 and 10.72 min after administration. This would allow obtaining both T_{1w} and T_{2w} information in the same exploration, instead of performing two explorations separated in time.

Fe-CNP were also proven to be non-toxic in *in vivo* studies, at least in the time frame studied, i.e., no toxic effects were observed 30 days after finishing the tolerability experiment. The administered dose of iron (0.4 mmol Fe/kg) is considered safe according to authors in [239] who reported that doses between 30 and 90 mg Fe/kg (0.54 and 1.6 mmol Fe/kg respectively), were non-toxic in rats, which may be probably valid for mice, in agreement with the lack of toxic symptoms. Authors in [240] administered higher Fe (33.3 mg Fe/kg, equivalent to 0.6 mmol Fe/kg) to mice and concluded that it was safe in mice, although the study was centered in joint inflammation and a more extensive follow-up would be needed for reliable conclusions. Other authors described administration of lower doses for mice, such as 5 mg Fe/kg (corresponding to 0.09 mmol Fe/kg) [252, 253], no toxic effects were found with this dose in [252]. However, authors in [253] reported some safety concerns while working in a cirrhosis mouse model and care should be taken whenever dealing with different pathological conditions.

Considering a translational potential for Fe-NCP, we should consider the feasibility of the Fe-administered doses in humans. According to what is described in [254] and due to differences in the body surface between the two species, doses are not calculated by direct extrapolation for the corporal weight. Instead, a factor of 1/12 is applied when calculating doses, and for a 70 kg human patient, the final administered dose would be around 130 mg of Fe (equivalent to 1.8 mg Fe/kg), far below the maximum Fe concentration for i.v injection in humans (15 mg/kg) described by authors in [255].

Results in this chapter suggest that Fe-NCPs are safe, biocompatible and well tolerated for mice in the period of time studied, with no harmful effects detected. In addition, dual enhancement in T_1 and T_{2w} MRI is seen in a reasonable time frame, allowing acquisition of both informations in the same exploration, which is a clear advantage over other described dual agents, with interesting translational potential for replacing Gd-based agents in the future. Further improvement of Fe-NCPs could also result in nanocarriers that could be of interest for tumour-drug release and therapy, apart from diagnosis [188, 235].

4.6 Conclusions

1. *Ex vivo* studies performed with a set of NCPs confirmed information provided by *in vitro* relaxivity studies and suggested that Fe-NCP was the best candidate to be tested in the GL261 GB murine model. Dual enhancement *ex vivo* images were generated with algebra algorithms and hotspots indicated the dual T_1-T_2 contrast potential, with a ratio RCE%T_{1w}/RCE%T_{2w} clearly higher than other CA (7.7±4.5 vs 3.6±1.4 for Gd-DTPA)
2. Fe-NCPs were well tolerated by administered mice in doses up to 0.4mmol Fe/kg, in agreement with data described for murine species [239, 240]. Follow-up was performed during 30 days after the tolerability experiment and no harmful or toxic effects were detected. No higher concentrations were studied in this chapter, and a final MTD was not calculated.
3. Experiments *in vivo* confirmed the dual T_1-T_2 enhancement for Fe-NCP after i.v. injection in mice with 0.4 mmol Fe/kg dose. Both T_{1w} and T_{2w} enhancement produced by Fe-NCP were significantly better than the commercial agent Gd-DTPA.
4. The maximum T_{1w} enhancement was observed at 9.4±1.1 min post injection, whereas the T_{2w} enhancement reached its maximum effect at 5.3 ±1.1 min post injection. These times were shorter than it was expected for nanoparticles with similar size, indicating that Fe-NCPs could behave as small CA, possibly due to their deformability properties. This provides a reasonable time frame for maximum T_1/T_2 effect (between 3.95 and 10.72 min after administration) allowing to gather T_1 and T_2 data in the same exploration, which certainly is a positive aspect of Fe-NCP.
5. Results obtained with the GL261 GB preclinical model suggest a translational potential for Fe-NCPs. The translated iron dose that would be needed for human patients is within the allowed doses for i.v. administration of iron. Accordingly, such nanoparticles could be a future alternative for Gd-based CAs.

5. Optimization of a MRSI multi-slice protocol for volumetric analysis of mouse brain tumour

5.1 Specific objectives

The main purpose of this chapter was to improve the single slice MRSI protocol established in our group [90, 116, 117, 256]. By their nature, GBs are heterogeneous tumours and TMZ treatment has proven to trigger heterogeneous response patterns in previously evaluated GL261 GB [117]. The use of a single slice MRSI protocol could probably hinder proper assessment of tumour response in such circumstances. Furthermore, there is a great interest in full 3D MRSI implementation [121, 257]. In this chapter an intermediate approach between full 3D and single-slice acquisition was optimized: a 2D multi-slice approach which would allow to gather information of most of the tumour volume.

5.2 Specific material and methods

5.2.1 Initial set up of MRSI grid size and position with wt mice

Two female wt mice (17 weeks of age) were used for this optimization. Combinations of two grid sizes were tested in different positions along the mouse brain. The MRSI acquisition parameters were essentially the same as in section 3.5.2, with exception of matrix size and VOI (see Table 5.1). Each MRSI grid was acquired individually for each position and shimming was performed individually in each grid using the FASTMAP method which is especially relevant for grids positioned away from the surface coil.

Table 5.1: Acquisition parameters of different MRSI grids used in the set-up experiments for the multi-slice protocol.

Grid size	Voxel dimension	Field of view	Pixel size	Acquisition time
10 x 10	5.5 x 5.5 x 1 mm	17.6 x 17.6 mm	0.55 mm	21 min 30 sec
12 x 12	6.6 x 6.6 x 1 mm	17.6 x 17.6 mm	0.55 mm	21 min 30 sec

Two different multi-slice combinations were performed:

5.2.1.1 MRSI grid size: 10 x10 vs 12 x 12

In a first approach, three MRSI grids with the same matrix size (10x10 voxels) were consecutively allocated along the mouse brain (Figure 5.1, top row). A second approach was done in a similar way except that the central grid (Grid 2) was increased to 12x12 voxels (Figure 5.1, bottom row). The total acquisition time for each approach was about 3 hours.

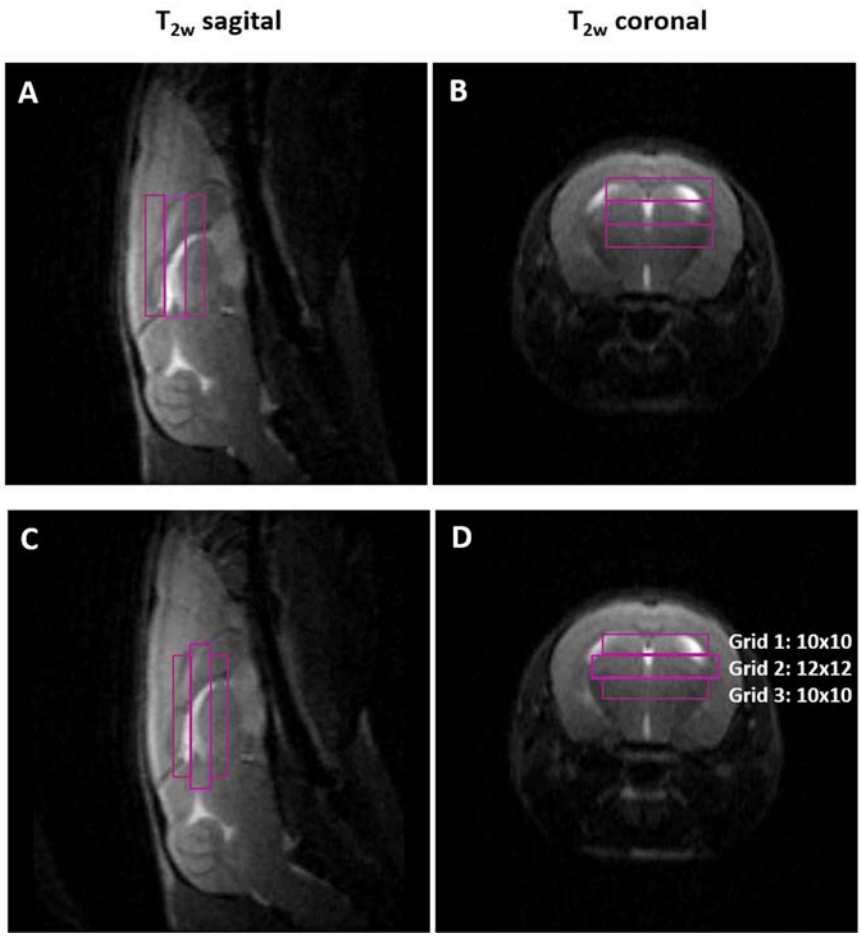

Figure 5.1: Different views of T_{2w} images from a wt mouse with consecutive MRSI grid positions. Top, 3 Grids of 10x10 voxels in **A)** sagittal plane and **B)** coronal plane. Bottom, middle Grid with 12x12 voxels. in **C)** sagittal plane and **D)** coronal plane.

5.2.2 Combination of MRSI grid size and position in tumour-bearing mice

Three mice of 17 weeks of age harbouring GL261 tumours were studied in the experiments described in this section. MRSI experiments were carried out at days 15-16 p.i and tumour volume at day of the experiment was 23.9±5.8 mm^3. A total of 4 consecutive MRSI grids were placed in order to cover the whole tumour extension. Different matrixes sizes were used: Grid 1 and Grid 4 with 10x10 voxels, Grid 2 and Grid 3 with 12x12 voxels (Figure 5.2). In addition, Grid 2 was acquired in triplicate in order to assess the reproducibility of the spectral pattern in this central slice (which is the position similar to the MRSI grids acquired previously in our group in single slice experiments [90, 116, 117, 127].

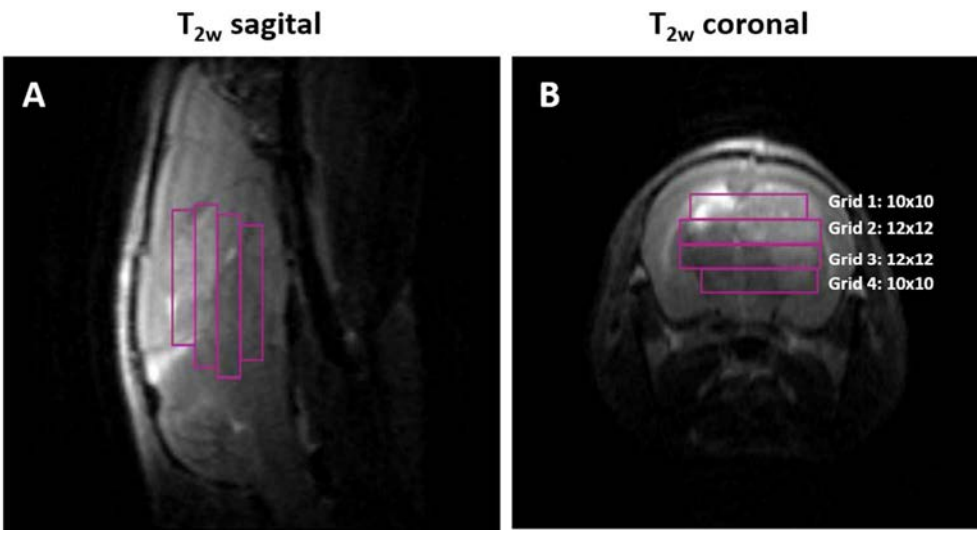

Figure 5.2: T_{2w} MRI of mouse C894 brain, with the position of the four MRSI slices in **A)** sagittal plane and B**)** coronal plane.

5.2.3 Spectral quality assessment of MRSI grids

Signal to noise ratio

Signal to noise ratio (SNR) was calculated as described in section 3.6.2 and coloured maps related to SNR values were generated for each grid. Spectra with SNR<10 were considered poor quality spectra (as indicated in [258]), and the percentage of voxels with SNR<10 was calculated for each grid). Spectral quality from the voxels placed in edges or centre of MRSI grids (Figure 5.3) were assessed for differences. However, voxels from the edge were avoided whenever possible in order to ensure comparable quality.

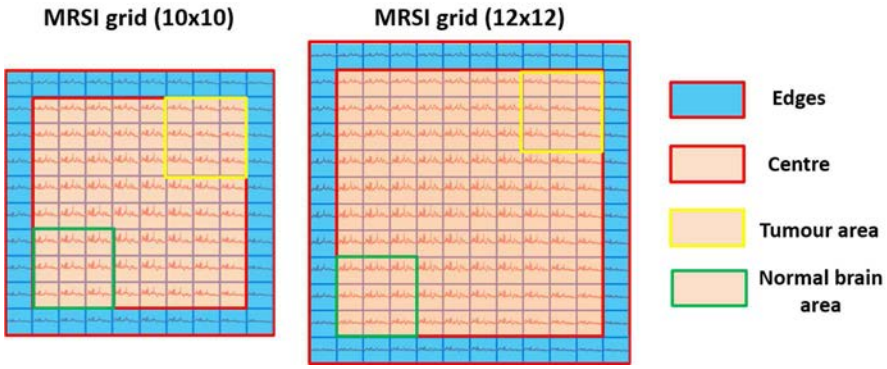

Figure 5.3: Schemes of MRSI grids of 10x10 voxels dimension (left) and 12x12 voxels dimension (right). The blue area was considered the edge and the orange area was considered the centre of the grids. The yellow area corresponds to the tumour injection point and the green area indicates the normal brain parenchyma region in a GL261 tumour-bearing animal.

Spectral pattern inspection and presence of artefacts

Mean spectra from the striatum area corresponding to the injection point in tumour-bearing animals (n=9 voxels, yellow area in Figure 5.3) and the area corresponding to non-affected brain parenchyma (n=9 voxels, green area in Figure 5.3) were calculated using 3DiCSI for a visual inspection of the average spectral pattern. Unsupervised sources (n=3 sources) were obtained as described in section 3.7.1, allowing us to inspect main paradigmatic patterns and also detect artifacts due to insufficient water suppression, poor homogeneity or lipid scalp contamination. Finally, semi-supervised source analysis was performed as described in section 3.7.2 to check about possible misclassification or incoherence due to different grid positioning.

5.3 Results and discussion

5.3.1 Assessment of Spectral Quality in MRSI grids of wt mice.

5.3.1.1 Consecutive grids with the same matrix size (10x10)

SNR, mean spectra and artifact analysis

The SNR maps generated from the three MRSI grids are shown in Figure 5.4, and numerical values are shown in Table 5.2. The percentage of voxels with SNR below the threshold of 10 increased for larger distances grid-coil, and this was indeed expected because being in the vicinity to the coil produces more intense signals. Significant differences ($p<0.05$) were found between SNR of the edges and center voxels of each grid, being SNR 1.6 to 1.8-fold higher in center voxels.

The SNR values of center voxels in different grids were compared and, as expected, Grid 1 (closer to the coil) presented the highest value, significantly better than Grids 2 and 3, although all values were within acceptable quality ranges. The same result was found for edge voxels, in which the highest SNR value was found in Grid 1. No significant differences were found between Grids 2 and 3.

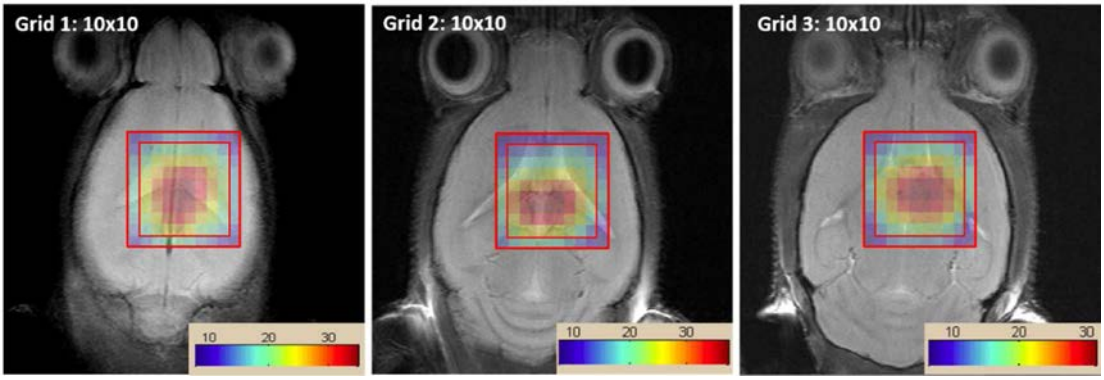

Figure 5.4: SNR maps calculated for each MRSI grid tested in this multi-slice experiment, superimposed to the T_{2w} images. The grid dimension was 10x10. The coloured scale indicates the SNR range. Highest SNR values were observed in the centre of the grids and lowest SNR values were observed in the edges.

Table 5.2: SNR data from the grids of the multi-slice combination of 10x10 voxels: Percentage of voxels with SNR<10, SNR of the edges and centre of the grids. Values are shown as mean ± SD

	Grid 1 (10x10)	Grid 2 (10x10)	Grid 3 (10x10)
% Voxels SNR<10	1.0	3.0	4.0
SNR Edge voxels	17.9±4.3 (n=36) *£	15.5±4.2 (n=36) *	15.4±4.8 (n=36) *
SNR Centre voxels	31.9±8.0 (n=64) £	25.8±6.2 (n=64)	28.2±7.3 (n=64)

* = p<0.05 in comparison with SNR of centre voxels of the same grid
£ = p<0.05 in comparison with Grid 2 and Grid 3.

Mean spectra was calculated for two different areas schematized in Figure 5.3. The area corresponding to future tumour cells-injection point (n=9 voxels) and to normal brain parenchyma (n=9 voxels). Figure 5.5 shows the spectral patterns obtained for these areas in each studied grid. No significant differences (p>0.05) were observed with Student's t-test in SNR neither between yellow and green areas within each grid, nor between corresponding areas (yellow or green) from different grid positions

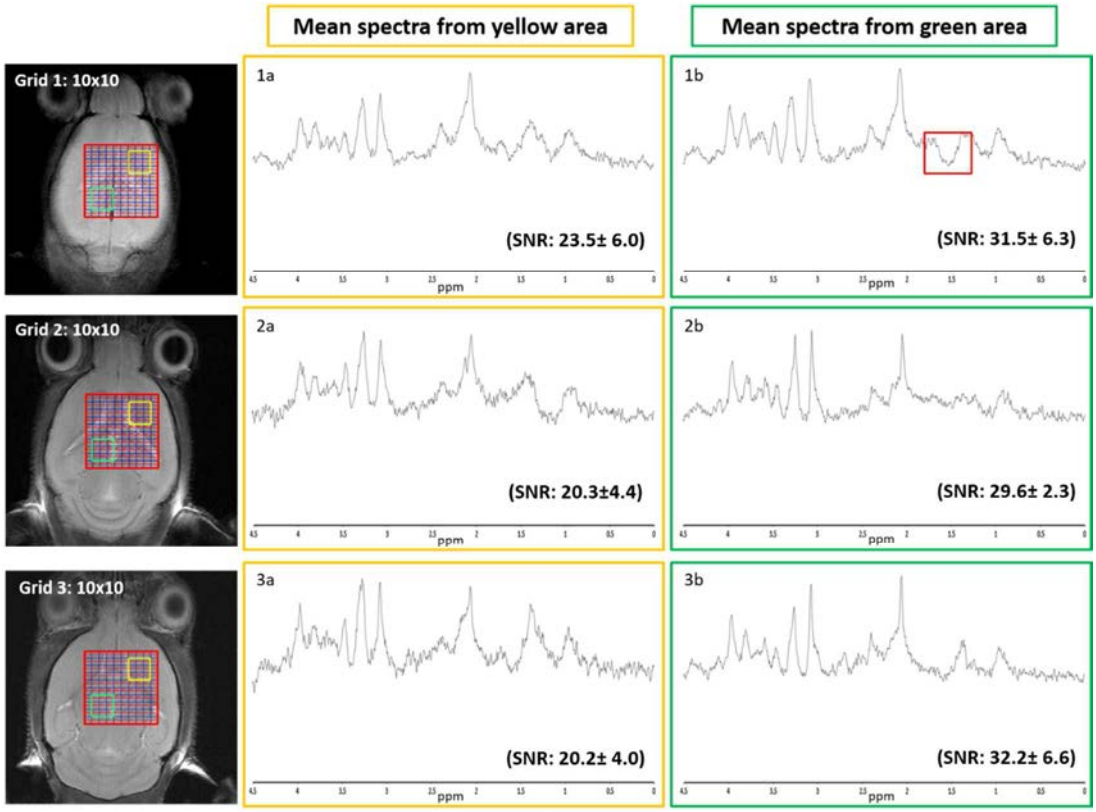

Figure 5.5: Mean spectra calculated in area corresponding to usual tumour injection point (yellow) and normal brain (green) areas selected in MRSI grids for this multi-slice experiment. From top to bottom: Grid 1, Grid 2 and Grid 3. The presence of a possible artifact is marked in red in mean spectrum 1b. SNR of each mean spectra is indicated.

The six mean spectra calculated presented a spectral pattern consistent with normal brain parenchyma as expected, showing sensible Cho/Cr and NAA/Cr ratios of 0.95±0.17 and 1.09±0.14, respectively. These values are in agreement with Cho/Cr and NAA/Cr ratios calculated previously in our group in [259] for normal brain (Cho/Cr= 0.98±0.03 and NAA/Cr=1.01±0.06). We can also appreciate a possible artefact at 1.53±0.01 ppm in mean spectra 1b, which after careful inspection was seen in 3 out of 9 voxels used for calculation, although it does not compromise the overall spectral quality. SNR was also calculated from yellow and green areas of each grid and significant differences ($p<0.05$) were observed between these areas in the 3 studied grids, SNR of green areas were 1.46 fold higher than SNR of yellow areas. No differences ($p>0.05$) were found between the same areas of different grids (see SNR values in Figure 5.5).

Unsupervised source analysis

In order to check for major artefacts in whole grids, unsupervised sources (n=3) were extracted from each individual grid. Figure 5.6 shows the 3 sources obtained for each grid, the maps associated to each source and these maps superimposed to the correspondent T_{2w} axial image.

As it can be appreciated, some possible artefacts were detected with this approach, namely: poor water suppression and low SNR in Grid 1 (source 2) in the upper-right corner; inversion artefacts at ca. 1.49 – 1.52 ppm were observed in Grids 1 and Grid 3 (sources 3 and 1 respectively) 0.9-1.32 ppm) usually near the edges of the grid. Another inversion artefact was observed in Grid 2 (source 3) at ca. 0.9-1.32 ppm. The inversion artefact detected in Grid 1 is coherent with mean spectra shown in Figure 5.5, spectra 1b. Such artefacts could be at least partially due to out-of-volume lipid artefact [260] even with the use of saturation bands. This slice is close to the scalp and this should be taken into account. However, at this point, due to the coherence of the rest of the spectral pattern, spectra would be useful and correctly classified in an adequate trained semi-supervised analysis.

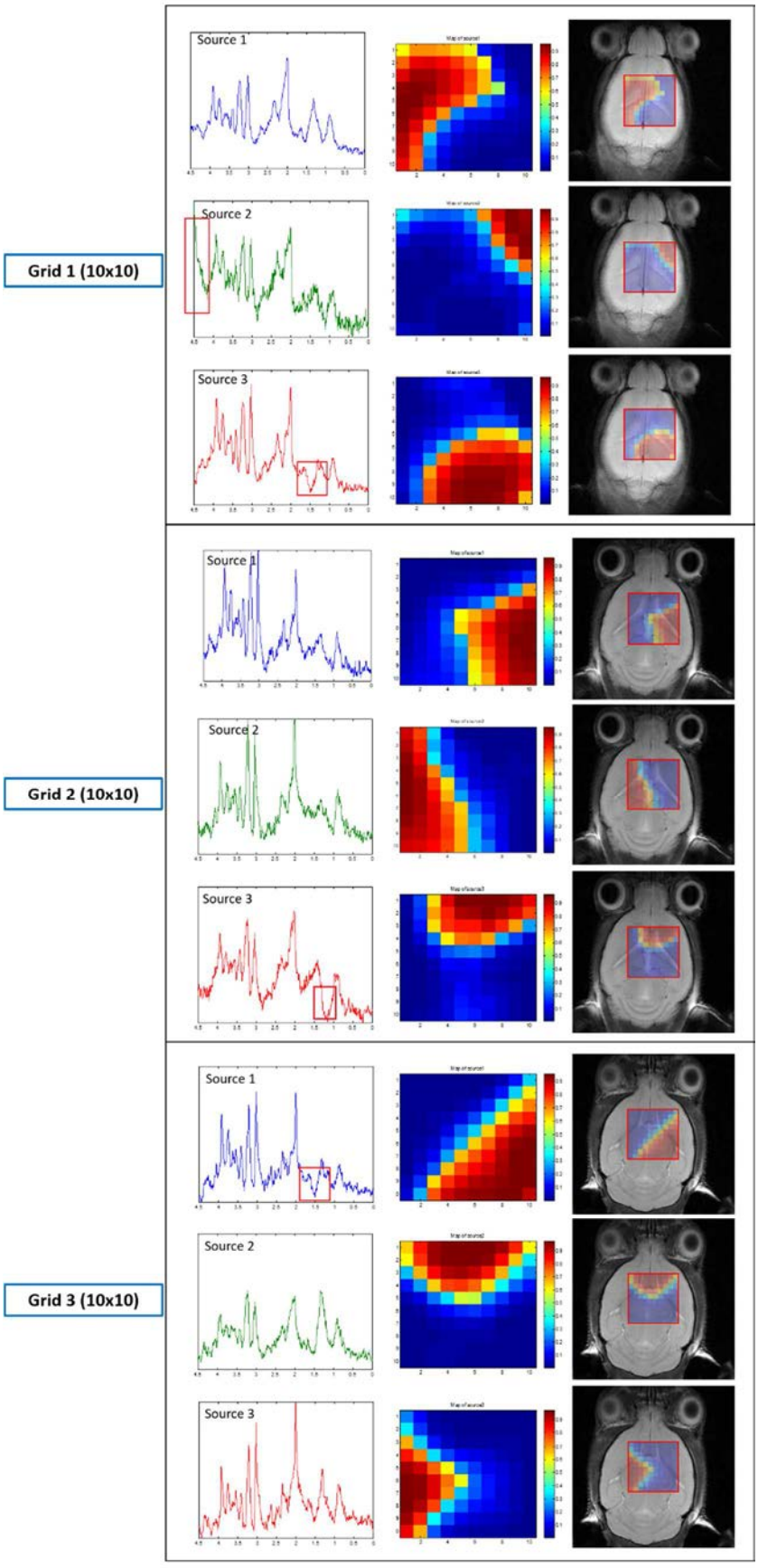

Figure 5.6: Results of the unsupervised analysis of the three grids of the 10x10-combination matrix. For each grid, 3 sources were obtained, the corresponding maps associated to each source were calculated and superimposed to the T2w axial MRI. Red squares indicate the possible artefacts observed in those sources

5.3.1.2 Consecutive grids with different matrix size (10x10 and 12x12)

SNR, mean spectra and artefact analysis

Most results obtained with this matrix size combination were essentially similar to results obtained with the 10x10 grid combination. SNR maps generated from the three MRSI grids are shown in Figure 5.7 and numerical values are stated in Table 5.3. Similarly, as described in section 7.3.1.1, lower grids presented a higher percentage of low quality spectra (SNR<10) in comparison with upper grids and Grid 1 did not show any spectra with SNR below 10. Spectra from edge voxels presented significantly worst quality in comparison with center voxels which had higher SNR value (1.7 to 1.8 fold higher). However, all of them were within acceptable values with average SNR ranging from 13.3 to 30.5.

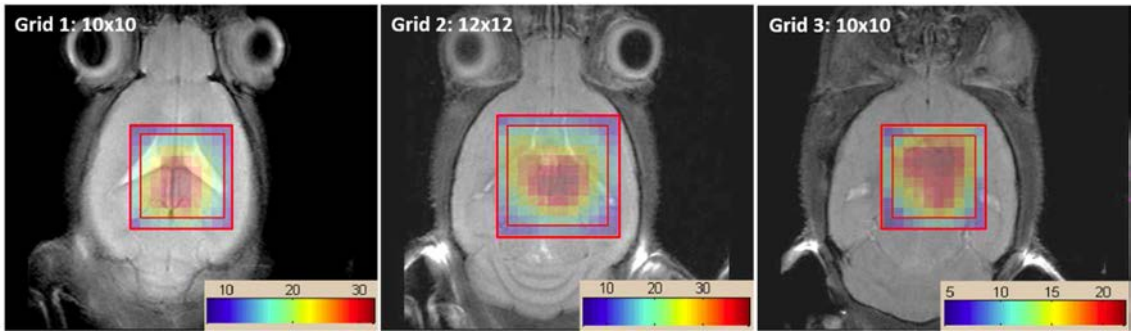

Figure 5.7: SNR maps calculated for each MRSI grid tested in this multi-slice experiment using different dimensions, superimposed to the T_{2w} images. From left to right: Grid 1 with 10x10 voxels, Grid 2 with 12x12 voxels and Grid 3 with 10x10 voxels. The coloured scale indicates the SNR range. Highest SNR values were observed in the centre of the grids and lowest SNR values were observed in the edges of the grids.

As performed in the previous subsection, mean spectra was calculated for the area corresponding to tumour injection point (n=9 voxels) and to normal brain parenchyma (n=9 voxels). Figure 5.8 shows the spectral pattern obtained for these areas in each studied grid.

Table 5.3: SNR data from the grids of the multi-slice combination of 10x10 and 12x12 voxels: Percentage of voxels with SNR<10, SNR of the edges and centre of the grids. Values are shown as mean ± SD

	Grid 1 (10x10)	Grid 2 (12x12)	Grid 3 (10x10)
% Voxels SNR<10	0.0	5.0	9.0
SNR Edge voxels	17.9±4.2 (n=36)*£	15.4±5.2 (n=44)*	13.3±3.8 (n=36)*
SNR Centre voxels	30.5±8.0 (n=64)	29.2±8.1 (n=100)	24.3±6.3 (n=64)**

* = p<0.05 in comparison with SNR of centre voxels of the same grid.
£ = p<0.05 in comparison with Grid 2 and Grid 3.
** = p<0.05 in comparison with Grid 1 and Grid 2.

The six mean spectra calculated presented a spectral pattern consistent with normal brain parenchyma as expected, showing the expected Cho/Cr and NAA/Cr ratios as in the 10x10 grid combination. For Cho/Cr the ratio obtained was 0.79±0.12 and 1.01±0.15 for NAA/Cr. As in the previous grid combination, the mean spectrum 1.b showed a similar inversion artefact at 1.60±0.02 ppm which was detected in 6 out of 9 voxels. Although its chemical shift was slightly different (1.53 ppm in previous combination), the artefact probably has the same origin and would not compromise the overall spectra quality.

SNR calculated from yellow and green areas presented significant differences ($p<0.05$) in the same grids. In the case of Grids 1 and 2, SNR of green areas was 1.35 fold higher than SNR of yellow areas. However, in Grid 3 it was the other way round: the SNR of the yellow area which was 1.33 fold higher than SNR of the green area. In the case of the same areas in different grids, significant differences were found between the green areas of Grids 3 and Grids 1 and between green areas of Grid 3 and Grid 2 (see SNR values in Figure 5.8).

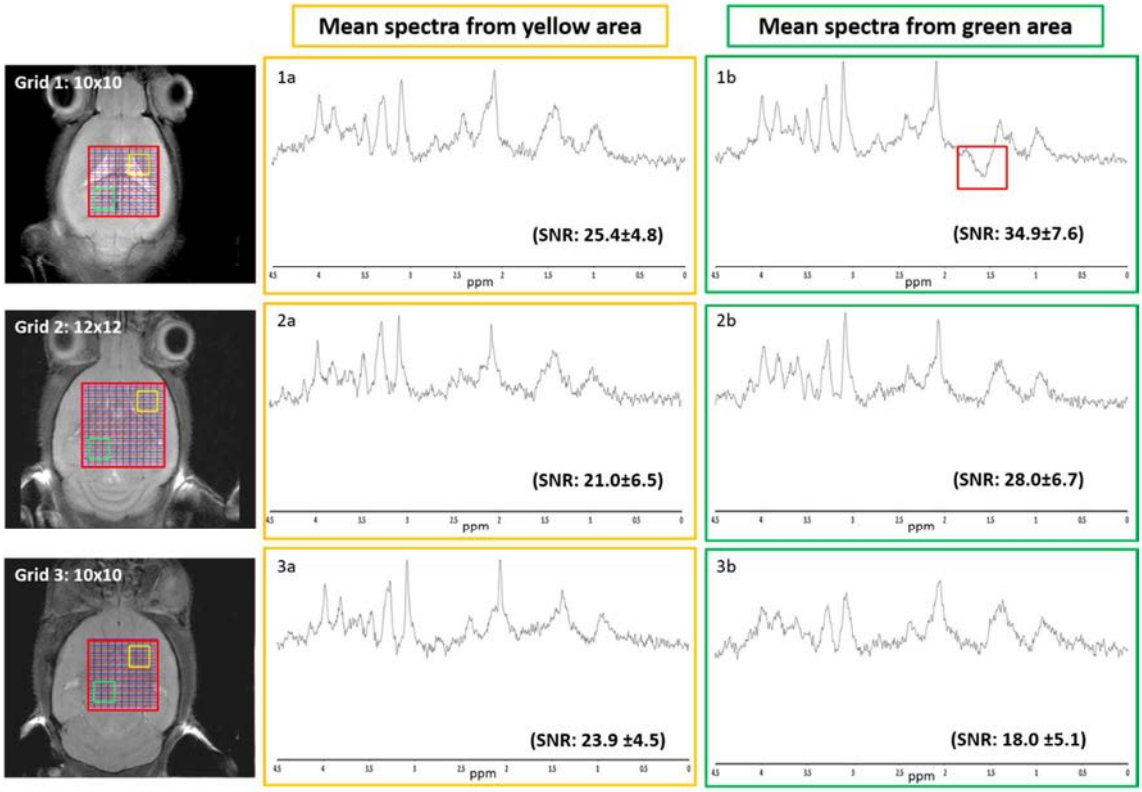

Figure 5.8: Mean spectra calculated in the area corresponding to tumour injection point (yellow) and normal brain (green) area selected in MRSI grids for this multi-slice experiment. From top to bottom: Grid 1, Grid 2 and Grid 3. The presence of a possible artefact is marked in red in mean spectrum 1b. SNR of each mean spectra is indicated.

Unsupervised source analysis

Unsupervised sources (n=3) were extracted from each individual grid. Figure 5.9 shows the 3 sources obtained for each grid, the maps associated to each source and these maps superimposed to the correspondent T_{2w} axial image. Inversion artefacts were detected at ca. 1.52-1.53 ppm, mostly at the bottom part of the Grid 1 (sources 1 and 3) and Grid 3 (source 2). Artefact is more prominent at Grid 3 and this source also has a poor SNR profile in comparison with the other ones, which is probably related to grid location and vicinity to heterogeneous zones and structures. Still, an inversion artefact seems to appear in Grid 2 (source 2) at ca. 2.76-2.89 ppm. None of the artefacts seems to distort the rest of the spectral pattern and those would be probably still useful in a basic semisupervised source analysis study such as tumour vs normal.

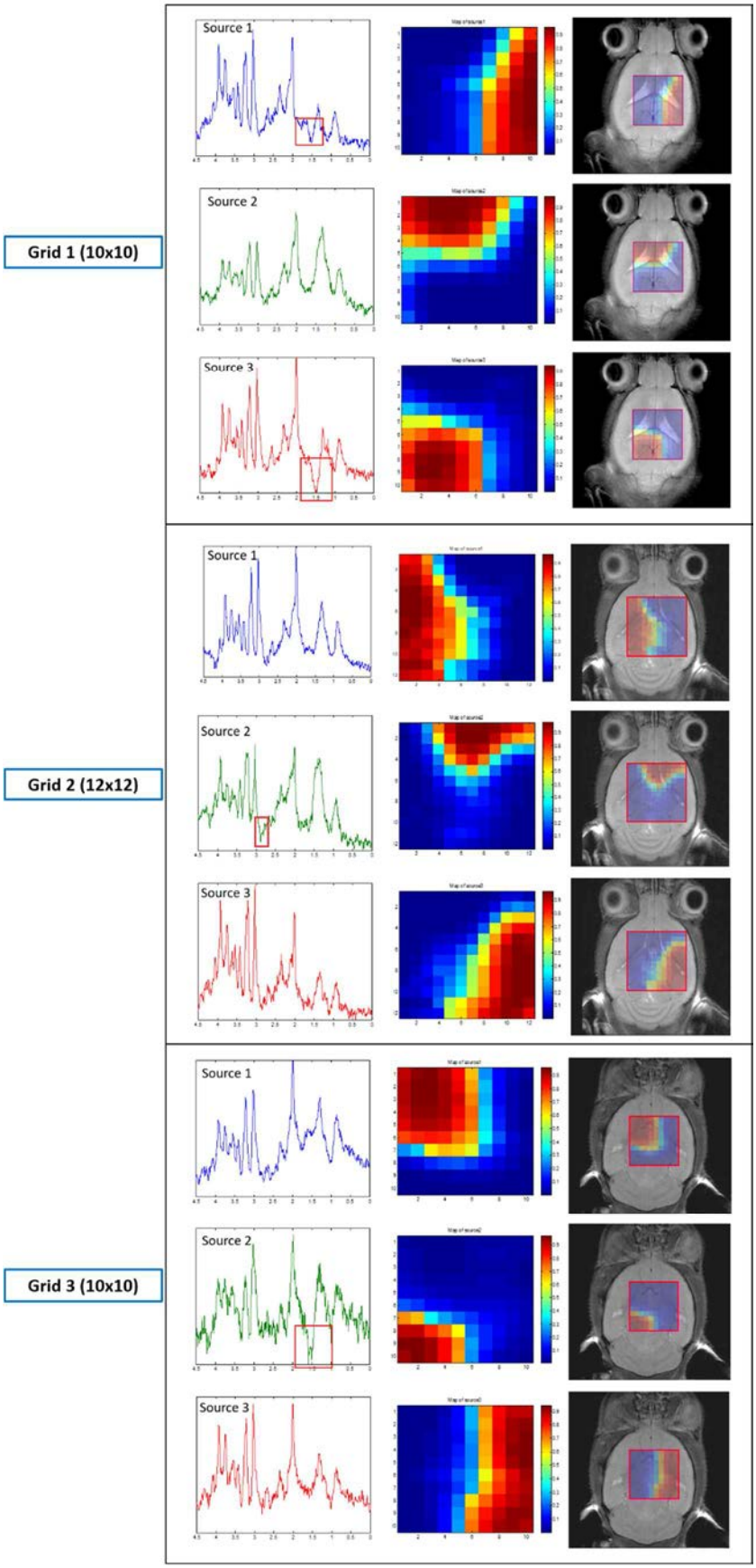

Figure 5.9: Results of the unsupervised analysis of the three grids of the 10x10 and 12x12 combination matrixes. For each grid, 3 sources were obtained, the corresponding maps associated to each source were calculated and superimposed to the T2w axial MRI. Red squares indicate the possible artefacts observed in those sources.

5.3.2 Preliminary experiments with GL261 tumour-bearing mice. Assessment of Spectral Quality

The multi-slice MRSI scheme of 10x10 and 12x12 combination was tested in 3 GL261 tumour-bearing mice to check for the robustness of the results. For complete coverage of the whole tumour, a 4th slice was added, in a lower position, with a matrix size of 10x10 voxels. In addition, Grid 2 was acquired by triplicate in order to ensure reproducibility of the observed pattern. The same analyses described in the previous subsection were performed, regarding SNR, mean spectra and unsupervised source analysis. In addition, a semi-supervised source analysis was carried out as in section 3.7.2 of the general materials and methods. Figures from one representative case (C894) are shown, whereas data from the remaining cases can be found in Annex II.

5.3.2.1 SNR, mean spectra and artifact analysis

The SNR maps of the representative mouse C894 are shown in Figure 5.10 and the mean values of the 3 studied animals are listed in Table 5.4, which also shows the SNR calculated values for tumour and normal brain parenchyma areas. SNR data from Grid 2 is shown as mean±SD of the 3 acquisitions performed for each of the 3 cases. As it was already seen with wt animal studies, the positioning of the grid is directly related with the amount of insufficient quality spectra (SNR<10) going from 3.0±2.0% in the first grid to 13.3±6.0% in the lower grid. These differences were statistically significant when comparing Grid 1 to Grids 3 and 4: the SNR of the edge voxels was lower than SNR in centre voxels which were 1.73-1.98-fold higher. This difference was even more evident in the central grids, in which it was almost two-fold (1.97±0.17). Regarding SNR in centre voxels, a decreasing trend was found as expected, which was related to grid positioning decreasing from 36.2±10.2 in Grid 1 to 23.3±7.3 in Grid 4. SNR of the centre voxels of Grid 4 was significantly lower ($p<0.05$, Mann-Whitney's U test) compared to the rest of the grid positions. Still, average SNR values obtained in multi-slice MRSI acquisitions were lower than values obtained in single-slice MRSI when considering the grid with equivalent positioning (see section 5.4 for more details in this comparison). Finally, as it was expected, SNR obtained in the triplicate acquisition of Grid 2 was consistent and values were not significantly different neither from edge nor from centre voxels ($p>0.05$).

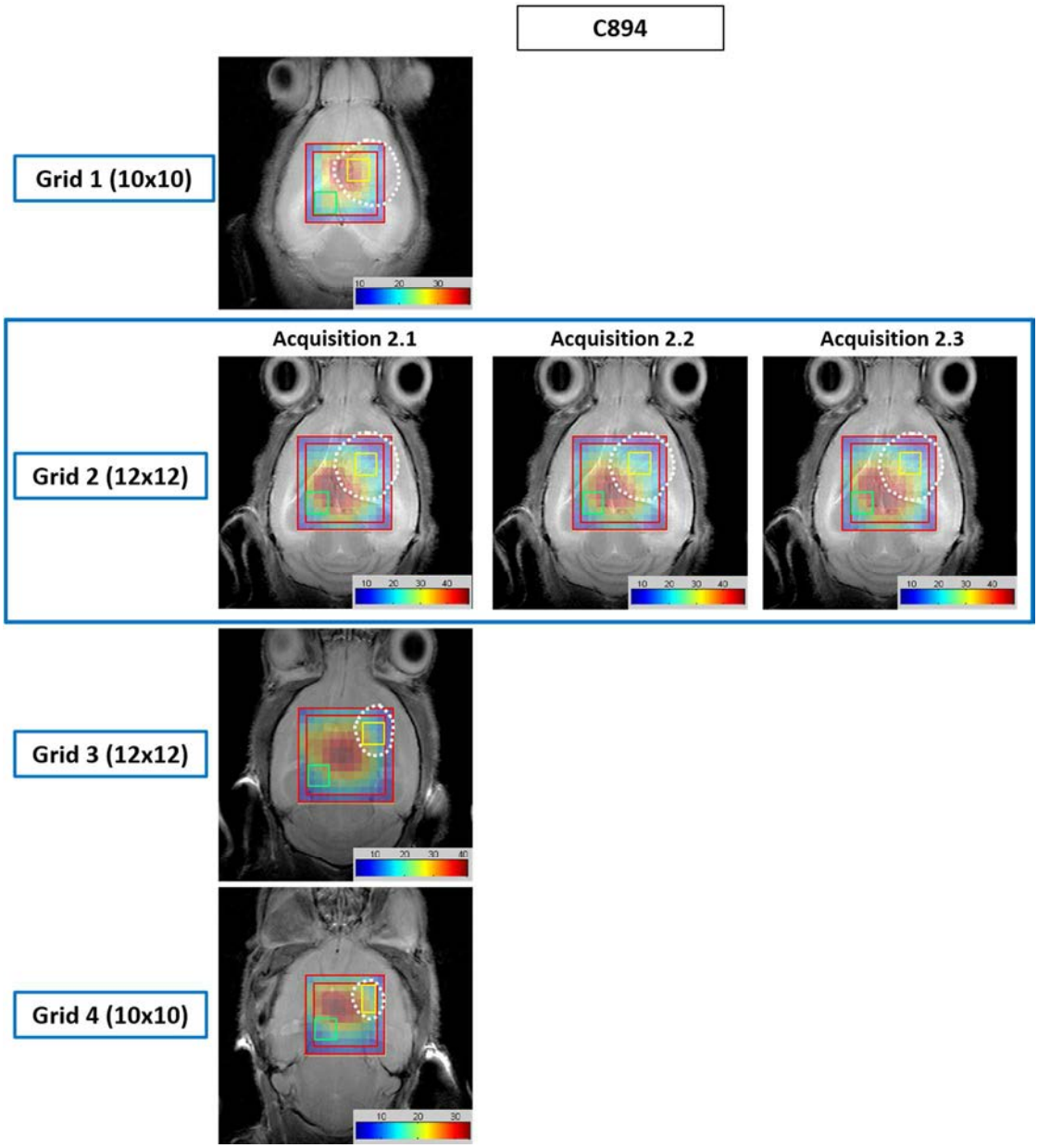

Figure 5.10: SNR maps calculated for each MRSI grid tested in this multi-slice experiment, superimposed to the T2w images in the representative case C894. Tumour borders are marked with dashed white lines in each grid. The yellow and green squares indicate the voxels selected to calculate SNR of the tumour and normal parenchyma area, respectively. SNR maps from repeated acquisitions of Grid 2 are shown as acquisition 2.1, 2.2 and 2.3, for reproducibility issues. The coloured scale indicates the SNR range. Note the different coloured scale for SNR range in grids 1 and 4, suggesting an overall lower SNR in Grid 4.

Table 5.4: SNR data from edges and centre voxels of the grids of tumour-bearing mice, as well as SNR from tumour and normal brain parenchyma zones. The second grid that was acquired 3 times is represented by the average value of the 3 acquisitions. Values are shown as mean ± SD.

GL261 mice (n=3)	Grid 1	Grid 2	Grid 3	Grid 4
% Voxels SNR<10	3.0±2.0	4.9±2.0	7.6±0.7*	13.3±6.0*
SNR Edge voxels (mean±SD)	20.9±8.1 £	17.2±7.9 ££	15.4±7.8	13.3±5.2
SNR Centre voxels (mean±SD)	36.2±10.2£	33.1±12.0££	30.5±10.8$	23.3±7.3
SNR Tumour voxels (mean±SD)	46.5±11.5**	45.7±15.2 **	26.1±8.3$	16.2±3.4
SNR Normal parenchyma voxels (mean±SD)	30.5±7.7$	33.2±6.1$	32.8±10.4$	23.9±4.9$

*= p<0.05 in comparison with Grid 1
£= p<0.05 in comparison with SNR of edges voxels of Grid 2, 3 and 4.
££= p<0.05 in comparison with SNR of edges voxels of Grid 3 and Grid 4.
$= p<0.05 in comparison with SNR of centre voxels of Grid 4
** p<0.05 in comparison with SNR of centre voxels of Grids 3 and 4.

SNR was calculated in voxels of tumour area (n=2-9 depending on the tumour area in each grid) and normal parenchyma area (n=9) for each case, indicated by yellow and green squares respectively in Figure 5.10, and mean SNR data of both areas of all mice are shown in Table 5.4. We have not observed a clear pattern (i.e. tumour zone SNR being always higher or always lower than normal brain parenchyma zones). SNR calculated from tumour voxels was 1.5-fold higher than normal zone in Grid 1, while a decrease in a 0.67 factor was seen in Grid 4 in comparison with the normal brain parenchyma zone. It is interesting to observe that in Grids 2 and 3, located in 'less extreme' positions in comparison with Grids 1 and 4, there were clearly less difference in SNR of tumour and normal zones. In Grid 2, SNR was only 1.37-fold higher in tumour and, on the other hand, Grid 3 showed a decrease on 0.8-fold comparing tumour area with normal brain parenchyma. The overall tendency to higher SNR values in upper grids was maintained in this study, as expected.

The spectral quality in tumour and normal parenchyma areas was assessed in the same voxels used for SNR studies. Figure 5.11 shows mean spectra from tumour (yellow-frame area) and normal brain parenchyma (green-frame area) for case C894 while remaining cases are shown in Annex II. For all cases, the mean spectra in both tumour and contralateral area presented the typical spectrum pattern expected for these areas i.e. ratio Cho/Cr of 1.65±0.37 and intense mobile lipids signals in case of tumours and ratios Cho/Cr and NAA/Cr of 0.91±0.13 and 1.17±0.19 respectively, in normal brain parenchyma zones. These values are in agreement with previous data from our group [259] showing that there is consistence across different grid

positions. Moreover, mean spectra from the three consecutive acquisitions from Grid 2 were reproducible in the three mice explored.

No noticeable artifacts were seen in mean spectra from Grids 1, 2 and 3. A small artifact was visible at 1.55±0.0 ppm (in 6 out of 9 spectra selected to calculate mean spectrum) in the normal appearing brain parenchyma zone in Grid 4, similarly to wt studies described in previous sections. However, it does not compromise the overall quality of the spectra, which were satisfactory in all grid positions.

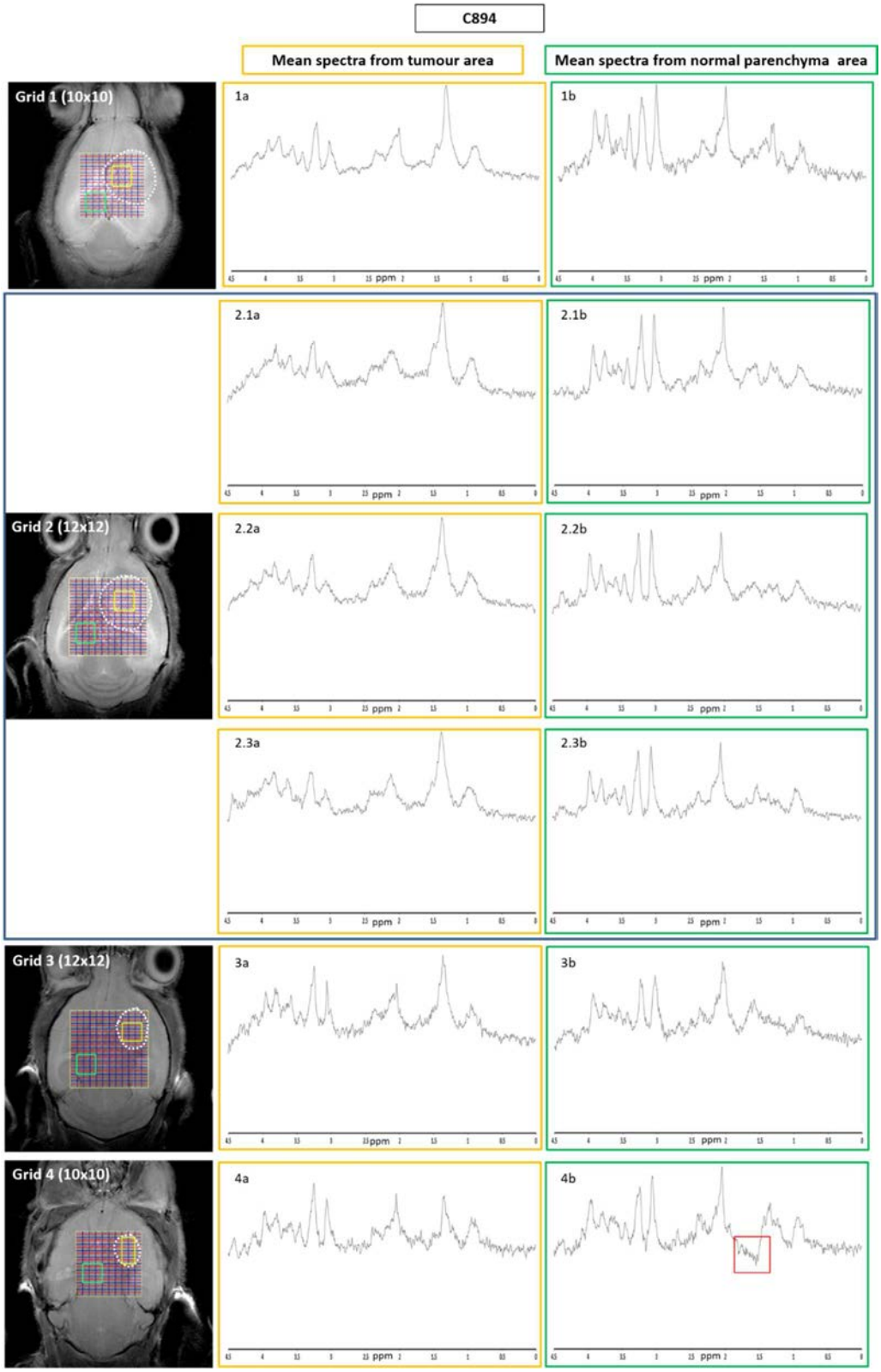

Figure 5.11: Mean spectra calculated for case C894 from tumour area (yellow) and contralateral area (green) in the four grids. Tumour borders are marked with dashed white lines in each grid. Most spectra were of excellent quality and free from artifacts. Triplicate acquisitions for Grid 2 were proven reproducible. The red square marked a possible small inversion artifact detected in Grid 4.

5.3.2.2 Unsupervised source analysis

Unsupervised source analysis (n=3 sources) was carried out with the three GL261 tumour-bearing animals in order to check for artefact presence in the whole grid and gone unnoticed in mean spectra analyses. It also allowed to visually evaluate whether a consistent segmentation between tumour and normal zones was achieved. It is worth noting that in the unsupervised analysis, the sources are not fixed and for this reason the colour of the sources could change in each analysis.

In the three studied cases, good segmentation was observed in Grids 1, 2 and 3 but not in Grid 4 as seen in Figure 5.12. Both the grid position and the small fraction of tumour occupying the grid could explain the obtained results. For the remaining grids, apart from the expected tumour and normal spectral pattern, a third source appeared related to spectral quality (this was more evident in Grids 2 and 3 with poor water suppression and/or SNR, but less evident in Grid 1). In Grid 2, acquired 3 consecutive times, high reproducibility was observed in this unsupervised analysis. See Table 5.5 for source identification.

In the representative case C894 illustrated in Figure 5.12, most of the artifactual patterns were found in the edges of the grids located at either upper or bottom corners and were also noticed in cases C891 and C895 (Annex II). In all cases, Grid 4 presented sources characteristic of poor SNR patterns.

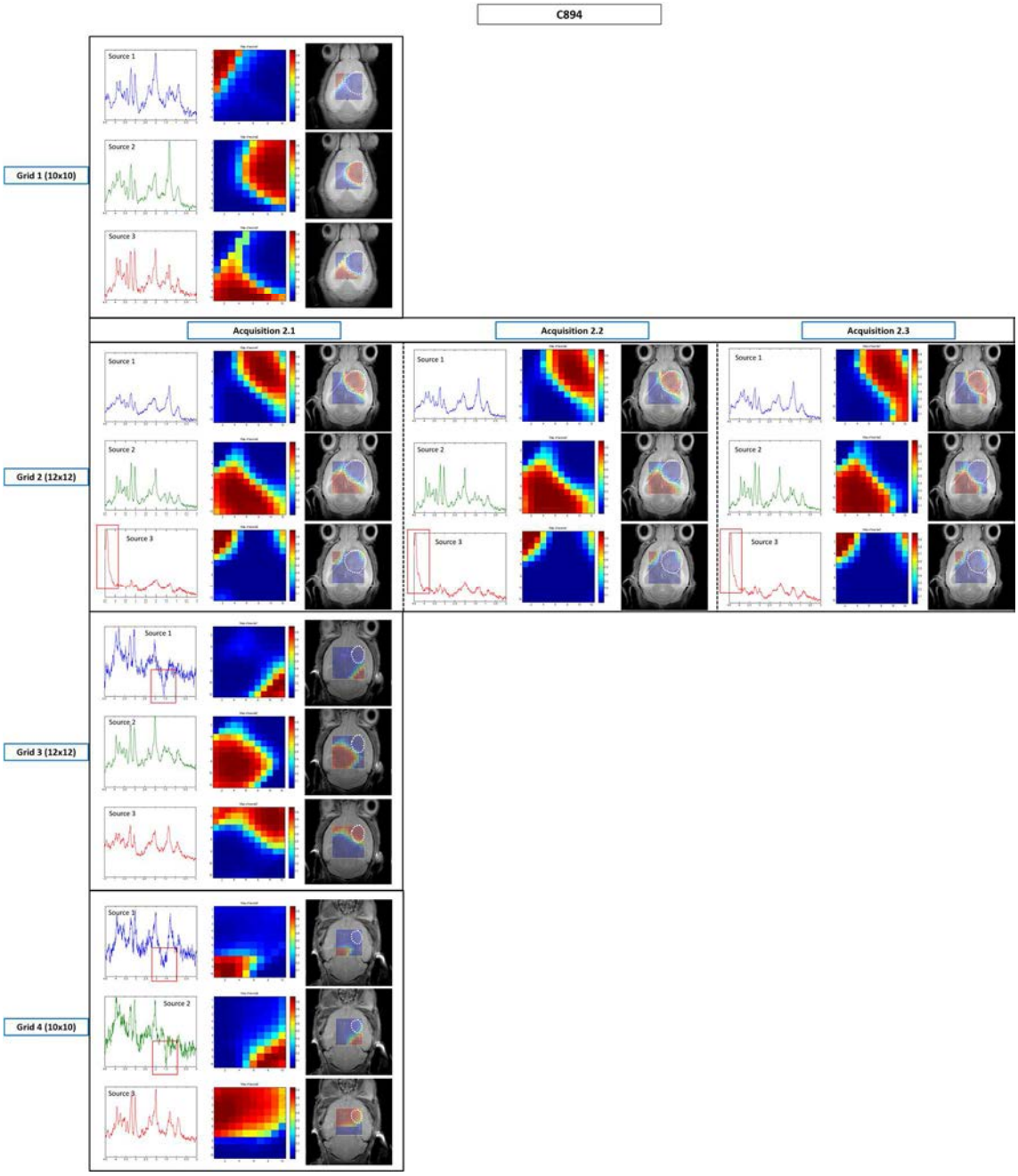

Figure 5.12: Calculated sources, intensity maps of each source and nosological images obtained from an unsupervised analysis for case C894, superimposed to the corresponding T_{2w} image. Tumour borders are marked with dashed white lines in each grid. In the three acquisitions of grid 2, one source corresponded to tumour pattern, another source corresponded to normal brain pattern and another source represented a poor water suppression pattern, confirming the reproducibility in the repeated acquisitions.

Table 5.5: Assignment of the predominant tissue pattern contributing to each source calculated in the unsupervised analysis of case C894. Sources identified as artifactual could provide less confident analysis in semi-supervised studies with fixed, good-quality sources.

	Predominant pattern of the source		
Grid	**1**	**2**	**3**
1	Normal brain parenchyma	Tumour	Normal brain parenchyma
2.1	Tumour	Normal brain parenchyma	Artefact (bad water suppression)
2.2	Tumour	Normal brain parenchyma	Artefact (bad water suppression)
2.3	Tumour	Normal brain parenchyma	Artefact (bad water suppression)
3	Artefact at 1.58 ppm, bad SNR	Normal brain parenchyma	Tumour
4	Artefact at 1.6 ppm, bad SNR	Artefact at 1.5 ppm, bad SNR	Normal brain parenchyma

5.3.2.3 Semi-supervised source analysis

After checking for SNR, spectral quality, spectral features and presence of artefacts, the semi-supervised analysis developed in our group [117] was applied to all acquired grids in order to visually confirm that tumour regions were properly segmented. In this type of analysis, the pattern of each voxel is compared with patterns of fixed sources previously extracted as explained in section 3.7.2. Nosological images are generated and the colour coding is as follows: unresponsive/untreated patterns are shown in red, tumour responding pattern in green, normal brain parenchyma pattern in blue, and black is the colour assigned to spectra considered as "unclassifiable" by the system. This protocol was applied to all grids and the results for the representative case C894 are shown in Figure 5.13, whereas cases C891 and C895 are shown in Annex II. Results show that most tumour voxels were correctly classified as unresponsive/untreated pattern, as expected (85% voxels correctly classified) and the peritumoural/non-affected zone was correctly identified, leading to proper tumour segmentation. Exceptions were seen in Grid 4, in which the tumour tissue was not properly identified, probably due to the small amount of tumour tissue included in the grid, and poor overall spectral quality. Undefined (black) pixels seen in cases C891 and C894 match the zones of the artefactual spectra identified in the top-left edge of the Grid 2 matrix. The case C895 was the only one in which an untreated tumour was classified as containing partially responding pattern in an increasing trend, i.e. each consecutive slice acquisition seems to show more pixels classified as responding even when the spectral quality in the unsupervised source extraction for this zone is similar. In previous studies from GABRMN [117] there were non-treated cases

which also presented responding pixels, but the problem with this case was the lack of reproducibility for unknown causes. To measure this lack of reproducibility in the case C895, the average spectra of the green coded pixels from the acquisition 2.3 and the average spectra of the same pixels position for acquisitions 2.1 and 2.2 were calculated. The superposition of those three average spectra is shown in Annex II. A difference among the three spectra was observed around the 3.93 ppm position, where a peak was observed in the average spectra from acquisition 2.1 and 2.2 but it was not observed in acquisition 2.3. The absence of this peak in acquisition 2.3, could be the reason why these pixels were displayed in green and not in red. Moreover, in order to check whether this spectral difference was detected in cases C891 and C894, the average spectra of tumour red pixels from the acquisitions 2.1, 2.2 and 2.3 were calculated and superimposed (Annex II). Similar patterns were observed in both cases and no visual differences were detected in the 3.93 ppm position, indicating that possibly the differences detected in the case C895 could be artefactual.

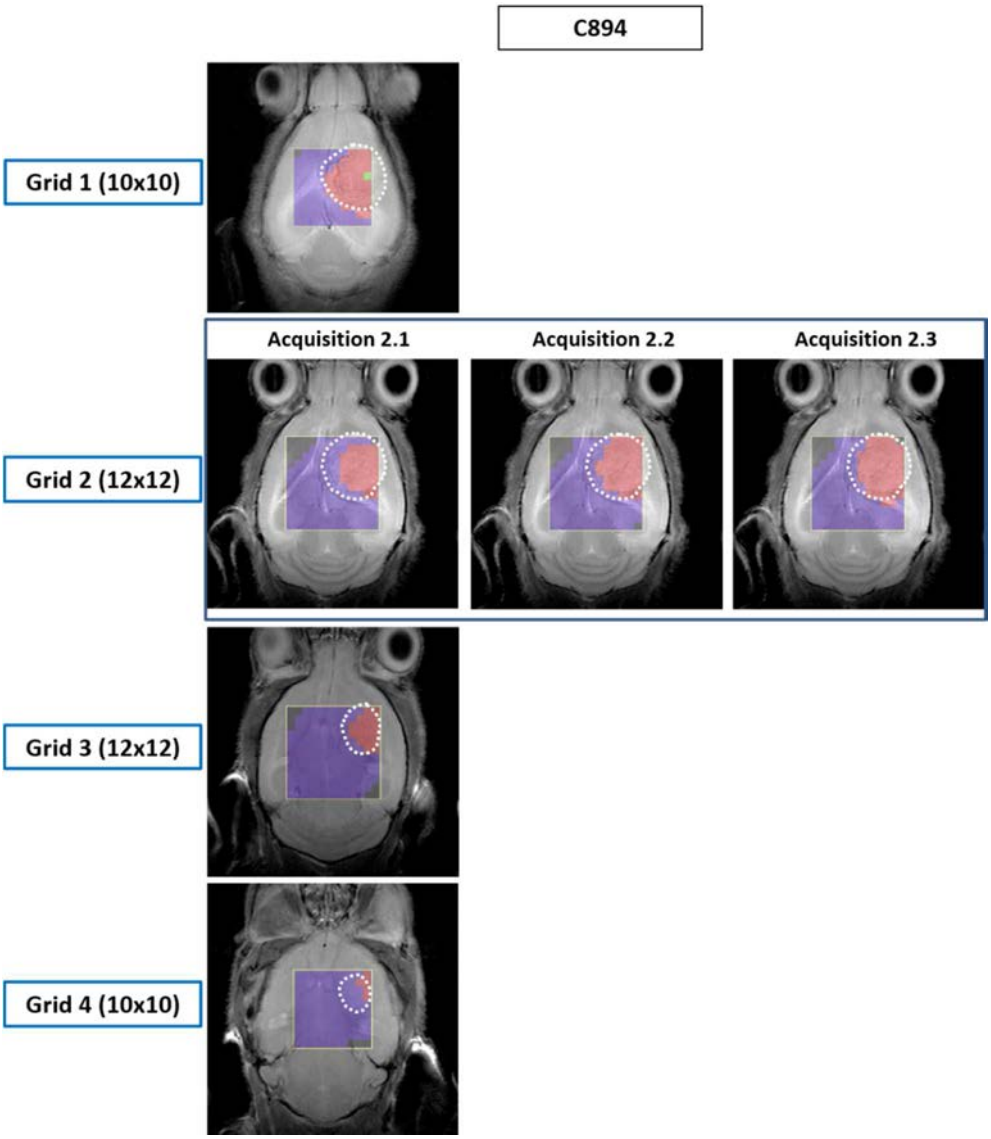

Figure 5.13: Nosological images obtained from semisupervised source analysis for case C894, superimposed to the correspondent T_{2w} images. Tumour borders are marked with dashed white lines in each grid. Red pixels corresponded to non-treated/unresponsive tumour spectral pattern, blue pixels to normal brain spectra pattern, green pixels to spectral pattern displayed by tumours responding to therapy and black pixels to voxels with 'undecided' classification.

5.4 General discussion for this section

5.4.1 Acquisition of MRSI multi-slice grids in wt and GL261 tumour-bearing mice

A multi-slice, 3D-like MRSI acquisition scheme was developed in order to obtain metabolomic information from preclinical glioblastoma in a volumetric approach. Glioblastomas are known to be heterogeneous [11, 12] and the use of a single-slice MRSI approach could hinder us to properly assess such heterogeneity. The existing 3D MRSI sequences [122, 257] were based in whole cubic VOI shapes and this lack of flexibility could limit the coverage of the whole tumour due to shimming problems and vicinity of lipid scalp to VOI edges. As opposed to this, a multi-slice with variable grid size may allow for a still acceptable tumour mass coverage while improving spectral quality by adjusting grid size and position according to tumour shape and volume. Two grid sizes were studied in combination: 10x10 grids as described in previous work from our group [90, 116, 117, 127] and larger grids of 12x12 in the central zones of the tumour, where diameters are usually higher in advanced stages, allowing for a good tumour mass coverage.

5.4.1.1 SNR results

SNR from edges and centre of the grids

Voxels from the edges of the grids presented lower SNR than voxels from the centre of the grids in both wt (Tables 5.2 and 5.3) and GL261 mice (Table 5.4). These results are in agreement with previous investigations [127, 153, 261], where it was described that SNR from voxels at the edge of MRSI grids tends to be lower than the rest. However, it is worth noting that even having a borderline SNR in some cases does not compromise the overall pattern and spectra may still be useful for further pattern recognition analysis.

In addition, both in wt and GL261 tumour-bearing mice a decreasing trend for SNR was observed from grids allocated at dorsal positions (Grid 1) to grids allocated in ventral positions (Grid 4). This decrease in SNR could be explained due to the proximity to the surface coil, where better signal is sampled, all of this added perhaps to a worse shimming for grids placed in a lower position in the brain anatomy, in a more heterogeneous zone [130, 262]. This tendency was also observed taking into account the percentage of low quality spectra, which higher percentage of voxels presenting SNR<10 in ventral grids.

Studies with wt mice

Combinations including only 10x10 and a mix of 10x10 and 12x12 voxels were tested in wt mice. No significant differences ($p>0.05$) using Student's t-test were observed comparing SNR from the edges of equivalent grids from both combinations. Regarding SNR from centre voxels,

significant differences ($p<0.05$) were observed in Grid 2 and in Grid 3 between the two combinations. One would expect that the use of a 12x12 matrix could imply an approximation to interface tissues which in turn could lead to poor quality spectra and lower SNR in those larger grids as already suggested [118], but the result obtained in our hands was the opposite, with higher SNR in the 12x12 matrix (29.2±8.1 vs 25.8±6.2). However, it is worth noting that although the difference is statistically significant, this only means a 13% variation in the overall SNR and both were within acceptable ranges. As these acquisitions were performed in different animals, these small differences can be attributed to inter-subject variability. From this preliminary set-up, we could deduce that a multi-slice MRSI acquisition was feasible as well as the MRSI acquisition matrix enlargement, and acquisitions could be obtained within an acceptable experimental time (~1.5-2h for a 3-slice acquisition).

Studies with GL261 tumour-bearing animals

Considering the satisfactory results obtained with wt animals, we proceeded to studies with GL261 tumour-bearing mice. However, to ensure whole tumour coverage, 4 grids were placed instead of 3 (Figure 5.2). In addition, Grid 2 (equivalent to the position of previous single-slice MRSI studies from our group) was acquired in triplicate for reproducibility assessment. The addition of a 4th grid was a differential parameter and although the SNR obtained is significantly lower ($p>0.05$) than the rest of the grids, due to its position from the surface coil, still it proved feasible with only 13.3±6.0% of voxels with SNR<10. The expected tendency of lower SNR in edges in comparison to centre voxel position was maintained in all grids and SNR was in average 1.85±0.12-fold higher in centre than in edges and was not significantly different from wt grids in equivalent positions.

Regarding SNR of the borders of equivalent grids were compared and no significant differences ($p>0.05$) were observed between wt and GL261 tumour-bearing MRSI acquisitions. However, higher SNR values ($p<0.05$) were found in the centre of the Grids 1 and 2 of GL261 tumour-bearing mice in comparison with the equivalent grids from wt mice.

Regarding the triplicate acquisition of Grid 2, the three studied cases presented slight variations. Case C894 presented highest reproducibility (<10% variability in all measurements) and case C895 the lowest (up to 15.9% variation for SNR in voxels from the tumour area). However, all acquisitions resulted in acceptable SNR and no drift was detected (i.e. a trend in getting worst SNR values with consecutive acquisitions, or subtle unexpected variations).

As expected, the grid positioning (dorsal-ventral) was a determinant factor for changes in measured parameters and it was closely related with SNR values in all mice. Average SNR values of centre voxels showed decreases of ca. 8% between Grids 1-2 and 2-3, and a drop of 23% in SNR values for Grid 4 (Grid 1: 36.2±10.2, n=192; Grid 2: 33.1±12.0, n=900; Grid 3: 30.5±10.8, n=300; Grid 4: 23.3±7.3, n=192). Significant differences were found in comparisons between all grids. In addition, a similar trend was found in edge voxels with an average decrease of 17% in SNR in each grid position. Regarding SNR calculated for the specific tumour areas in tumour bearing mice, values ranged from 46.5±11.5 in Grid 1 (n=27) to 16.2±3.4 in Grid 4 (n=12). For normal parenchyma areas, values presented lower variability and ranged from 33.2±6.1 in Grid 2 with the highest value (n=81) to 23.9±4.9 in Grid 4 (n=27) which was found to be significantly different from other grids. The SNR for the tumour areas in GL261 tumour bearing mice showed to be consistently higher in comparison with similar brain areas chosen in wt studies for calculation (1.9 fold higher in average comparing equivalent zones and grids), whereas normal brain parenchyma areas presented less punctual variability, and in general of lower magnitude. From these studies, it became clear that a multi-slice MRSI study with 4 different grids was possible within an acceptable experimental time (~3.5h hours) and with adequate SNR even in larger matrixes (12x12). However, we wondered whether these results were compared with the single-slice MRSI acquisitions and with 10x10 voxel matrixes performed previously in our group.

Comparisons between multi-slice and single-slice MRSI results from previous studies

Data obtained from grids acquired by the MRSI multi-slice approach was compared with data obtained from previous cases using single-slice MRSI acquisitions in order to check for consistency. Specifically, 6 untreated GL261 tumour-bearing mice from [117] were chosen for comparison purposes (C255, C288, C351, C520, C529 and C583). The SNR (mean±SD) calculated from these acquisitions was compared to data gathered from tumour-bearing mice studied by multi-slice approach (Table 5.6). It is worth noting that the equivalent grid to be directly compared with the single-slice acquisition would be essentially Grid 2.

Table 5.6: SNR data (mean±SD) from edges, centre, tumour and normal parenchyma voxels and percentage of voxels with SNR<10 of 6 previous cases studied with MRSI single-slice from GABRMN compared to the 3 mice studied using the MRSI multi-slice approach in this thesis.

	GABRMN Single-slice MRSI (n=6)	Grid 1 Multi-slice (n=3)	Grid 2 Multi-slice (n=9)	Grid 3 Multi-slice (n=3)	Grid 4 Multi-slice (n=3)
% Voxels SNR<10	1.3±1.0	3.0±2.0	4.9±2.0*	7.6±0.7*	13.3±6.0*
Edge voxels	23.2±9.7	20.9±8.1	17.2±7.9 *	15.4±7.8*	13.3±5.2*
SNR Centre	45.6±17.4	36.2±10.2*	33.1±12.0*	30.5±10.8*	23.3±7.3*
SNR Tumour	54.6±13.4	46.5±11.5*	45.7±15.2 *	26.1±8.3*	16.2±3.4*
Normal parenchyma	30.9±10.5	30.5±7.7	33.2±6.1	32.8±10.4	23.9±4.9*

*= p<0.05 in comparison with single-slice MRSI cases

It can be readily seen that the calculated SNR was somewhat higher in single-slice MRSI acquisitions, being this difference significant in several instances. Still, the percentage of voxels with insufficient SNR was lower for single-slice aquisitions. Direct comparison with Grid 2 resulted in fold changes from 0.72 to 1.07 but still, resulting in more than 95% spectra having enough SNR to be used. Of course, comparison with other grid positions should take into account the influence of coil vicinity and comparisons are not straightforward. Further adjustments in coil positioning may be undertaken in the future, in order to improve SNR obtained in multi-slice MRSI acquisitions.

5.4.1.2 Presence of artefacts

The presence of artefacts was inspected with the help of unsupervised source analysis. Most artefacts were found in upper and lower corners of the grids, and were more evident in GL261 tumour-bearing mice acquisitions (Figure 5.12 and Annex II). In wt mice, the enlargement of the central matrix from 10x10 to 12x12 voxels did not produce additional artefacts and the distance from matrix to scalp ranged from 0.4 mm to 2.5 mm (from the right corner of the grid to the scalp), resulting in a determinant factor in their appearance. The most common artefacts in wt acquisitions were inversions observed at 1.58±0.05 ppm, probably due to vicinity of lipids, which could distort the registered signal. Those were also seen in multi-slice acquisitions from tumour-bearing mice, but were not noticed in single-slice MRSI acquisitions. Prominent artefacts due to poor water suppression were observed in Grid 2 of the multi-slice acquisition and were consistent in triplicate acquisitions. It is worth mentioning that the presence of artefacts related to matrix corners and insufficient water suppression was also observed in some individuals from single-slice acquisitions studied by our group (see Figure 5.14) even though in these cases the

distance from grid to the scalp did not seem to be a determinant factor. However, in future studies the meticulous positioning of grids should decrease the appearance of this type of artefacts, for example, avoiding grid placement near to tissue interfaces.

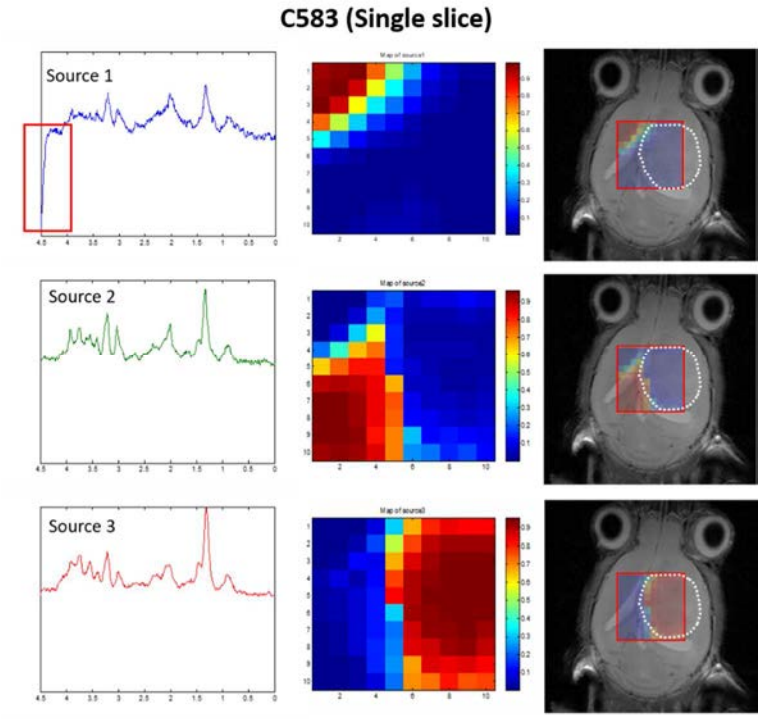

Figure 5.14: Calculated sources, intensity maps of the sources and nosological images obtained from an unsupervised analysis superimposed to the corresponding T_{2w} image in the case C583 (untreated tumour-bearing mice studied with single-slice MRSI approach) from [117]. Tumour borders are marked with dashed white lines in each grid. Poor water suppression artefact was observed in source 1 (red square).

The identification of possible artefactual voxels in a given case could be useful to explain possible erroneous classifications in the semi-supervised system. Future optimizations of the semi-supervised classification software would be useful for automatic tagging and removal of artefactual voxels with unsuitable quality for classification purposes, a work still in progress within our group.

5.4.1.3 Semi-supervised analysis

In the semi-supervised source analysis carried out in GL261 tumour-bearing mice explored with the multi-slice MRSI approach, a good discrimination between proliferating tumour and normal parenchyma area with the expected classification was found in 87.2 % of the voxels. Some cases presented pixels classified with the "tumour responding" pattern (i.e. green), up to 17.7% of tumour pixels in case C895, which was unexpected as these cases were all untreated mice. However, this was already seen in some isolated cases explored by single-slice MRSI described in [117]. One possible hypothesis to explain this classification is that some tumours present

specific metabolic changes that are shared with tumours responding to therapy and these changes are sampled by the classification system. We should also take into account that the semi-supervised system works with fixed sources, forcing the analysed data to fit in one of them or in the undecided "black" category. We cannot discard that the system is sampling tumour heterogeneity and some zones could metabolically resemble more a responding tumour than an actively proliferating zone. Moreover, results obtained in Grid 4 showed unclear segmentation and lead us to consider whether the acquisition of this zone would be useful in tumour follow-up depending on tumour size. These results reinforce the interest in applying a multi-slice MRSI protocol in longitudinal studies of noninvasive assessment of therapy response, possibly improving results obtained with the single-slice MRSI methodology and potentially giving more insight into tumour heterogeneity and evolution of response to therapy.

5.5 Conclusions

1. A multi-slice MRSI protocol was developed and proven feasible in wt mice using a combination of 3 MRSI grids with the same or different dimensions. Enlargement of matrix from 10x10 to 12x12 resulted in spectra with acceptable quality, either regarding SNR, presence of artifacts and consistency of the spectral features.
2. The developed protocol was applied successfully to GL261 tumour-bearing mice acquisitions, even adding a 4^{th} grid to ensure whole tumour coverage. Good quality spectra were obtained, although the calculated SNR was slightly lower than for single-slice MRSI acquisitions. Artifacts, mainly related to poor water suppression, were seen in grid corners of 12x12 grids. This could be related to the proximity of the grid borders to the scalp, but it did not affect directly the tumour core zone.
3. SNR varied with position of a voxel inside the grid (central voxels having SNR in average 1.85-fold higher than edge voxels) and also with grid positioning, having dorsal grids higher values in comparison with ventral grids (average SNR in Grid 1 was 1.55-fold higher than SNR in Grid 4). These results were expected and in general they did not compromise the overall spectral quality.
4. The spectral features observed both in wt and GL261 tumour-bearing mice in chosen grid zones were consistent with normal brain parenchyma and GL261 tumour spectra in all grids, showing that even lower grids can produce acceptable spectra that can be used for classification purposes.

5. The semi-supervised source analysis applied to acquisitions from GL261 tumour-bearing mice visually resulted in proper segmentation between tumour and normal parenchyma area in which most voxels were correctly classified either as tumour or normal brain parenchyma pattern. The appearance of a "responding tumour" pattern in some voxels from untreated cases should be investigated, but it suggests that the system is sampling tumour heterogeneity or local changes that can be mislabelled as "responding" due to the use of fixed sources. Still, small tumour volumes could not be adequately sampled in nosological images, which suggests that depending on the tumour volume, the inclusion of a 4th grid would not be informative.
6. Due to the enlargement of the matrixes and the vicinity of some grids to tissue-interface regions, care should be intensified regarding grid positioning and coil placement adjustment, in order to minimize the appearance of artifacts.
7. The overall results obtained in this chapter indicate that this multi-slice MRSI approach is ready to be applied in longitudinal studies of therapy response follow-up for tumour heterogeneity sampling and further histopathological validation.

6. Unraveling therapy response heterogeneity in preclinical GL261 tumour-bearing mice with a multi-slice MRSI approach

6.1 Specific objectives

The main purpose of this chapter was to apply the multi-slice MRSI method developed in chapter 5 to a cohort of GL261 tumour-bearing mice (either control/untreated or under TMZ treatment). This should allow checking whether consistent results with the already described for single-slice MRSI studies [117] were obtained, and also to gain more insight into the histopathological validation of the MRSI-derived information from the different tumour regions corresponding to each sampled slice. Considering the intrinsic heterogeneity of glioblastomas and their response to therapy, the use of a single slice protocol could hinder us from obtaining relevant information while this can be tackled by a multi-slice approach, producing more representative results. Most of the work described in this chapter was published in the scientific journal Metabolites (Arias-Ramos N et al, 2017 [263]).

6.2 Specific material and methods

6.2.1 Animals

Tumours were induced in a total of 39 C57BL/6J female wt mice (weighing 21.1±1.3 g), although not all of them were selected for therapy administration (final n=26). In addition, not all animals receiving therapy met criteria for inclusion in classes described in section 6.2.4, resulting in a final number of studied animals being lower than the initial number of generated GL261 animals.

Two different groups of animals were produced:

Group A: Tumours were generated in different series of animals separately in time for proper schedule allocation in the NMR facility. In the first part of the study, 5- 7 animals were injected in each cell-injection series. Mice were weighed every day and tumour volumes were followed twice or three times a week using T_{2w} MRI acquisitions. Welfare parameters were followed up as explained in Annex I. From the animals injected in each series, the three mice with the most homogeneous weights and tumour sizes were chosen for the multi-slice MRSI experiment before starting therapy.

Group B: In the second part of the study, tumours were induced in 19 mice. Four of them were discarded because no tumour was detected after 10 days p.i. Regarding the remaining 15 mice, they were weighed every day and tumour volumes were followed twice or three times a week

using T_{2w} MRI acquisitions. However, an inclusion criterion was established: only TMZ-treated mice showing tumour volume decrease in comparison with the previous measurement were selected for multi-slice MRSI experiments.

Finally, four control (non-treated) tumour-bearing mice were also explored with the multi-slice MRSI approach.

6.2.2 Animal treatment with Temozolomide

Therapy administration followed slightly different schemes in groups A and B. In the first part of the study (group A), therapy administration started at day 11 p.i. with 3 cycles of therapy administration as previously described by our group [90] (see also section 3.4). In the second part of the study (group B), the therapy starting day was not always the same: it was adapted to start when the tumour volume was between 2.5 and 5.5 mm^3.

6.2.3 In vivo MRI and MRSI studies and nosological images generation

In the first part of the study, MRSI experiments were acquired every 2-3 days, from the day before starting therapy until animal euthanization, using the approach described in chapter 5. Briefly, Consecutive MRSI grids were acquired individually across the tumour, using as reference T_{2w} high resolution images, as shown in Figure 6.1. The final number of acquired slices depended on the tumour coverage (3 or 4 slices). The total acquisition time for MRI/MRSI 4 grids full protocol was ca. 3.5 hours per animal.

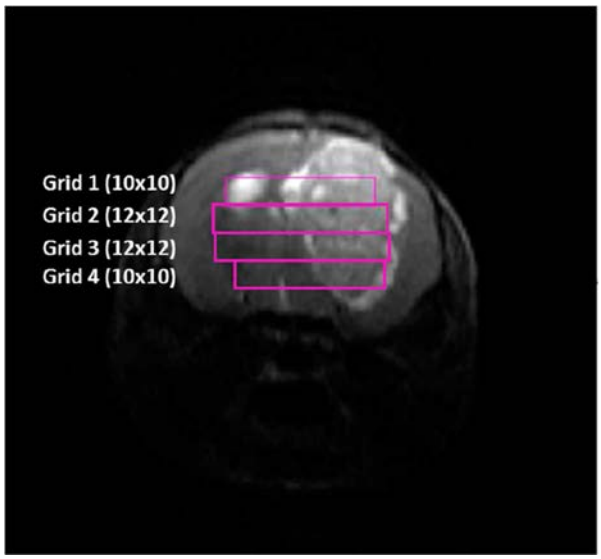

Figure 6.1: Coronal T_{2w} MRI of mouse C971 brain, with the position of the four MRSI slices.

However, in the second part of the study (Group B), MRSI experiments were not acquired from the beginning of therapy administration. Tumour volume was followed up by MRI and when a reduction in the tumour volume was detected (in comparison to previous measurement), MRSI studies started every 2-3 days until animal euthanization. For control GL261 tumour-bearing animals, only one MRSI was performed at day 13±2 p.i. MRSI data was processed and postprocessed as described in section 3.6. For all groups, nosological images were obtained from each MRSI grid using a semi-supervised source extraction methodology (see materials and methods section 3.7.2). Colour coding was as follows: red (unresponsive/untreated), green (tumour responding to therapy), blue (normal brain parenchyma) and black ("unclassifiable" voxels).

6.2.4 Tumour Responding Index (TRI) calculations

In order to measure the level of response to treatment using the obtained nosological images, an arbitrary parameter named Tumour Responding Index (TRI) was estimated (Equation 6.1).

$$TRI = \frac{Tumour\ responding\ pixels}{Total\ tumour\ pixels}\ x\ 100 \qquad \textbf{Equation 6.1}$$

TRI is stated as the percentage of green responding tumour pixels of all grids over the total tumour pixels taking into account all recorded grids. Then, arbitrary ranges of TRI categories were established to classify the different response to treatment levels observed in the studied animals, taking into account both TRI percentage and volumetric data from MRI measurements according to adapted RECIST criteria (i.e. comparing tumour size respect to tumour volume observed in the previous MRI measurement, see also Annex III for details).

-**High response cases (HR)**: TRI>65%, and also tumour size should be reduced with respect to tumour volume observed in the previous MRI measurement (meeting response or stable disease according to adapted RECIST criteria). Green pixels should be observed in at least two consecutive MRSI grids

-**Intermediate response cases (IR)**: TRI range 35-65%, also tumour size should be unchanged, reduced or increased (in case of increase, no more than 20%) with respect to tumour volume observed in the previous measurement, meeting response or stable disease stage by the adapted RECIST. Green pixels should be observed in at least two consecutive MRSI grids

-**Low response cases (LR)**: TRI<35% and also tumour size more than 20% larger in comparison with the previous measurement, meeting progressive disease criteria.

In addition, selected mice from a previous longitudinal single-slice MRSI study from GABRMN in [117] were analysed retrospectively and TRI calculated. The chosen cases C817 and C819, were considered as "partial response" cases, while C821 was considered as "stable disease" following the adapted RECIST criteria.

6.2.5 Animal euthanasia and sample storage

Animals were followed up by MRI-MRSI and when one animal met the requirements to be included in one of the TRI categories, this animal was euthanized by cervical dislocation and its brain was resected and stored in paraformaldehyde 4% for histopathological analysis.

6.2.6 Histopathology studies

Fixed brains were embedded in paraffin and serial horizontal sections were performed to correlate the histological preparations with the reference nosological images from the MRSI acquisition. The upper half of the brain was cut in horizontal sections of 5 µm at different heights for correlating the histological preparations with the reference images of Grid 1 and Grid 2 positions. The lower half of the brain was processed in the same way for correlating the histological preparations with the reference images of Grid 3 and Grid 4 positions.

These sections were analysed by Hematoxylin-Eosin (HE) staining in order to identify the different cells from normal brain and tumour tissue. Then, one section corresponding to each MRSI grid position was selected for Ki67 (BD Biosciences, Madrid, Spain) immunohistochemical staining for detecting cell proliferation. After immunostaining, the preparations were digitized for quantification using a Nanozoomer 2.0HT (Hamamatsu Photonics France, Massy, France). Then, Ki67 positive cells were counted in each section in areas that corresponded to green or red tumour areas observed in the nosological images. From each area (either green or red), 5 fields of 0.0635 mm^2 were selected to count Ki67 positive cells at 40x magnification, using NDPview 1.2.53 software (Hamamatsu Photonics France, Massy, France). In all tumours, the five fields were placed in the more highly cellular areas, avoiding poor or acellular areas. Exceptionally, in some samples, fewer fields were counted if the corresponding green or red area of the nosological image was not large enough to count 5 fields (the average number of fields counted considering all samples was 6.3±2.1 fields per grid)

This counting was carried out by 2 independent researchers: a) Nuria Arias-Ramos who established the areas (green or red) to be counted, placing fields in areas where a suitable number of cells was observed, and b) Dr. Martí Pumarola, who did not know if the animal was treated or not, or whether the field corresponded to a green or red area. Both observers have

analysed the same magnification and fields, also taking into account the area occupied by cells or acellular spaces.

For Ki67 estimation, different approaches of counting were attempted, namely:

- Ki67% for each field as described in Equation 6.2:

$$\frac{Number\ of\ tumoral\ Ki67\ positive\ cells}{Number\ of\ total\ tumoral\ cells}\ x\ 100 \qquad \textbf{Equation 6.2}$$

- Global Ki67% for each case was calculated as the average Ki67% of all analyzed fields of a given case.

- Ki67/mm^2, calculated for each field as described in Equation 6.3:

$$\frac{Number\ of\ tumoral\ Ki67\ positive\ cells}{Field\ area\ (mm^2)} \qquad \textbf{Equation 6.3}$$

Where 'field area' was 0.0635 mm^2 in the studied fields

Finally, the volume of Ki67 positive cells was also calculated taking into account the average cell diameter of cells in chosen fields, which was used with the sphere volume formula, assuming cells with a spherical form.

6.2.7 Volumetric representation of the multi-slice nosological images

A preliminary volumetric representation of tumour volume of the nosological images of all MRSI slices obtained at day 32 p.i. of the case C971 was attempted using the software *Autocad 2007* (Autodesk Inc., San Rafael, California (USA)) running in a personal PC. For this representation, each grid was manually drawn and coloured as the corresponding nosological image.

6.3 Results

6.3.1 MRSI Multi-slice protocol applied to TMZ-treated GL261 tumour-bearing mice

Summary of studied cases and basic data. Table 6.1 shows relevant parameters for all studied cases: tumour volume pre-treatment, tumour volume at euthanasia, and classification of response to therapy according to RECIST criteria and TRI criteria.

Table 6.1: Data summary of tumour volume the day before starting therapy administration and the day in which euthanasia was carried out. Classification with RECIST and TRI criteria the day of euthanasia.

Case	Tumour volume (mm^3) (pre therapy)	Tumour volume (mm^3) (day of euthanasia)	Classification by adapted RECIST criteria	Classification by TRI criteria
C971	5.0	80.7 (34 p.i.)	Stable disease	Intermediate
C974	7.3	220.5 (40 p.i.)	Stable disease	Intermediate
C975	7.2	100.7 (26 p.i.)	Stable disease	Intermediate
C1022	3.1	35.7 (23 p.i.)	Stable disease	Intermediate
C1023	4.3	64.7 (23 p.i.)	Stable disease	Intermediate
C1026	4.4	64.0 (23 p.i.)	Stable disease	Intermediate
C979	8.4	146.7 (19 p.i.)	Progressive disease	Low
C981	8.1	143.5 (19 p.i.)	Progressive disease	Low
C1100	2.9	27.3 (26 p.i.)	Stable disease	High
C1108	3.0	25.7 (29 p.i.)	Stable disease	High
C1109	Control	47.5 (11 p.i.)	Progressive disease	Control
C1110	Control	81.7 (13 p.i.)	Progressive disease	Control
C1111	Control	88.9 (16 p.i.)	Progressive disease	Control
C1112	Control	88.7 (13 p.i.)	Progressive disease	Control

-Although mean values of tumour volumes pre-therapy were indeed different between groups (HR 2.95±0.07 mm^3, IR 5.21±1.69 mm^3, LR 8.25±0.21mm^3), there were not enough cases to perform statistical tests. The same was observed for tumour volume at the euthanization day (HR 26.50±1.13 mm^3, IR 94.38±65.39 mm^3, LR 145.1±2.26 mm^3)

-Control mice were euthanized when tumour volume was between 45-90 mm^3, in order to avoid reaching necrotic stage in tumours, when higher heterogeneity in MRI and MRSI would be expected, which could complicate the interpretation of the results.

6.3.1.1 Group A: Cases starting therapy at day 11 p.i.: inclusion into different groups of response level

Twelve animals out of 19, with the most homogeneous tumour volumes at therapy start (average 7.5±5.0 mm^3) were chosen for longitudinal multi-slice MRSI studies: from those, 6 mice (C971, C974, C975, C1022, C1023 and C1026) were classified as intermediate response (IR) cases and 2 mice (C979 and C981) were classified as low response (LR) cases. All but one case (C974) were euthanized at the time point they accomplished criteria for inclusion into IR or LR groups. Regarding case C974 (IR), it was maintained alive until the endpoint in order to follow-up the possible TRI changes along time. No high response (HR) cases were found in this first part of the

experiment, being the maximum calculated TRI of 46.5% (see also section 6.2.4 for TRI calculation and 6.3.1.2 for analysis of Group B and appearance of HR cases). In addition, four control cases (C1109, C1110, C1111 and C1112) were also analysed with multi-slice MRSI studies, although only one measurement was carried out at days 11 p.i., 13 p.i., 16 p.i. and 13 p.i. respectively and they were euthanized when tumour volumes were about 70.2±18.7mm^3. The evolution of tumour volume was assessed in all cases until the euthanization point. It is worth mentioning that in addition to the 4 control cases explored in this work, 28 additional cases from previous work from our group were added to confirm consistent evolution of the pattern by MRI follow-up, reaching a total of n=32 control cases (Figure 6.2).

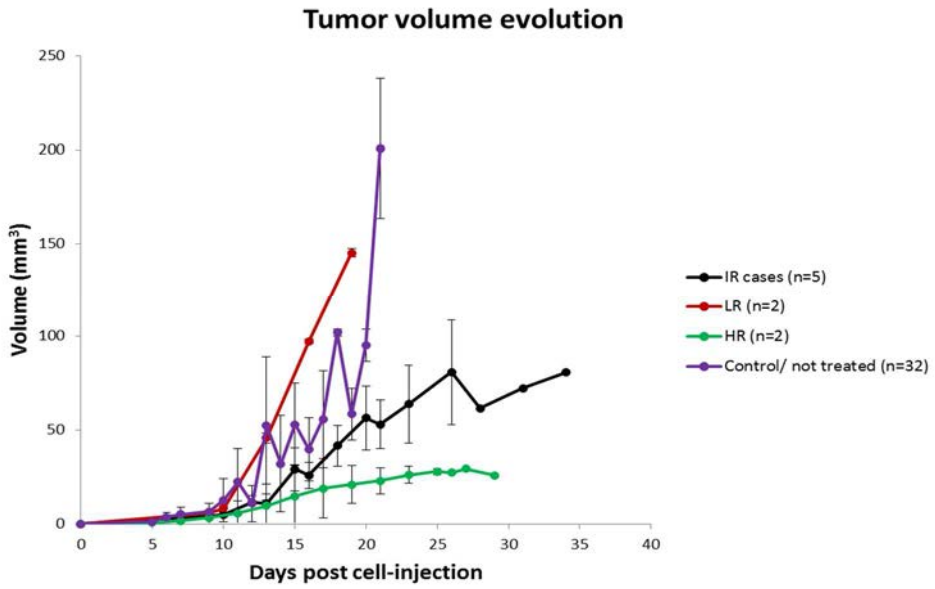

Figure 6.2: Mean tumour volume evolution ± SD of different cases studied in this thesis and previous work from the GABRMN group. IR cases until euthanization day (n=5, case C974 was not included because it was followed up until endpoint) are represented with black line; LR cases (n=2) with red line; HR cases (n=2) with green line and control cases (n=32, in addition to the 4 control cases explored in this work, 28 additional cases from previous work from our group were added to confirm consistent evolution pattern by MRI follow-up) with purple line. Significant differences ($p<0.05$) were observed for tumour volume evolution between IR cases and HR cases, and LR cases and control cases. The TMZ administration period is not represented in the graph due to different schedules used in HR cases. This graph is not representative of the overall survival of mice because mice were euthanized at specific time points to perform histopathological validation (i.e. it was not an endpoint study).

Body weight evolution of all treated groups (Figure 6.3), confirmed the maintenance of an acceptable body weigh range for longer times in IR and HR cases (mean body weight loss <20%), in comparison with LR cases, which presented poor response to therapy and worsening of their health status (mean body weight loss >20%).

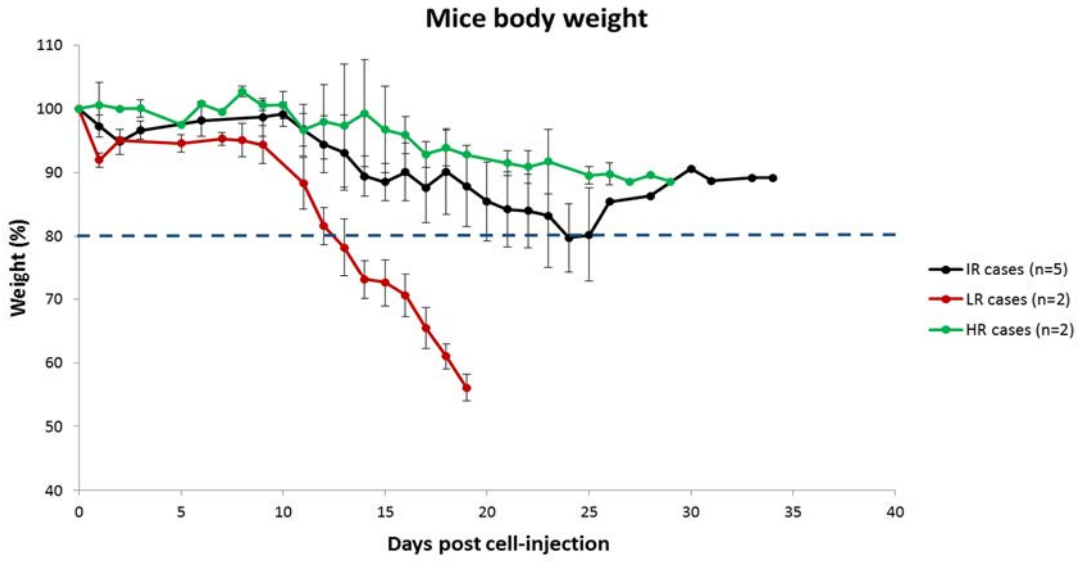

Figure 6.3: Mean ±SD evolution of body weight of mice studied by multi-slice MRSI (mouse weight at day of cell injection (day 0 p.i.) was considered 100%). IR cases are represented in black. C974 was not included in this graph because it was followed up until endpoint, and at that point it could be no longer classified as an IR case. LR cases are represented in red and HR cases are represented in green. The dashed blue line indicates the 20% weight reduction point.

TRI and nosological images evolution vs tumour volume evolution

IR cases: the relationship between TRI and tumour volume evolution of IR cases is shown in Figures 6.4 and 6.5. Euthanasia was performed when TRI values met the inclusion criteria for IR class, namely: TRI ranging between 35-65% and tumour volume meeting criteria for 'stable disease' according to adapted RECIST (see section 6.2.4). These criteria were met in 5 out of 6 IR cases at the euthanization time. The mean TRI value of these 5 cases (C971, C975, C1022, C1023 and C1026) was 44.1±4.2 %. The remaining case (C974) met IR conditions during part of the evolution period, and was not euthanized but followed-up until endpoint, and it will be described in a separate subsection. In IR cases, TRI values increased after the second therapy cycle, concurring with tumour growth arrest (stable disease stage according to adapted RECIST criteria). The maximum variation in tumour volume in the stable disease period of IR cases was of 17.6%. Figure 6.4 shows two chosen examples of IR cases: C971 and C1022 (Figure 6.4.A and 6.4.B respectively). In case 1022, TRI increase (46.5%) was found 4 days after the second therapy cycle during tumour growth arrest. Still, in case C971, we can observe that TRI also increased its value during the 'stable disease' stage (31.2% at day 26 p.i., 6 days after the second therapy cycle), but it did not follow a continuous increasing trend during the whole tumour development. In fact, it experienced a decrease during days 28-31 p.i. (TRI 11.7% and 13.9% respectively) and a further increase (44.1% at day 34 p.i., 9 days after the third therapy cycle),

when the mouse was euthanized for histopathological validation. The interval between the two TRI peak values was of 8 days.

Other examples of IR cases, as well as their nosological images and TRI evolution can be found in Annex III. For example, in case C975, TRI increase was first observed at day 20 p.i. just after the second therapy cycle, with a further increase at day 26 p.i. (TRI= 40.3%), 6 days after the second therapy cycle. In cases C1023 and C1026 (Annex III), TRI started increasing at day 18 p.i., after the first therapy cycle with further increases (35.8% and 38.9% respectively) at day 23 p.i., 4 days after the second therapy cycle and 8 days after the first cycle. These TRI increases were in the same time frame as in case C1022. Regarding nosological images for these cases, in general, green responding pixels started to be observed in Grid 1 (a pattern shared by IR cases) and then "spread" to the remaining grids with a predominance in the upper grids. Accordingly, there was a variation in the response level in different grids being TRI values higher in the upper grids.

LR cases: (C979 and C981) did not respond to therapy with TMZ and they had to be euthanized due to welfare parameters at day 19 p.i. (their body weight loss was higher than 20% compared to the day pre GL261 cell injection, C979: 51.55 % loss and C981: 54.22% loss, before starting the second therapy cycle). The mean TRI value of these 2 cases was 13.4±14.3%. Figures 6.4.C and 6.4.D show the relationship between tumour volume and TRI evolution as well as nosological images for cases C979 and C981. Very few green responding pixels were observed in the nosological images of case C979 and only in the first grid (TRI= 3.3 % at the euthanasia day). In case C981, green pixels were observed first in Grid 1 and at the euthanasia day in Grids 1 and 2, being its TRI value higher than case C979, reaching a value of 21.5 %.

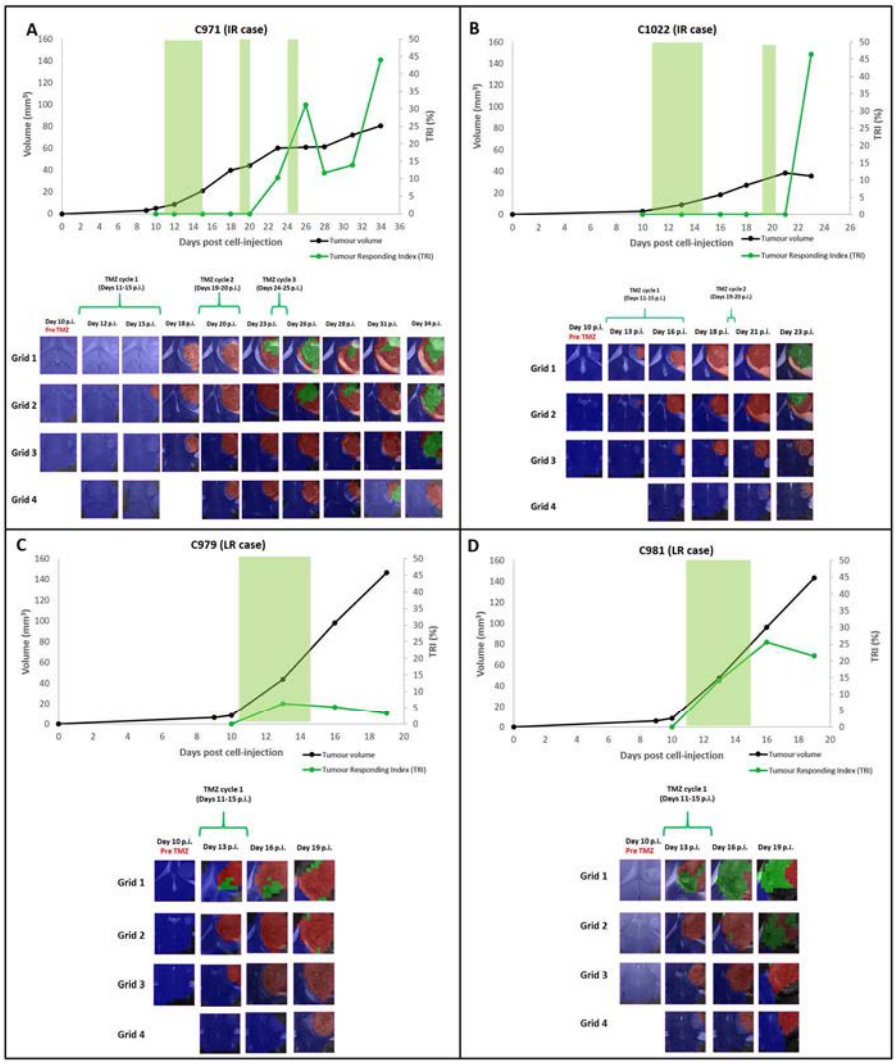

Figure 6.4: Graphical representation of the tumour volume evolution (in mm^3, black line, left axis), and the percentage of responding "green" pixels obtained after the application of source analysis to MRSI data acquired in the multi-slice set as in [117] (in %, green line, right axis). The green shaded columns indicate TMZ administration periods. For chosen time points, the evolution of the nosological images obtained with the semisupervised source extraction system is shown in four columns of colour coded grids, superimposed to the T_{2w}-MRI for each slice (colour coding as follows: blue pixels: normal parenchyma, red pixels: non responding, green pixels: responding). Green brackets indicate TMZ administration periods. **A.** Corresponds to the IR case C971, green pixels were observed first at day 23 p.i., increasing until 32.2% at day 26 p.i., when tumour growth arrest was observed. Then, TRI decreased: 11.7% at day 28 p.i. and 13.9% at 31 day p.i., followed by a new increase up to 44.1% at day 34 p.i. **B.** Corresponds to the IR case C1022, only red tumour pixels were observed in MRSI measurements until day 23 p.i., tumour volume decrease was observed and green pixels were observed in grids 1 and 2 (TRI= 46.5%). **C.** Corresponds to the LR case C979, green pixels were observed only in grid 1 at days 13 p.i., 16 p.i. and 19 p.i. (TRI= 6.3%, 5.2%, 3.3%, respectively), tumour growth arrest was not observed. **D.** Corresponds to the LR case C981, green pixels were observed only in grid 1 at days 13 and 16 p.i. At day 23 p.i., green pixels were observed in Grids 1 and 2 (TRI= 21.5%).

Case C974: tracking the evolution of an IR case along time

This was a case for which euthanasia was not performed at an intermediate tumour evolution point for histopathological validation. Indeed, the tumour was allowed to evolve until endpoint in order to assess TRI changes all along the tumour growth curve. The tumour volume evolution and its relationship with TRI, as well as the corresponding nosological images obtained are shown in Figure 6.5. The TRI started increasing at day 18 p.i., three days after finishing the first therapy cycle, reaching a value of 41.4% at day 20 p.i. (just after finishing the second cycle). At this particular moment, although TRI values would meet criteria for classification as IR, the 21% increase in tumour volume would not agree with 'stable disease' according to the adapted RECIST criteria. Then, from day 20 to day 31 p.i., volume growth arrest was observed ('stable disease' stage by the adapted RECIST criteria), with maximum volume variation of 11.2% regarding previous measurements. During this period of growth arrest, an oscillating pattern in TRI values was observed, as follows: TRI value decreased to 11% at day 22 p.i. (between cycles 2 and 3), then increased again reaching a value of 36.8% at day 26 p.i. (one day after finishing the third therapy cycle), moment at which criteria for IR would be accomplished for this case. Further TRI decreases to 11.7% and 0% were seen at days 28 and 31 p.i. respectively.

Finally, progressive disease stage by the adapted RECIST criteria was observed between days 34 and 37 p.i. (tumour volume increased 29.9% and 73.9% regarding the previous measurements), and TRI during this period also increased to 21.1% and 52.1% values respectively. This mouse died during MRI acquisition at day 40 p.i. During this period, body weight loss (as compared to the body weight observed at the day of cell injection) was of 7.3% at day 34 p.i. and 33% at day 40 p.i., in agreement with frank disease progression.

Regarding the nosological images, green pixels were observed first in the upper grid, as in other IR cases. It is worth noting that the TRI high peaks were observed 5-6 days after the first and second therapy cycle.

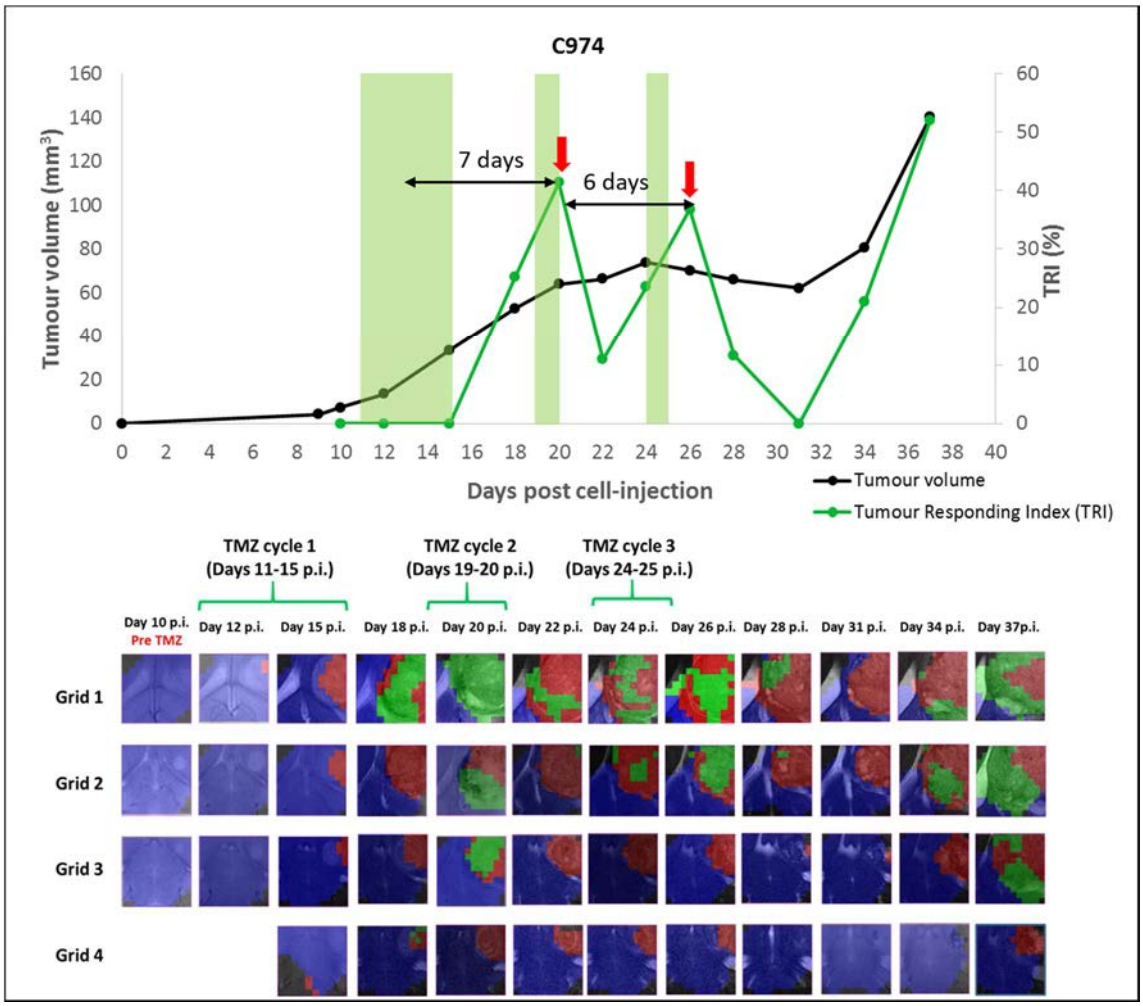

Figure 6.5: Graphical representation of the tumour volume evolution (in mm^3, *black* line, left axis), and the percentage of responding "green" pixels obtained after source analysis of MRSI data acquired in the multi-slice set as in [117] (in %, green line, right axis) for case C974 (IR case). The green shaded columns indicate TMZ administration periods. For chosen time points, the evolution of the nosological images obtained with the semi-supervised source extraction system is shown in four columns of colour coded grids, superimposed to the T_{2w}-MRI for each slice (colour coding as follows: blue pixels: normal parenchyma, red pixels: non responding, green pixels: responding). Green brackets indicate TMZ administration periods. A cyclical pattern of response (6-7days days) was observed, marked by the black arrows in the graphical representation. Red arrows indicate the maximum values observed of TRI during tumour volume growth arrest.

Control cases: tumour volumes of 4 control mice (C1109, C1110, C1111 and C1112) are shown in Figure 6.6. These mice were studied with multi-slice MRSI acquisition but in a single time point, carried out at the same day these animals were euthanized. TRI was also calculated and average TRI value for these control cases was of 6.2±2.8%. In case C1109, no green pixels were observed. However, green responding pixels were found in the other control cases: in case C1110, a total of 6 green pixels were observed after analysing all grids (TRI= 3.5%); in case C1111 only 3 pixels were observed (TRI= 1.9%), whereas in case C1112 green pixels were observed in Grid 1 and 2 (TRI= 19.3%).

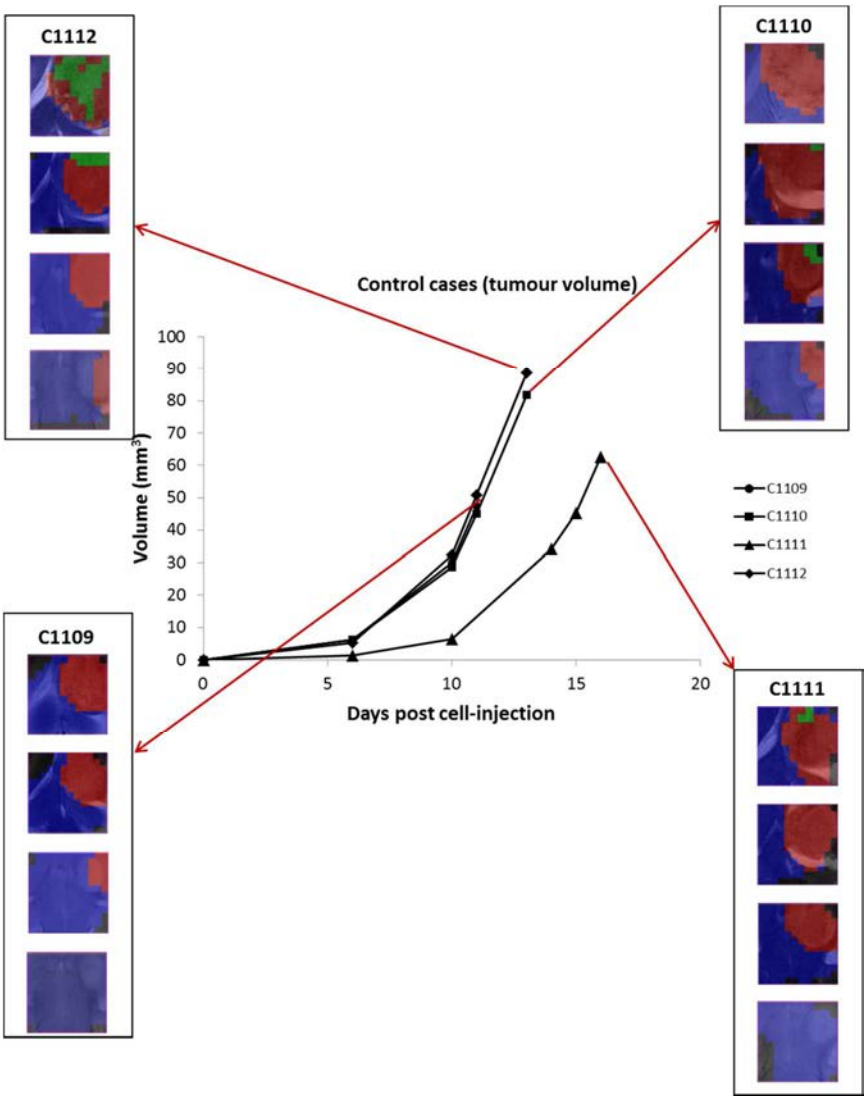

Figure 6.6: Tumour volume evolution (in mm^3, *black* line) of untreated, control cases (C1109, C1110, C1111 and C1112). Only one multi-slice MRSI measurement was carried out in these cases. Red arrows point to the nosological images obtained with the source analysis system (four columns of colour coded grids, superimposed to the T_{2w}-MRI for each slice). Colour coding as follows: blue pixels: normal parenchyma, red pixels: non responding, green pixels: responding. TRI values obtained for each case were: 0% (C1109), 3.5% (C1110), 1.9% (C1111) and 19.3% (C1112).

6.3.1.2 Group B: Therapy response in cases starting therapy with tumour volume 2.5-5.5 mm^3: Finding high response (HR) cases

Since no HR cases were found in the first part of the experiment, the objective of this second part of the study was to introduce modifications in the therapy protocol in order to increase the probability of finding HR cases. For this, therapy administration started when tumour size was between 2.5-5.5 mm^3, disregarding the day p.i. of the tumours.

From 15 GL261 tumour-bearing mice which were followed up by MRI, 11 of them started therapy administration at day 7 p.i., whereas the other four mice started therapy at days 9, 11, 13 and 15 p.i., respectively. The mean tumour size of these cases at the starting therapy day was

of 3.7±0.8 mm^3. From these 15 mice, only 2 (C1100 and C1108) presented measurable decrease in tumour volume (5.9% and 12.0% respectively) compared to the previous day of measurement, which was a criterion set by us to start the multi-slice MRSI acquisitions. During follow up, these two cases met the requirements for being classified as HR cases (TRI>65% and volume decrease with respect to the previous day of measurement). TRI and other parameters of these cases are shown in Table 6.1. Significant differences ($p<0.05$) were observed for tumour volume at starting therapy day and for tumour volume at the euthanasia day for HR mice in comparison with IR and LR cases (see Table 6.1). The mean TRI value found in HR cases was 68.2±2.8%. Evolution of tumour volume and nosological images of C1100 and C1108 are shown in Figure 6.7.

For case C1100, therapy administration started at day 7 p.i., when tumour volume was 3.0 mm^3. This mouse was explored by MRI until day 17 p.i. (6 days after finishing the first therapy cycle), when a 7.1% decrease in volume was observed compared to the previous measurement. From days 17 p.i. to 21 p.i., tumour growth arrest was observed in MRI measurement. At day 21 p.i., a 0.6% of tumour volume decrease was detected and a multi-slice MRSI measurement was performed, being the calculated TRI of 36.8%. The next measurement took place at day 26 p.i. when a TRI of 61.6 % was detected and a most clear decrease in volume was observed with respect to the previous measurement (5.9% decrease). The mouse was then euthanized for histopathological validation. In the nosological images (Figure 6.7.A), green pixels were observed in the 2 upper grids at the first day of MRSI acquisition, and in grids 1, 2 and 3 in the last day of acquisition. In the fourth grid, the tumour could not be properly segmented with our analysis, probably due to the small tumour area found in this grid, composed mostly by normal/peritumoural tissue.

Regarding case C1108, therapy administration started at day 15 p.i., when tumour volume was 2.9 mm^3. This mouse was explored by MRI until day 29 p.i. (5 days after finishing the second therapy cycle, when a 12% decrease in volume was observed compared to the previous measurement). The value found for TRI that day was 70.3% and the mouse was euthanized for histopathological validation. In nosological images (Figure 6.7.B), green pixels were observed in Grid 1 and Grid 2. In Grid 3, the tumour could not be segmented, as previously mentioned for case C1100.

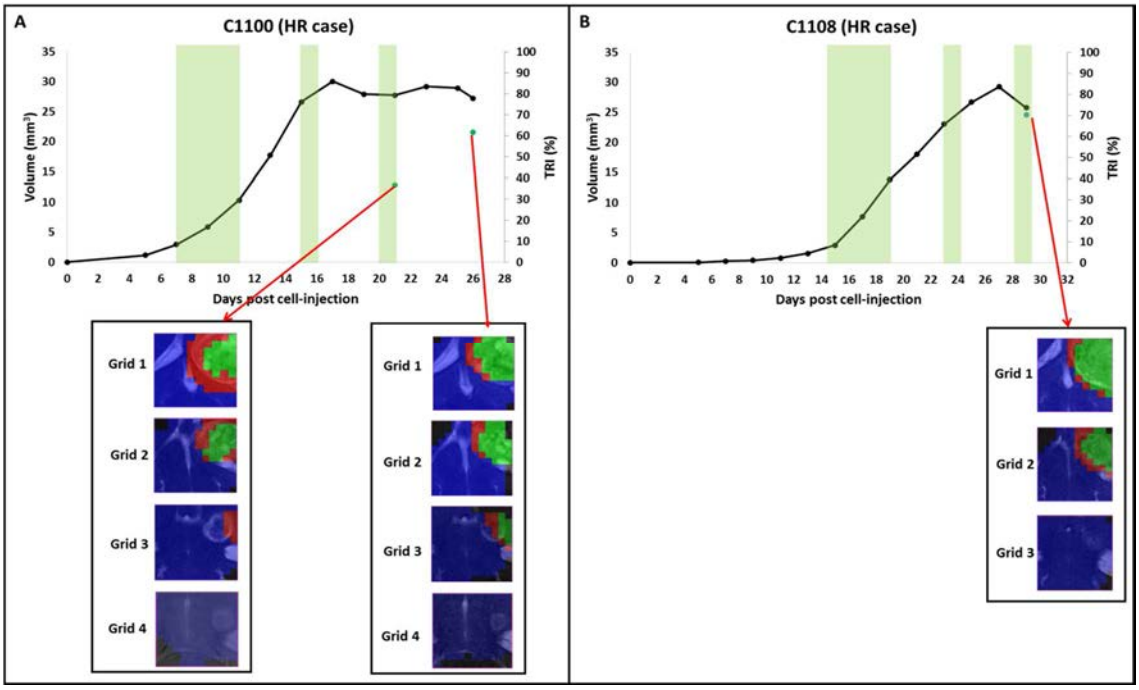

Figure 6.7: Graphical representation of the tumour volume evolution (in mm^3 , *black* line, left axis), and the percentage of responding "green" pixels obtained after source analysis of MRSI data acquired in the multi-slice set as in [117] (in %, green dots, right axis) of HR cases. The green shaded columns indicate TMZ administration periods. For chosen time points, the evolution of the nosological images obtained with the semi-supervised source extraction system is shown, superimposed to the T_{2w}-MRI for each slice (colour coding as follows: blue pixels: normal parenchyma, red pixels: non responding, green pixels: responding). The number of grids (3 or 4) depended of the coverage of the tumour: if tumour was totally covered with 3 grids, no additional grids were acquired. **A.** Corresponds to the case C1100: green pixels were observed in grids 1 and 2 with a TRI= 36.8% at day 21 p.i. during tumour growth arrest. Then at day 26 p.i., tumour volume decreased and a TRI of 61.8 % was observed. **B.** Corresponds to the case C1108: green pixels were observed in grids 1 and 2 with a TRI= 70.3% when tumour volume decrease was observed.

6.3.2 Metabolic Pattern Contributing to Responding and Non-Responding (Red and Green) Areas Detected in MRSI Studies of the Investigated Mice

Different metabolites have been described to contribute to the spectral pattern of preclinical glioblastoma [90, 112, 116, 117, 264–269] and some of them are listed in Table 6.2, being also observed in cases analyzed in this study. Figure 6.8 shows examples of average spectra extracted from blue, red and green zones of a HR case (C971), whereas in the figure shown in Annex III.III examples of average spectra from red and green zones can be seen, in comparison with the sources extracted from treated and untreated cases reported in [117]. It is worth mentioning that the changes observed in the whole metabolic pattern, rather than isolated changes in few metabolites, is what allows the semi-supervised source extraction system to classify MRSI voxels in different classes (normal brain, responding tumour and non-responding tumour) [117].

Table 6.2: List of the main metabolites contributing to the spectral pattern recorded in tumour/peritumoural MRSI of responding and non-responding mice, with the corresponding approximate ppm position. Metabolite assignments according to [90, 112, 116, 141, 264–269].

Metabolite	ppm
Mobile Lipids + Macromolecules	0.90
Mobile Lipids+Lactate	1.33
Alanine	1.47
N-acetyl-aspartate + N-acetyl containing compounds + Mobile lipids	2.02
Glutamate + glutamine	2.10- 2.40 + 3.80
PUFA (Mobile Lipids)	2.80
GABA	3.00
Total Creatine	3.03
Choline-containing compounds	3.21
Scyllo-inositol	3.34
Taurine	3.42
Myo-inositol + glycine	3.55
Lactate	4.10

The main differences between normal brain parenchyma and tumour areas (blue vs. green/red areas) were: higher choline/creatine (Cho, 3.21/Cr, 3.03 ppm) ratios, higher mobile lipids (ML, 0.9 and 1.3 ppm) and lactate (Lac, 1.3 ppm and 4.1 ppm) peak intensities in tumour areas, as well as lower N-acetyl-aspartate (NAA/NAc, 2.02 ppm) signal, already described by us in [90]. The zones classified as “normal brain parenchyma” by the source extraction approach presented the expected features, such as lower ML and ML/Lac signals in comparison with tumours, and a ca. 1:1 ratio for Cho and Cr. See [112] for more examples of control spectra in mice brain. Although the responding and non-responding spectra (which are present in green and red areas respectively) could seem quite similar, relevant differences between them are sampled by the source analysis especially related to polyunsaturated fatty acids in ML (PUFA, 2.8 ppm), as already described by [90, 141]. Other minor contributions are Lac (4.1 ppm), glutamine plus glutamate and alanine (Glx + Ala, 3.8 ppm) and myo-inositol and glycine (Ins + Gly, both seen at 3.55 ppm). See also Figure 6.8 for further details.

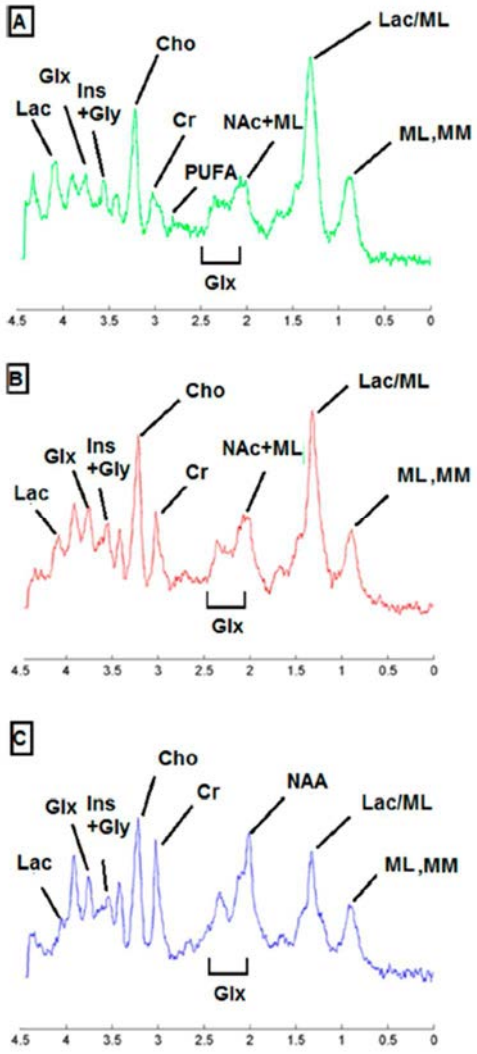

Figure 6.8: Example of mean spectra extracted from the MRSI grid of a treated case (IR case C971: Grid 1, Day 34 pi): (A) mean spectra of responding area (n = 26); (B) mean spectra of non-responding area (n = 35); and (C) mean spectra of normal brain parenchyma area (n = 39). Some of the main metabolites contributing to different patterns of response to therapy are shown: mobile lipids 0.9 + macromolecules (ML, MM, 0.9 ppm), mobile lipids 1.3 + lactate (ML/Lac, 1.3 ppm), N-acetyl-aspartate and N-acetyl group containing compounds (NAA and NAc, 2.02 ppm) (see also [270]), glutamate + glutamine (Glx, 2.1–2.4 ppm) polyunsaturated fatty acids in mobile lipids (PUFA, 2.8 ppm), total creatine (Cr, 3.03 ppm), choline-containing compounds (Cho, 3.21 ppm), myo-inositol + glycine (Ins + Gly, 3.55 ppm), glutamine + glutamate (Glx, 3.8 ppm, which is also partially contributed by alanine), and lactate (Lac, 1.3 and 4.1 ppm).

6.3.3 Histopathology validation

Cases used for histopathological validation were, according to TRI response: 2 HR cases (C1100 and C1108), 3 IR cases (C971, C1022 and C1026), 1 LR case (C979) and 2 Control cases (C1110 and C1111).

6.3.3.1 Haematoxylin/Eosin morphology analysis

Different cell morphology (namely, aberrant large and giant cells and multinucleated cells) and presence of large acellular spaces were observed in samples of treated mice, in comparison to non-treated mice, for which those characteristics were not found. In Figure 6.9, examples of histopathological preparations with Ki67 immunostaining, corresponding to green pixels and red pixels areas in tumours, are shown for representative examples of each class (C1110, C979, C971 and C1108). Ki67 immunostainings and nosological images of remaining cases evaluated by histopathology, C1111, C1022, C1026 and C1100, are shown in Annex III.

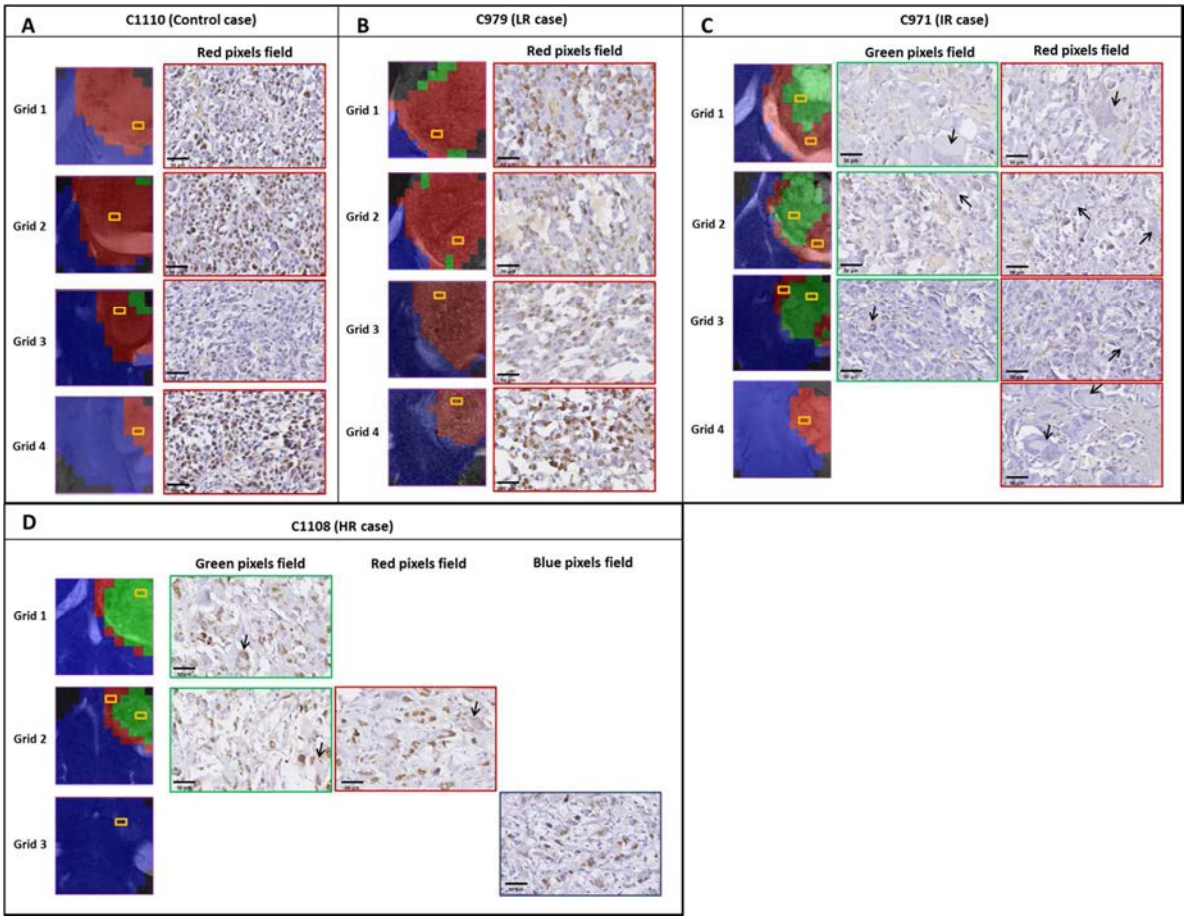

Figure 6.9: Ki67 immunostainings (40x magnification, the scale bar corresponds to 50 µm) in histological areas corresponding to red or green regions in nosological images, from different grids of chosen cases. The yellow rectangles in the nosological image identify the approximate origin of the histopathological preparations shown. The nuclei of Ki67 positive cells are stained in brown. **A.** Control case C1110, with a global Ki67 of 63.9±13.0% and a highly dense cellular population showing a typical tumoural morphology with small to medium-sized polygonal or irregular cells with rounded nuclei and scanty cytoplasm without any giant cells visible. **B.** LR case, C979: in this case, Ki67 positive cells were also observed (64.8±7.3%) but with less cellular density due to presence of large acellular spaces in comparison with the control case. **C.** IR case C971, presented lower Ki67 immunostaining (22.0±17.2%) than control and LR cases, with presence of giant cells with several nuclei (black arrows), and also acellular spaces. No significant differences were observed for Ki67 between red and green areas from nosological images of this case, although the trend to higher Ki67 in red areas is maintained (Ki67 for red areas 25.7±17.0% and Ki67 for green areas 17.2±16.8%) **D.** HR case C1108, with an average Ki67 of 79.3±10.1%, although it is worth noting that HR cases present lower number of total tumoural cells per field in comparison with IR cases (57.1±16.9 and 86.7±63.9 cells/field respectively), which could have an influence in the final result of Ki67% calculation. Still, acellular areas and giant cells (black arrows) were also observed. See Discussion section (section 6.4.3) for a possible explanation with respect to apparently high Ki67 values in green nosological image regions.

6.3.3.2 Ki67 analysis

Comparison of responding and non-responding zones

Green and red areas of the nosological images, disregarding the case categorization, showed a trend, with green zones having lower Ki67 values (42.9±32.6%, n=50 fields) than red zones (59.9±25.1%, n=121 fields) (see Figure 6.10). Significant differences were found with Mann-Whitney's U test ($p<0.05$), although there is considerable dispersion within the data. The Ki67% value found for red zones of treated cases was not significantly different from values obtained in red zones of control untreated cases. Analysing green and red zones in a case-by-case study (i.e. comparing Ki67 for red and green zones within the same case), the obtained results varied depending on the case: IR cases presented either statistical significance ($p<0.05$, C1022) (Figure 6.11) or a trend towards significance ($0.1>p>0.05$, 1026, C971), whereas HR cases did not present statistical significance.

Taking into account these results, we wondered whether green and red zones could have significantly different Ki67 values depending on the classification of the case according to TRI level (e.g. all green zones of IR cases vs. all green zones of HR cases). For IR cases, we found Ki67 values of 52.0% for red zones and 21.1% for green zones, whereas cases classified as HR presented values of 84.1% for red zones and 77.7% for green zones. This would suggest that although there is indeed a correlation between a responding/non-responding pattern and its Ki67 immunostaining, the absolute values could be quite different between intermediate response and high response cases, which could be at least partially explained due to different cellularity between these cases.

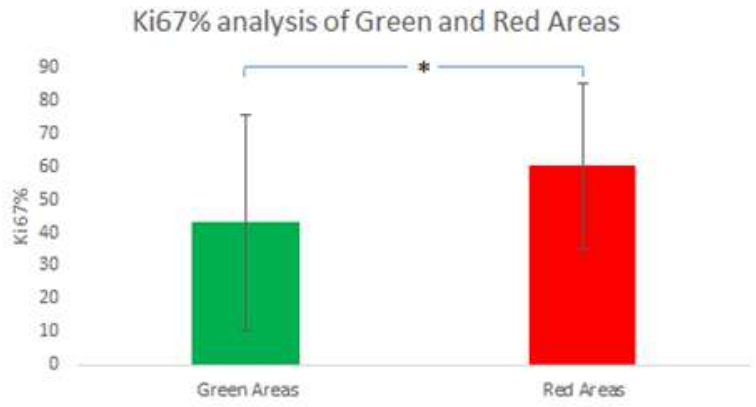

Figure 6.10: Graph bar of mean ± SD of Ki67% values found in green and red areas from nosological images of all studied cases. Significant differences ($p<0.05$ with Mann-Whitney's U test) were found between them, with higher values in red (59.9±25.1 %) areas in comparison with green areas (42.9±32.6 %).

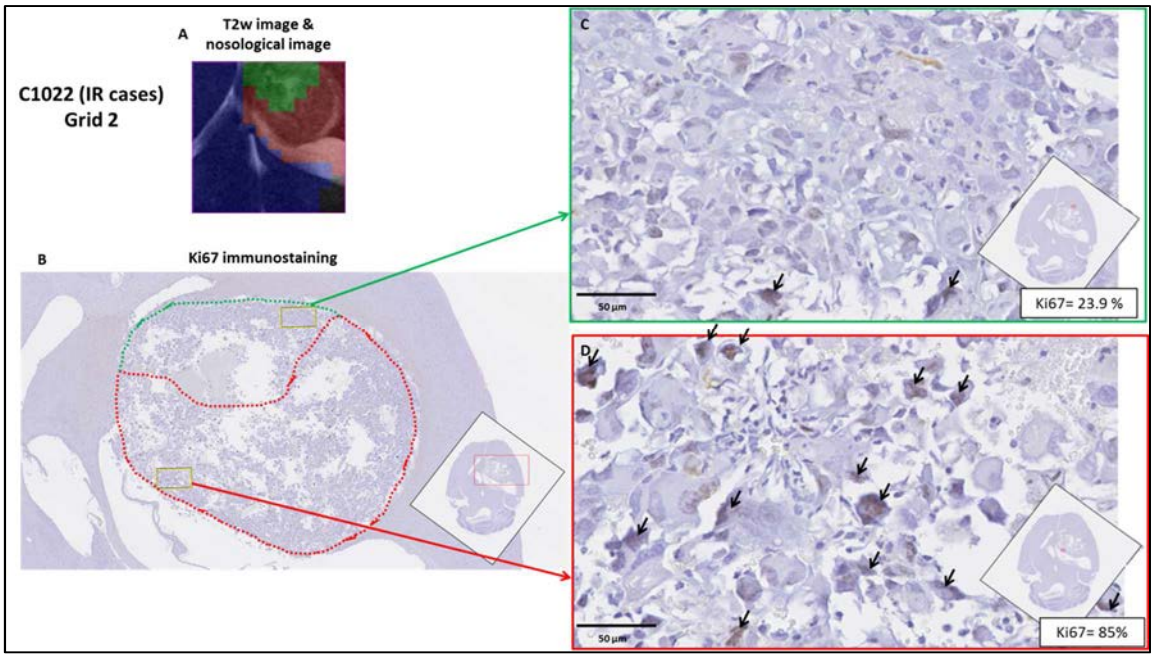

Figure 6.11: Example of the histopathological validation of a nosological image of Grid 2 of the case C1022 (IR case). A. Nosological image obtained from Grid 2 of the case C1022 superimposed to the T2w-MRI. Both green and red zones could be distinguished within the tumour, showing a heterogeneous pattern of response. B. Ki67 immunostaining colocalized with the grid 2, in which the red and green areas from the nososological image have been manually drawn over the tumour (shown in red and green dashed lines). One representative field has been selected in each area (yellow rectangles have the same area). C. 40 x magnification of the yellow field from the green area, with an average Ki67% value of 23.9%, and black arrows pointing to Ki67 positive cells. D. 40 x magnification of the yellow field from the red area, with a Ki67% value of 85%, and black arrows pointing to Ki67 positive cells.

The global Ki67% for each case was also analysed taking into account the Ki67 values found for all slices of a given case, which would reflect an average proliferative state of the whole tumour. Global Ki67 values are shown in Table 6.3. Still, higher global values were observed in control cases than in treated cases as a whole (Figure 6.12.A, 68.6%, n=40 fields vs 52.6%, n=139 fields respectively). Significant differences were found with Mann-Whitney's U test ($p<0.05$). Regarding treated cases, higher global Ki67 values were observed in LR cases (64.8±7.3%) than in IR cases (41.9±32.2%), as expected (Figure 6.12.B). However, surprisingly, HR cases presented a value higher than expected and a possible explanation, which will be further elaborated in the Discussion Section, can be related to the lower cellularity observed in these cases and the different cell volume observed in treated cases with intermediate or high response, as mentioned before.

Table 6.3: Results of Ki67 percentage ±SD of fields corresponding to green and red pixels in nosological images, as well as the global percentage of Ki67 for the studied cases. Percentage of TRI and its classification by TRI criteria are also shown.

Case	Ki67%±SD (Green fields)	Ki67%±SD (Red fields)	Ki67%±SD (Global)	TRI%	Classification by TRI criteria
C971	17.2±16.8	25.7±17.0	22.0±17.2	44.1	Intermediate
C1022	19.0±20.9	54.9±32.6*	42.5±33.5	46.5	Intermediate
C1026	53.5±30.3	73.0±26.8	66.0±39.1	38.9	Intermediate
C979	n.a.	64.8±7.3	64.8±7.3	3.3	Low
C1100	82.9±4.6	92.5±0.6	82.2±7.7	66.3	High
C1108	75.1±9.5	75.8±0.2	79.3±10.1	70.3	High
C1110	n.a.	63.9±13.0	63.9±13.0	0	Control
C1111	n.a.	73.3±6.4	73.3±6.4	0	Control

n.a. = not available (the low number of green pixels observed in the case C979 (7 in Grid 1 and 4 in Grid 2), did not allow to confidently establish a field for corresponding histopathology evaluation in that tumour region). * = significant differences in Ki67% between red and green areas for this case.

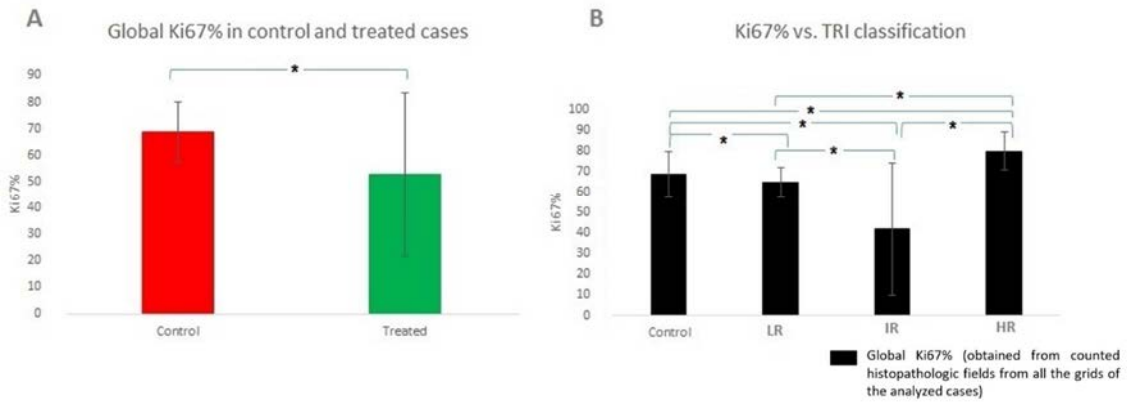

Figure 6.12: Graph bars representing global Ki67% values (mean ± SD). A. Global Ki67% was higher in control cases than in treated cases. B. Global Ki67% in different cases classified by TRI criteria. A descending trend was observed between control, LR and IR cases, as expected. An unexpectedly high Ki67% value was found in HR cases. * = $p<0.05$ with Mann-Whitney's U test.

Significant differences were observed for Ki67 ($p<0.05$) between groups of cases classified by their TRI response level (LR cases, IR cases, IR cases) (Figure 6.12.B). The Ki67% of the different groups classified by TRI and their TRI values are also summarized in Figure 6.13.

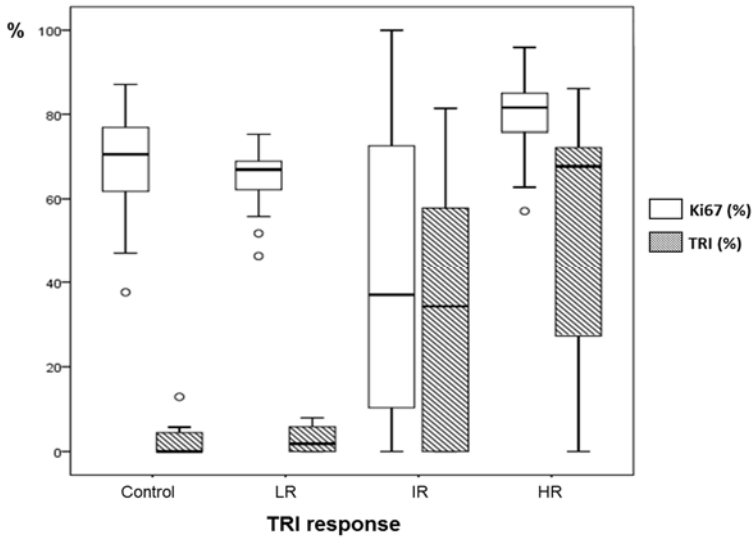

Figure 6.13: Boxplot of global percentage of Ki67 (white boxes) and percentage of TRI values (striped boxes) of each MRSI grid of different groups of cases classified by TRI response and analyzed by histopathology. Control and LR cases with low values of TRI (2.7±1.1% for control cases and 3.3±0% for LR cases) showed higher Ki67 values (71.6±10.9% for control cases and 64.8±0% for LR cases). IR cases showed similar mean values of TRI 42.1±5.6% and Ki67: 43.5±22.0%, presenting also a very high dispersion as well. HR cases showed higher values of TRI (as expected, 68.3±2.8%) but unexpectedly high Ki67 values (77.8±6.3%). Boxplot: the limits of the box represent quartiles 1 (Q1) and 3 (Q3) of the distribution, the central line corresponds to the median (quartile 2). The whiskers symbolize the maximum and minimum values in each distribution. Outliers (values higher than 1.5 X IQR, interquartile range, obtained by difference of Q3 and Q1) are represented with round symbols.

6.3.4 TRI calculation in retrospective TMZ-treated mice:

TRI was calculated in the nosological images obtained from 3 mice (C817, C819 and C821) in which therapy response was assessed by single-slice MRSI acquisitions in a previous study of the GABRMN group and the three cases responded transiently to therapy [117, 124]. In this re-analysis, the three cases also showed an oscillatory pattern of response when TRI was calculated. A representative case (C817) is shown in this section (Figure 6.14) and the other two cases C819 and C821 are shown in Annex III. It is worth mentioning that cases C817 and C821 had an extra cycle of therapy administration at days 44 and 45 p.i.

C817: This case showed tumour growth arrest after the second therapy cycle (Figure 6.14). The tumour volume variation (compared to the previous measurement) from day 20 to 32 p.i. showed a decreasing trend in tumour volume of in average 4.06±10.46%, in agreement with

stable disease according to the adapted RECIST criteria. Then, partial response was observed from day 34 to 36 p.i., with tumour volume presenting a decrease of 30.29%. From day 38 to 61 p.i., an increase in tumour volume of 10.77±25.26% was observed (stable disease, according to the adapted RECIST criteria). Finally, from day 61 p.i., tumour relapsed, growing fast until the day 70 p.i. when the animal was euthanized due to animal welfare conditions. The mean tumour volume increase was 37.27±20.05% during the relapse stage

TRI was calculated using nosological images obtained from the single MRSI grids acquired at different time points along the longitudinal study. The evolution of TRI suggested a cyclical oscillation when tumour growth arrest was observed after the second therapy cycle, with values of 50% at day 28 p.i. and 44.44% at day 32 p.i. Between these 2 days, tumour volume decreased in average 15.60±7.71%, in agreement with partial response according to adapted RECIST criteria. The first TRI peak was observed at day 20 p.i. (TRI= 18.8%) and appeared 7 days after the middle point of the first therapy cycle (day 13 p.i.). A second TRI peak of 26.7% was observed at day 24 p.i., 5 days after the beginning of the second therapy cycle. Then, further TRI increase (50%) was observed at day 28 p.i., 8 days after finishing the second therapy cycle. Finally, another TRI peak of 44.44% was seen at day 32 p.i., 8 days after the beginning of the third therapy cycle. The oscillation frequency in this case seems to be about 7 days. TRI could not be calculated between days 35 p.i. and 58 p.i., because the small tumour volume prevented the segmentation with the semi-supervised system. When tumour relapsed at day 61 p.i., responding pixels appeared again and TRI increased until 60%. It is worth mentioning that an extra therapy cycle of 2 days was administered to this case in days 44 p.i. and 45 p.i.

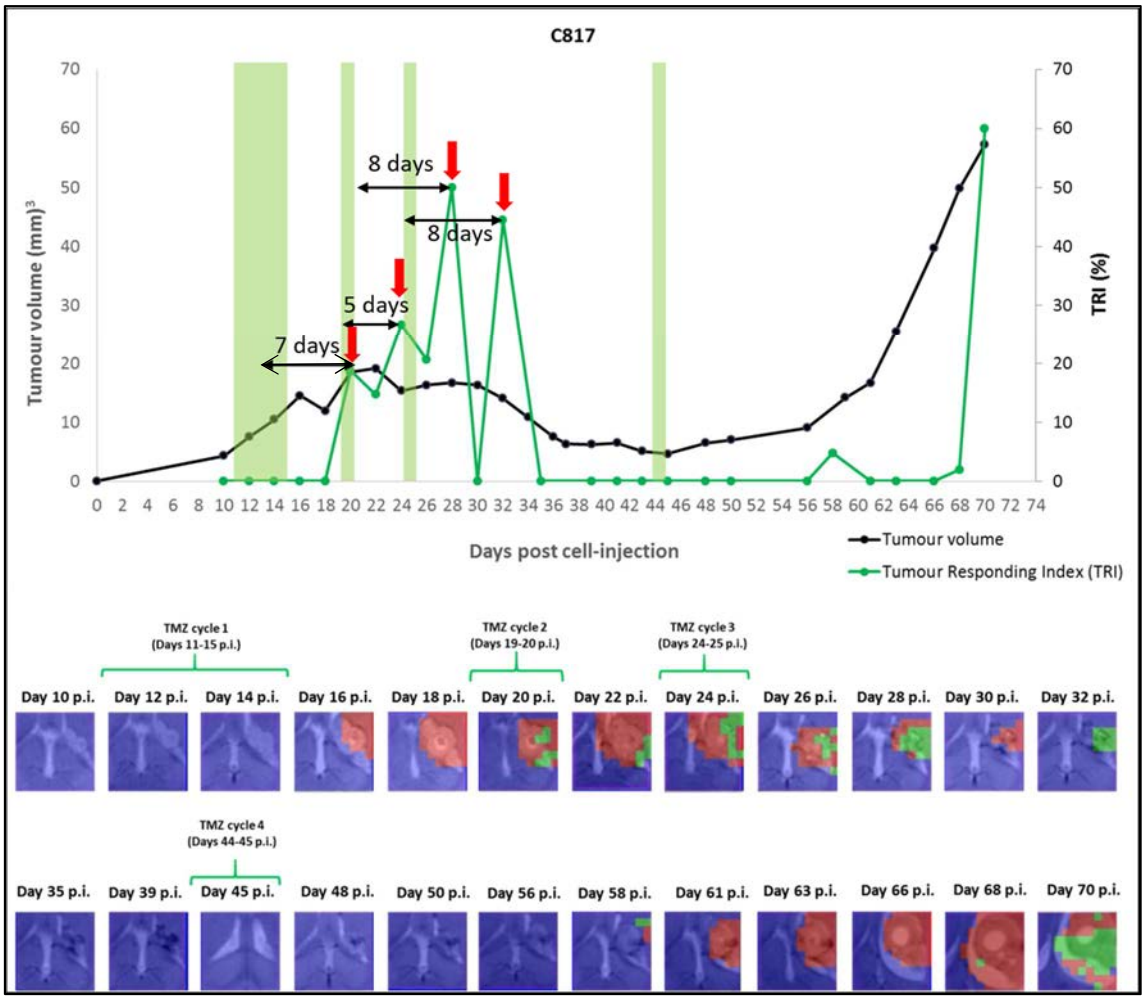

Figure 6.14: The first graph shows a representation of evolution of tumour volume (black line) and evolution of TRI (green line) along time in the retrospective case C817. Green bars show therapy administration cycles (this case had an extra therapy cycle on days 44 - 45 p.i.). Then, nosological images obtained from semi-supervised source analysis from longitudinal studies using only one MRSI grid, are shown. Therapy cycles are indicated by green brackets. A cyclical pattern of response (5-8 days) was observed, marked by the black arrows in the graphical representation. Red arrows indicate the maximum values observed of TRI during tumour volume growth arrest.

C819: This case showed tumour growth arrest after the second therapy cycle between days 22 and 24 p.i. (stable disease according to RECIST criteria). Then, it was classified as partial response case according to adapted RECIST from day 24 p.i. to 26 p.i since tumour volume decrease was of 31.20%. Finally, this case met stable disease criteria again from day 26 to 39 p.i. (tumour volume decrease of 8.14±13.04%). Finally, tumour relapsed until the day 45 p.i. when the animal was euthanized due to animal welfare conditions.

TRI oscillations were observed at days 18 (TRI= 60%) and 22 p.i., (TRI=100%) period which matched with tumour growth arrest period. Then, a decrease in TRI was observed during the

partial response stage (from day 22 p.i. to 39 p.i.) until reaching a TRI value of 32%. In the final stage of tumour relapse, another TRI peak was observed at day 41 p.i. with a TRI value of 82.1%.

C821: This case also showed tumour growth arrest (stable disease according to the adapted RECIST criteria) after the second therapy cycle from day 20 to 30 p.i (the mean tumour volume increase was of 10.93±8.36%). However, no partial response was observed, tumour relapsed from day 30 to 34 p.i and the animal was euthanized.

TRI oscillations were observed at days 24 and 28 p.i. (during stable disease stage) with TRI values of 69.74% and 80.81%. Then, TRI increasing was observed at day 32 p.i. (TRI= 96.34%) during tumour relapse stage.

Although the example shown in Figure 6.14 (C817) presented a maximum TRI of 50%, cases in this retrospective set presented values ranging from 4.23% to 100%. A 100% TRI case means a fully "green", responding tumour, which was not seen in the multi-slice approach. This reinforces the idea that the analysis of a single slice MRSI is not able to adequately represent the changes taking place in a heterogeneous tumour as GB. The first detection of green pixels was seen at days 18 to 24 p.i., depending on the case, which was similar to the first detection of green pixels in the multi-slice acquisitions (from 18 to 23 p.i.). For these 3 retrospective cases, the average frequency of TRI oscillations was 6.3±2.0 days.

6.3.5 Preliminary volumetric-rendering of nosological data

The four nosological images obtained from case C971 at day 32 p.i were reconstructed voxel by voxel (1:50 scale), and the position of each grid followed the real coordinates of the multi-slice experiment MRSI.

In Figure 6.15, several views of this reconstruction are shown; superimposition with MRI was not feasible with this software and, accordingly, only MRSI data is shown. With this example, we wanted to show that a volumetric reconstruction is possible, although there is still much work to be done towards an improvement of this type of representation. Ideally, superimposition with the T_{2w} image, taking into account the difference in resolution of both techniques, and the use of transparencies could give 3D information about therapy response and show possible foci of no response/relapse within a given tumour. The fact that the 3D MRSI grid is not a perfect aligned cubic shape is challenging and better rendering attempts are being currently performed in collaboration with the group of Prof. Andrés Santos from *Universidad Politécnica de Madrid* (Biomedical Image Technologies Group).

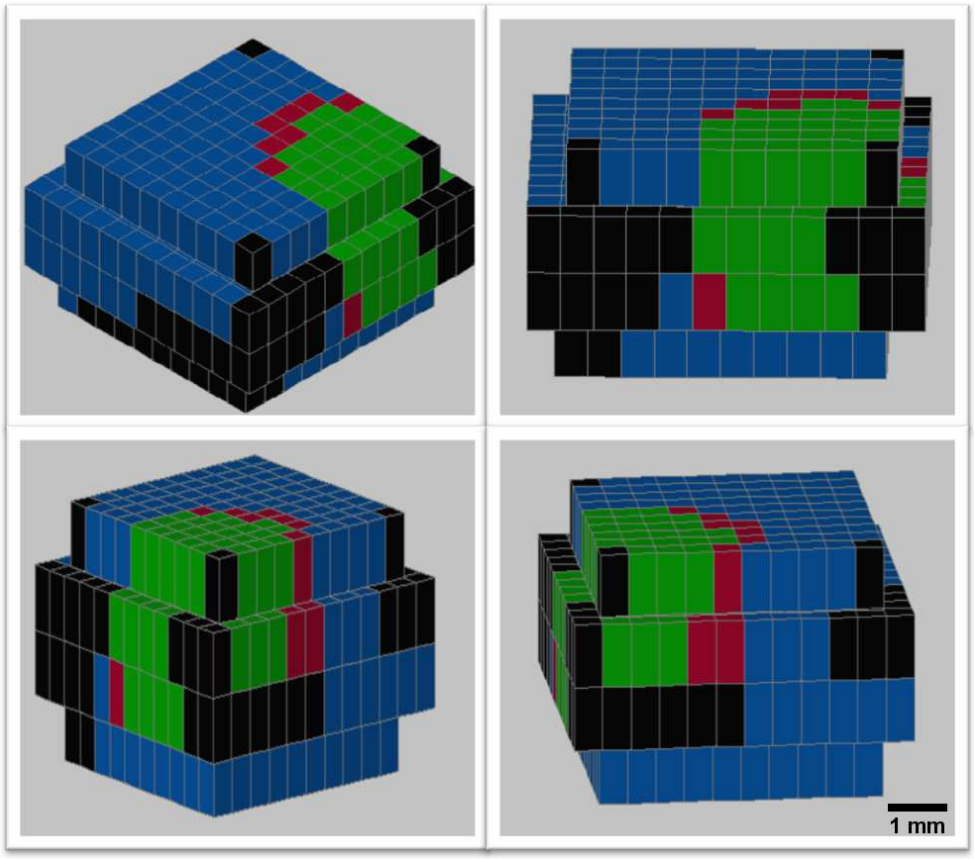

Figure 6.15: Volumetric 3D representation of nosological images obtained from case C971 at day 34 p.i. before animal euthanization. The four images are different rotation views from the volumetric map. The scale bar is indicated in black. Colour coding as in Figure 6.4.

6.4 General discussion for this section

6.4.1 Multi-slice MRSI and TRI for therapy response level evaluation

MRSI acquisitions allowed us to obtain differential metabolomic patterns from treated and control tumours. Although it is true that other authors have also applied MRSI techniques in order to assess the effect of therapy in brain tumours [115, 271–273], they were mainly focused in some particular signals or ratios (such as quantitation of NAA, Cho, Cr or ratios between them). These ratios have proved useful in our model [90] only when using single voxel MRS data, but did not succeed to produce robust discrimination when individual spectra from MRSI grids classified as responding and non-responding were used for the calculation (data not shown). This probably suggests that the distinction of responding from non-responding zones cannot be explained by a single change or a set of few changes/ratios. In this sense, the source-based approach applied to MRSI data takes into account the whole set of metabolic changes in the spectral pattern and can handle the information in a way that may not be straightforward to

perform after standard quantification, for example with LCModel [274]. Table 6.2 lists the main metabolites thought to contribute to the spectral patterns recorded, and their meanings are also described in Introduction, section 1.2.1.3. The detection of signals at 2.8 ppm, compatible with presence of PUFA is in agreement with authors in [141], who reported similar signals in their preclinical model, as early as 2 days after therapy with ganciclovir, being indicative of apoptosis in their case.

After acquiring MRSI data from our mice, nosological images were then generated to follow-up the evolution of tumour response to treatment. Previous studies from our group using MRSI-based source analysis from a single slice acquisition allowed us to distinguish between responding and non-responding cases [117], with metabolomics pattern-derived changes preceding the anatomical derived information provided by MRI in several instances. However, the use of a single slice, ignoring the response level taking place in other tumour areas, could prevent us to gather relevant information, as GB is widely accepted to be highly heterogeneous [275]. The multi-slice MRSI technique used in this study has allowed us to obtain nosological images from different areas of the investigated tumours, unraveling heterogeneous response levels that we were unable to see with the single slice examination. In work presented in [117], several treated cases presented a response level (when recalculated for the presently proposed TRI index) close to 100% (mean TRI= 92.9±8.2%, n=8) whereas in the present work with whole tumour examination, the maximum value achieved was of 70.3% and the mean±SD TRI of all treated mice was 40.8±20.5%. Still, we observed that not all MRSI slices had the same response level after treating mice bearing GL21 GB tumours with TMZ, with upper, dorsal slices presenting higher levels of TRI (53.0±28.4%) than lower, ventral ones (8.6±20.0%) ($p<0.05$). Once TRI was calculated, it allowed us to quantify the evolution of response to treatment and also to classify cases in different arbitrary categories. It is worth noting that the generation of nosological images poses some limitations, namely: highly heterogeneous or haemorrhagic zones could result in poor quality MRSI spectra, preventing the system to classify them correctly. In addition, the smallest tumour correctly segmented had a volume of 18.4 mm^3, which should be taken into account when interpreting data of apparently non-responding or normal parenchyma regions.

6.4.2 Classification of TMZ-treated mice after TRI calculation and evolution of TRI values

Treated mice were classified into different categories regarding response level, as explained in section 6.3.1.1 and this study was divided into two different parts in order to ensure that all categories were represented. The first part of the study only produced LR and IR cases, and a modification of the initial protocol was needed in order to obtain cases fulfilling proposed

criteria for HR cases. The fact that some cases presented only partial response to therapy had already been found in our previous work [117] with one single MRSI slice in cases C418, C527 and C584 (with TRI response calculated for those single-slice acquisitions of 21.3%, 60.6% and 49.0%, respectively). However, the detailed subdivision in "response groups" and heterogeneity observation was only possible after performing a multi-slice MRSI acquisition, confirming the heterogeneous pattern of response usually seen in GB. This heterogeneous pattern of response has also been reported in other preclinical studies using diffusion-weighted MRI techniques [276] and using PET-MRI techniques in humans [277].

The evolution of TRI in the different cases studied with longitudinal measurements indicated that increases in TRI corresponded essentially to periods of growth arrest (stable disease stage according to the adapted RECIST criteria) and were related to therapy cycles. Regarding IR cases, the TRI increase was seen around 6.5±1.0 days after the first therapy cycle (n=4), except in n=2 cases in which the highest increase was seen 6 days after the second therapy cycle. It is worth mentioning that in IR cases (see Figure 6.4.A and B), the first appearance of the responding pixels preceded the growth arrest observed in MRI acquisitions. On the other hand, LR cases presented a slightly different evolution: these cases did not show tumour growth arrest and TRI pixels were observed during the first therapy cycle (earlier than in IR cases, see Figure 6.4.C and D). Still, some cases, i.e. C971, seemed to show an oscillating pattern for TRI (see Figure 6.4.A) in which 2 peaks of increased TRI (31.2% and 44.1%) were separated by 8 days.

The protocol designed for this study was focused in allowing the histopathological validation of nosological images recorded at certain time points, meaning that mice fulfilling criteria for inclusion in a response group were euthanized after MRSI acquisition to allow for in vivo / in vitro correlation. Accordingly, we could not observe the evolution of TRI along the whole treatment period for the investigated mice. To overcome this restriction, one of those mice (C974, Figure 6.5) was saved to be followed up until end-point. In this mouse we could clearly observe an oscillatory pattern in TRI values, as opposed to tumour volume, which remained stable during 6 days (maximum variation of 11.20%, corresponding to stable disease according to the adapted RECIST criteria). The TRI values varied along tumour evolution, with the first maximum peak of TRI (41.4%) being observed at day 20 p.i., 5 days after finishing the first therapy cycle. The second maximum peak of TRI (36.8%) was observed at day 26 p.i., 6 days after finishing the second therapy cycle. This oscillatory behavior of TRI peaks (5-6 days after therapy cycles) was taking place at the same time that tumour volume measurements indicated "stable disease" according to the adapted RECIST criteria. Then, a last peak of TRI was observed at day

37 p.i., when tumour relapsed (at progressive disease stage). This was 12 days after finishing the last therapy cycle and the animal died due to tumour mass effect with a final volume of 140.5 mm^3. Since this case was not intended to be used for histopathological validation, no samples of C974 were saved for such analysis.

This cyclical pattern of response was not obvious in other IR cases (C975, C1022, C1023 and C1026), in which TRI increases were observed during tumour growth arrest, or when tumour growth arrest started to be observed. However, it is possible that the prompt animal euthanization, when these TRI increases were observed, could have prevented us to observe further TRI oscillations.

The HR cases were only observed when the protocol was adjusted to start therapy with smaller tumour volumes (3.7±0.8 mm^3). In these cases, TRI increase was observed 5 days after the second therapy cycle, although we should also consider that MRSI acquisition was conditioned to tumour volume decrease and no previous MRSI data was acquired – accordingly, we do not have enough data for frequency estimation. Finally, LR cases did not respond to therapy and no TRI oscillations were observed. The reason why these cases were not responding could be due, among other reasons, to individual tumour resistance to alkylating agents through overexpression of the MGMT protein [41], although preliminary data from GABRMN does not seem to point to a relevant role of MGMT in tumour relapse in GL261 GB. Another possible reason for tumour resistance could be related to overexpression of PD-L1 as described by authors in [278] and also supported by GABRMN preliminary results, not described in this thesis. Still, different glioma-initiating cells (GIC) clones from the same GB tumour may have variable levels of therapy resistance to different therapies, resulting in a heterogeneous pattern of response to therapy within the same tumour [275]. It was beyond the scope of our present study to establish whether a correlation between TRI level and overall survival exists or not. However, from the data gathered, it was clear that the behaviour of TRI, as opposed to the relatively unchanged tumour volume during growth arrest, presented an oscillating pattern with an approximated frequency around 6.3±1.3 days (n=4). See possible explanations for this in section 6.4.4.

Intuitive cyclical changes in TRI at stable disease stages could be observed in 3 longitudinal cases included in previous work from our group [117]. These cases (C817, C819 and C821) were followed up until endpoint by single slice MRSI acquisitions. The average frequency of these TRI oscillations now recalculated (6.3±2.0 days, n=3) was very similar to the one calculated using the multi-slice approach in this work (6.3±1.3 days). Nonetheless, the representation of TRI

evolution is more clear and confident in cases studied by the multi-slice approach than in single slice MRSI cases.

6.4.3 Histopathology results

Histopathology analysis was conducted for all acquired grids in chosen animals (see section 6.2.6) in order to confirm the results previously described in [117], in which significant correlation between the responding pattern and the proliferation marker Ki67 was found, with green, responding zones presenting significantly lower Ki67% value than red, unresponsive zones. This histopathological biomarker was also chosen by other authors in order to estimate therapy response in preclinical brain tumours [279, 280] and in human GB [281, 282].

As it can be seen in Figure 6.10, this trend has been confirmed in our work with multi-slice MRSI acquisition, although the fold change when comparing green and red zones was slightly different (1.4 fold change in this study, compared to 2.4 fold change obtained in previous studies single slice MRSI [117]). Although the dispersion of values was really large, especially within green zones, we have been able to confirm that lower mean values of Ki67 immunostaining were found in green zones, whereas higher values were seen in red zones, either from controls or treated tumours.

One of the unexpected findings in this work was that HR cases had the highest calculated Ki67% values, in disagreement with tumour volume behaviour, which was showing signs of volume decrease. The lower cellularity in investigated fields from those cases, with large acellular spaces between abnormal giant cells (in agreement with the morphology described by other authors in human glioma treated with radiotherapy [283] and in human treated sarcoma [284]) could be partially responsible for that. We wondered whether analyzing the number of Ki67 positive cells by mm^2 instead of % tumour cells would be helpful for clarification, and the results can be seen in Figure 6.16, in which the number of Ki67 positive cells/mm^2 is illustrated. A descending trend is clearly seen between control (2,912.4± 692.7 cells/mm^2, n=40 fields), LR (1,799.2± 369.7 cells/mm^2, n=20 fields) and IR (372.7± 264.7 cells/mm^2, n=92 fields) cases. Regarding HR cases, values found (713.6± 211.5 cells/mm^2, n=27 fields) were slightly higher than IR cases, but lower than LR and control cases. Also, significant differences ($p<0.05$) were found between the groups. This would probably suggest that the absolute number of Ki67 positive cells for mm^2 would not be quite different in IR and HR cases, but the overall abnormal morphology of the cells as well as tumour behaviour and the metabolomics pattern from MRSI acquisitions are indicating that the response level is higher in HR cases.

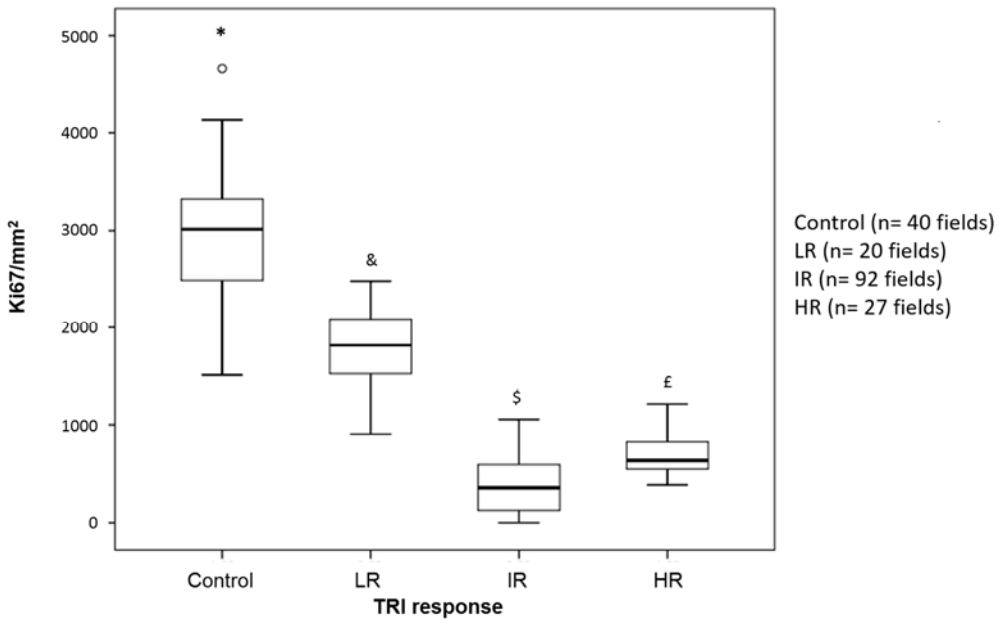

Figure 6.16: Boxplot of global number of Ki67 positive cells/mm^2 of different groups of cases classified by TRI response. Outliers (values higher than 1.5 X IQR, interquartile range, obtained by difference of Q3 and Q1) are represented with round symbols.

* = p<0.05 in comparison with LR, IR and HR cases
&=p<0.05 in comparison with control, IR and HR cases.
$= p<0.05 in comparison with control, LR and HR cases.
£=p<0-05 in comparison with control, LR and IR cases

Having in mind the different morphology observed in cases under treatment and the effect that it seemed to produce in Ki67% calculation, we measured the average cell volume in each group of cases, as well as the amount of acellular space observed in histopathological slides in order to better understand which type of elements would be essentially contributing to the observed MRSI pattern. For this, we calculated the average volume of Ki67 positive cells present in a representative field of different cases (n=8 cases, 2 HR, 1 LR, 3 IR and 2 control, Figure 6.17.A), and also the percentage of acellular space observed (Figure 6.17.B). In Figure 6.17.A, a trend of increasing cell volume is observed: volumes were 372.1±178.8 µm^3 (control cases, n=50 cells counted), 1,867.3±1,698.9 µm^3 (LR cases, n=25 cells), 6,179.9±9,855.5 µm^3 (IR cases, n=54 cells) and 8,180.6±7,608.3 µm^3 (HR cases n=45 cells). Significant differences were found with Mann-Whitney's U test (p<0.05) between the groups. This could probably distort the Ki67% estimation value if the calculations are done in the same way for control and responding tumours, because the average cell volume could be 22 fold higher in an HR case than in a control case, and a given field, accordingly, will be represented by a lower number of cells. Furthermore, a high number of histological fields with plenty of acellular space was observed in treated cases, which cannot be neglected either. Regarding them, in Figure 6.17.B an increasing trend in the percentage of

acellular space is observed: control cases presented only 19.1±6.9%, whereas ascending values were observed in treated cases: LR cases with 27.5±8.2%, IR cases with 37.4±11.0 % and HR cases 44.±15.3 % which is almost half of the field. Significant differences were found with Mann-Whitney's U test ($p<0.05$) between groups.

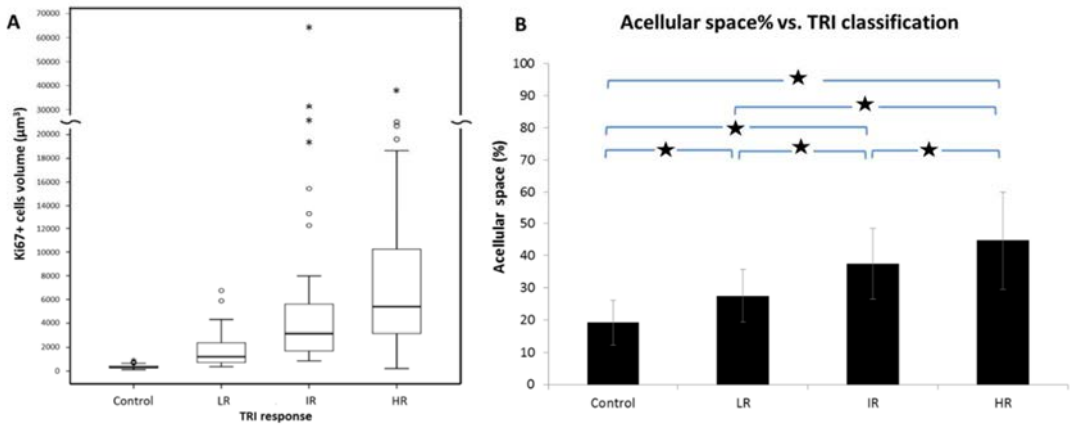

Figure 6.17: A. Boxplot of volume of Ki67 positive cells in each TRI group (cells were analyzed in one representative field of each of the following cases: 2 HR, 1 LR, 3 IR and 2 control, and the volumes found were represented in boxplot format). Ki67 positive cells showed a smaller volume in control than in treated cases; and in treated cases, bigger cells were observed as increase in TRI response was observed. Outliers (values higher than 1.5 X IQR, interquartile range, obtained by difference of Q3 and Q1) are represented with round symbols and * represent extreme outliers. B. Representation of percentage of acellular spaces observed in different TRI groups, an increase in such acellular spaces was observed in treated cases, the more TRI response classification, the more acellular spaces were observed. stars = $p<0.05$ with Mann-Whitney's U test.

These acellular spaces are large, irregular and they are usually observed in the central part of treated tumours which indicates that they were caused by therapy with temozolomide and not by tissue fixation and processing. In case of acellular spaces due to tissue fixation, those spaces are usually observed in the tumour periphery at the border zone between tumour and normal brain parenchyma.

Therefore, control (untreated) cases showed smaller cell volumes of Ki67 positive stained cells, and also much less acellular space than treated cases, resulting in fields with high average cellularity. On the other hand, in treated cases, the increase in response level (TRI values) was accompanied by an increase in cell volume (with presence of giant cells) and a higher presence of acellular space in histological fields. Accordingly, the difference in cell volume and percentage of acellular space in the evaluated histopathological fields could partially explain why an apparently high Ki67 value is found in HR cases if a standard percent counting is performed. It

may be more adequate to analyse results the way shown in Figure 6.16, for which the number of Ki67 stained cells is seen to significantly decrease between control, LR and IR+HR cases.

To illustrate the cellular elements used to calculate data shown in Figure 6.17, representative fields of control, LR, IR and HR cases are depicted in Figure 6.18. In control cases, uniform smaller cells and fewer acellular spaces were observed in comparison with treated cases. In those treated cases, with higher TRI response levels, cell morphology changed with presence of giant cells and an increase in acellular space (white spaces shown in Figure 6.18).

An interesting additional finding was that in IR and HR cases, small lymphocyte-like cells were observed (red arrows in Figure 6.18), which would be compatible with tumour infiltration by lymphocytes, and a full validation procedure for immune system population characterization is being currently performed in the group, with preliminary results supporting this hypothesis. These lymphocyte-like cells were not observed in LR and control cases.

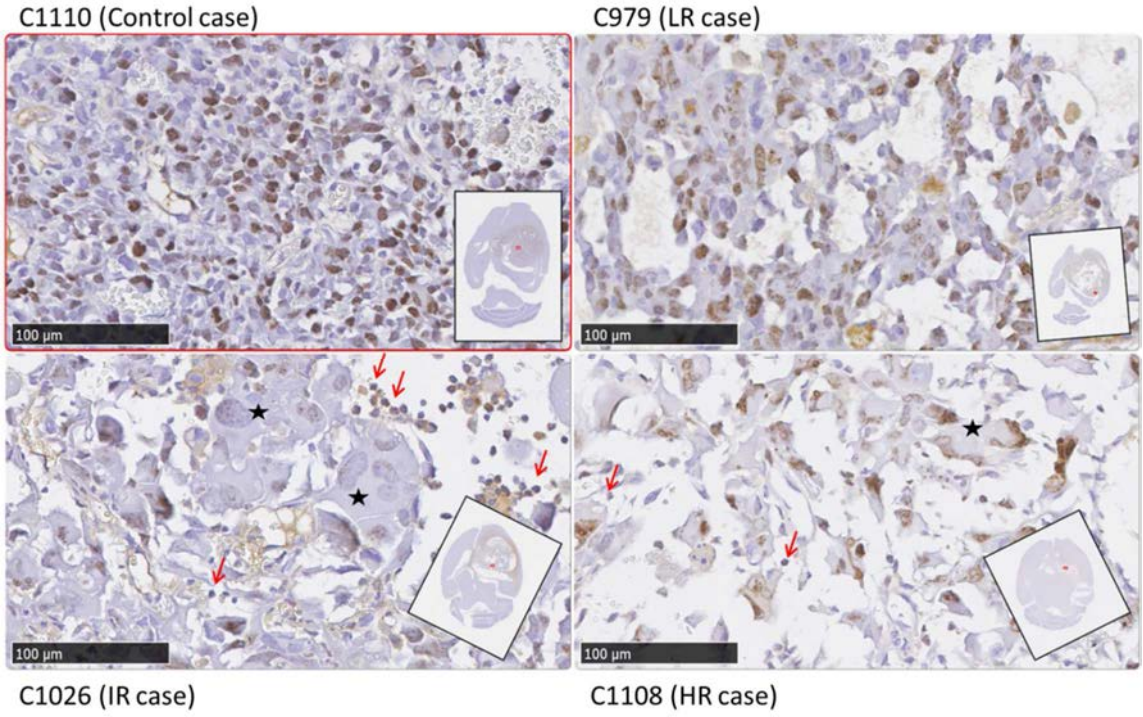

Figure 6.18: Histopathological regions (20x magnification) from representative fields of control, LR, IR and HR cases. A higher number of uniform and small tumoural cells were observed in the control case in comparison to LR, IR and HR cases. A low number of large tumoural cells were observed in treated cases (with many of them possibly converting to giant cells in IR and HR cases). Regarding acellular spaces, in control cases, cells were more densely organized and few such spaces were observed. On the other hand, in treated cases, especially HR cases, the percentage of acellular space was significantly higher (see also Figure 6.17). In IR and HR cases, numerous lymphocyte-like cells (red arrows) and giant cells (black stars) were also observed.

It is worth stressing that obtaining HR cases was not straightforward and required modifications of the initially designed protocol. Even when modifications were introduced, and this is one of the relevant findings in this study, the metabolomics-based analysis of multi-slice MRSI showed that there were no 100% responding tumours in our hands, reinforcing the idea that GBs present high heterogeneity, probably with clonal selection of resistant cells after therapy administration. The use of combined therapeutic agents, as well as modified administration schedules such as metronomic administration, could be of help, since promising results have been recently obtained in our group with the same preclinical GB model [285], and these studies are currently in progress.

In this multi-slice study, in which a tridimensional-like reconstruction approach was attempted, it was possible to establish a relationship between groups of cases with different TRI levels and Ki67 values. The global analysis case by case of multi-slice acquisitions can provide a good estimation of the response level of the whole tumour probably better than using the single slice approach, which could provide an overoptimistic outcome. The reason for this being that the slice used for single slice protocol usually corresponded to the Grid 2 in the multi-slice protocol, and as previously stated, most of the pixels identified as 'responding pattern' were located in Grids 1 and 2. In this sense, the multi-slice approach provided a more realistic analysis while the inverse correlation found between TRI and the Ki67 "global" value (see for example Figures 6.12 and 6.16) confirmed the findings from previous work of our group [117].

6.4.4 A possible explanation for the oscillatory TRI behaviour: TMZ therapy triggering immune response in host

From previous and present data from our group, TRI has been proven to follow a non-linear behaviour, with an oscillating pattern, which was intuitive in single-slice cases from [117] but became clear in the multi-slice recordings of mice in this work. This is suggesting that the metabolomic pattern changes are dynamic and vary along time. They not only vary among different cases, but they vary inside the same tumour as well, indicating a differential behaviour which seems to display an apparent frequency of ca. 5-7 days. One of the possible explanations for that lies in the mechanism of cell damage triggered by TMZ. Some authors have described that after alkylating agents (e.g. TMZ) treatment a recruitment of the host immune system takes place [67, 286] which is relevant in the response to therapy, eventually triggering tumour cell death. Still, it is described in [52] that the whole immune cycle (see Figure 6.19) in mice brain usually requires around 6 days, which agrees with the oscillation period recorded in this work (see Figure 6.5). The process includes recognition of local antigens by antigen presenting cells (APCs), migration to regional lymph nodes, where they present processed tumour-derived

peptides to naïve CD8+ and CD4+ T cells, which leave afterwards lymphoid organs to infiltrate tumour tissues and exert effector functions, killing tumour cells direct or indirectly.

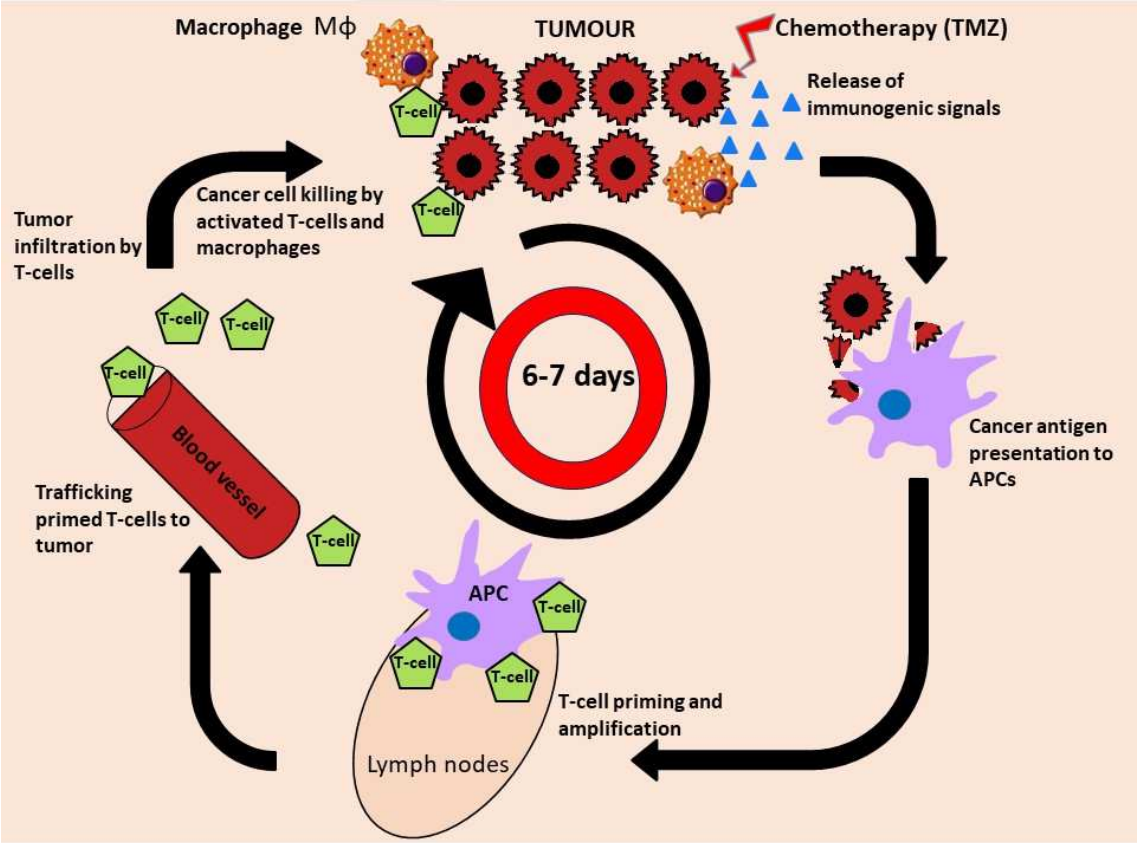

Figure 6.19: Scheme of the cycle for immune response against a brain tumour. The whole cycle in mouse brain is assumed to take around 6-7 days [52]. The malignant cells may release immunogenic signals, after the chemotherapeutic agent (TMZ) effect on them. These signals attract antigen presenting cells (APCs) precursors to the tumour, were they are activated by compromised tumour cells. Then, activated APCs migrate to local lymph nodes (LN), like dorsal cervical lymph node for brain, and present processed tumour-derived peptides to naïve T and B-lymphocytes. In case of antigen match, they are then activated to become plasma cells producing antibodies, CD4+ helper T lymphocytes or CD8+ T lymphocytes. Those CD8+ lymphocytes leave LN to infiltrate brain tumour tissues become activated cytotoxic T lymphocytes (CTLs) and exert effector functions, killing tumour cells either direct or indirectly [49, 287].

All this taken into account suggests that the metabolomics responding pattern could act as a surrogate biomarker of these immune cell "waves" killing sensitive tumour cells. Preliminary findings of infiltrative cells compatible with lymphocytes (Figure 6.18), seen in IR and HR cases, would agree with this interpretation. Nevertheless, further histopathological validation is being currently performed to fully confirm the identity of these cells and their possible contribution to the recorded metabolic pattern. In case of some immunostainings for microglia/macrophages, these could represent up to 30-40% of tumour zone ([50] and preliminary GABRMN results not shown in this thesis), suggesting that their contribution to the metabolomic pattern could not be neglected. The rich information contained in these oscillatory metabolomics pattern changes

is discrepant with the lack of tumour volume changes during the growth arrest phase. New "repopulation" of the tumour mass with actively proliferating GL261 cells with new clonal characteristics may cause the oscillating peaks of non-responding tumour (red pixels). The initially activated $CD8^+$ T cells would not be effective against those new sub-clones of GL261 cells and another cycle of cell priming and new CTL clones activation would be required.

The participation of the immune system in the response to therapy has been widely described by different authors [288, 289] and GBs are known to exhibit varying degrees of infiltration with mononuclear cells, consisting primarily of T-lymphocytes, reinforcing the idea of a cell-mediated immune response [290] although these tumours are also known to secrete a number of immunosuppressive factors. This intratumoural infiltration with CD4+ and CD8+ T cells was also seen in preclinical glioblastoma (GL26 glioma- bearing C57BL/6J mice) after immunomodulatory treatment [291]. The described GB infiltration with T-lymphocytes and other immune system elements and changes in macrophage polarization, on the other hand, could be a likely explanation for the appearance of green, responding pixels even in nosological images of mice which did not receive treatment.

Other evidences also support the hypothesis of the immune system participation in response to therapy. For example, the use of a metronomic scheme of therapy administration, optimized in order to activate host immune responses, has been used with excellent results in ectopic GL261 preclinical models [286] even producing the cure of animals, as well as inducing long-term immune memory against the tumour. Authors in [286] used a 6-day interleave period for therapy administration (cyclophosphamide), demostrating that this interval was optimal in their case for improving the immune system participation. Metronomic administration, usually referring to administrations of low and equally spaced doses of chemotherapeutics without long rest periods in between [67, 286] has been used to improve immune responses to potentiate tumour regression and avoid regrowth [286]. Our group has also used this scheme in work reported in [285], obtaining a survival time slightly higher (38.7±2.7 days, n=6) than the traditional scheme with 3 cycles [90] used in the present work (5-2-2 days with a 3 day interleave between them (33.9±11.7 days, n=38). Still, work reported in [285] highlighted the relevance of the metronomic strategy in comparison with traditional administration schemes in which results suggested an impairment of the immune system related response due to continuous therapy administration, probably interfering with T-cell amplification.

It is important to remark that the 5-2-2 cycle therapy does not follow a metronomic schedule, although data in Figure 6.5 clearly show a close to 6-day oscillation of "responding pixels"

percentage. On the other hand, data gathered in [90] showed that a single cycle of TMZ during 5 days did not produce any improvement in animal survival (20.6 ± 6.8 days for 1 TMZ cycle vs 20.5 ± 4.1 days for control animals). It was only when the 2 additional cycles were introduced with a 3-day interleave between them that the survival rate increased significantly to 33.8 ± 8.7 days. The interleave between the middle time point of each cycle is of 6 days between the first and second cycle, and 5 days between the second and third cycle, which could have contributed to configure a "metronomic-like" therapeutic scheme, favouring the host immune system participation in response to therapy in our present study. Nevertheless, it is also possible that the duration of the first TMZ cycle (5 days) partially prevented the full immune cycle recruiting, with a balance between favourable and unfavourable conditions. The sub-optimal length of TMZ administration could trigger cell damage in tumour cells but also in proliferating primed $CD8^+$ lymphocytes in the lymph nodes, which should later infiltrate the tumour. Accordingly, the second "response" peak (seen after the second therapy cycle in Figure 6.5) would be a mixture of new immune system attraction through immunogenic signalling caused by the previous TMZ treatment, and a wave of the remaining $CD8^+$ lymphocytes not compromised by TMZ administration. Further work will be needed in this sense: if the 6-7-day cycle for immune system activation is proven correct in our GB preclinical system, an adjustment of cycles should be done and the interleave between the first and second cycles should be 6-7 days for future work, as well as a shortening of the first cycle to a single administration to avoid interfering with T-cell amplification. This is currently being studied in our group.

In addition, in order to fully characterize the immune system cells differentially present in responding and non-responding zones (red and green patterns in nosological imaging), additional immunostaining methods may be attempted, such as CD8a and FoxP3 as described in [51] and also CD3 [292] and Iba-1 immunostainings [293], as well as extensive profiling of the infiltrating immune system cells as suggested by [294]. This would be of help to better understand potential contributors to the metabolomics pattern of responding and non-responding tumour zones. Last, but not least, the nosological images here described could be of relevance to design personalized therapeutic schemes, being able to detect when a tumour starts failing to respond to a first line therapy, providing a time frame for considering a second line or a combination therapy approach.

6.5 Conclusions

1. A volumetric, 3D-like MRSI analysis has been applied to a cohort of GL261 GB tumour-bearing mice either control GL261-bearing GB or under TMZ treatment. In addition, pattern recognition using semisupervised source analysis could be successfully applied to the whole set of MRSI grids and nosological images could be generated with the standard protocol previously developed in our group. This allowed us to gain more insight into the GB heterogeneity during response to TMZ therapy.
2. We have established the parameter TRI, Tumour Responding Index, which allowed an estimation of the response level in the whole tumour taking into account the percentage of responding pixels detected. This parameter was calculated in the studied mice and those were categorized within arbitrary cut-off values: low response, intermediate response and high response.
3. Only low response cases (TRI<35%) and partial response cases (TRI=35-65%) were obtained with the standard GABRMN therapy cycle. A further modification of the protocol consisting in starting therapy with smaller tumours (2.5-5.5mm^3) was needed in order to obtain “high response” cases.
4. Histopathological studies with global Ki67 confirmed results from previous work from our group in which an inverse correlation was seen between the responding level (TRI) and Ki67 proliferation rate. Still, we could break down responding cases in different response levels calculated from nosological imaging which, accordingly, were related to global Ki67 for each of those cases. However, a word of caution should be raised when interpreting Ki67 data from cases with widely different cell morphology and cellular volume, as this could cause an apparent mismatch between Ki67 and metabolomics data producing nosological images. In this sense, we showed that measuring the number of Ki67 cells/mm^2 is a more adequate parameter to use instead of the percentage of Ki67.
5. TRI presented an oscillatory pattern with peak maxima every 6-7 days, as opposed to tumour volume changes, which were maintained essentially stable or slightly decreased during the response therapy period. There are evidences that suggested an oscillating pattern with single slice MRSI cases, analysed retrospectively. This 6-7 day oscillation would be in agreement with host immune system recruitment for therapy response in our experimental GB model. This is also supported by histopathological findings of lymphocyte-like cells infiltrating IR and HR cases but not observed in LR and control cases. Further work on infiltrating immune cells characterization is currently in progress and will allow to confirm or discard this hypothesis.

6. TRI analysis would be a robust method to gather information about response to therapy, due to the heterogeneity of GB tumours. The analysis of a single slice would hinder us to obtain relevant information of the whole tumour. Still, if histopathological analysis confirms that the green voxels are related to the immune system cells presence/action in tumours, this would be of great interest to take into account in the planification of chemotherapeutic treatment cycles, i.e. to optimize administration of therapeutic agent whenever signs of productive immune system attack disappear, pointing to the appearance of now, resisting clones.
7. Volumetric-nosological maps could be drawn to represent whole tumour information regarding therapy response. However, it is clear that further and more detailed work is needed in order to reach a more intuitive representation which could have fast translational potential.

7. Development of a system for Hyperthermia with Gold nanoparticles for preclinical GB therapy

Glioblastomas are highly heterogeneous and invasive tumours, with a poor prognosis. The survival rates for glioblastoma are low, with a median survival of 14.6 months even when aggressive therapy is applied [8], and second line therapies do not really improve patient overall survival [43, 44]). Even after best available therapy, relapse is the norm, probably arising from resistant clones which can repopulate the tumour. Having this in mind, there is an urgent need of new therapies which could be applied once glioblastoma resistance to initial treatment is detected. Hyperthermia has been described in preclinical studies with different tumour types [178, 191–193] and the collaboration with *Instituto de Nanociencia de Aragón* (INA) at *Universidad de Zaragoza* allowed us to design an experimental path for choosing and testing gold-based nanoparticles for hyperthermia therapy in our preclinical GB model. It is worth mentioning that part of the results reported in this chapter were produced by other GABRMN members before the starting of this thesis and this will be properly indicated in the corresponding sections. However, they were not described in previous theses and will be summarized here in order to provide proper context for the additional hyperthermia-related work.

7.1 Specific objectives

The main goal of this chapter was to set up a hyperthermia protocol for preclinical GB therapy with gold nanoparticles (Gold NPs) administration, to be used as an alternative therapy or superimposed to the standard treatment. In preliminary studies, different types of gold nanoparticles were investigated in *vitro* in order to select the best nanoparticle to be used in the *in vivo* hyperthermia studies. Simultaneously, a NIR laser set-up for irradiation inside the MR scanner was developed for mouse brain irradiation, in which tissue temperature changes were monitored by MRS.

7.2 Specific materials and methods

7.2.1 Preliminary studies: performed before the starting of this thesis

7.2.1.1 Nanoparticles studied

The Gold NPs investigated in this chapter were synthesized by the Nanostructured Films and Particles group (IP Dr. Jesús Santamaría), from *Instituto de Nanociencia de Aragón* (INA) at *Universidad de Zaragoza*. Two types of NPs were studied: Hollow Gold Nanospheres (HGNPs) (non-PEGylated and PEGylated) and PEGylated Gold Nanorods (NRs). The basic initial

characterization was performed by providers and consisted of Transmission Electron Microscopy and NIR absorbance spectrum, among other parameters (see below).

The **HGNPs** are composed by a thin gold shell with a hollow interior and display a strong resonance absorption peak tuneable in the NIR region. Two types of HGNPs were used:

- Non-PEGylated HGNPs (Batch 1) synthesized following the protocol described in [295]. The average described diameter of these HGNPs was 36 nm and the gold thickness 8 nm, as described in [296].
- PEGylated HGNPs (PEG-HGNPs) (Batch 2 and Batch 4) synthesized following the protocol described in [297]. They showed an average diameter of 40.5 nm and a gold thickness of 4.9 nm as described also in [297]. These HGNPs were coated with poly(ethylene glycol)methyl-ether- thiol (PEG), with a molecular weight (Mw) of 5,000 Da.

Regarding PEGylated **Gold NRs** (Batch 3), they are rod-shaped NPs which were synthetized as described in [298] and coated with PEG with a Mw of 10,000 Da. The dimensions of the long and short diameters of these NRs were ~60 nm and ~25 nm, respectively (measured by TEM).

Both HGNPs and NRs show a Surface Plasmon Resonance (SPR) around 800 nm, which means that are able to absorb Near Infrared Radiation (NIR) [296–298]. In the case of NRs, due to their anisotropy, they show two SPR peaks corresponding to the longitudinal (~800 nm) and transverse (~570 nm) plasmon bands [298] (please refer to Annex IV for data and figures from this preliminary characterization of the supplied nanoparticles).

7.2.1.2 Set up of NIR (808 nm) laser device for irradiation inside the MR scanner

The NIR Laser System employed in the hyperthermia studies consisted of an 808 nm wavelength laser diode coupled to a power controller (Model PD300- 3W, Ophir Laser Measurement Group, Logan, UT, USA) and an optical fibre of 400 µm in diameter (Optilas model MDL-III-808-2W, Changchun New Industries Optoelectronics Technology Co., Ltd., Changchun, China) shown in Figure 7.1.A (green square). The optical fibre was extended (length of 6 m) allowing to conduct light from the diode to the MR scanner (Figure 7.1.B) in order to irradiate the mouse brain inside such scanner. The distance between the optical fiber tip and the animal brain was ca. 0.5 cm. This system could be used in a "**continuous**" or "**pulsed**" laser mode. In case of the pulsed laser, an extra device (home built) was needed in order to generate the laser pulses controlling the duty cycle[6] (Figure 7.1.A, black arrow).

[6] Duty cycle is the time fraction in which the laser signal is active (10% duty cycle means that in one second interval, the laser is on during 100 ms and off during 900 ms).

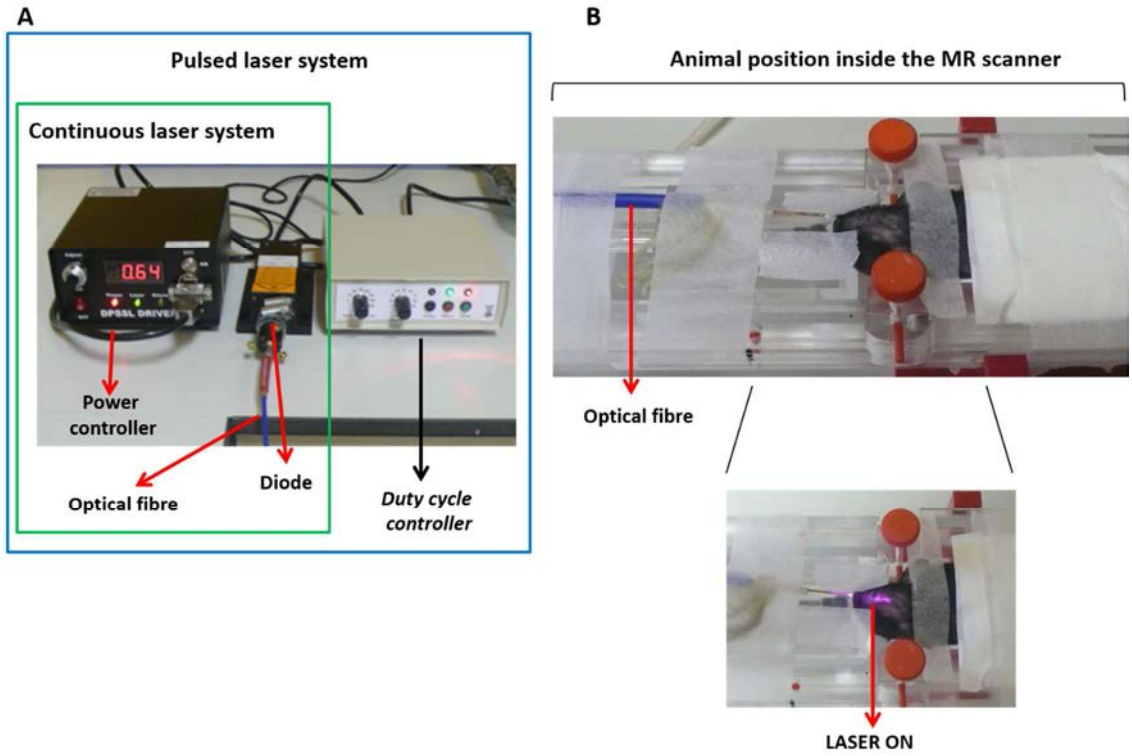

Figure 7.1: Hyperthermia laser set-up (continuous and pulsed modes). A: Green square: continuous laser system devices: laser diode coupled to a power controller and an optical fiber (indicated by red arrows). Blue square: continuous laser system plus a home built duty cycle control device (black arrow) for pulsed laser experiments. B: Animal position for hyperthermia laser irradiation inside the MR scanner. In the upper image, the optical fiber position is indicated by a red arrow (the laser is off). The bottom image shows the same animal when is being irradiated (the laser is on).

7.2.1.3 In vitro and in vivo temperature measurement by MRS (I)

The temperature evolution during the hyperthermia experiments was calculated using either Single Voxel (SV) MRS or MRSI, and was performed both in phantoms (*in vitro* experiments) and mice brain (*ex vivo/in vivo* experiments).

MRS experiments were performed using long TE (136 ms) SV spectra using PRESS localization and VAPOR water attenuation sequences. The voxel size was 2- 3 mm^3 and the parameters were: SW, 4006.41 Hz; TR, 2500 ms. The NA and TAT were variable according to the experiment (ranging 8 - 128 for NA and 0.5 min - 5 min 30 s for TAT).

In vivo SV MRS spectra were processed with TopSpin v1.3 software (Bruker Daltonik, GmbH): Lorentzian filter with 4 Hz of line broadening was applied before Fourier transformation, followed by manual zero- and first-order phase correction and chemical shift referencing to total creatine (3.03 ppm).

In order to calculate the temperature in the voxel, the distance (in ppm) between water and Cho peaks was measured. Then, the temperature was calculated using Equation 7.1. as described in

[116], where *Dist water-Cho* indicates the distance in ppm between the water and choline signals:

$$Temperature\ (°C) = -82.33\ x\ ((Dist\ water - Cho) + 1.21) + 255.94 \qquad \textbf{Equation 7.1}$$

Regarding **MRSI**, long TE (136 ms) acquisitions were performed in order to obtain temperature maps of the whole mouse brain pre- and post-laser irradiation. Acquisition parameters were essentially the same as described for the standard MRSI in material and methods section 3.5.2 , except by the following: TE, 136 ms; VOI, 8.8 x 8.8 x 1.0 mm, matrix size of 16 x16 and TAT, 21 min 20 s.

MRSI acquisitions were processed using DMPM module described in material and methods section 3.6.2. This module contains a temperature maps sub-routine which allows to calculate the temperature in each voxel of the MRSI grids using the Equation 7.1 and displays the result as colour-coded maps.

7.2.1.4 Hyperthermia experiments in vitro

In vitro hyperthermia experiments were performed using phantoms of PBS-dissolved NPs. Phantoms consisted of glass high resolution NMR tubes of 10 mm of diameter filled with 5 ml of the NP solution. Moreover, an insert was placed inside the tubes in order to avoid the formation of air bubbles and allow horizontal placement inside the MR scanner (similar orientation to mouse body in Figure 7.1).

The NPs concentrations used in the experiment were as indicated by providers:

- **HGNPs (non-PEGylated)** (Batch 1): 0.056 mg Au/ml.
- **NRs** (Batch 3): 0.51 mg Au/ml.

A phantom containing only PBS was used as a control without NPs. PEG-HGNPs were not available when the *in vitro* experiments started and, accordingly, were not assayed *in vitro*.

Laser irradiation protocol and temperature control

Phantom irradiation (preliminary studies)

The phantom tubes were irradiated inside the MR scanner using continuous laser with a power of 1.3 W. To perform temperature measurements, SV MRS spectra were acquired at different time frames, with and without laser irradiation as indicated in Figure 7.2. The total laser irradiation time was 3 min and 30 s. The SV parameters used for *in vitro* experiments were: VOI, 2 mm^3; NA, 8 and TAT, 30 s.

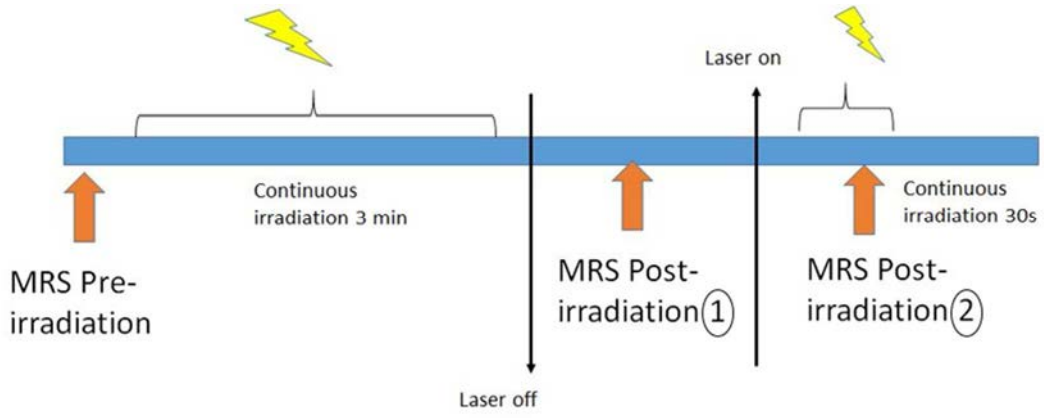

Figure 7.2: Design of a continuous NIR laser irradiation protocol for NP-phantom studies. See section 7.3.1.1 and Table 7.2 for further details.

Temperature evolution of a HGNPs phantom along an irradiation experiment

The phantom containing non-PEGylated HGNPs was also used to measure the temperature evolution under laser irradiation. One SV was acquired before irradiation and then SV spectra were consecutively acquired during 30 minutes of irradiation with the same power (1.3W). The SV parameters used for *in vitro* experiments were: VOI, 2 mm^3; NA, 8 and TAT of each SV, 30 s.

7.2.1.5 Hyperthermia experiments ex vivo

C57BL/6J wt female mice (n=11) of 14 weeks of age were euthanized with an overdose of intraperitoneal sodium pentobarbital (200 mg/kg, Vetoquinol, Madrid, Spain). Then, animals were stereotactically injected with non-PEGylated HGNPs dissolved in 4 µl of PBS at different concentrations in the *striatum* of mice brain (as described in material and methods section 3.2.3, and relying on values described in the literature [193]). Table 7.1 lists the NPs concentration as well as number of animals in each group.

Table 7.1: Different groups of animals injected with non-PEGylated HGNPs *ex vivo*.

	Number of animals	**NPs dose (mg Au/kg of mouse)**
Non-pegylated HGNPs	n= 3	0.00056
	n= 3	0.0056
	n= 3	0.56
PBS (Control)	n= 2	-

Laser irradiation protocol and temperature follow-up during the *ex vivo* experiment

Each euthanized mouse was irradiated using a continuous laser protocol with a power of 1.3 W. The SV MRS spectra were acquired in the ipsilateral and contralateral areas (see Figure 7.3),

starting with one SV in each area before laser irradiation and then, proceeding to alternating ipsilateral and contralateral acquisition of SV MRS during 30 minutes of laser irradiation. The parameters used for *ex vivo* SV were: VOI, 2.5 mm^3; NA, 128 and TAT, 5 min and 30 s.

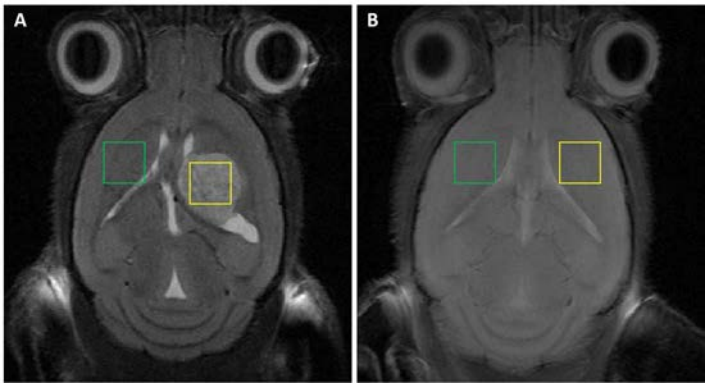

Figure 7.3: Example of voxel position in SV MRS hyperthermia experiments. **A**: T_{2w} image of a GL261 bearing mouse. **B**: T_{2w} image of a wt mouse. Yellow squares represent a voxel placed in the tumour area in A and in the equivalent area in a wt mouse (ipsilateral) in B. Green squares represent a voxel placed in the contralateral area in A and B images. Since there is no tumour in B, in this context "contralateral" is used to indicate the similar brain area in tumour-bearing mice.

7.2.1.6 Hyperthermia experiments in vivo

Several experiments were performed in order to properly assess the effects of laser power/laser protocol and starting body temperature (normothermia or hypothermia) over the temperature changes observed. Normothermia was defined as a body temperature of 36-38°C and hypothermia as 30-32°C. Both wt and GL261 tumour-bearing mice were used in different protocol combinations as follows:

7.2.1.6.1 Continuous laser irradiation – single laser power

wt mice - normothermia

The wt mice (n=2, 14 weeks of age) were irradiated using a continuous laser protocol with a power of 0.7 W during 15 minutes[7]. Consecutive SV MRS were acquired in the area equivalent to GL261 cell injection in the preclinical model of GB, and also in the contralateral area. Three SV spectra were acquired before starting the laser irradiation and another three SV MRS were acquired during laser irradiation in each area. The specific SV parameters used for this experiment were: VOI, 2.5 mm^3; NA, 128 and TAT, 5 min and 30 s.

[7] It is worth noting that in vivo, the maximum laser power output achieved was 0.7 W, possibly because of power losses due to optic fibre deterioration.

7.2.1.6.2 Continuous laser irradiation – varying laser powers

wt mice - mild hypothermia

The wt mice (n=2, 14 weeks of age) were irradiated in 3 consecutive days using a continuous laser protocol. In each day, a different laser power was tested. The first day of irradiation, the power used was 0.07 W, the second day it was 0.28 W and the last day it was 0.49 W. Four SV MRS spectra were acquired before starting the laser irradiation and then, consecutive SV were acquired during 30-35 minutes of irradiation. The SV MRS spectra were acquired only in the area equivalent to GL261 cell injection in our preclinical GB model. The specific SV parameters used for this experiment were: VOI, 2.5 mm^3; NA, 32 and TAT, 1 min and 30 s.

GL261 tumour-bearing mice - mild hypothermia - HGNP injection

A continuous laser irradiation protocol similar to the one previously described for wt mice was applied in a first approach to GL261 tumour-bearing mice (n= 4), using 0.07W and 0.28 W laser powers during 20-30 minutes. In this case, SV MRS data were acquired in tumour and contralateral areas. GL261 tumours were generated as explained in section 3.2.2 and non-PEGylated HGNPs (Batch 1) were i.v. injected (100 µl) at a dose of 2.8mg Au/kg kg of mouse. The experimental design is summarized in Figure 7.4:

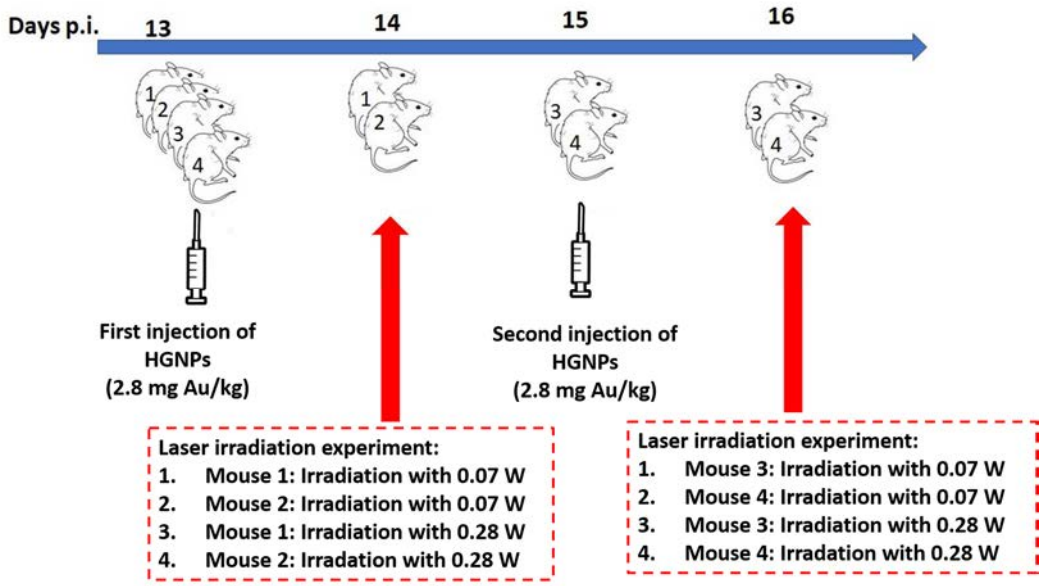

Figure 7.4: Scheme of a preliminary experiment with GL261 tumour-bearing mice using continuous NIR laser irradiation with different laser powers.

wt and GL261 tumour-bearing mice - normothermia - stepwise power increase approach

Mice wt (n=3) and GL261 tumour-bearing (n=3, day 11 p.i.) with no NP injection were irradiated using a continuous laser protocol of stepwise power increase approach (0.07, 0.14 and 0.21 W) during 85 minutes. In GL261 tumour-bearing mice, the voxel was placed in tumour area whereas

in wt mice, the area equivalent to the GL261 cell injection point in tumour-bearing mice was explored (see Figure 7.3). Four SV MRS spectra were acquired before starting the laser irradiation and 56 SV MRS were acquired during laser irradiation. The specific SV parameters used for each MRS acquisition were: VOI, 2.5 mm^3; NA, 32 and TAT, 1 min and 30 s.

In addition, wt mice (n=2) stereotactically injected with PEG-HGNPs (Batch 2) (as explained in section 3.2.3) with a dose of 20 mg Au/kg of mouse (the same dose used by authors in [178]) were also irradiated using the same protocol of stepwise power increase approach described in this subsection for wt and GL261 tumour-bearing mice.

7.2.1.6.3 Pulsed laser protocol

wt mice -normothermia

To investigate the effect of a pulsed laser protocol in brain temperature, wt mice (n=3) were irradiated during 75 minutes with the protocol shown in Figure 7.5. Four SV MRS were acquired before laser irradiation. Then, 7 to 12 SV MRS spectra were acquired in each step of irrradiation power/duty cycle combination, which resulted in 10-15 minutes of irradiation in each step. Voxel was placed in the area equivalent to GL261 cell injection in the GB model. The specific SV MRS parameters used for each MRS in this experiment were: VOI, 2.5 mm^3; NA, 32 and TAT, 1 min and 30 s.

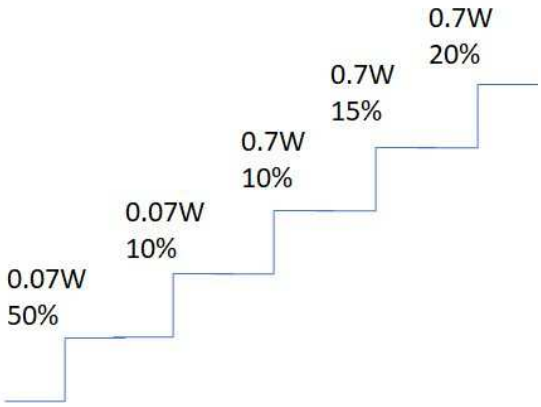

Figure 7.5: Design of pulsed protocol for laser increasing power applied to wt mice. Percentages indicate the percentage of duty cycle used in each step.

7.2.1.6.4 Specific hyperthermia studies using Nanorods (Batch 3)

The PEGylated Nanorods (NRs) (Batch 3) were used in a reduced set of experiments in which one of the questions to address was whether it was possible using the PEG MRS signal as an approach for tracking NR presence in mice brain, in addition to its potential for producing local heating.

wt mice – stereotactic injection

Mice (n=3) were stereotactically injected with NRs (as explained section 3.2.3) with a dose of 20 mg Au/kg of mouse. These animals were explored by SV MRS with the same parameters described in subsection 7.2.1.6.3 but without any laser irradiation.

Preliminary studies with GL261 tumour-bearing mice – i.v. injection

GL261 mice (n= 3) were i.v. injected (100 µl) at day 8 p.i. with NR doses equivalent to 20 mg Au/kg of mouse. One of these mice was reinjected at day 9 p.i. with a dose of 40 mg Au/kg of NRs.

Tolerability assessment in wt mice

Mice (n=6) were i.v. injected (100 µl) with a single administration of NRs. Two doses were tested: 10 mg Au/kg (n=3) and 20 mg Au/kg of mouse (n=3). All animals were followed up for 2 weeks for toxicity symptoms and their body weight was measured every 2 days. An additional observation was carried out 103 days after the first injection.

Hyperthermia experiment after i.v. injection

One GL261 tumour-bearing mouse was i.v. injected (100 µl) with a single dose of 20 mg Au/kg of mouse of NRs and irradiated using the same pulsed laser system protocol described in subsection 7.2.1.6.3.

MRSI temperature maps and temperature control during pulsed laser protocol

The same GL261 tumour-bearing mouse described in the previous sub-section was used for producing MRSI temperature maps for testing differential heating (MR parameters described in section 7.2.1.3). One MRSI was acquired before the irradiation (the irradiation protocol is shown in Figure 7.5). Then, SV MRS were acquired during 18 minutes using the pulsed laser protocol of irradiation. Finally, the second MRSI was acquired when the pulsed laser protocol was finished, but with the laser still on (power: 0.7W, duty cycle: 20%).

7.2.2 Studies performed in this thesis

The basic set of analyses for HGNPs characterization (particle size, UV-vis-NIR spectrophotometry, zeta potential) had already been performed by providers and hence, it was not repeated at this point.

7.2.2.1 Endotoxin assay of PEGylated HGNPs (Batch 4)

Detection of potential endotoxin contamination was carried out with an *Endotoxins kit assay* (Lonza, Switzerland) which follows the principles described in section 1.4.6.1. This analysis was performed by the INA group for the PEG-HGNP batch used for *in vivo* studies.

7.2.2.2 Confocal microscopy studies: nanoparticle internalization

Confocal microscopy studies were carried out with a Leica SP5 microscope (Leica, Germany) at the *Servei de Microscòpia* of the *Universitat Autònoma de Barcelona*. All experiments were performed using 35 mm Mat Tek dishes (Mat Tek, United States). 3D stacks of images were acquired along 10 µm in depth using a magnification of 63x. Image size was 164.02 µm x 164.02 µm with 0.3 µm of thickness. The number of pixels per image was 1024x1024 and the pixel size was 160.3x160.3 nm. Image processing and analysis was carried out using IMARIS software (BITPLANE, Switzerland). Confocal microscopy studies were performed for GL261 cells exposed to PEG-HGNPs.

GL261 cells exposed to PEG-HGNPs

In order to check whether the PEG-HNPs could be internalized by GL261 cells, a total of $8x10^3$ GL261 cells were cultured in RPMI medium in Mat Tek dishes (n=6). PEG-HGNPs (0.01 mg Au/ml) were added to 3 culture dishes whereas the remaining three were used as control. Confocal microscopy studies were carried out at 24, 48 and 72 hours after cell culturing. In each time point, one control and one PEG-HGNP incubated plates were observed in order to check if the cell-culturing time affected the PEG-HGNPs internalization.

Previous to the confocal microscopy study, the cell medium was replace with fresh RPMI medium and cells were stained with 2 dyes: Cell Mask (1 µl/ml), which is a cell membrane marker producing red colour, and Hoechst (0.5 µl/ml) which is a nuclear marker producing blue colour. In order to observe the blue-dyed nuclei, 405 nm wavelength was used for the excitation channel and 420-475 nm for the emission channel. For red-dyed cell membranes observation, 633 nm wavelength was used for the excitation channel and 650-775 nm for the emission channel. Finally, the reflection channel at 633 nm was used for PEG-HGNPs observation. Then, the number of HGNPs internalized by cells at different time points of study was estimated using the IMARIS software.

7.2.2.3 Influence of PEG-HGNPs in GL261 cell viability

The effect of the PEG-HGNPs in the viability of GL261 cells was studied by seeding $8x10^3$ GL261 cells in Mat Tek dishes (n=6) with RPMI medium. The PEG-HGNPs (0.01 mg Au/ml diluted in deionized water) were added to 3 dishes whereas the remaining 3 were used as control. Living and dead cells were counted 72 hours after NPs addition in control and in GL261 with PEG-HGNPs dishes, as described in section 3.1.2. Cell viability was calculated following Equation 7.2:

$$Cell\ viability\ (72\ h)(\%) = \frac{Number\ of\ living\ GL261\ cells}{Number\ of\ living\ GL261\ cells + Number\ of\ dead\ GL261\ cells}\ x\ 100 \qquad \textbf{Equation 7.2}$$

7.2.2.4 PEG-HGNPs in vivo tolerability studies

7.2.2.4.1 Dose calculation

Taking into account the PEG signal observed by SV-MRS in sterotactically injected mice (see results section 7.3.1.3.4: *Stereotactic injection in wt mice*), we have calculated the dose of PEG-HGNPs needed for i.v. injection in GL261 tumour-bearing mice allowing PEG MRS signal to be used as a marker of PEG-HGNPs presence. For this, different parameters were taken into account as the total blood volume, percentage of haematocrit [299, 300] and estimation of extracellular tumour matrix volume (50%, [301]). Having all these factors taken into account, a total amount of 8.12 mg of Au should be i.v. injected in order to be able to detect the MRS PEG (signal with SNR>10 [126]). This was equivalent to a dose of 406 mg Au/kg (considering a mouse of 20 g of weight). In order to assess whether this dose would be well tolerated by mice, a tolerability experiment was set.

7.2.2.4.2 Dose fractioning and protocol design

Since the dissolution of the calculated dose (406 mg Au/kg) was not feasible in 100 µl of physiological serum (0.9 % NaCl), a sequential approach with dose fractioning was designed in order to reach the final dose through administration along several consecutive days. For this, different doses of PEG-HGNPs ranging from 33.8 to 135.3 mg Au/kg were i.v. injected in wt mice in order to find the maximum tolerated dose (MTD). This would allow the estimation of the minimum fractioning suitable to achieve the cumulative dose of 406 mg Au/kg needed for PEG detection. Necropsy studies were performed at the Department of Medicine and Surgery at the Veterinary Faculty of the *Universitat Autònoma de Barcelona*.

7.3 Results and discussion

For a comprehensive understanding of the whole hyperthermia chapter, results and discussion will be divided in two major sections: the first one (section 7.3.1) regarding the set-up of the desired protocols and choosing of the most suitable NP, and the second one about the extensive studies related to the chosen NP (section 7.3.2).

7.3.1 Preliminary set-up of protocols and choosing the best NP

7.3.1.1 In vitro studies: which was the most promising NP for in vivo use?

The temperatures measured in the hyperthermia experiments using NP and control phantoms are shown in Table 7.2. The highest temperature value was obtained with the Gold Nanorods (Batch 3) phantom, reaching 34.9°C at the end of the experiment with a maximum increase of 9.2°C. In the case of non-PEGylated Hollow Gold Nanospheres (Batch 1), an increase of 6.8°C was observed. PBS also showed temperature increase (2.7°C) but it was always lower than the

temperature increase observed in NPs phantoms. Statistical significance was not evaluated due to the number of measurements (n=1 for each condition).

Table 7.2: Temperatures obtained with the different NP phantoms in *in vitro* hyperthermia studies. Post 1 is the temperature calculated 3 minutes after irradiation and turning the laser off; Post 2 is the temperature in the same study but irradiating while MRS was being acquired (30 s) after Post 1, resulting in a total time of irradiation of 3 minutes and 30 s. See Figure 7.2 for more details.

	Temperature (°C)		
	Pre-irradiation	Post-irradiation 1	Post-irradiation 2
Hollow Gold Nanospheres	24.7	28.6	31.4
Gold Nanorods	25.7	31.5	34.9
PBS (control)	25.5	26.8	28.2

The best nominal results were observed with gold NRs, but the required dissolution was difficult to achieve in PBS. Taking this into account, non-PEGylated Hollow Gold Nanospheres were selected to proceed with the *in vitro* verification. Figure 7.6 shows the temperature curve obtained using the non-PEGylated HGNPs phantom (n=1) after continuous laser irradiation at 1.3 W. The temperature increased from 22.7 °C (before turning on laser) to 37.3 °C after 30 minutes of continuous irradiation. A plateau in the temperature evolution was observed after 18 minutes of irradiation (purple ellipse). This temperature stabilization could be explained by convection currents present in the solution that may produce a refrigeration process through the walls of the phantom-tube due to the recirculating air at 20 °C inside the NMR scanner. Therefore, refrigerating mechanisms in the sample may have a strong effect in these experiments that may not have a direct equivalence in an in vivo environment.

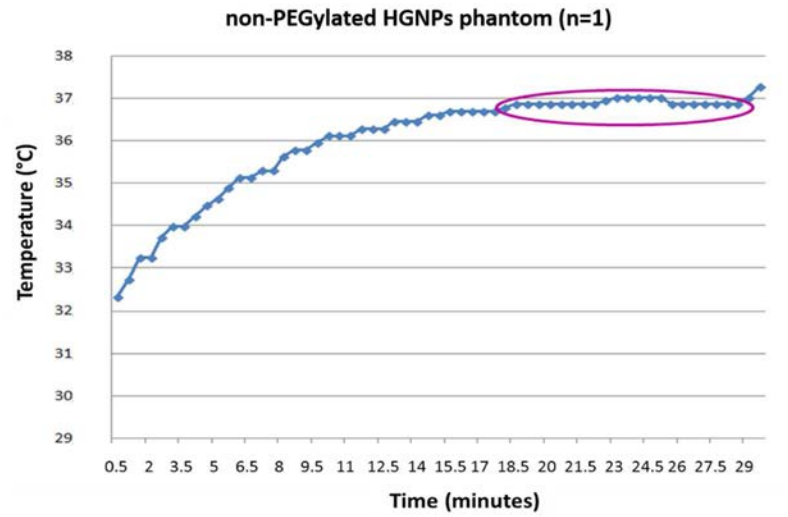

Figure 7.6: Temperature curve increase (measured by SV MRS) obtained with a 5 ml phantom with non-PEGylated HGNPs (0.056 mg Au/ml) after continuous laser exposition at 1.3 W. Temperature increased 14.6°C, from 22.7 °C (before turning on the laser, not shown in graph) to 37.3 °C in 30 minutes. However, the temperature reached a plateau after 18 minutes of irradiation (purple ellipse).

7.3.1.2 Ex vivo studies with non-PEGylated HGNPs (Batch 1)

In ex vivo studies performed with mice stereoactically injected with non-PEGylated HGNPs, significant differences ($p<0.05$) were found between the pre-irradiation temperature and the temperature at the end of the irradiation in the brain regions of all studied groups. No significant differences ($p>0.05$) were observed in temperature evolution between the injection area and the contralateral area of animals injected with the same dose of non-PEGylated HGNPs (Figure 7.7). Also, the temperature stabilization plateau was observed after 17.8±3.0 minutes of laser irradiation for contralateral and injection areas for all groups injected with either HGNPs or PBS.

In the case of the group injected with 0.00056 mg Au/kg of mouse (Figure 7.7.A), the mean temperature variation was 19.2±6.7°C and 21.4±8.9°C for contralateral and injection areas respectively. For mice injected with 0.0056 mg Au/kg of mouse (Figure 7.7.B), the mean temperature variation was of 22.0±2.1°C and 25.5±2.5°C and finally, in the case of mice injected with 0.56 mg Au/kg of mouse (Figure 7.7.C), the mean variation was of 21.7±1.7°C and 22.5±2.1°C for contralateral and injection areas, respectively. The animals injected with PBS (Figure 7.7.D), showed a mean temperature variation of 17.7±2.9°C both for contralateral and injection areas.

This could suggest that the basal effect of the laser heating hides any additional contribution of the injected NPs. However, in this case a word of caution is needed while interpreting the *ex vivo* studies, since euthanized animals were used for checking the performance of non-PEGylated HGNPs in an *in vivo*-like environment. *Ex vivo* experiments imply that the cooling

effect produced by continuous blood flow in living mice is not observed in this case [302], which could lead to a misinterpretation of the obtained results, perhaps preventing the detection of a potential differential heating between two chosen brain zones due to the presence of NPs.

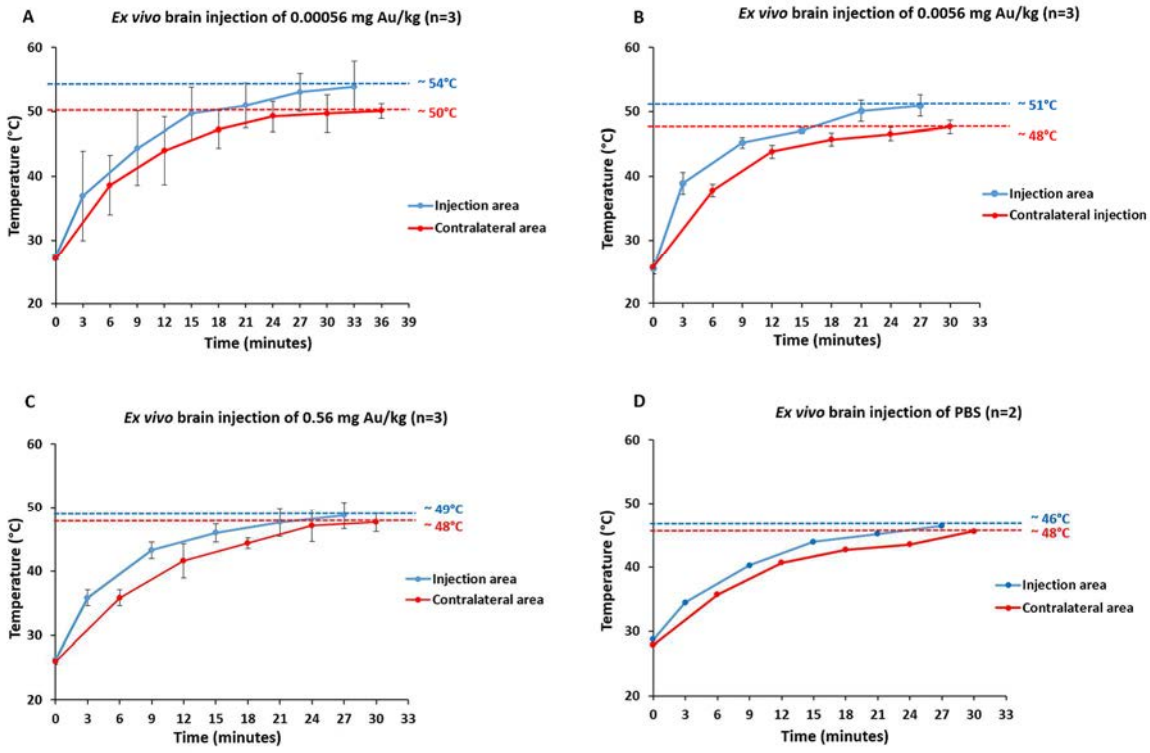

Figure 7.7: Temperature curves evolution (measured by SV MRS) (mean±SD) of injection area (blue) and contralateral area (red) in *ex vivo* brain HGNPs or PBS injections. A: Mice injected with a dose of 0.00056 mg Au/kg (n=3). B: Mice injected with a dose of 0.0056mg Au/kg (n=3). C: Mice injected with a dose of 0.56 mg Au/kg (n=3). D: Mice injected with PBS (n=2). Dotted lines represent the maximum value of temperature achieved in the injection area (blue) and contralateral area (red).

7.3.1.3 In vivo experiments: choosing laser protocol and power; checking for differential heating

As previously stated, the maximum laser power reached *in vivo* was 0.7W, possibly because of power-loss due to optic fibre wear. Accordingly, this was the highest power used for *in vivo* experiments. The main questions addressed in this subsection were the most suitable laser power to be used in the available range, and the better starting conditions for mice (normothermia or hypothermia). Finally, the potential differential heating due to nanoparticles in tumour-bearing animals was addressed.

Several conditions were tested in these set-up experiments. Continuous laser irradiation of wt mice with 0.7W laser power in normothermia resulted in temperature increases of 5.8°C and 3.7°C for ipsilateral and contralateral brain. However, mice (n=2) died during the experiment when the body temperature was 38.8°C and 39.7°C , while the measured brain temperature was

41.1°C and 42.7°C, respectively, in their ipsilateral laser-irradiated areas. It became clear that this protocol was not suitable for these experiments due to abrupt temperature increase followed by animal death whenever the brain temperature approaches 42-43°C. We wondered whether the use of a lower laser power and/or initial hypothermia conditions would be of interest in these protocols, due to the neuroprotective effect of hypothermia that has been described in other CNS diseases, such as traumatic brain injury, intracranial pressure elevation, stroke, subarachnoid haemorrhage and spinal cord injury [303].

The use of different laser powers in mild hypothermia in mice without HGNPs injection with wt mice (n=2) showed more encouraging results: maximum mean brain temperature achieved was 39.0±1.8°C, using a laser power of 0.28 W after 30 min of irradiation. This variation of laser power proved to work better than the previous protocol with 0.7W power and the next question to be addressed was whether this protocol could produce differential heating in case of tumour-bearing animals administered with non-PEGylated HGNPs.

7.3.1.3.1 Studies with continuous laser irradiation using different laser powers in mild hypothermia

Tumour-bearing mice with i.v. injection of non-pegylated HGNPs (Batch 1)

In order to better understand this subsection, please refer to Figure 7.4 for the experimental design. A group of animals was injected with non-PEGylated HGNPs, either one or two injections, followed by laser irradiation and MRS acquisition for temperature measurement to check for differential heating in tumour and contralateral brain.

One injection of non-PEGylated HGNPs

Two GL261 tumour-bearing mice (C742 and C743) were i.v. injected with one dose of 2.8 mg Au/kg of non-PEGylated HGNPs at day 13 p.i. and the following day they were irradiated with 0.07W and 0.28W (Figure 7.8). Temperature stabilization was observed in normal brain parenchyma 12 minutes after irradiation in both cases. Regarding the temperature observed in the tumours, only 3 temperature measurements inside the tumour were performed at the time points of 0, 9 and 18 minutes.

Even though the mice cohort was small for statistics robustness, it is worth noting that there was a difference of 4°C in the final normal parenchyma temperature between mice irradiated with 0.07W (33.2°C) and 0.28W (37.4°C). The slope was calculated in each graph from the beginning of the irradiation to the stabilization time point (12 minutes): a value of 0.16 was

found for mice irradiated with 0.07W, lower than values found for mice irradiated with 0.28W, which was 0.37.

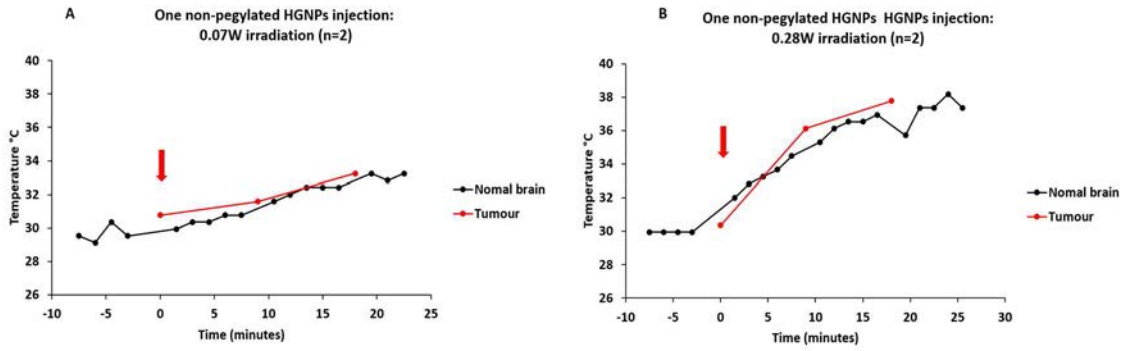

Figure 7.8: Mean temperature increase curves measured by SV MRS for two GL261 tumour-bearing mice (C742 and C743) irradiated after one injection of non-PEGylated HGNPs. Laser power was 0.07W and 0.28W in continuous laser protocol. The red arrow represents the starting of laser irradiation.

At this point, data suggested that a) 0.28W laser power produced slightly better heating results than 0.07W and b) at least at this HGNPs concentration and administration protocol used, no differential heating between tumour and contralateral brain was achieved. Moreover, the maximum temperature achieved inside the tumour did not reach the expected values that could lead to cell death, usually described to range between 42-47°C [304].

Two injections of HGNPs

Tumour-bearing mice C744 and C745 were i.v. injected with two doses of 2.8 mg Au/kg at days 13 and 15 p.i. (one injection each day) and laser-irradiated at day 16 p.i with 0.07 and 0.28W laser power (Figure 7.9). As for mice with single HGNPs injection, 3 temperature measurements inside the tumour were performed during the irradiation. There was a difference of 6°C between final temperature achieved in normal brain parenchyma with the irradiation using 0.07W (32.4°C) or 0.28W (38.2°C) laser power. Nevertheless, as opposed to animals receiving only one HGNPs dose, the temperature did not seem to stabilize in this experiment. The slope of temperature variations was calculated from the start of the irradiation until 12 minutes, in order to be comparable with the one-injection experiment. In this case, values were 0.13 for mice irradiated with 0.07W, and 0.30 for mice irradiated with 0.28W, 0.30 (similar to values obtained in mice injected with one injection of non-PEGylated HGNPs).

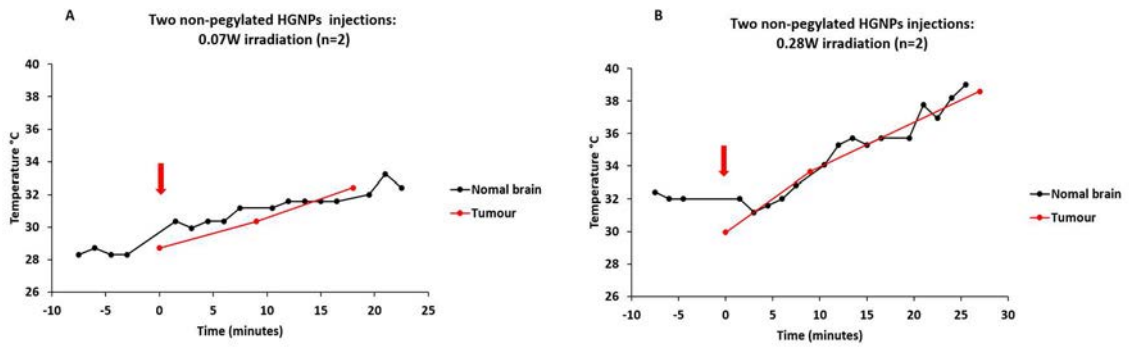

Figure 7.9: Mean temperature increase curves (measured by SV MRS) for two GL261 tumour-bearing mice (C744 and C745) irradiated after 2 injections of HGNPs; 0.07W and 0.28W laser irradiation in continuous laser protocol. The red arrow represents the starting of laser irradiation.

All the GL261 tumour-bearing animals studied survived to the laser irradiation experiments and did not show short-term toxic effects after the HGPNs injection. Nevertheless, temperature stabilization was not achieved using a power of 0.28W and differential heating was not observed between the normal brain parenchyma and the tumour. It was wondered whether this lack of differential heating between the tumour and normal brain tissue could be explained by the retention of the non-PEGylated HGNPs by EPR effect in the liver which has a portal vascular system including endothelial cells with vascular fenestration, reducing their blood circulation and accordingly, their arrival to the tumour [305]. This could be at least partially addressed with addition of PEG covering to nanoparticles (such as PEG-HGNPs which were synthesized by INA, or the use of PEGylated NR) [210]. However, the evolution of the contralateral brain temperature under laser irradiation was still a factor to be optimized.

7.3.1.3.2 Sequential increase of laser powers in normothermia

wt and GL261 tumour-bearing animals without HGNPs injection

The lack of temperature stabilization in experiments using a single laser power with hypothermia conditions lead us to wonder whether the difference between inputs of body and brain temperature could be relevant. If so, the use of initial normothermia conditions would be more suitable for additional experiments and, on the other hand, perhaps the use of increasing laser powers could lead to a more gradual brain temperature increase. For this, continuous laser irradiation was used in this first approach with 3 different laser powers: 0.07W, 0.14W and 0.21W being sequentially used. This new laser irradiation approach was tested in GL261 tumour-bearing animals (n=3), in which the temperature was measured by SV MRS in the tumour mass and in wt animals (n=3), in which the temperature was measured in the brain parenchyma equivalent to the injection area in a GL261 tumour-bearing mouse (Figure 7.10). No significant differences ($p>0.05$) were observed using UNIANOVA test in the temperature evolution between

wt brain temperature and tumour temperature in GL261 tumour-bearing mice. Moreover, no differences were obtained between the two groups ($p>0.05$, Student's t-test) for the temperature reached at the end of the study (41.6±2.1 °C for wt and 40.2±0.8 °C for GL261 tumour-bearing animals). All animals survived the laser irradiation experiment.

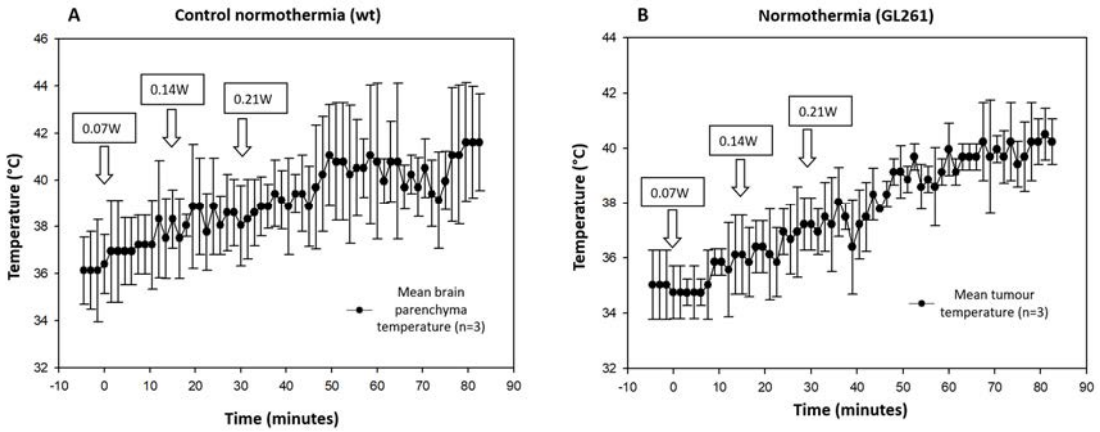

Figure 7.10: Evolution of brain temperature increase (mean ± SD) in animals irradiated by continuous laser irradiation combining 3 laser powers in the same irradiation: 0.07; 0.14 and 0.21W. A. control wt mice (n=3). B. GL261 mice (n=3). Slopes for temperature increase were 0.06 in A) and 0.08 in B).

The sequential increase of laser power seemed to produce a gradual increase in brain temperature in both wt and tumour-bearing mice, at least in non-injected animals, although temperature stabilization in lower values would be desirable. The next step was to attempt the injection of PEGylated nanoparticles (HGNPs and NRs) in an attempt to improve local accumulation in the tumour with differential heating with respect to contralateral and, if possible, exploit PEG MRS signal as a marker of nanoparticle presence within the tumour.

7.3.1.3.3 Hyperthermia experiments using PEGylated NPs with stepwise power increase approach

Stereotactic injection of PEG-HGNPs (Batch 2) in wt mice

Mice (n=2) were stereotactically injected with a dose of PEG-HGNPs equivalent to 20 mg Au/kg. They were then irradiated with the stepwise power increase approach previously described with 0.07, 0.14 and 0.21 W laser power. The temperature evolution of these 2 mice is shown in Figure 7.11 (A and B), as well as the obtained slopes (C and D) and an increasing trend was observed in the 2 injected mice. The mouse wt 35 showed a temperature slope of 0.24, which was clearly higher than slopes calculated for the non-injected mice in section 7.3.1.3.2: 3-fold higher than the slope of non-injected GL261 mice and 4-fold higher than the slope calculated for non-injected wt mice. The other injected case, wt 36, showed a lower temperature slope 0.12 (still higher than slopes obtained in non-injected subjects, showing a potential improvement in local

heating) – reaching a maximum temperature value of 41.1°C in wt35 and 43.5°C in wt36. The 2 animals survived to the irradiation experiment.

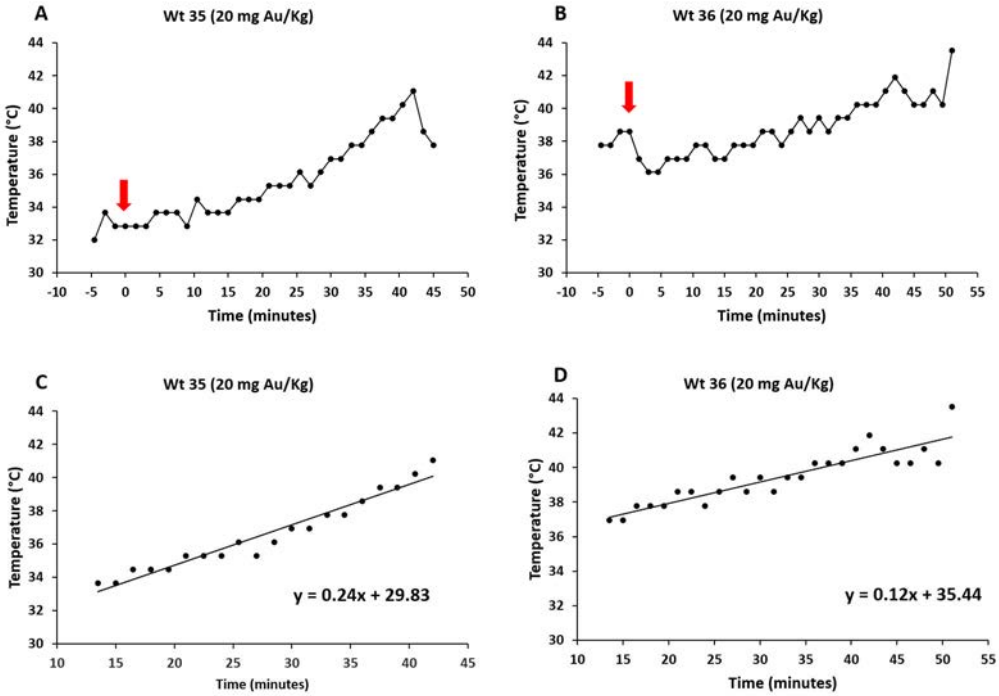

Figure 7.11: Evolution of brain temperature increase in the mice brain of two wt animals after stereotactical injection of PEG-HGNPs in the brain with a dose of 20 mg Au/kg. A and B show the evolution of brain temperature of wt35 and 36 respectively. C and D show the calculated temperature slopes for wt 35 and wt36 respectively. The red arrow represents the starting of laser irradiation.

This experiment also confirmed that the PEG signal could detected with excellent SNR at 3.71 ppm in SV MRS spectra of the brain parenchyma of wt mice stereotactically injected with the PEGylated nanoparticles (Figure 7.12). This information reinforces the potential of PEG signal as a potential marker of PEGylated-nanoparticles accumulation in the tumour.

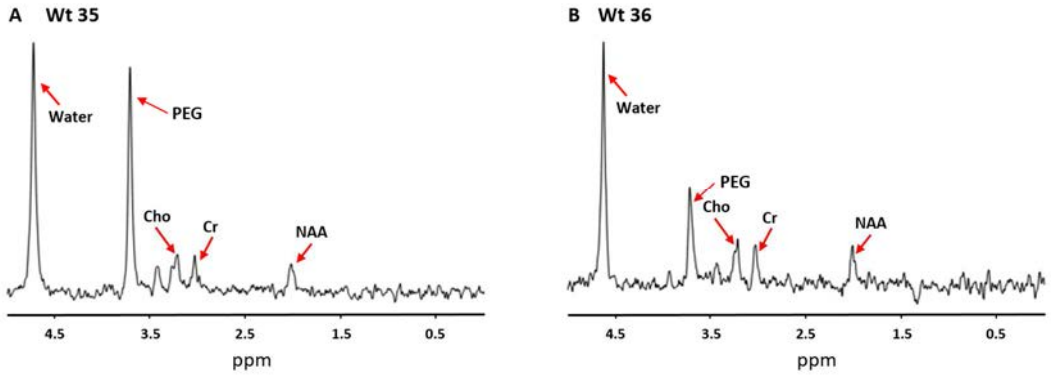

Figure 7.12: Example of SV spectra (TE=136 ms) acquired *in vivo* from the brain parenchyma of control mice injected stereotactically with 20 mg Au/Kg of PEG-HGNPs (A: wt 35. B: wt 36). PEG resonance peak at 3.71 ppm was observed (red arrow) in both spectra. Red arrows also point water and another observed metabolite peaks of Cho, Cr and NAA.

Additionally, the higher accumulation of nanoparticles in wt35, indicated by the higher apparent PEG/NAA ratio, would also agree with the higher heating slope for wt35 (0.24) vs wt36 (0.12).

7.3.1.3.4 Pulsed laser protocol in normothermia: pursuing better temperature stabilization

In this subsection, an optimization of a pulsed laser system instead of continuous irradiation is described. This was evaluated in order to produce a better stabilization of the brain temperature during the hyperthermia experiments. The pulsed laser protocol was applied to wt mice (n=3) without NP administration and results are shown in Figure 7.13. The combination of power and duty cycle parameters allowed a more progressive increase of brain temperature. A stabilization of brain temperature was observed between 60 and 80 minutes after irradiation and all irradiated mice survived the experiment. The average temperature obtained at the end of the experiment was 39.4±1.7°C.

Despite this apparently improved result, no significant differences were found neither in the temperature evolution, nor for temperatures reached at the end of the study or temperature slopes in comparison with mice irradiated with a continuous laser protocol (See Figure 7.14 for overall comparison). However, more gradual temperature increase was achieved, reinforcing the suitability of this protocol for application in future experiments with NP administration. See Annex IV for non-lethal temperature slopes data obtained in this chapter.

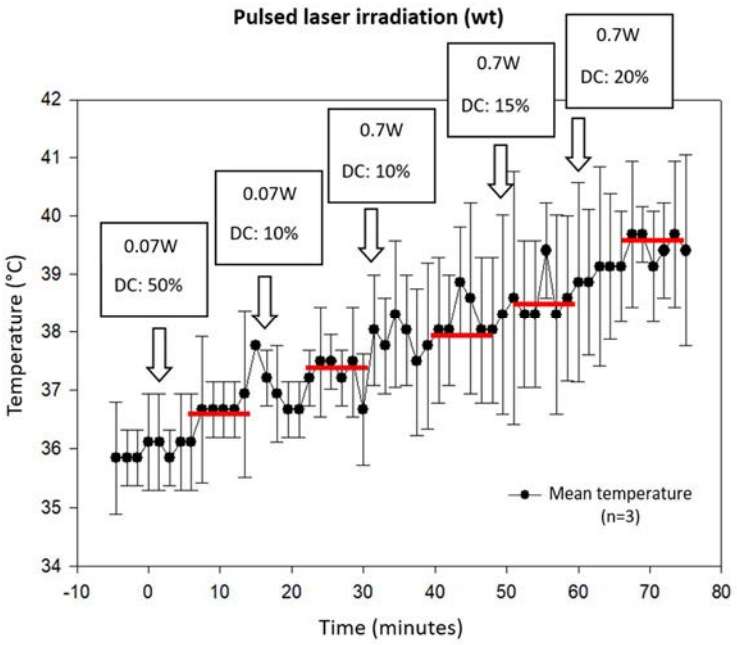

Figure 7.13: Temperature evolution (mean±SD) in 3 wt animals irradiated with a pulsed laser protocol. The combination of laser power and duty cycle (DC) made it possible to achieve a progressive increase in brain temperature. Red lines indicate the possible regions of temperature stabilization.

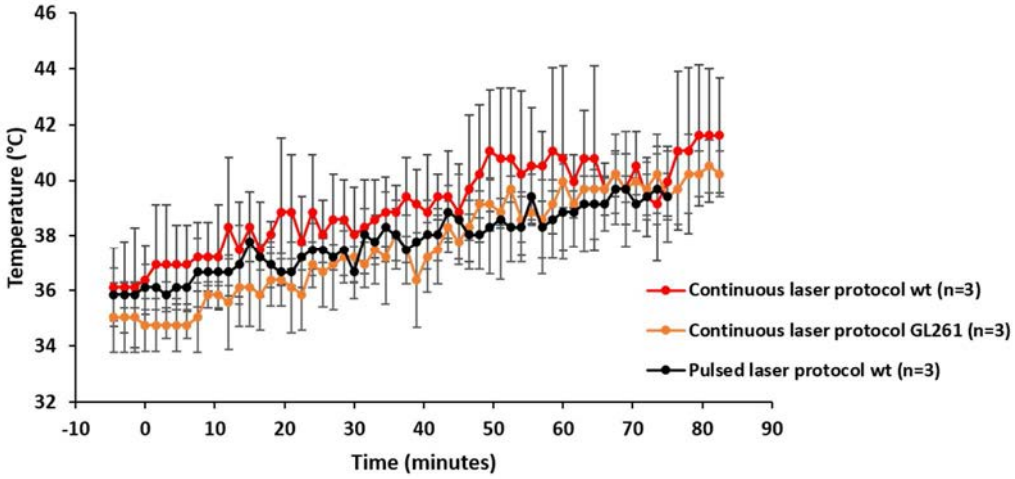

Figure 7.14: Temperature evolution (mean±SD) in the animals studied by continuous laser protocol irradiation: 3 wt animals (in red), 3 GL261 tumour-bearing mice (in orange) and in the 3 wt animals studied by pulsed laser irradiation protocol (in black). Non-significant differences were observed among the three studied groups ($p>0.05$).

7.3.1.3.5 Application of pulsed laser protocol to wt mice injected with PEGylated Nanorods (Batch 3)

Stereotactic injection and PEG signal detection

Although PEGylated Nanorods were initially discarded due to solubility issues, they were considered a reasonable option for the *in vivo* use of another type of PEGylated nanoparticle for evaluating differential heating between tumour and normal brain tissue in comparison with HGNPs.

Three wt mice were stereoactically injected with PEGylated Nanorods (PEG 5,000; 20mg Au/kg). In this first experiment, no irradiation took place: only SV MRS acquisitions to ensure that PEG signal peak was detected as in mice injected with PEG-HGNPs (see Figure 7.12 for PEG-HGNPs and 7.15 for NRs).

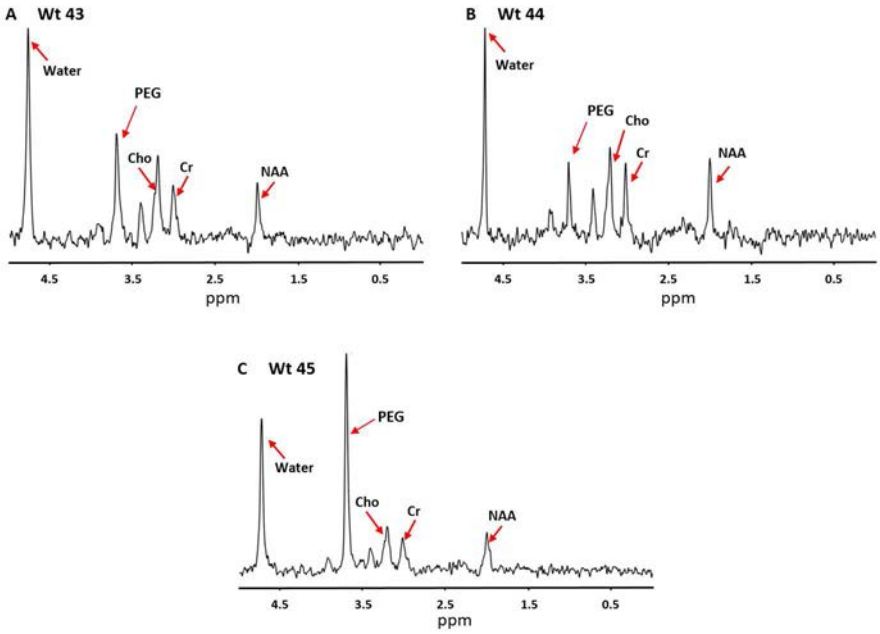

Figure 7.15: SV MRS (TE=136 ms) spectra acquired *in vivo* from brain parenchyma in control wt mice injected stereotactically with 20 mg Au/Kg of Nanorods. PEG resonance signal at 3.71 ppm was clearly observed (red arrow) in the three recorded spectra. Red arrows also point water and another observed metabolite peaks of Cho, Cr and NAA.

Intravenous injection of NRs in GL261 mice

Three GL261 tumour-bearing animals were injected with 20 mg Au/kg of NRs at day 8 p.i with devastating results. Two out of three animals died after this first injection: one immediately after being injected (C786) and the other one 24 hours after the injection (C788). The third animal (C785) was injected with a second dose of 40 mg Au/kg at day 9 p.i. and it was found dead in the cage few minutes after injection. It became clear that a more detailed tolerability test with low doses was needed before proceeding with NR administration.

Tolerability experiment using Nanorods

A tolerability experiment in wt mice using a single dose of 10 mg Au/kg (n=3) or 20 mg Au/kg (n=3) of NRs was performed. Figure 7.16 shows the evolution of the body weight variation of the animals injected during 14 days. The blue line corresponds to animals injected with a dose of 10 mg Au/Kg and the black line to animals injected with 20 mg Au/Kg. Body weight decrease did not reach the 20% point in any mice, indicating that no evident toxic symptoms took place in this period. In addition, no significant differences ($p>0.05$) with UNIANOVA test were observed between the two groups of animals. Mice were observed again at day 104 after the injection and all of them were alive and showed weight gain (Figure 7.16). These results suggest that, despite the results obtained with GL261 mice, a dose of 20mg Au/kg could be safely administered to mice and this was the dose chosen to proceed with hyperthermia experiments.

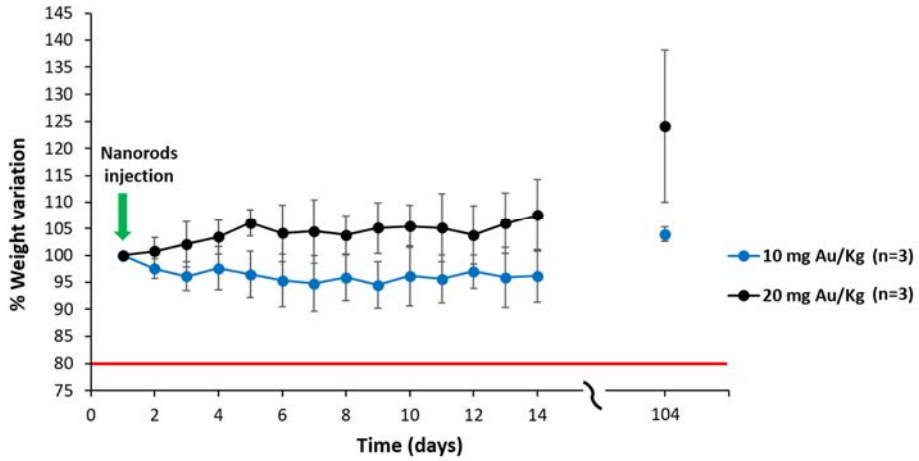

Figure 7.16: Evolution of percentage weight variation (mean±SD) of animals i.v. injected with a single dose of Nanorods, 10 mg Au/kg (in blue) and animals injected with a single dose of 20 mg Au/kg (in black).The green arrow indicates the day of NRs injection. The red line indicates the 20% weight reduction point.

Hyperthermia experiment with NRs in a GL261 tumour-bearing mouse

One GL261 tumour-bearing mouse (C787) was injected intravenously with a dose of 20 mg Au/kg of NR, at day 8 p.i. and it was irradiated after injection with the pulsed laser protocol. Temperature evolution is shown in Figure 7.17. At the experiment starting point, the body temperature was higher than the brain temperature (body: 37.1°C, brain: 33.7°C), which is a characteristic of small animals under anaesthesia [306]. After 25.5 minutes of irradiation, the brain temperature became higher than the body (body: 37.9 °C, brain: 40.2 °C). At the end of the experiment, similar brain/body temperatures were observed, 39.4°C and 40.0°C, respectively. The temperature slope of C787 was 0.17, comparable to wt mice stereotactically injected with the same dose of PEGylated HGNPs (Figure 7.11). Although stereotactic and i.v.

doses are not comparable (i.e. only a fraction of the administered dose reaches the tumour), probably the blood dilution was compensated with a better heating potential of NRs. On the other hand, only a small PEG signal was observed in the SV-MRS acquisitions of mouse C787. Figure 7.18 summarizes a comparison of SV MRS spectra between the two aforementioned mice and one non-administered mouse. Mouse C787 died 24 hours after the Nanorods administration, again suggesting harmful effects triggered by these NP, even after satisfactory results with wt mice in tolerability studies. A further experiment with sequential doses of 10 mg Au/kg was planned in order to check for safety and heating effects.

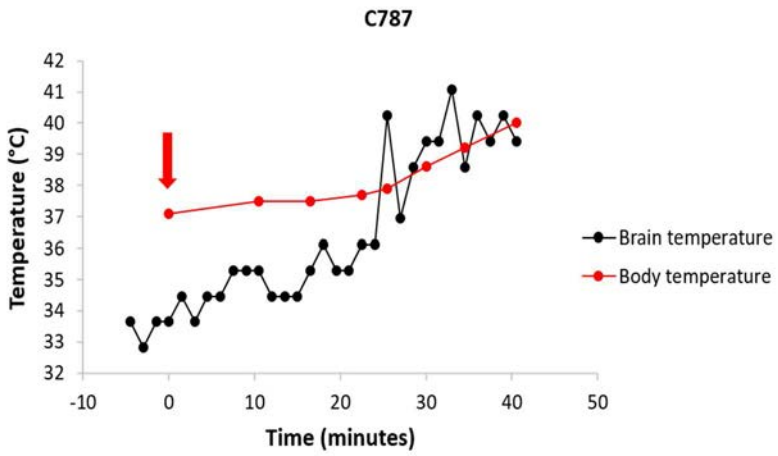

Figure 7.17: Temperature evolution of the brain (in black) and body temperature (in red) of the animal C787 after i.v injection of 20 mg Au/kg of Nanorods followed by head pulsed laser irradiation. Results were comparable with stereotactically injection of PEG-HGNPs (wt35 mouse). The red arrow indicates the irradiation starting point.

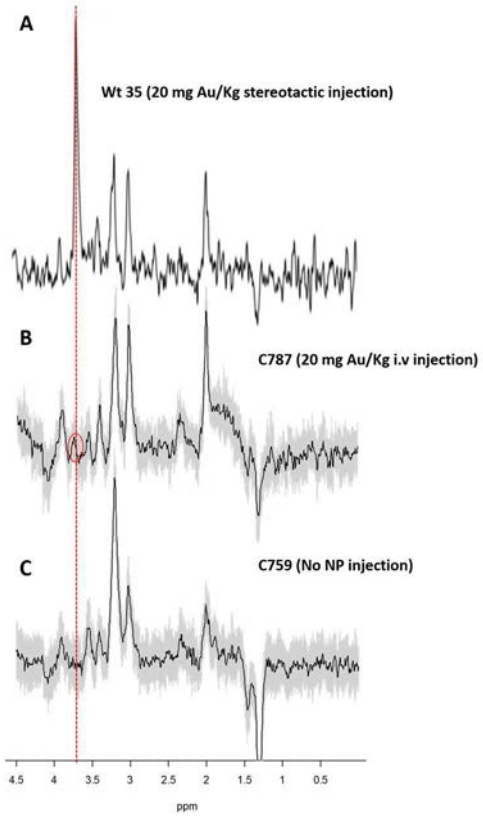

Figure 7.18: **A.** SV spectrum (TE= 136 ms) of the animal wt35, injected sterotactically with a dose of 20 mg Au/kg of PEG-HGNPs. **B.** Mean spectra of all the SV acquisitions (TE= 136 ms, n= 28) during the hyperthermia experiment of the mouse C787, injected i.v. with a dose of 20 mg Au/kg of NRs, the red circle indicates the signal attributed to PEG. **C.** Mean spectra of all the SV acquisitions (TE= 136 ms, n= 59) during the hyperthermia experiment of the mouse C749 which was not injected with nanoparticles. The dashed red line points at the PEG chemical shift in all spectra.

MRSI temperature maps in a GL261 mouse administered with NRs:

The GL261 tumour-bearing mouse C789 was i.v. injected with a dose of 10 mg Au/kg of Nanorods at day 8 p.i. and another dose of 10 mg Au/kg was injected at day 9 p.i. Then, 72 hours after the last injection (time frame reported for NRs blood clearance [178]), at day 12 p.i., the mice was irradiated with the pulsed laser protocol. MRSI-based temperature maps were acquired before the irradiation and after the pulsed laser protocol with the laser still on. In the meanwhile, brain temperature was monitored by SV MRS. Brain and body temperature evolution during the pulsed laser protocol are shown in Figure 7.19. The body temperature was higher than the brain temperature during the whole experiment (39.6°C and 38.6°C respectively). The animal died several minutes after the end of the experiment.

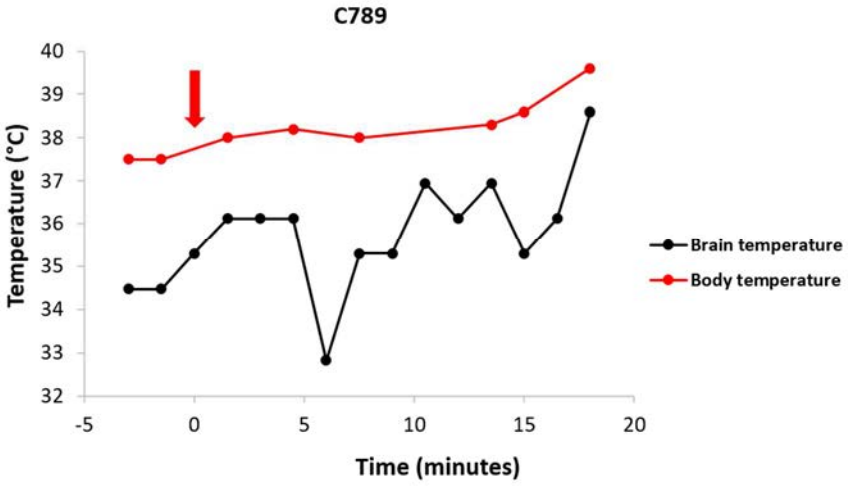

Figure 7.19: Temperature evolution registered during the pulsed laser protocol in mouse C789, 72 hours after being injected with 2 sequential doses of 10 mg Au/Kg of NRs. The black line represents the temperature of the brain measured with SV-MRS and the red line, the evolution of the body temperature measured with the rectal probe. The red arrow indicates the irradiation starting point.

The temperature maps obtained before and at the end of the irradiation protocol are shown in Figure 7.20. No significant differences were found ($p>0.05$) between the temperature measured within the tumour (35.9±1.4°C, n=52 voxels) and normal brain parenchyma (35.8±0.8°C, n=35 voxels) before the laser irradiation. After the pulsed laser irradiation, temperature was measured in the same voxels, and unfortunately no significant differences were found (37.4±2.5°C in tumour and 37.0±1.3°C in normal brain parenchyma), showing no differential heating between these 2 zones. When comparing temperatures pre- and post-irradiation in the same zones, significant differences ($p<0.05$) were obtained for tumour (35.9±1.4°C and 37.4±2.5°C respectively), and normal brain parenchyma (35.8±0.8°C and 37.0±1.3°C respectively). These differences are probably a consequence of laser irradiation rather than NRs

accumulation, since no differential heating was observed and, in addition, no PEG signal was detected in MRSI individual spectra.

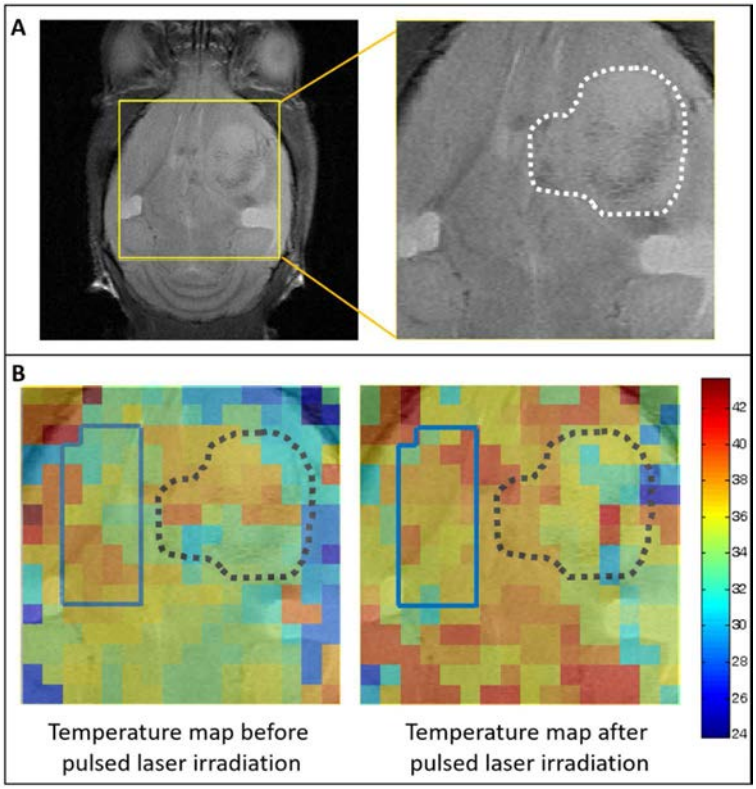

Figure 7.20: GL261 tumour-bearing mouse C789 administered with 2 sequential doses of 10mg Au/kg of NRs. A. T2w image for MRSI with the MRSI-grid selected in yellow is shown, and tumour area is indicated by white dashed lines. B. Temperature maps acquired in normothermia (left) and post-laser irradiation (right) with the temperature colour scale shown in the right. The tumour area is indicated by blackdashed lines. Blue rectangle indicates normal brain parenchyma voxels selected to measure temperature for statistical comparisons.

All attempts of using NRs with GL261 animals resulted in disappointing results. All mice died after being injected or right after the hyperthermia experiments. The fact that a cohort of wt mice survived after a similar NR dose without irradiation lead us to hypothesize that the harmful effect of NRs could be potentiated by laser irradiation, at some level. Checking with providers about possible residual chemicals or contaminants from synthesis, we were informed that Cetyltrimethylammonium bromide (CTAB) was currently used for NRs synthesis and although a process for elimination was performed, they could not ensure that NRs were free of CTAB and the residual amount was unclear. This could perfectly explain the toxic effects observed after NR i.v. injection as described by other authors [215] and the irradiation possibly helped to release the entrapped CTAB, increasing the harmful effects. Taking into account these results, and the no- availability of a CTAB-free batch of NRs, it was clear that NR were not suitable for

further experiments in this thesis. The continuation of the hyperthermia experiments was planned with a new batch of PEG-HGNPs (Batch B) taking into account that a tolerability test would be needed prior to administration and, depending on the results, a sequential administration protocol applied and irradiation should be performed with the optimized pulsed laser protocol.

7.3.2 Experiments performed during this thesis: PEG-HGNPs

The results described in section 7.3.1, which took place mostly before or just along the first period of this thesis, helped to pave the way for the continuation of the hyperthermia protocol, taking into account the valuable experience gained: use of pulsed laser system, improvement of PEG-HGNPs loading in the tumour in order to improve differential heating, and need to control variables related to synthesis that could lead to incompatibility with the administration to mice, such as CTAB presence in NRs. The whole remaining work was focused into PEG-HGNPs and its characterization in order to use it as an alternative treatment strategy in GL261 preclinical GB.

7.3.2.1 Studies with the new batch of HGNPs (PEG-HGNPs) (Batch 4)

Since the basic characterization of PEG-HGNPs was already performed by providers, more detailed studies involving the interaction of these nanoparticles with GL261 cells were performed.

7.3.2.1.1 Confocal microscopy results

Assessment of PEG-HGNPs internalization by GL261 cells at different cell-culture time points

In order to evaluate whether GL261 cells were able to internalize PEG-HGNPs, confocal microscopy studies were performed. Figure 7.21 shows examples of different fields observed either with control GL261 cells or cells with PEG-HGNPs at 0.01mg Au/ml added to culture media. Internalized PEG-HGNPs are marked with white arrows and non-internalized NPs with yellow arrows. Time points analysed were 24h, 48h and 72h after cell seeding. Intracellular aggregates of PEG-HGNPs were detected infrequently. This could be partially explained by the fact that the reflection observed is due to the gold thickness of the NP (8 nm in the case of PEG-HGNPs) rather than the whole nanoparticle. In order to be properly observed in these experiments, aggregates should present a size above the resolution limit of the technique being used (in this case, 200 nm). In other words, aggregates showing sizes smaller than 200 nm would not be visible by confocal microscopy and underestimation of the total amount of internalized of PEG-HGNPs would take place. Nevertheless, Gold NPs have been observed in confocal microscopy studies using reflexion mode, such as the visualization of non-pegylated HGNPs aggregates [296], Gold Nanospheres aggregates visualization [307] or Gold Nanords visualization [308].

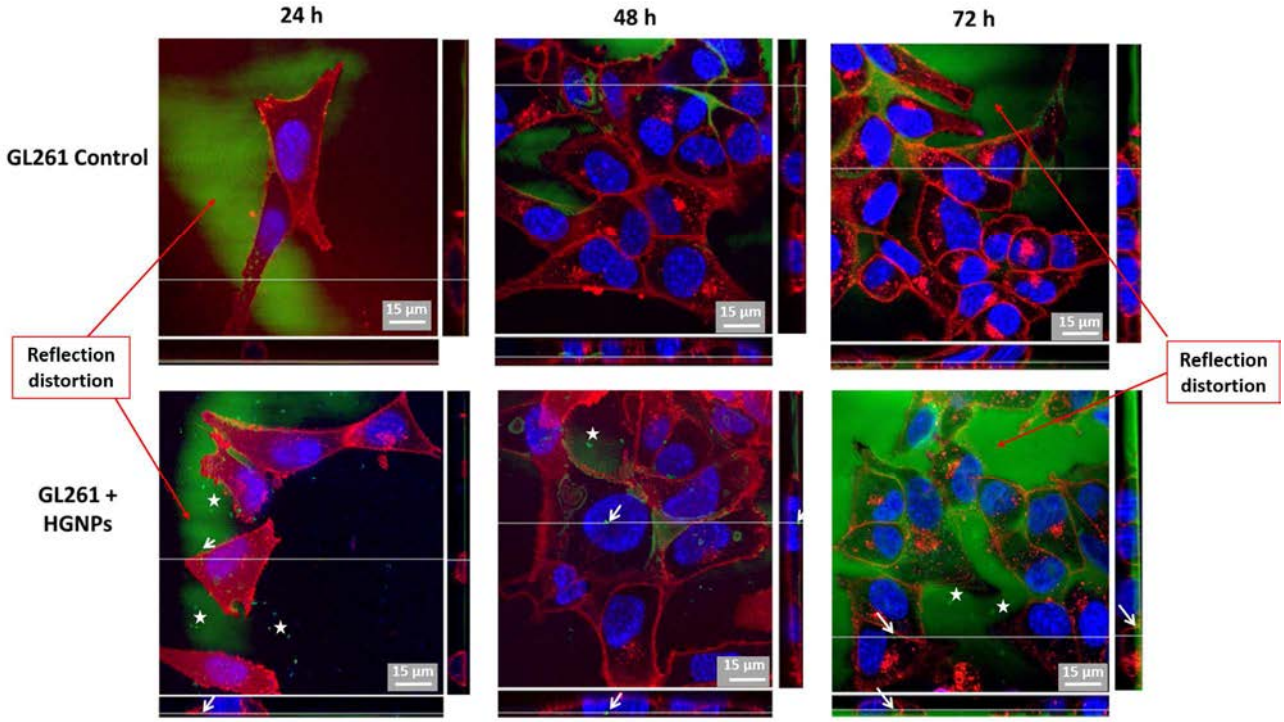

Figure 7.21: Selected regions from the different studied fields by confocal microscopy: First row corresponds to GL261 cells without nanoparticles and the second row corresponds to GL261 cells with prior nanoparticles addition. First column indicates fields acquired 24 hours after cell seeding and/or nanoparticle addition, while the second and third columns correspond to 48 and 72 hours after cell seeding and/or nanoparticle addition, respectively. Cell nuclei are dyed in blue, cell membranes in red, and nanoparticle reflection is detected in green. White arrows indicate the internalized NPs whereas white stars indicate example of non-internalized NPs. Red arrows indicate the presence of distortions in the reflection mode due to the plastic of the Mat-Tek dish (also seen in green).

The internalization of PEG-HGNPs by GL261 cells was observed in the three studied time points, and a cell was considered to have internalized NPs if at least one NPs aggregate was observed in such cell. The percentage of cells with internalized PEG-HGNPs after 24h of incubation was of 33±8% (n=3 fields, average cell counting per field= 4.0±1.0). Then, this value increased to 39±12% at 48h and 40±14% at 72h (n=6 fields, average cell counting per field = 11.3±3.8 and 11.7±3.1 at 48h and 72h, respectively). Average cell counting includes both cells with and without PEG-HGNPs internalization.

No significant differences ($p>0.05$) were found in the number of cells with internalized NPs, between the three analysed time points. It is reasonable to assume that these percentages of cells with internalized NPs are reflecting only the detectable aggregates, but there may be a non-negligible percentage of aggregates below the detection limit of the method used. Nevertheless, results in this subsection point to the fact that PEG-HGNPs would be indeed internalized by the GL261 cells provided suitable amounts arrive to the tumours.

It must be mentioned that a reduced number of fields was analysed after 24h of incubation (n=3) due to the low number of cells observed at this time point, which in other hand is the expected situation for this time period. A similar situation was observed in the control dishes. The mean of total cells per field in control dishes were 3.7±1.5 at 24h, 15.4±4.4 at 48h and 15.7±6.8 at 72h. No significant differences ($p>0.05$) were observed in the mean number of cells per field when comparing control cells and cells with added HGNPs at any of the studied time points.

7.3.2.1.2 Effects of PEG-HGNPs over GL261 viability after addition

The results acquired in this subsection refer to control GL261 cells (n=3 Mat-Tek dishes) and GL261 cells with PEG-HGNPs addition (n=3 Mat Tek dishes) after 72h of cell-culturing. This experiment was done in order to check if the PEG-HGNPs could affect the GL261 cells viability regardless of laser irradiation. The average of total cell counting/ml (counting of living and dead cells), the number of viable cells/ml (counting of living cells only) and the average of percentage of cell viability (calculated as described in Equation 7.2, see subsection 7.2.2.3) are shown in Table 7.3. No significant differences were found for any of the aforementioned parameters ($p> 0.05$).

Table 7.3: Results obtained with cell counting and viability assessment of GL261 cells with and without PEG-HGNPs.

	Total number of cells/ ml (mean±SD)	Number of viable (live) cells/ ml (mean±SD)	% Cell viability (mean±SD)
GL261 (Control)	491,000 ± 63,872	398,833 ± 70,924	81.7±7.1
GL261 + HGNPs	402,167 ± 97,860	293,167 ± 49,568	74.9±9.0

The percentages of cell viability obtained for control GL261 and GL261 cells with PEG-HGNPs were 81.7±7.1% and 74.9±9.0 respectively, which are clearly lower (although no statistically different ($p>0.05$)) than GL261 cell viability observed before injection for GL261 tumour generation (94.3±1.7 % of viable cells, n=3 countings). These differences could be explained by the non-optimum environment for cell culture provided by Mat-Tek dishes, as opposed to an optimal surface in cell culturing flasks. Still, these results suggested that the PEG-HGNPs, without NIR irradiation, were not harmful for GL261 cells. Having this in mind, a tolerability experiment was planned with wt C57BL/6J mice in order to estimate the maximum tolerated dose that could be administered to tumour-bearing mice to produce the maximal loading of heat-generating NPs into GL261 tumours.

7.3.2.2 Tolerability studies of PEG-HGNPs in C57BL/6J mice

As explained in section 7.2.2.4, a dose of PEG-HGNPs equivalent to 406mg Au/kg should be administered to mice in order to produce a clear MRS PEG signal. However, it was not feasible to perform this administration in a single injection due to dissolution limitations. The maximum volume to be i.v. injected in a mouse should not be higher than 100 µl, which in turn limits the amount of nanoparticles to be dissolved for tail vein injection. The starting point was ⅓ of the desired dose, i.e. 135 mg Au/kg which was i.v. administered to n=3 wt mice aged 17 weeks. Two out of three injected mice showed unusual signs and symptoms after PEG-HGNP administration:

a) Enlargement of the required period for anaesthesia recovery after vein cannulation (~1h vs ~2 minutes as usual).
b) Uncoordinated movements, especially from hind legs, after anaesthesia recovery.

These two mice were found dead in their cage the day after PEG-HGNPs injection and the corpses were preserved in paraformaldehyde in order to perform a necropsy study in the Histopathology Unit of the *Unitat de Patologia Murina i Comparada*, Veterinary Faculty from UAB. The findings reported in the necropsy study can be found in Annex IV. The main findings were related to brain congestion with haemorrhage, nonspecific cardiopathy, hepatopathology and lung oedema collapse.

These results indicated that 135 mg Au/kg was not a safe dose for mice and, accordingly, a dose lowering was planned for the next step, using 67.5 mg Au/kg (⅙ of the desired final dose of 406mg Au/kg). Only one mouse was injected, and it showed similar symptoms as described for the mice injected with 135 mg Au/kg. This mouse was also found dead the day after PEG-HGNPs injection and necropsy study was performed (Annex IV). Taking into account that 67.5 mg Au/kg did not prove to be safe in mice, a new dose lowering was performed and the dose used was 33.8 mg Au/kg, corresponding to 1/12 of the desired cumulative dose. This also meant that 12 consecutive i.v. injections would be needed in order to reach the final dose of 406 mg Au/kg, a challenging procedure due to the small calibre of mouse veins.

In this experiment, C57BL/6J mice of 16 weeks age (n=3) were i.v. injected with a dose of 33.8 mg Au/kg of PEG-HGNPs during 12 consecutive days. All animals survived the PEG-HGNPs injection period. Body weight control and animal welfare supervision were carried out during 2 months after the last PEG-HGNPs administration, and no toxic symptoms/signs were observed. Figure 7.22 shows average percentage of body weight variation for control and PEG-HGNPs injected mice. UNIANOVA test was carried out to evaluate differences between the two curves

of weight variation from day 1 to day 85 post first-injection and no significant differences were observed ($p>0.05$).

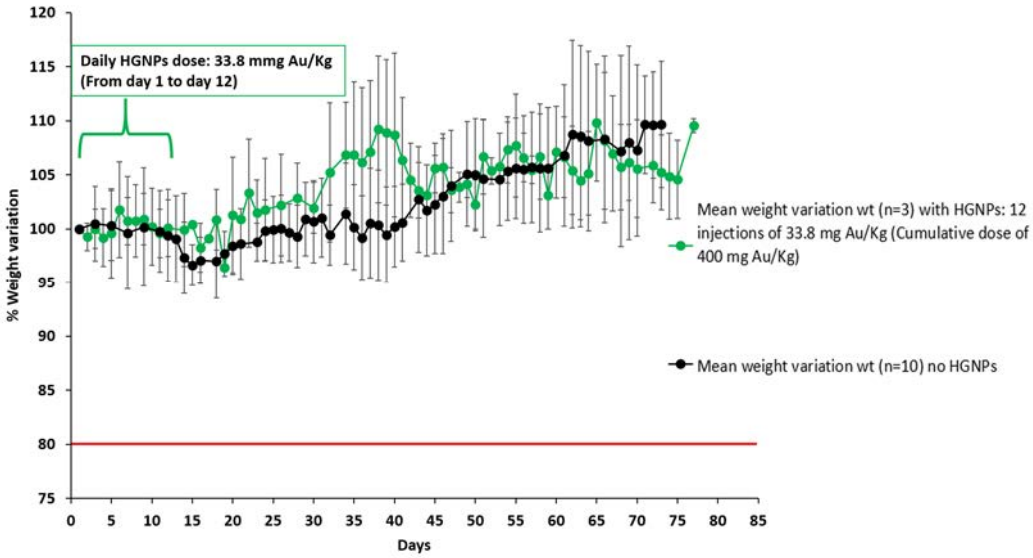

Figure 7.22: Percentage of body weight variation (mean±SD) of mice injected with PEG-HGNPs: 33.8 mg Au/kg repeated along 12 injections (green symbols) compared to control mice (black symbols). The red line indicates the 20% weight reduction point, not reached by any animal investigated within this protocol.

Although all animals survived the administration period, two mice (wt69, wt70) presented unexpected symptoms just after PEG-HGNPs injection, showing respiratory distress after injections corresponding to cumulative doses of 135 and 236.6 mg Au/Kg respectively. The next day, no evident symptoms were observed in these animals and the protocol continued. The symptoms described here are similar to the ones described in [225, 227], that could be at least partially due to endotoxin contamination [226]. Having this in mind, providers were contacted and tests for endotoxin detection performed in the batch of interest.

7.3.2.2.1 Endotoxin assay

The toxicity symptoms observed in mice wt69 and wt70 after PEG-HGNPs injection, although non-mortal, lead us to suspect that the last PEG-HGNPs batch used in this thesis could present endotoxin contamination above the allowed/recommended values. In order to corroborate or discard this hypothesis, a sample of the PEG-HGNPs used was sent back to NFP-INA for analysis.

Results showed that the chosen dose of 33.8mg Au/kg- which corresponded to 2.7 mg of PEG-HGNPs in 100 µl injected- would be equivalent to the injection of 72.46 EU (endotoxin units) to each mouse (or, in other words, each mg of administered PEG-HGNPs had 26.8 EU of endotoxin). To check for the safe limits in a given preclinical model, the endotoxin limit (K/M) was calculated as described by others in [309]. In this formula, K is 5 EU/kg, which is assumed the threshold

pyrogenic dose for individual preclinical species, and M means the maximum dose of product per hour and the body weight of the mouse model. The endotoxin limit calculated for our model assuming an average body weight of 20 g was of 0.037 EU for each mg of nanoparticulated material administered, indicating that the administered nanoparticles had endotoxin amounts well above the safe limit (more than 700-fold higher). It became clear that future developments should include either improvements in synthesis to ensure endotoxin-free materials or the application of decontamination procedures [310]. Unfortunately, at this point, the only solution to this problem was to proceed with the synthesis of an endotoxin-free batch of PEG-HGNPs, which was not feasible during this thesis, and the potential of these nanoparticles for preclinical GB treatment and nanoparticle tracking through PEG MRS signal could not be properly assessed.

7.3.2.3 Security issues in hyperthermia studies: lessons learned

During the final set-up steps of the pulsed laser irradiation protocol inside the MR scanner, a firebreak took place inside the scanner during the laser power change from 0.07W to 0.7W. This unfortunate incident lead to an undefined delay of hyperthermia protocols while repairing tasks took place and efforts were directed towards elucidation of possible causes triggering the firebreak incident.

After some confirmatory checks, we concluded that a combination of factors was the responsible for triggering the firebreak:

- Sparks can be produced due to the ignition of the C57BL/6J mouse dark hair under the focus of the laser optical fibre
- The vicinity of flammable materials such as the mouse blanket (see Figure 7.1.B), which is made from paper tissue and can burn if sparks are produced
- The use of 100 % O_2 as anaesthesia gas carrier. Oxygen is a flame accelerator and the risk of a fire becoming large quickly increases in environments with high oxygen levels.

In this sense, actions for improving safety in hyperthermia studies were proposed as follows, while some of them could be implemented and tested during this thesis.

1. To eliminate the “hair” factor. This could be achieved using hairless mice or shaved C57BL/6J mice.
2. To improve the control of local temperature increase. For this, installation of extra temperature sensors (apart from the rectal probe) near the irradiation zones was planned.

3. To decrease the oxygen accelerator factor. To achieve this, the use of air as gas conductor of anaesthesia instead of oxygen should be implemented. It also implies to control the blood oxygenation level (pO_2) in mice to prevent hypoxia (see subsection 7.3.2.3.1 below: *Use of air-anaesthesia system in wt mice during MR experiments*).

7.3.2.3.1 Implementation of safety measures for hyperthermia studies

Use of extra temperature sensors

A strict control of temperature oscillation inside the MR scanner was set-up with the inclusion of four extra temperature sensors. In order to automate action in case of abrupt temperature increase, sensors were connected to a device able to halt the laser irradiation immediately in case of temperature increase above pre-established safety thresholds, in addition to sounding an acoustic alarm. This set-up was tested with satisfactory results: the threshold was set to 40°C and once sensors detected a temperature increase up to this limit, which was simulated through placement of sensors in a glass of water at 40°C, the laser power was automatically disconnected.

Use of air as anaesthesia carrier instead of oxygen during MR experiments

Some of the relevant biological effects of anaesthesia are the depression of respiratory and cardiac rates and a decrease in body temperature. Accordingly, during a long-term anaesthesia period such as in MR studies, there is an increasing risk of developing hypoxia if oxygen supplementation is not provided, which in turn could lead to hypercapnia and acidosis [311]. This is the reason why oxygen is the most commonly used gas for carrying anaesthesia with inhalatory anaesthetic agents, such as isoflurane. This also explains why the pO_2 control with the use of pulse oximeters is relevant, especially if air is employed as carrier gas [311].

The pulseoximeter is a device that measures arterial oxygenation, useful for detection of arterial hypoxemia that may be related to hypoventilation and airway obstruction, before the animal becomes cyanotic. The pulse oximeter device consists of a probe with a light-emitting diode and a photo-detector, which can be placed over the animal skin, and the light is transmitted across the tissues. The emitted light alternately transmits red light at two different wavelengths (visible and infrared) which are absorbed to different degrees by oxyhaemoglobin and deoxyhaemoglobin present in the blood vessels close to the surface. The intensity of transmitted light reaching the photodetector is converted to an electrical signal. This information is processed, and the absorption due to the tissues and venous blood, which is static, is subtracted from the best-to-beat variation to display the peripheral oxygen saturation as both a waveform (the interval between peaks corresponds to a cardiac cycle) and a digital reading. The system provides real-time continuous measurements of arterial O_2, saturation, pulse strength, breath

rate, blood flow and effort to breathe. The absolute accuracy of pulse oximeters seems to be slightly lower for animals than for humans [312], but the information provided has acceptable reliability. In general, a saturation higher than 95% is considered as good, whereas for values below 90% user must be cautious, although corrective action may not be necessary. Nevertheless, when the saturation falls below 80%, corrective actions should be taken to improve animal oxygenation.

In order to gain experience with the use of air as anaesthesia-carrier gas in murine models and pO_2 control with the use of the pulseoximeter in mice, a fruitful three-month research stage was performed at the UT Southwestern Medical Centre, in Dallas (Texas, USA) in Dr. Ralph Mason's laboratory. This group has a long track in tumour hypoxia studies (especially breast and prostate) using MRI techniques [313, 314]. They are also experts in physiological monitorization of murine models during MRI explorations in order to control the animal health status. The techniques learnt in this stage were set-up in our group and are currently ready to be applied. A system dedicated to alternate delivery of sterile air or oxygen for anaesthesia into the MR scanner was installed (see Annex IV.V) and a preliminary test using tumour-bearing mice was performed. A brief description of the procedures is given below.

First of all, before placing mice inside the MR scanner and to ensure proper pO_2 measurement with the pulseoximeter, the animal should be "naired" (depilated) 24 hours before the experiment (Figure 7.23, left). Then, the mouse should be placed inside the scanner (while breathing oxygen) and the pulseoximeter placed in a leg, paw, or tail until a good signal is achieved (blue waveform in Figure 7.23, right). In our case, the best signal was obtained with the pulseoximeter placed in the leg.

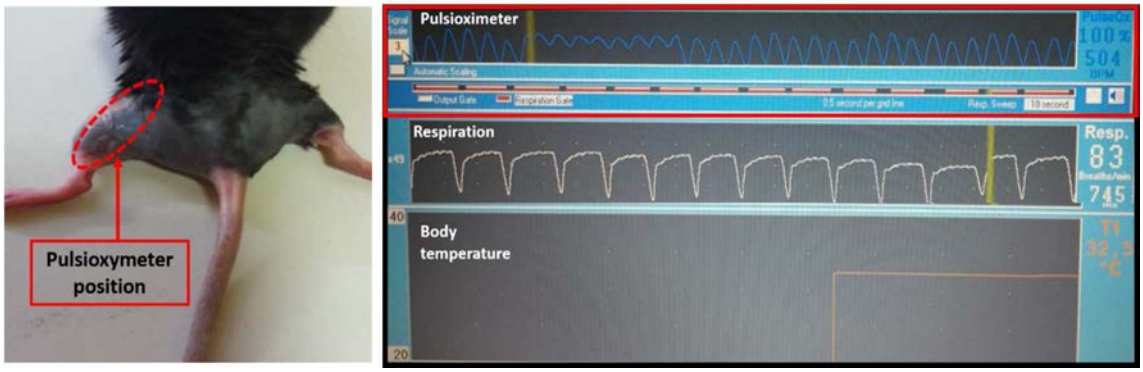

Figure 7.23: Left, C57BL/6J mouse after hair depilation in legs and abdomen. The red ellipse points to the place where the pulse oximeter is usually placed. Right (red rectangle), the plethysmogram from pulseoximeter measurements: pO_2 display while breathing oxygen (100%) and the waveform signal (in blue) which indicates the cardiac cycle (interval between peaks).

Once the optimal recording conditions were achieved (100% pO_2 and regular oscillations observed in the pulseoximeter measurements), a simulated hyperthermia experiment was performed using the recirculating water bath of the scanner to change the body temperature of the mouse. The experiment started in hypothermia conditions (28-30°C) after getting a good pulse oximeter signal breathing oxygen during the first 10 minutes (100% pO_2). After that, the anaesthesia gas carrier was changed to air, with the corresponding drop of the pO_2 level to 95% and an MRSI temperature map was acquired in hypothermia conditions. Once MRSI acquisition was finished, the bath temperature was increased until normothermia temperature (36°C) was reached and animal continued breathing air with the pO_2 registered values oscillating between 90-95%. Finally, another MRSI-based temperature map was acquired and after that the anaesthesia gas carried was changed to oxygen during the last 10 minutes with the corresponding increase in pO_2 (up to 98%) (See Figure 7.24). Significant differences ($p<0.05$, Student's t-test) were observed in tumour temperature between hypothermia (25.8±0.9°C, n=6 voxels) and normothermia (38.4±0.8°C, n=6 voxels) in the example shown.

The studied animal survived 21 days (the expected survival rate for untreated GL261 mice) and no harmful symptoms/signs were observed after this preliminary experiment with different anaesthesia carriers.

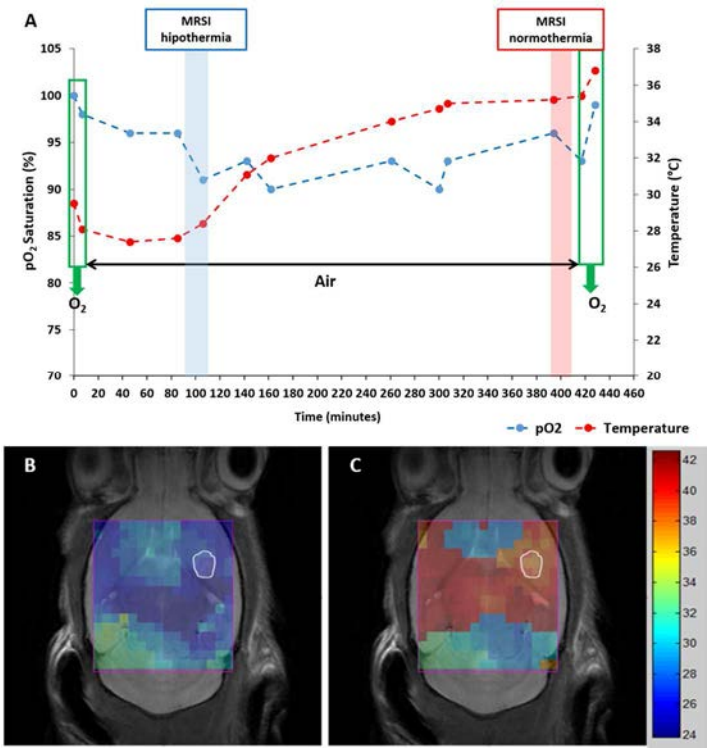

Figure 7.24: A. Evolution of pO_2 (blue line) and temperature (red line) of a GL261-bearing mouse along experimental time and while breathing oxygen or air. Colour columns indicate the MRSI acquisition points: blue column (hypothermia acquisition) and red column (normothermia acquisition). Green rectangles indicate the period while the animal was breathing pure oxygen. In the second row, temperature maps (as described in subsection 7.2.1.3) overlaid to the corresponding T_{2w} image, obtained in **B.** Hypothermia conditions and **C.** Normothermia conditions. Maps are shown with the temperature colour scale at right. The white-line circles indicate the tumour borders in T2w MRI .

The safety system was then properly implemented and satisfactory results were obtained, being ready to be tested with in a real irradiation experiment inside MR scanner. Unfortunately, this stage was not achieved during this thesis but the experimental set-up developed will be available for future work in this respect.

7.4 General discussion for this section

7.4.1 NIR hyperthermia inside the MR scanner: Real time temperature monitoring and animal irradiation conditions

Hyperthermia using gold nanoparticles for cancer treatment has been described in preclinical murine models. However, most of the described work has focused on subcutaneous tumours [178, 192–194], with satisfactory results within the follow-up period (e.g. 90 days for GB subcutaneous model in [194]). It is worth remembering that the lack of blood brain barrier in GB subcutaneous tumours and, in addition, the feasibility of a more direct NIR irradiation without absorption or scattering of NIR laser by other brain structures surrounding the tumour, can also play a role in their favourable outcome (e.g. as described by [315, 316]). In addition, several approaches for the temperature control during irradiation (which is a main issue found in the hyperthermia studies) are described for these subcutaneous tumour models. For instance, a thermographic camera was used in [178, 316] and an infrared-based thermometer in [193]. These methods are useful for subcutaneous tumours, but not for othotopic brain tumours, which are located in deep brain tissue. Thermal image thermometer and intracranial

thermocouple thermometer were used in orthotopic GB tumours in [317], which permits real time temperature measurements, but with an invasive component in the case of the thermocouple. Also, there are some studies without *in vivo* temperature measurements in subcutaneous tumours [194] and in orthotopic tumours [318], reflecting a lack of common accepted procedures in this point.

One of the main advantages of performing NIR irradiation inside the MR scanner was the "real time" and non-invasive brain temperature monitoring through MRS(I) approaches [127], especially for orthotopic brain tumours. An MRI approach based in temperature-sensitive interleaved gradient-echo images was used in [195, 319]. This MRI method is much faster than MRSI, obtaining real time temperature MRI maps each ~6 seconds [195, 320, 321], in comparison with MRS(I)-based temperature measurements used in this thesis, in which the time needed for acquisition is 1.5 minutes for MRS and 21 minutes for MRSI. However, one possible drawback for MRI temperature method is the presence of certain artefacts caused by water imaging alone. Thus, if properly calibrated, MRI-based temperature imaging should be superior to MRSI-based, if fast response time is required.

Another challenging point of this study was to test the influence of laser irradiation itself into brain temperature of wt mice and to investigate the best irradiation protocol in order to ensure gradual and acceptable temperature increases without harm to the life of the animals. Several laser powers with a continuous protocol irradiation were tested, but finally a pulsed laser protocol produced the best results. The brain temperature stabilized after 60-80 min of pulsed irradiation at 39.4±1.7°C. This point was especially relevant because the brain has a high thermal sensitivity. The brain can handle relatively low temperatures, as in mild hypothermia, which were proven to be neuroprotective in some conditions [306]. However, the increase in brain temperature above a certain threshold can lead to irreversible neuronal damage, and some authors point to temperatures higher than 40°C as a cut point leading to harmful effects when exceeded [302].

Still, it is also true that irradiation times described in this thesis were usually longer (30-80 min) than most of the described work in the literature, which used irradiation periods ranging 3-5 minutes and with higher laser powers, 2-6 W [178, 180, 195]. A larger irradiation period could produce differences in the accumulated heating of peritumoural brain parenchyma and in this sense, a strict real-time control of brain temperature should be always accessible.

Therefore, in order to properly assess the actual potential of hyperthermia in intracranial tumours such as GB, the use of orthotopic brain tumour models should be considered. Also, in order to use MR approaches for real time non-invasive measurement of the achieved temperature during NIR irradiation following nanoparticle administration, a set-up for irradiation inside the MR scanner should be designed and implemented, and this was one of the relevant achievements of this thesis. As far as we are concerned, this is the first *in vivo* study of hyperthermia with gold nanoparticles monitoring the temperature of the brain by MRS(I) in real time in living animals.

7.4.2 Effect of the studied Nanoparticles in brain and tumour heating

At the same time that safe conditions of NIR irradiation and non-invasive and feasible MRS(I) temperature measurement in brain were investigated, the possible differential heating produced in the tumour after gold nanoparticle administration was also studied. This was checked either through stereotactical or i.v. administration with different results. The stereoactically injected mice presented temperature slopes upon NIR irradiation which were 2 to 4 fold higher than non-injected animals (see Figure 7.10 and Figure 7.11) with the same irradiation protocol.

Then, for mice which were i.v. injected with gold nanoparticles, none or very poor differential heating was observed between tumour and contralateral areas (see Figures 7.8 and 7.9). These results suggested that the accumulation of gold nanoparticles inside the tumours was not enough to produce the desired results. In animals injected with non-PEGylated HGNPs (Batch 1), this could be explained due to “naked” NPs being more prone to be retained by the RES system [210, 212] and not accumulating enough in the tumour. Still, the lack of differential heating observed using PEGylated HGNPs, cannot discard that the penetration depth of the laser could also play a role, as described by von Maltzahn et al. [178], which showed that the temperature achieved after irradiation was inversely proportional to the depth of the tissue studied. Another factor that should be considered is the time elapsed between nanoparticle administration and NIR irradiation, which could influence in the final accumulation of nanoparticles and the temperature achieved after irradiation. This would be related in turn to nanoparticle administration route and biodistribution profile: in this thesis, this period ranged from 24 to 72h after nanoparticle i.v. injection whereas values reported in literature varied from 5.30 min [192], 6h [193], 24h [194] to 72h [178].

It must be emphasized that the temperature values achieved in the studies described in this thesis (40-43°C), even being safe temperature values, were below values described by others in

the literature, as in the intracranial canine model described by [195] using i.v. injected gold nanoshells (65.8±4.1°C in brain tumour and 48.6±1.1°C in contralateral brain parenchyma). Or in the case of [319], where a maximum temperature of 57.8±0.5°C was measured in orthotopic brain tumours in nude mice i.v. injected with PEG-HGNPs targeted to integrins (overexpressed in glioma and angiogenic blood vessels). In this same study, animals injected with non-targeted NPs presented a tumour temperature of 48.1±0.1°C. On the other hand, the temperature values obtained in these studies disagree with other authors who showed that adverse effects are observed in the brain when temperature exceeds 40°C [302].

However, the results found in this thesis are in agreement with [317], where rats injected orthotopically with C6 glioma cells where irradiated without NPs injection and the maximum temperature achieved in the tumours was ~42°C. Our measurements also agree with authors in [319], where tumours injected with saline showed a maximum temperature of 41.7±0.1°C. Taken together, results suggest that either the NPs studied in this thesis showed a low calorific power compared with other NPs from the literature or NPs were not accumulating in the brain tumour tissue or the laser was not reaching the tumour properly.

In the case of PEGylated NRs, the lack of differential heating for tumour-contralateral was probably due to the insufficient amount of NPs reaching the tumour, in part due to the low dose that could be injected due to tolerability issues in mice. The PEGylated Nanorods were withdrawn from the study due to the toxic effects observed after its administration, probably due to residual amounts of CTAB used in its synthesis [215]. It has been reported that CTAB is toxic *in vitro* and *in vivo* [219, 322] and although it can be removed in the synthesis procedure during the PEGylating process [323], free CTAB molecules may remain due to an inadequate purification or desorption of the surfactant from the surface of the Nanorods [215]. This issue should be addressed in future syntheses by the providing groups if Nanorods are expected to be used in preclinical (or clinical) applications.

Having all this in mind, efforts must be made in synthetizing well tolerated PEG-coated nanoparticles with higher specific heating capacity that would circulate long enough in blood to accumulate passively in tumours by EPR or using specific tumour-targeted nanoparticles [324] to achieve a larger accumulation of NPs inside the tumour mass in order to produce differential heating effects *in vivo.*

7.4.3 Characterization of a new batch of PEG-HGNPs (batch 3): NP stability, cell uptake and *in vivo* tolerability studies

Detailed studies were performed with a new batch of PEG-HGNPs (batch B) for evaluating cell uptake, effects over cell viability and *in vivo* toxicity in our preclinical GB model.

The *in vitro* cell studies revealed that the viability of GL261 cultured cells with PEG-HGNPs (74.9±9.0%) and control GL261 cells (81.7±7.1%) in Mat Tek plates were lower in comparison with the viability observed in standard GL261 cultured in flasks (94.3±1.7%). These results show that slight, although non-significant decrease in cell viability is observed when cells are cultured in Mat Tek plates even when no PEG-HGNPs are added. Nanoparticle aggregates were seen by confocal microscopy inside and outside the GL261 cells, as described for other Gold NPs with other cell-types [296, 307, 308]. The percentage of PEG-HGNPs internalization by GL261 cells ranged from 33 to 40% of monitored cells depending on the incubation time. However, a word of caution should be expressed because of the resolution limit of the technique used, which only allow the detection of aggregates larger than 200 nm.

As mentioned before, an interesting result found in this work was the clear PEG MRS signal which could be seen at 3.71 ppm in the results obtained with stereotactic injection of the Batch 2 of PEG-HGNPs. Our results suggest that whenever a dose equivalent to 20mg Au/kg arrives to the tumour, local heating can be higher than in non-injected animals with the same irradiation protocol, when a clear PEG MRS signal is visible. In this sense, the possibility of PEG signal tracking would be an advantage allowing to perform NIR irradiation only when suitable amounts of PEG-HGNPs accumulate into the tumour. Having this in mind, the equivalent i.v. dose to the one injected stereotactically was estimated in this thesis to be 406 mg Au/kg.

Taking into account this calculation, an *in vivo* tolerability study was planned in order to test if the 406 mg Au/kg dose would be well tolerated in wt mice. For that, a dose fraction study was designed, since it was not feasible to dissolve and administer the desired amount in a single dose. The first attempt was done with 1/3 of the desired final dose (135 mg Au/kg i.v. during three consecutive days) in order to get a cumulative dose of 406 mg Au/Kg. A second attempt was done with 1/6 of the target dose, i.e. 67.5 mg Au/kg i.v. during six consecutive days in order to get the desired cumulative dose. Nevertheless, in the first day of testing these dose fractions, toxic symptoms were detected followed by mice death. This led us to investigate the possible reason for animal death after nanoparticle administration, in conjunction with the providers. The symptomatology pointed to possible endotoxin contamination: lengthening of the required period for anaesthesia recovery after vein cannulation and uncoordinated movements,

especially from hind legs, after anaesthesia recovery, which were in agreement with the toxic symptoms derived by endotoxin exposition described by other authors [225–227].

Despite the observed toxic symptoms, the tolerability experiment continued with 1/12 of the desired dose, injecting i.v. 33.8 mg Au/kg during twelve consecutive days in 3 wt mice to achieve the cumulative dose of 406 mg Au/Kg. The three animals survived to the 12 injections and no toxic symptoms were observed after 3 months of follow-up after the first injection. Therefore, 33.8 mg Au/kg was considered the daily maximum tolerated dose (MTD) for the batch B of PEG-HPNPs.

Finally, the endotoxin test was carried out by the providers using the MTD found in the tolerability study (33.8 mg Au/kg). The test confirmed the presence of endotoxin, showing a value more than 700-fold higher than the safe limit established for mouse animal models. However, in the tolerability study carried out with this dose, no evident toxic symptoms were observed such the ones observed in the animals tested with higher doses (67.5 and 135 mg Au/kg), which could be explained by the high presence of endotoxin in this batch of PEG-HGNPs being more evident and toxic-related when higher PEG-HGNPs doses are administered.

In addition, there are other relevant variabilities, apart from endotoxin contamination, that can influence the toxicity caused by Gold NPs. For instance, NP size may also play a role in their toxicity, and NPs with small hydrodynamic diameters (10-20 nm, TEM measurements) have been described to induce harmful effects when compared with NPs with larger sizes (40-60 nm, TEM measurements) [223, 325, 326]. Thus, the characterized PEG-HGNPs (Batch 3) should not cause toxic effects due to their hydrodynamic diameter (40.5 nm, measured by TEM). Other relevant variabilities can be NP coating [327, 328], the administration route [329] and possible residual contaminants [330].

This suggests that MTD may need to be evaluated for each individual nanoparticle batch targeted for *in vivo* studies. In addition, efforts should be directed to produce safe, non-contaminated, endotoxin-free samples to be used in those *in vivo* experiments [229] even if mice can tolerate samples which are above the safe recommended limit.

7.4.4 Safety actions for future hyperthermia studies

Finally, main lessons learned with the set-up of the laser NIR irradiation inside the MR scanner are related to safety measures that should be taken into account for future studies. The main actions that could avoid future accidents as the one described in this thesis are:

I) Strict control of temperature increases inside the scanner around the laser/animal cradle set-up with an automatic laser power shutdown device.

II) Avoid using haired (or dark haired) mice.

III) Elimination of as much flammable materials as possible (e.g. hair).

IV) Replacement of pure oxygen as anaesthesia gas carrier by air.

7.5 Conclusions

1. A set-up for laser NIR irradiation inside the MR scanner was implemented for hyperthermia *in vivo* experiments with mice, using gold nanoparticles. The MR and laser instruments were compatible and did not presented mutual interference.
2. A pulsed laser protocol for NIR irradiation was optimized in order to ensure that brain temperature did not increase beyond acceptable limits during hyperthermia procedures in C57BL/6J mice. This pulsed protocol produced more suitable results than the continuous laser irradiation and was the chosen irradiation scheme for further studies
3. The measurement of brain temperature using in vivo MRS(I) approaches proved feasible, either right after laser irradiation or during laser irradiation, allowing a real-time assessment of brain temperature translated in temperature maps in case of MRSI. This is relevant because orthotopic preclinical models are needed in case of brain tumour studies and the brain temperature measurement is not possible using external probes as in subcutaneous models.
4. A group of PEGylated and non-PEGylated gold nanoparticles were evaluated in preliminary studies in order to assess their differential heating potential of normal parenchyma brain after stereotactic injection of HGNPs or Nanorods (20 mg Au/ kg). For PEG-coated nanoparticles, it was possible to detect PEG signal in MRS spectra with good SNR. This could allow *in vivo* monitoring of nanoparticle accumulation inside tumours and, accordingly, proceed to NIR irradiation with the knowledge of actual nanoparticle accumulation in tissue.
5. The highest temperatures using NPs in these experiments were achieved with the stereotactical injection of PEG-HGNPs in wt mice, the heating produced, ca. 42°C after 50 minutes of NIR irradiation, was below common values described in literature (~50°C).
6. PEGylated Nanorods had to be discarded from the *in vivo* study due to toxic effects attributed to residual CTAB from synthesis. Improvement of removal protocols or replacement by other similar compounds with less toxicity should be investigated in the future if in vivo studies with this type of Nanorods are foreseen.

7. A specific batch of PEG-HGNPs was synthesized for the final *in vivo* study. No deleterious effects over the cultured GL261 cells were observed. Moreover, confocal microscopy results showed that 33-40% of GL261 cultured cells internalized PEG-HGNPs.
8. Toxic symptoms followed by animal death while testing PEG-HGNPs doses for the *in vivo* study lead to an investigation of possible endotoxin contamination. Positive results were found, 700 fold above the recommended safe limit in preclinical mouse models. However, animals survived an administration of 33.8mg Au/kg which proved safe for sequential administration during 12 days. Unfortunately, the fire break inside the MR scanner during laser NIR irradiation prevented us to further assess PEG-HGNPs accumulation inside the tumour through PEG MRS signal quantitation, which would guide NIR irradiation timing. This may be the next step towards the use of this therapeutic strategy, although it will be also essential to have access to endotoxin-free nanoparticle batches for *in vivo* studies, to ensure that all observed effects are due to hyperthermia rather than effects produced by contaminants.
9. A complete safety assembly was installed in the MR scanner to prevent future accidents like the one described in this chapter. It includes additional temperature sensors connected to a device for automatic shutdown triggering in case of temperature increase above pre-chosen thresholds and the use of air as anaesthesia gas carrier. The system was tested with satisfactory result in a simulated experiment with temperature increase and animals could be anesthetized with the use of air, with a strict control of blood oxygenation performed with a pulse oximeter. This system is ready for use in future studies of our group.

8. General Discussion

Glioblastoma is the most common and aggressive primary brain tumour with poor prognosis and survival, and nowadays there is no cure for it [6]. Even after the application of the most aggressive therapeutic schemes, only a slight improvement in overall survival is achieved [331] and relapse usually takes place in a short time. There is urgent need of new and effective therapies, as well as an improvement in therapy follow-up for an early and reliable assessment of changes in response, allowing informed clinical decision for patient management. Due to obvious ethical restrictions, studies requiring a control-untreated group, as well as repeated explorations or tissue sampling cannot be performed in clinical patients and, in this sense, the use of preclinical models which mimic the human pathology is needed to explore new paths in glioblastoma diagnosis, treatment and follow-up. For example, A PUBMED search with the keywords "glioblastoma", "therapy" and "preclinical murine", covering the period of this thesis show the amount of efforts being made towards new breakthroughs in this field with more than 40 published papers/year in average. However, there is still much room for improvement: some studies are performed with orthotopic tumours generated in immunocompromised mice in which the immune component of the response to therapy is total or partially lost [332, 333] or subcutaneous models [286, 334] in which the brain environment is not faithfully reproduced as in orthotopic models. In addition, due to accelerated validation purposes, in many protocols animals are euthanized before overall survival can be assessed, and relevant information about the actual efficacy of new therapeutic agents may be compromised or overoptimistic. Magnetic resonance is one of the most suitable approaches for tumour diagnosis and follow-up in orthotopic glioblastoma models either with MRI alone [335, 336] or combined with MRS(I) information [117, 337], with some authors even using hyperpolarization approaches for their work [338, 339]. Other authors have used interesting approaches such as optical imaging [340, 341] but it is worth noting that this last type of imaging does not have application in human clinical practice for brain tumours. Accordingly, in this thesis MRI/MRS/MRSI approaches have been applied in order to embrace different aspects of GB management as follows:

1. The study of novel, dual contrast agents (T1/T2) based in iron instead of gadolinium, which could have direct application in preclinical and clinical GB diagnosis.
2. Investigation of the potential of gold nanoparticles for hyperthermia to be used as an alternative treatment in preclinical GB.

3. Improvement of therapy response follow-up in preclinical GB under TMZ treatment, through the use of metabolomic information from MRSI and application of pattern recognition techniques, followed by histopathological validation.

8.1 Studies with novel dual contrast agents

A brain tumour with enough size can be easily spotted by radiologists in a standard MRI exploration, even without the use of a contrast agent. However, several clinical decisions are usually based in tumour features/behaviour which are assessed through administration of contrast agents. Examples are evaluation of tumour grade based on contrast uptake, estimation of tumour perfusion or evaluation of response to therapy, mostly based in MRI characteristics, including quantitation of the total enhancing area [342]. Most contrast agents currently used in clinical practice for brain tumour diagnosis and follow-up are based in gadolinium such as Omniscan (gadodiamide), Dotarem (gadoterate meglumine), Eovist (gadoxetate disodium), Clariscan (gadoteric acid), Gadovist (gadobutrol), Vasovist (gadofosveset trisodium), ProHance (gadoteridol) (source: Spanish vademecum[8]). Although the chelated gadolinium should not be toxic itself, the use of these agents could be problematic in patients with kidney perfusion problems, leading to nephrogenic systemic fibrosis [102, 246, 247] and a recent review has reported a possible neurotoxic effect after repeated administrations of gadolinium-based agents [343]. Some new synthetic strategies have been attempted in order to reduce such harmful effects [344, 345], but the conventional approaches are still predominating in the clinical setting. In this sense, there is an increasing interest in developing contrast agents non-gadolinium based such as manganese or iron-based contrast agents. Moreover, the applicability of dual T1/T2 contrast agents is relevant to solve MRI artifacts or imaging ambiguities, as described by [346]. Accordingly, novel nanoparticle contrast agents with dual T1/T2 contrast enhancement properties have been evaluated in this thesis. Preliminary *in vitro* data from providers and *ex vivo* studies performed in our group following a protocol developed by us [231] allowed to confirm dual enhancement properties and to select the best agent to proceed with in vivo studies, which was an Fe-based NCP, a platform that offers new opportunities for engineering multifunctional systems. The outstanding results obtained showed that Fe-NCP was well tolerated by animals and safe at the dose of 0.4 mmol Fe/kg, although the real MTD was not calculated during this work, being considered as equal as or higher than 0.4 mmol Fe/kg. The biodistribution profile performed by providers showed that with the exception of the spleen, there was no worrying accumulation of iron in organs such as lungs, bladder, kidneys or liver. A

[8] www.vademecum.es

residual amount of iron could be detected in GL261 tumours after 24h of its administration, although no T1 contrast was measured at this time point, which could point to gradual disassembly and degradation of the NCP. Taking into account that it is a Fe-based nanomaterial, the release of Fe within the tumour, or other organs, would probably lead to scavenging through macrophage processing, as suggested by [347]. This lack of toxicity would be a clear advantage in comparison with Gd-based contrast agents and ensure that repeated administration could be performed in preclinical subjects or even patients. The dual enhancement produced was significantly better than commercially available contrast agents and, more importantly, in a comparable and acceptable time frame post-administration (between 4 and 11 min after administration for maximum T_1/T_2 effect) avoiding the need of performing two different explorations with large intervals between them. This Fe-NCP could be proposed in the future as a reasonable alternative to Gd-based contrast agents, with favorable biodistribution and toxicological profile and excellent contrast enhancement results.

8.2 Non-invasive assessment of therapy response: what are we sampling?

One of the key questions to be addressed in this thesis was to evaluate whether the GABRMN approach for MRSI-based non-invasive therapy response assessment could be improved. For this, we decided to improve and extend the previously developed, single-slice MRSI method [117] and explore the well described GB heterogeneity [12, 15, 348] under TMZ therapy in a 3D-like volumetric application of our method, which is based in semi-supervised source analysis of MRSI data.

Our main goal was to improve and extend the system previously developed by our group for non-invasive assessment of therapy response, based in pattern recognition analysis of single-slice MRSI data obtained from GL261 tumour bearing tumours, either untreated or TMZ-treated. Semi-supervised source analysis was the PR approach applied and three 'sources' or paradigmatic spectra were extracted: normal brain parenchyma, actively proliferating tumour and responding tumour [117]) with the generation of coloured nosological images for each analysed grid showing the colour of the prevailing source in each voxel. Several options were considered for data acquisition, such as the cubic 3D acquisition which is being implemented in some scanners [121]. However, and due to the homogeneity problems that can appear when the MRSI grid is placed near from scalp or other interface areas, this would not ensure proper tumour coverage. In this sense, a 2D multi-slice acquisition would possibly provide more flexibility in this regard, allowing adjusting matrix size, position and shim adjustments for each

slice, and providing good region of interest coverage. Then, an optimized 3D-like 2D multi-slice protocol was set up with a set of wt and GL261 tumour-bearing mice (detailed in chapter 5), in order to ensure that adequate spectral quality and SNR were obtained in all slices, even at increasing distances from the surface coil used for signal acquisition. In addition, the semi-supervised source analysis was applied to all slices and consistent results were obtained, suggesting that we could proceed to a longitudinal study with treated and untreated animals. The overall acquisition time for a 2D multi-slice sequence, (3.5h) is indeed larger than a 3D cubic acquisition (45 min) but it is still within acceptable range.

The main advantage of the multi-slice acquisition protocol developed is the collection of information from most of the tumour volume instead of sampling only the central slice. Relevant questions addressed were: how much heterogeneity would be observed in control and treated tumours, and whether the correlation of the non-response/response detected regions with the Ki67% reported in [117] was maintained if we analysed the whole tumour. In order to assess the "response level" in each tumour and transform it into a numerical parameter, we calculated what we named TRI or tumour responding index, based in the percentage of responding (green) pixels over the total tumour pixels. Arbitrary thresholds were established to categorize tumours according to their "response" level (TRI value): control (average ca. 6%), low response (<35%), intermediate response (range 35-65%) and high response (>65%).

Regarding tumour heterogeneity, the answer became clear soon: control/untreated tumours were essentially red in nosological images (i.e. actively proliferating tumour spectral pattern) at the studied point (15.2±3.4 days postimplantation), with few exceptions. On the other hand, large heterogeneity was observed in responding tumours, with different response levels. The first important message from the volumetric assessment of therapy response was that, according to our system, there were no "fully green" (fully responding) tumours. The maximum TRI value observed in a high response case was of 70.3%. Histopathological studies were performed in chosen cases, corroborating the correlation between the spectral pattern ("red" vs "green" zones) and Ki67% values. However, when considering the global Ki67% value from all studied slices, unexpectedly high values were found for high response cases when the opposite was expected. A detailed analysis of the histopathological slides showed that morphological local changes (presence of giant multinucleated cells, acellular spaces) in responding cases could be responsible for this inconsistent result, and the calculation of Ki67 positive cells per mm^2 of evaluated field reconciled i*n vivo* and *in vitro* information. Namely, 'green' regions in nosological

images *in vivo* display low number of Ki67 positive cells when corresponding regions are analyzed *in vitro*, while the opposite happens for 'red' regions.

Preliminary work from our group [117] with single-slice MRSI and nosological imaging generation from cases in longitudinal studies until endpoint, suggested that the response level was not 'static' along the response time evaluated through volumetric tumour data. On the contrary, TRI seemed to oscillate between high and low values with an average period of 6.3 days. This was corroborated with our 3D-like multi-slice approach with one case being followed until endpoint, and a cyclical behaviour observed in TRI with maximum values ca. 6-day apart, whereas tumour volume remained essentially unchanged, being compatible with stable disease according to endpoint RECIST criteria. This is a clear case in which MRI is "blind" to local metabolomic changes, which are tackled by MRSI and can provide relevant response-related information even before any anatomical changes are observed.

A possible explanation for this TRI cyclical pattern could be the presence/action of the immune system participating in therapy response, which is widely recognized for different tumour types, including brain (e.g. [286]). The whole length of the immune cycle described in mice is of 6-7 days [52], which is in agreement with the period found in TRI oscillations. The cell damage triggered by TMZ administration would lead to the recruitment of the immune cells (see Figure 6.19 for a representation of the proposed hypothesis) which in turn would be able to recognize and kill tumour cells. Our hypothesis is that our MRSI-based method is sampling these local changes due to effects of immune system cells over tumour cells, and those spectral pattern changes would be different enough to be recognized as "responding", i.e. green in nosological images. This wave of immune cells and tumour attack would be effective until a resistant clone appears and immune cells would not be able to recognize and kill tumour cells anymore. At this moment, the proliferating pattern would reappear and the responding pattern would decrease or disappear, configuring the TRI cycle. For a new productive attack, new TMZ cycles should produce further damage and new recruiting of immune cells [67]. This is also supported by two findings in this study: first, the PUFA signal at 2.8 ppm which was one of the main spectral differences between the responding and unresponsive sources described in [117]. This metabolite was also described by other authors [141, 142] in preclinical gliomas after ganciclovir therapy, being related to tumour cell apoptosis. This spectral change is probably one of the spectral biomarkers for our method to recognize the response to therapy. The second finding that could support this hypothesis is the presence of lymphocyte-like cells in histopathological slides of responding tumours (see Figure 6.18). Altogether, these data suggest that our system could be sampling the waves of productive attack of immune system to tumour cells and could

be used to monitor therapeutic efficacy, not only from TMZ but also from other therapeutic approaches, such as hyperthermia.

Indeed, there is still room for improvement, because immune-respectful therapeutic cycles such as the ones described by authors in [51, 286] can help and improve this immune cycle activation. Indeed, satisfactory results were already obtained by our group with immune-enhancing metronomic administration of TMZ [337] and preliminary unpublished histopathological studies corroborate this hypothesis (work in progress).

8.3 Hyperthermia generation for GB: lessons learned

Nanoparticle-based hyperthermia treatment has a great potential for GB treatment. As opposed to radiotherapy, it does not imply the use of ionizing radiations, heating effects should theoretically be restricted to the region of accumulation of nanoparticles, and it may also be able to produce immunogenic cell death [190]. Challenging points are the arrival of large amount of nanoparticles to tumours and the distance between skin surface and tumours, leading to possible laser scattering when irradiating tumour-bearing mice. This, in addition to minor movements from the anesthetized mice could cause changes in placement and irradiation of a slightly different zone than the target one. Additionally, the real-time measurement of temperature in brain is not straightforward, but it may be achieved through the MRS/I signal, as explained in chapter 7. However, to achieve this in an acceptable time frame, a set-up needs to be assembled for laser NIR irradiation inside the MR scanner, which was fully accomplished in this thesis, as well as the optimization of an irradiation protocol in mice. This is not the first on-site irradiation in a MR scanner, but other approaches have used percutaneous- invasive laser [195] which was not our case. Detailed studies have been performed to establish the best irradiation protocol to avoid excessive and abrupt increases in brain temperature which could affect tumour surrounding tissues. Ideally, only the area with maximum accumulation of gold nanoparticles should experiment heating and the influence of laser NIR irradiation over global brain temperature should be minimal and within narrow physiological limits. It is also worth noting that the brain is the responsible for body temperature homeostasis, and a conflictive input (i.e. extremely different temperatures in body and brain) could lead to mice cardio-respiratory arrest and death [349, 350].

Unfortunately, results obtained with the tested nanoparticles, disregarding the administration route, were discrete or undetectable in comparison with other results described in literature [178, 193, 195] which could be at least partially due to not insufficient nanoparticle accumulation inside the tumour. Regarding PEG-Nanorods, although they displayed a good

heating potential, severe toxic effects took place after their administration to mice, which was attributed to residual CTAB from the synthesis process, a problem that needs to be solved in future work if these nanoparticles should be used in *in vivo* experiments. In this sense, and taking into account that the PEG-coating in these nanoparticles provided an excellent marker for monitoring their accumulation inside the tumour, a detailed characterization and in vivo experiments were planned with PEG-HGNPs. Additionally, its MRS signal could be also used for temperature calculation as described by authors in [351]. The PEG-HGNPs did not present significant deleterious effects over GL261 cultured cells viability and were internalized by these cells during the observation period evaluated (24 to 72h). An *in vivo* experiment was designed in order to monitor the nanoparticle tumour loading using the PEG signal as a marker.

Despite PEG-HGNPs were not harmful for cultured GL261 cells, toxic effects followed by animal death were seen after injection of doses corresponding to 135mg Au/kg and 67.5mg Au/kg, pointing that this toxic effect was specific to *in vivo* administration but not to cultured cells. On the other hand, animals survived without toxic symptoms or signs to a dose of 33.8mg Au/kg repeated during 12 days, followed-up during ca. 3 months.

One possible explanation for the toxic symptoms observed with the higher doses, was the presence of endotoxin which has a role in the activation of the immune system and release of pro-inflammatory mediators, leading to endotoxin shock, tissue injury and sometimes death [352]. The absence of immune cells in culture would explain the absence of deleterious effects which appeared later *in vivo*. Indeed, the endotoxin test detected its presence with amounts above the limits estimated as indicated in [309]. For future work, ideally a new endotoxin-free batch from the providers would be needed for *in vivo* studies, with an acceptable toxicological profile, such as the one obtained for Fe-NCPs.

A proof-of-concept experiment with hyperthermia therapy in overall survival of GL261 tumour-bearing mice was not finished during this thesis, due to the firebreak, which revealed important safety failures that had to be addressed before performing any additional experiment. Those were related either to mice (with dark fur) and lack of temperature control near to the irradiation point and the use of oxygen (accelerator in case of firebreak) as anaesthesia carrier gas. Corrective measures were taken and tested, basically consisting of two aspects: first, additional temperature sensors connected to a device with capability for automated shutdown in case the local temperature exceeded the threshold set by user. Second, the replacement of oxygen by air as anaesthesia carrier, which also requires strict control of mice blood oxygenation. One possibility that could be also helpful in the future is the use of higher laser

powers during short periods of time as described by authors in [178, 180, 195] which would help to reduce the overall anaesthesia period and accordingly, reducing the risk of hypoxia in studied mice. The system for safe hyperthermia irradiation inside the MR scanner is presently ready for its use in future studies.

It is worth noting that although the use of nanoparticles has been proposed as a revolutionary way to treat cancer, in most cases the results have not been as good as initially expected. For example authors in [214] stated that one of the possible reasons for disappointing results could be low efficiency in tumour targeting (0.7% of the total dose of injected NPs) whereas authors in [209] reported that the plasma protein binding could have a decisive role in biodistribution, although PEG coating would have a favourable effect in reducing this binding. The nanoparticle specificity should be improved in future synthesis and combined platforms for targeting/therapy/contrast or monitoring would be probably of great relevance. Additional relevant issues should be taken into account while scaling up nanoparticle production for a possible translational use (provided preclinical results were promising), most of them related to lack of standardisation leading to differences between batches. Parameters such as aggregate size, charge, coating should be reproducible and constant in order to ensure consistent results. Sill, pharmacokinetic studies in order to estimate this amount of bound nanoparticle could help to understand biodistribution-related results.

8.4 Interweaving of different issues studied in this thesis

This thesis was focused on the improvement of GB management, including detection, therapy and follow-up. The information provided by MRI and refined by contrast uptake is essential for tumour detection grading and response assessment following clinical criteria. However, and even considering that most agents currently used in clinical practice are based in Gd, the limitations for repeated use in some patients are not negligible. The development of new contrast agents, with comparable (or better) potential enhancement and less risk for patients is a new and promising field. If proven useful, the information provided by the simultaneous use of positive and negative contrast enhancement could be incorporated in the pipeline for tumour response follow-up through MRI criteria. In addition, recent studies are using combinations of MRS and MRI information for tumour delineation [353] and although this work only incorporated T2 weighted regular MRI with no contrast, the inclusion of contrast uptake and enhancement could be of interest in future applications.

The GL261 GB treatment with hyperthermia could not be properly assessed with a proof-of-concept experiment due to the already stated handicaps, but it has still potential, provided

suitable nanoparticles are made available. It could be an excellent alternative treatment whenever GL261 tumours become resistant to standard therapy or after an initial tumour reduction, which could be promptly monitored with our non-invasive system of therapy response assessment. Superimposition of therapy-loaded nanoparticles and TMZ such as described in [175], in which the enhanced efficacy of the combination is attributed to immune-mediated factors, could also be tested. Whatever the treatment used, if no waves of productive attack by the immune system are detected, a second line treatment should be considered. On the other hand, whenever signals of efficient immune system attack are seen (i.e. green in nosological images), metronomic therapeutic administrations may be continued until tumour mass disappears or remains stable. This approach would contribute to the personalization of GBs therapeutics administration in preclinical models and could have strong translational potential.

9. General Conclusions

Individual conclusions have already been listed at the end of each chapters, and this section will just outline the most relevant general conclusions from this thesis:

1. Non Gd-based contrast agents can have great translational potential, and the Fe-NCP characterized in chapter 4 is a clear example of this. A dual enhancement performance was corroborated in in vivo studies with GL261 GB (T_1 and T_2 concurrent enhancement at a short period after administration), and satisfactory toxicological profiles were observed. It is still unclear whether the additional information provided by T_2 enhancement will be relevant for tumour diagnosis and follow-up, but the possibility of contrast administration to patients in which Gd used is discouraged is a clear advantage of this agent.

2. A volumetric, non-invasive approach for therapy response assessment was developed, based on MRSI single-slice previous studies from our group, and the application of the developed semi-supervised source analysis PR methodology.
    a. The expected GB tumour heterogeneity was confirmed by the obtained nosological imaging patterns with regions corresponding to actively proliferating, responding and normal tissue. In addition, we were able to categorize tumours into different response levels under TMZ therapy through the calculation of the TRI, tumour responding index, taking into account the percentage of responding pixels in images.
    b. The sources obtained and their location in nosological images correlated with Ki67% measurements, when displayed as number of $Ki67^{+}cells/mm^2$.
    c. An oscillating behaviour (ca. 6 day period) of TRI was seen in a GL261 GB case evaluated until endpoint, although no apparent volumetric changes took place according to T_{2w} MRI, which would be in agreement with the adaptive immune cycle length in mice. This suggests that local changes in spectral MRSI pattern could be sampling the immune system presence and attack to the tumour, which is also supported by the presence of lymphocyte-like cells in the histopathological slides of responding GL261 GB.

       If proven correct, this approach for therapy response assessment may be viable for assessing the efficiency of any therapeutic agent able to elicit immune system participation in response and could also be used for personalization of therapy cycles. This would allow to maintain or change therapy according to nosological

imaging information about immune system waves, with an evident translational interest.

3. Nanoparticle-based hyperthermia studies with laser NIR irradiation inside the MR scanner proved to be highly challenging and safety issues should be considered for future experiments.
    a. Special care should be taken with the preclinical model chosen and experimental conditions of irradiation with a tight temperature control of the system inside the scanner.
    b. Regarding nanoparticles, their synthesis should be improved to exclude presence of interfering substances which could result in confusing and harmful effects for mice viability.
    c. In addition, before embarking in hyperthermia proof-of-concept in preclinical brain tumours, it would be important to monitor adequate tumour loading with nanoparticles through PEG MRS signal in PEG-coating nanoparticles, as well as to check for differential heating with contralateral brain. Real-time brain temperature could be readily measured with the help of MRSI-based approaches.

10. References

1. Observatory GC (2012) . http://gco.iarc.fr/ . Accessed 22 Mar 2019
2. McNeill KA (2016) Epidemiology of Brain Tumors. Neurol Clin 34:981–998. https://doi.org/10.1016/j.ncl.2016.06.014
3. Eichler AF, Loeffler JS (2007) Multidisciplinary Management of Brain Metastases. Oncologist 12:884–898. https://doi.org/10.1634/theoncologist.12-7-884
4. Louis DN, Ohgaki H, Wiestler OD, et al (2007) The 2007 WHO classification of tumours of the central nervous system. Acta Neuropathol 114:97–109. https://doi.org/10.1007/s00401-007-0243-4
5. Louis DN, Perry A, Reifenberger G, et al (2016) The 2016 World Health Organization Classification of Tumors of the Central Nervous System: a summary. Acta Neuropathol 131:803–820. https://doi.org/10.1007/s00401-016-1545-1
6. Ostrom QT, Gittleman H, Fulop J, et al (2015) CBTRUS Statistical Report: Primary Brain and Central Nervous System Tumors Diagnosed in the United States in 2008-2012. Neuro Oncol 17:iv1-iv62. https://doi.org/10.1093/neuonc/nov189
7. Huse JT, Holland EC (2010) Targeting brain cancer: advances in the molecular pathology of malignant glioma and medulloblastoma. Nat Rev Cancer 10:319–331. https://doi.org/10.1038/nrc2818
8. Stupp R, Mason WP, van den Bent MJ, et al (2005) Radiotherapy plus concomitant and adjuvant temozolomide for glioblastoma. N Engl J Med 352:987–996. https://doi.org/10.1056/NEJMoa043330
9. Molnár P (2011) Classification of Primary Brain Tumors: Molecular Aspects. In: Management of CNS Tumors. Miklos Garami, IntechOpen. https://doi.org/10.5772/22484
10. Rouse C, Gittleman H, Ostrom QT, et al (2016) Years of potential life lost for brain and CNS tumors relative to other cancers in adults in the United States, 2010. Neuro Oncol 18:70–77. https://doi.org/10.1093/neuonc/nov249
11. Eder K, Kalman B (2014) Molecular Heterogeneity of Glioblastoma and its Clinical Relevance. Pathol Oncol Res 20:777–787. https://doi.org/10.1007/s12253-014-9833-3
12. Soeda A, Hara A, Kunisada T, et al (2015) The Evidence of Glioblastoma Heterogeneity. Sci Rep 5:7979. https://doi.org/10.1038/srep07979
13. Stieber D, Golebiewska A, Evers L, et al (2014) Glioblastomas are composed of genetically divergent clones with distinct tumourigenic potential and variable stem cell-associated phenotypes. Acta Neuropathol 127:203–219. https://doi.org/10.1007/s00401-013-1196-4
14. Bao S, Wu Q, McLendon RE, et al (2006) Glioma stem cells promote radioresistance by preferential activation of the DNA damage response. Nature 444:756–760. https://doi.org/10.1038/nature05236
15. Auffinger B, Spencer D, Pytel P, et al (2015) The role of glioma stem cells in chemotherapy resistance and glioblastoma multiforme recurrence. Expert Rev Neurother 15:741–752. https://doi.org/10.1586/14737175.2015.1051968
16. Wainwright DA, Chang AL, Dey M, et al (2014) Durable therapeutic efficacy utilizing combinatorial blockade against IDO, CTLA-4, and PD-L1 in mice with brain tumors. Clin

Cancer Res 20:5290–5301. https://doi.org/10.1158/1078-0432.CCR-14-0514

17. Szulzewsky F, Pelz A, Feng X, et al (2015) Glioma-associated microglia/macrophages display an expression profile different from M1 and M2 polarization and highly express Gpnmb and Spp1. PLoS One 10:e0116644. https://doi.org/10.1371/journal.pone.0116644
18. Reya T, Morrison SJ, Clarke MF, Weissman IL (2001) Stem cells, cancer, and cancer stem cells. Nature 414:105–111. https://doi.org/10.1038/35102167
19. Gilbertson RJ, Rich JN (2007) Making a tumour's bed: Glioblastoma stem cells and the vascular niche. Nat Rev Cancer 7:733–736. https://doi.org/10.1038/nrc2246
20. Chang SM, Parney IF, Huang W, et al (2005) Patterns of Care for Adults With Newly Diagnosed Malignant Glioma. JAMA 293:557–564. https://doi.org/10.1001/jama.293.5.557
21. Almeida JP, Chaichana KL, Rincon-Torroella J, Quinones-Hinojosa A (2015) The Value of Extent of Resection of Glioblastomas: Clinical Evidence and Current Approach. Curr Neurol Neurosci Rep 15:517. https://doi.org/10.1007/s11910-014-0517-x
22. Spetzler RF, Sanai N (2012) The quiet revolution: retractorless surgery for complex vascular and skull base lesions. J Neurosurg 116:291–300. https://doi.org/10.3171/2011.8.JNS101896
23. Sanai N, Mirzadeh Z, Berger MS (2008) Functional outcome after language mapping for glioma resection. N Engl J Med 358:18–27. https://doi.org/10.1056/NEJMoa067819
24. Senft C, Bink A, Franz K, et al (2011) Intraoperative MRI guidance and extent of resection in glioma surgery: A randomised, controlled trial. Lancet Oncol 12:997–1003. https://doi.org/10.1016/S1470-2045(11)70196-6
25. Halani SH, Adamson DC (2016) Clinical utility of 5-aminolevulinic acid HCl to better visualize and more completely remove gliomas. Onco Targets Ther 9:5629–5642. https://doi.org/10.2147/OTT.S97030
26. Sologuren I, Rodríguez-Gallego C, Lara PC (2014) Immune effects of high dose radiation treatment: implications of ionizing radiation on the development of bystander and abscopal effects. Transl Cancer Res 3:18–31. http://dx.doi.org/10.3978/j.issn.2218-676X.2014.02.05
27. Baskar R, Lee KA, Yeo R, Yeoh KW (2012) Cancer and radiation therapy: current advances and future directions. Int J Med Sci 9:193–199. https://doi.org/10.7150/ijms.3635
28. Barker HE, Paget JTE, Khan AA, Harrington KJ (2015) The tumour microenvironment after radiotherapy: mechanisms of resistance and recurrence. Nat Rev Cancer 15:409–425. https://doi.org/10.1038/nrc3958
29. Short S, Tobias J (2010) Radiosurgery for brain tumours. BMJ 341:c3247. https://doi.org/10.1136/bmj.c3247
30. Ken S, Vieillevigne L, Franceries X, et al (2013) Integration method of 3D MR spectroscopy into treatment planning system for glioblastoma IMRT dose painting with integrated simultaneous boost. Radiat Oncol 8:1. https://doi.org/10.1186/1748-717X-8-1
31. Guo L, Wang G, Feng Y, et al (2016) Diffusion and perfusion weighted magnetic resonance imaging for tumor volume definition in radiotherapy of brain tumors. Radiat Oncol 11:123. https://doi.org/10.1186/s13014-016-0702-y
32. Garden AS, Maor MH, Alfred Yung WK, et al (1991) Outcome and patterns of failure following limited-volume irradiation for malignant astrocytomas. Radiother Oncol 20:99–

110. https://doi.org/10.1016/0167-8140(91)90143-5
33. Norden AD, Drappatz J, Wen PY (2009) Antiangiogenic therapies for high-grade glioma. Nat Rev Neurol 5:610–620. https://doi.org/10.1038/nrneurol.2009.159
34. Stupp R, Hegi ME, Mason WP, et al (2009) Effects of radiotherapy with concomitant and adjuvant temozolomide versus radiotherapy alone on survival in glioblastoma in a randomised phase III study: 5-year analysis of the EORTC-NCIC trial. Lancet Oncol 10:459–466. https://doi.org/10.1016/S1470-2045(09)70025-7
35. Hirst TC, Vesterinen HM, Sena ES, et al (2013) Systematic review and meta-analysis of temozolomide in animal models of glioma: was clinical efficacy predicted? Br J Cancer 108:64–71. https://doi.org/10.1038/bjc.2012.504
36. McConville P, Hambardzumyan D, Moody JB, et al (2007) Magnetic resonance imaging determination of tumor grade and early response to temozolomide in a genetically engineered mouse model of glioma. Clin Cancer Res 13:2897–2904. https://doi.org/10.1158/1078-0432.CCR-06-3058
37. Dubois LG, Campanati L, Righy C, et al (2014) Gliomas and the vascular fragility of the blood brain barrier. Front Cell Neurosci 8:418. https://doi.org/10.3389/fncel.2014.00418
38. Villano JL, Seery TE, Bressler LR (2009) Temozolomide in malignant gliomas: Current use and future targets. Cancer Chemother Pharmacol 64:647–655. https://doi.org/10.1007/s00280-009-1050-5
39. Kim TG, Kim CHCKCH, Park JS, et al (2010) Immunological factors relating to the antitumor effect of temozolomide chemoimmunotherapy in a murine glioma model. Clin Vaccine Immunol 17:143–153. https://doi.org/10.1128/CVI.00292-09
40. Hegi ME, Diserens A-C, Gorlia T, et al (2005) MGMT Gene Silencing and Benefit from Temozolomide in Glioblastoma. N Engl J Med 352:997–1003. https://doi.org/10.1056/NEJMoa043331
41. Yoshimoto K, Mizoguchi M, Hata N, et al (2012) Complex DNA repair pathways as possible therapeutic targets to overcome temozolomide resistance in glioblastoma. Front Oncol 2:186. https://doi.org/10.3389/fonc.2012.00186
42. Nakada M, Nakada S, Demuth T, et al (2007) Molecular targets of glioma invasion. Cell Mol Life Sci 64:458–478. https://doi.org/10.1007/s00018-007-6342-5
43. Gilbert MR, Sulman EP, Ph D (2014) Bevacizumab for Newly Diagnosed Glioblastoma. N Engl J Med 370:2048–2049. https://doi.org/10.1056/NEJMc1403303
44. Gilbert MR, Dignam JJ, Armstrong TSTS, et al (2014) A Randomized Trial of Bevacizumab for Newly Diagnosed Glioblastoma. N Engl J Med 370:699–708. https://doi.org/10.1056/NEJMoa1308573
45. Nikkhah G, Reithmeier T, Graf E, et al (2010) BCNU for recurrent glioblastoma multiforme: efficacy, toxicity and prognostic factors. BMC Cancer 10:30. https://doi.org/10.1186/1471-2407-10-30
46. Brandes AA, Tosoni A, Amistà P, et al (2004) How effective is BCNU in recurrent glioblastoma in the modern era? A phase II trial. Neurology 63:1281–1284. https://doi.org/10.1212/01.WNL.0000140495.33615.CA
47. Vacchelli E, Aranda F, Eggermont A, et al (2014) Trial watch: IDO inhibitors in cancer therapy. Oncoimmunology 3:e957994. https://doi.org/10.4161/21624011.2014.957994
48. Zitvogel L, Apetoh L, Ghiringhelli F, Kroemer G (2008) Immunological aspects of cancer chemotherapy. Nat Rev Immunol 8:59–73. https://doi.org/10.1038/nri2216

49. Tabbekh M, Mokrani-Hammani M, Bismuth G, Mami-Chouaib F (2013) T-cell modulatory properties of CD5 and its role in antitumor immune responses. Oncoimmunology 2:e22841. https://doi.org/10.4161/onci.22841
50. Glass R, Synowitz M (2014) CNS macrophages and peripheral myeloid cells in brain tumours. Acta Neuropathol 128:347–362. https://doi.org/10.1007/s00401-014-1274-2
51. Wu J, Waxman DJ (2015) Metronomic cyclophosphamide eradicates large implanted GL261 gliomas by activating antitumor Cd8+ T-cell responses and immune memory. Oncoimmunology 4:e1005521. https://doi.org/10.1080/2162402X.2015.1005521
52. Karman J, Ling C, Sandor M, Fabry Z (2004) Initiation of immune responses in brain is promoted by local dendritic cells. J Immunol 173:2353–2361. https://doi.org/10.4049/jimmunol.173.4.2353
53. Gajewski TF, Meng Y, Blank C, et al (2006) Immune resistance orchestrated by the tumor microenvironment. Immunol Rev 213:131–145. https://doi.org/10.1111/j.1600-065X.2006.00442.x
54. Heimberger AB, Sampson JH (2011) Immunotherapy coming of age: What will it take to make it standard of care for glioblastoma? Neuro Oncol 13:3–13. https://doi.org/10.1093/neuonc/noq169
55. Platten M, Wick W, Weller M (2001) Malignant glioma biology: Role for TGF-β in growth, motility, angiogenesis, and immune escape. Microsc Res Tech 52:401–410. https://doi.org/10.1002/1097-0029(20010215)52:4<401::AID-JEMT1025>3.0.CO;2-C
56. Beatty PL, Cascio S, Lutz E (2011) Tumor immunology: Basic and clinical advances. Cancer Res 71:4338–4343. https://doi.org/10.1158/0008-5472.CAN-11-0717
57. Sadun RE, Sachsman SM, Chen X, et al (2007) Immune signatures of murine and human cancers reveal unique mechanisms of tumor escape and new targets for cancer immunotherapy. Clin Cancer Res 13:4016–4025. https://doi.org/10.1158/1078-0432.CCR-07-0016
58. Vauleon E, Avril T, Collet B, et al (2010) Overview of cellular immunotherapy for patients with glioblastoma. Clin Dev Immunol 2010:1–18. https://doi.org/10.1155/2010/689171
59. Kanaly CW, Ding D, Heimberger AB, Sampson JH (2010) Clinical Applications of a Peptide-Based Vaccine for Glioblastoma. Neurosurg Clin N Am 21:95–109. https://doi.org/10.1016/j.nec.2009.09.001
60. Kreisl TN, Kim L, Moore K, et al (2009) Phase II trial of single-agent bevacizumab followed by bevacizumab plus irinotecan at tumor progression in recurrent glioblastoma. J Clin Oncol 27:740–745. https://doi.org/10.1200/JCO.2008.16.3055
61. Dillman RO (2011) Cancer Immunotherapy. Cancer Biother Radiopharm 26:1–64. https://doi.org/10.1089/cbr.2010.0902
62. Phuphanich S, Wheeler CJ, Rudnick JD, et al (2013) Phase I trial of a multi-epitope-pulsed dendritic cell vaccine for patients with newly diagnosed glioblastoma. Cancer Immunol Immunother 62:125–135. https://doi.org/10.1007/s00262-012-1319-0
63. Fadul CE, Fisher JL, Gui J, et al (2011) Immune modulation effects of concomitant temozolomide and radiation therapy on peripheral blood mononuclear cells in patients with glioblastoma multiforme. Neuro Oncol 13:393–400. https://doi.org/10.1093/neuonc/noq204
64. Galluzzi L, Senovilla L, Zitvogel L, Kroemer G (2012) The secret ally: Immunostimulation by anticancer drugs. Nat Rev Drug Discov 11:215–233. https://doi.org/10.1038/nrd3626

65. Pasquier E, Kavallaris M, André N (2010) Metronomic chemotherapy: New rationale for new directions. Nat Rev Clin Oncol 7:455–465. https://doi.org/10.1038/nrclinonc.2010.82
66. Doloff JC, Waxman DJ (2012) VEGF receptor inhibitors block the ability of metronomically dosed cyclophosphamide to activate innate immunity-induced tumor regression. Cancer Res 72:1103–1115. https://doi.org/10.1158/0008-5472.CAN-11-3380
67. Liikanen I, Ahtiainen L, Hirvinen MLM, et al (2013) Oncolytic adenovirus with temozolomide induces autophagy and antitumor immune responses in cancer patients. Mol Ther 21:1212–1223. https://doi.org/10.1038/mt.2013.51
68. Penel N, Adenis A, Bocci G (2012) Cyclophosphamide-based metronomic chemotherapy: After 10 years of experience, where do we stand and where are we going? Crit Rev Oncol Hematol 82:40–50. https://doi.org/10.1016/j.critrevonc.2011.04.009
69. Lien K, Georgsdottir S, Sivanathan L, et al (2013) Low-dose metronomic chemotherapy: A systematic literature analysis. Eur J Cancer 49:3387–3395. https://doi.org/10.1016/j.ejca.2013.06.038
70. Vogelbaum MA, Jost S, Aghi MK, et al (2012) Application of novel response/progression measures for surgically delivered therapies for gliomas: Response Assessment in Neuro-Oncology (RANO) working group. Neurosurgery 70:234–243. https://doi.org/10.1227/NEU.0b013e318223f5a7
71. Eisenhauer EA, Therasse P, Bogaerts J, et al (2009) New response evaluation criteria in solid tumours: Revised RECIST guideline (version 1.1). Eur J Cancer 45:228–247. https://doi.org/10.1016/j.ejca.2008.10.026
72. Weller M, van den Bent M, Hopkins K, et al (2014) EANO guideline for the diagnosis and treatment of anaplastic gliomas and glioblastoma. Lancet Oncol 15:395–403. https://doi.org/10.1016/S1470-2045(14)70011-7
73. Hygino Da Cruz LC, Rodriguez I, Domingues RC, et al (2011) Pseudoprogression and pseudoresponse: Imaging challenges in the assessment of posttreatment glioma. Am J Neuroradiol 32:1978–1985. https://doi.org/10.3174/ajnr.A2397
74. Omuro A, Beal K, Gutin P, et al (2014) Phase II study of bevacizumab, temozolomide, and hypofractionated stereotactic radiotherapy for newly diagnosed glioblastoma. Clin Cancer Res 20:5023–5031. https://doi.org/10.1158/1078-0432.CCR-14-0822
75. Antunes L, Angioi-Duprez KS, Bracard SR, et al (2000) Analysis of tissue chimerism in nude mouse brain and abdominal xenograft models of human glioblastoma multiforme: What does it tell us about the models and about glioblastoma biology and therapy? J Histochem Cytochem 48:847–858. https://doi.org/10.1177/002215540004800613
76. Ferrer-Font L (2017) Tuning response to therapy in preclinical GL261 glioblastoma through CK2 targeting and temozolomide metronomic approaches: non-invasive assessment with MRI and MRSI-based molecular imaging strategies. Tesis Doctoral, Universitat Autònoma de Barcelona. In: TDX (Tesis Doctorals en Xarxa). http://www.tdx.cat/handle/10803/402400. Accessed 22 Mar 2019
77. Anido J, Sáez-Borderías A, Gonzàlez-Juncà A, et al (2010) TGF-β Receptor Inhibitors Target the CD44high/Id1high Glioma-Initiating Cell Population in Human Glioblastoma. Cancer Cell 18:655–668. https://doi.org/10.1016/j.ccr.2010.10.023
78. Pelleitier M, Montplaisir S (1975) The nude mouse: a model of deficient T-cell function. Methods Achiev Exp Pathol 7:149–166
79. Bankert RB, Egilmez NK, Hess SD (2001) Human – SCID mouse chimeric models for the

evaluation of anti-cancer therapies and their possible solutions. Trends Immunol 22:386–393. https://doi.org/10.1016/S1471-4906(01)01943-3

80. Killion JJ, Radinsky R, Fidler IJ (1998) Orthotopic models are necessary to predict therapy of transplantable tumors in mice. Cancer Metastasis Rev 17:279–284. https://doi.org/10.1023/A:1006140513233
81. Oh T, Fakurnejad S, Sayegh ET, et al (2014) Immunocompetent murine models for the study of glioblastoma immunotherapy. J Transl Med 12:107. https://doi.org/10.1186/1479-5876-12-107
82. Huszthy PC, Daphu I, Niclou SP, et al (2012) In vivo models of primary brain tumors: Pitfalls and perspectives. Neuro Oncol 14:979–993. https://doi.org/10.1093/neuonc/nos135
83. Szatmári T, Lumniczky K, Désaknai S, et al (2006) Detailed characterization of the mouse glioma 261 tumor model for experimental glioblastoma therapy. Cancer Sci 97:546–553. https://doi.org/10.1111/j.1349-7006.2006.00208.x
84. Zurita E, Chagoyen M, Cantero M, et al (2011) Genetic polymorphisms among C57BL/6 mouse inbred strains. Transgenic Res 20:481–489. https://doi.org/10.1007/s11248-010-9403-8
85. Murray WS, Little CC (1935) The Genetics of Mammary Tumor Incidence in Mice. Genetics 20:466–96. https://www.ncbi.nlm.nih.gov/pmc/articles/PMC1208626/
86. Zimmerman HM, Arnold H (1941) Experimental Brain Tumors I. Tumors Produced with Methylcholanthrene. Cancer Res 1:919–938. http://cancerres.aacrjournals.org/content/1/12/919
87. Seligman AM, Shear MJ (1939) Experimental Production of Brain Tumors in Mice with Methylcholanthrene. Stud Carcinog 37:364–395. https:// cancerres.aacrjournals.org/content/37/3/364
88. Scott OCA (1991) Tumor Transplantation and Tumor Immunity: A Personal View. Cancer Res 51:757–763. https://doi.org/10.1021/la063254s
89. Ausman JI, Shapiro WR, Rall DP (1970) Studies on the chemotherapy of experimental brain tumors: development of an experimental model. Cancer Res 30:2394–2400. http://cancerres.aacrjournals.org/content/30/9/2394
90. Delgado-Goñi T, Julià-Sapé M, Candiota AP, et al (2014) Molecular imaging coupled to pattern recognition distinguishes response to temozolomide in preclinical glioblastoma. NMR Biomed 27:1333–1345. https://doi.org/10.1002/nbm.3194
91. Gadian DG (1995) NMR and its applications to living systems, Second Edi. Oxford University Press, New York
92. MRI - Magnetic Resonance Imaging: Relaxation. https://mri-alyshamankotia.weebly.com/relaxation.html. Accessed 22 Mar 2019
93. Image contrast - Questions and Answers in MRI. http://mriquestions.com/image-contrast-trte.html. Accessed 22 Mar 2019
94. Weishaupt D, Köchli VD, Marincek B (2008) How Does MRI Work? An Introduction to the Physics and Function of Magnetic Resonance Imaging, 2nd ed. Radiology 246:724--724. https://doi.org/10.1148/radiol.2463072568
95. Kanal E, Maravilla K, Rowley HA (2014) Gadolinium contrast agents for CNS imaging: Current concepts and clinical evidence. Am J Neuroradiol 35:2215–2226. https://doi.org/10.3174/ajnr.A3917
96. Radbruch A, Lutz K, Wiestler B, et al (2012) Relevance of T2 signal changes in the

assessment of progression of glioblastoma according to the Response Assessment in Neurooncology criteria. Neuro Oncol 14:222–229. https://doi.org/10.1093/neuonc/nor200

97. Namkung S, Zech CJ, Helmberger T, et al (2007) Superparamagnetic iron oxide (SPIO)-enhanced liver MRI with ferucarbotran: Efficacy for characterization of focal liver lesions. J Magn Reson Imaging 25:755–765. https://doi.org/10.1002/jmri.20873
98. Wang Y (2011) Superparamagnetic iron oxide based MRI contrast agents: Current status of clinical application. Quant Imaging Med Surg 1:35–40. https://doi.org/10.3978/j.issn.2223-4292.2011.08.03
99. Weigle JP, Broome DR (2008) Nephrogenic systemic fibrosis: Chronic imaging findings and review of the medical literature. Skeletal Radiol 37:457–464. https://doi.org/10.1007/s00256-008-0464-1
100. Rogosnitzky M, Branch S (2016) Gadolinium-based contrast agent toxicity: a review of known and proposed mechanisms. BioMetals 29:365–376. https://doi.org/10.1007/s10534-016-9931-7
101. Ramalho J, Semelka RC, Ramalho M, et al (2016) Gadolinium-based contrast agent accumulation and toxicity: An update. Am J Neuroradiol 37:1192–1198. https://doi.org/10.3174/ajnr.A4615
102. Khawaja AZ, Cassidy DB, Al Shakarchi J, et al (2015) Revisiting the risks of MRI with Gadolinium based contrast agents-review of literature and guidelines. Insights Imaging 6:553–558. https://doi.org/10.1007/s13244-015-0420-2
103. Huang J, Zhong X, Wang L, et al (2012) Improving the magnetic resonance imaging contrast and detection methods with engineered magnetic nanoparticles. Theranostics 2:86–102. https://doi.org/10.7150/thno.4006
104. Borges M, Yu S, Laromaine A, et al (2015) Dual T_1 /T_2 MRI contrast agent based on hybrid SPION@coordination polymer nanoparticles. RSC Adv 5:86779–86783. https://doi.org/10.1039/C5RA17661A
105. Cheng K, Yang M, Zhang R, et al (2014) Hybrid nanotrimers for dual T 1 and T 2-weighted magnetic resonance imaging. ACS Nano 8:9884–9896. https://doi.org/10.1021/nn500188y
106. Tegafaw T, Xu W, Ahmad MW, et al (2015) Dual-mode T_1 and T_2 magnetic resonance imaging contrast agent based on ultrasmall mixed gadolinium-dysprosium oxide nanoparticles: synthesis, characterization, and *in vivo* application. Nanotechnology 26:365102. https://doi.org/10.1088/0957-4484/26/36/365102
107. Peng E, Wang F, Tan S, et al (2015) Tailoring a two-dimensional graphene oxide surface: dual T_1 and T_2 MRI contrast agent materials. J Mater Chem B 3:5678–5682. https://doi.org/10.1039/C5TB00902B
108. Zhao M, Beauregard DA, Loizou L, et al (2001) Non-invasive detection of apoptosis using magnetic resonance imaging and a targeted contrast agent. Nat Med 7:1241–1244. https://doi.org/10.1038/nm1101-1241
109. Sun C, Fang C, Stephen Z, et al (2008) Tumor-targeted drug delivery and MRI contrast enhancement by chlorotoxin-conjugated iron oxide nanoparticles. Nanomedicine 3:495–505. https://doi.org/10.2217/17435889.3.4.495
110. Cheng Y, Morshed RA, Auffinger B, et al (2014) Multifunctional nanoparticles for brain tumor imaging and therapy. Adv Drug Deliv Rev 66:42–57.

https://doi.org/10.1016/j.addr.2013.09.006

111. Hajek M, Dezortova M (2008) Introduction to clinical in vivo MR spectroscopy. Eur J Radiol 67:185–193. https://doi.org/10.1016/j.ejrad.2008.03.002
112. Simões R V., García-Martín ML, Cerdán S, Arús C (2008) Perturbation of mouse glioma MRS pattern by induced acute hyperglycemia. NMR Biomed 21:251–264. https://doi.org/10.1002/nbm.1188
113. Horska A, Barker PB (2010) Imaging of brain tumors: MR spectroscopy and metabolic imaging. Neuroimaging Clin N Am 20:293–310. https://doi.org/10.1016/j.nic.2010.04.003
114. De Edelenyi FS, Rubin C, Estève F, et al (2000) A new approach for analyzing proton magnetic resonance spectroscopic images of brain tumors: nosologic images. Nat Med 6:1287–1289. https://doi.org/10.1038/81401
115. Nelson SJ (2011) Assessment of therapeutic response and treatment planning for brain tumors using metabolic and physiological MRI. NMR Biomed 24:734–749. https://doi.org/10.1002/nbm.1669
116. Simões R V., Delgado-Goñi T, Lope-Piedrafita S, et al (2010) 1H-MRSI pattern perturbation in a mouse glioma: The effects of acute hyperglycemia and moderate hypothermia. NMR Biomed 23:23–33. https://doi.org/10.1002/nbm.1421
117. Delgado-Goñi T, Ortega-Martorell S, Ciezka M, et al (2016) MRSI-based molecular imaging of therapy response to temozolomide in preclinical glioblastoma using source analysis. NMR Biomed 29:732–743. https://doi.org/10.1002/nbm.3521
118. Zhu H, Barker PB (2010) MR spectroscopy and spectroscopic imaging of the brain. Methods Mol Biol 711:203–226. https://doi.org/10.1007/978-1-61737-992-5_9
119. Van Der Graaf M (2010) In vivo magnetic resonance spectroscopy: Basic methodology and clinical applications. Eur Biophys J 39:527–540. https://doi.org/10.1007/s00249-009-0517-y
120. Lupo JM, Cha S, Chang SM, Nelson SJ (2007) Analysis of metabolic indices in regions of abnormal perfusion in patients with high-grade glioma. Am J Neuroradiol 28:1455–1461. https://doi.org/10.3174/ajnr.A0586
121. Muruganandham M, Clerkin PP, Smith BJ, et al (2014) 3-dimensional magnetic resonance spectroscopic imaging at 3 Tesla for early response assessment of glioblastoma patients during external beam radiation therapy. Int J Radiat Oncol Biol Phys 90:181–189. https://doi.org/10.1016/j.ijrobp.2014.05.014
122. Zeng QS, Li CF, Zhang K, et al (2007) Multivoxel 3D proton MR spectroscopy in the distinction of recurrent glioma from radiation injury. J Neurooncol 84:63–69. https://doi.org/10.1007/s11060-007-9341-3
123. Nelson SJ, Vigneron DB, Dillon WP (1999) Serial evaluation of patients with brain tumors using volume MRI and 3D1H MRSI. NMR Biomed 12:123–138. https://doi.org/10.1002/(SICI)1099-1492(199905)12:3<123::AID-NBM541>3.0.CO;2-Y
124. Ciezka M (2015) Improvement of Protocols for Brain Cancer Diagnosis and Therapy Response Monitoring Using Magnetic Resonance Based Molecular Imaging Strategies. Tesis Doctoral, Universitat Autònoma de Barcelona. In: TDX (Tesis Doctorals en Xarxa). https://www.tdx.cat/handle/10803/666281. Accessed 22 Mar 2019
125. Nelson SJ (2003) Multivoxel Magnetic Resonance Spectroscopy of Brain Tumors. Mol Cancer Ther 2:497–507. https://doi.org/http://mct.aacrjournals.org/content/2/5/497
126. Tate AR, Underwood J, Acosta DM, et al (2006) Development of a decision support system

for diagnosis and grading of brain tumours using in vivo magnetic resonance single voxel spectra. NMR Biomed 19:411–434. https://doi.org/10.1002/nbm.1016

127. Simões RV, Ortega-Martorell S, Delgado-Goñi T, et al (2012) Improving the classification of brain tumors in mice with perturbation enhanced (PE)-MRSI. Integr Biol 4:183–191. https://doi.org/10.1039/c2ib00079b
128. Simões R V., Candiota AP, Julià-Sapé M, Arús C (2013) In vivo magnetic resonance spectroscopic imaging and ex vivo quantitative neuropathology by high resolution magic angle spinning proton magnetic resonance spectroscopy. Neuromethods 77:329–365. https://doi.org/10.1007/7657_2011_31
129. Verma A, Kumar I, Verma N, et al (2016) Magnetic resonance spectroscopy - Revisiting the biochemical and molecular milieu of brain tumors. BBA Clin 5:170–178. https://doi.org/10.1016/j.bbacli.2016.04.002
130. Cecil KM (2013) Proton magnetic resonance spectroscopy: technique for the neuroradiologist. Neuroimaging Clin N Am 23:381–392. https://doi.org/10.1016/j.nic.2012.10.003
131. Tong Z, Yamaki T, Harada K, Houkin K (2004) In vivo quantification of the metabolites in normal brain and brain tumors by proton MR spectroscopy using water as an internal standard. Magn Reson Imaging 22:1017–1024. https://doi.org/10.1016/j.mri.2004.02.007
132. Maniega SM, Cvoro V, Armitage PA, et al (2008) Choline and creatine are not reliable denominators for calculating metabolite ratios in acute ischemic stroke. Stroke 39:2467–2469. https://doi.org/10.1161/STROKEAHA.107.507020
133. Glunde K, Bhujwalla ZM, Ronen SM (2011) Choline metabolism in malignant transformation. Nat Rev Cancer 11:835–848. https://doi.org/10.1038/nrc3162
134. Berthet C, Lei H, Thevenet J, et al (2009) Neuroprotective role of lactate after cerebral ischemia. J Cereb Blood Flow Metab 29:1780–1789. https://doi.org/10.1038/jcbfm.2009.97
135. Castillo X, Rosafio K, Wyss MT, et al (2015) A probable dual mode of action for both L-and D-lactate neuroprotection in cerebral ischemia. J Cereb Blood Flow Metab 35:1561–1569. https://doi.org/10.1038/jcbfm.2015.115
136. Candiota AP, Majós C, Julià-Sapé M, et al (2011) Non-invasive grading of astrocytic tumours from the relative contents of myo-inositol and glycine measured by in vivo MRS. JBR-BTR 94:319–329. http://doi.org/10.5334/jbr-btr.698
137. Soares DP, Law M (2009) Magnetic resonance spectroscopy of the brain: review of metabolites and clinical applications. Clin Radiol 64:12–21. https://doi.org/10.1016/j.crad.2008.07.002
138. Hattingen E, Lanfermann H, Quick J, et al (2009) 1H MR spectroscopic imaging with short and long echo time to discriminate glycine in glial tumours. Magn Reson Mater Physics, Biol Med 22:33–41. https://doi.org/10.1007/s10334-008-0145-z
139. Bertholdo D, Watcharakorn A, Castillo M (2013) Brain Proton Magnetic Resonance Spectroscopy. Neuroimaging Clin N Am 23:359–380. https://doi.org/10.1016/j.nic.2012.10.002
140. Howe FA, Barton SJ, Cudlip SA, et al (2003) Metabolic profiles of human brain tumors using quantitative in vivo 1H magnetic resonance spectroscopy. Magn Reson Med 49:223–232. https://doi.org/10.1002/mrm.10367

141. Hakumäki JM, Poptani H, Sandmair AM, et al (1999) 1H MRS detects polyunsaturated fatty acid accumulation during gene therapy of glioma: implications for the in vivo detection of apoptosis. Nat Med 5:1323–1327. https://doi.org/10.1038/15279
142. Griffin JL, Lehtimäki KK, Valonen PK, et al (2003) Assignment of 1H nuclear magnetic resonance visible polyunsaturated fatty acids in BT4C gliomas undergoing ganciclovir-thymidine kinase gene therapy-induced programmed cell death. Cancer Res 63:3195–3201. http://cancerres.aacrjournals.org/content/63/12/3195.long
143. Choi C, Raisanen JM, Ganji SK, et al (2016) Prospective longitudinal analysis of 2-hydroxyglutarate magnetic resonance spectroscopy identifies broad clinical utility for the management of patients with IDH-mutant glioma. J Clin Oncol 34:4030–4039. https://doi.org/10.1200/JCO.2016.67.1222
144. Gallagher FA, Kettunen MI, Hu D-E, et al (2009) Production of hyperpolarized [1,4-13C2]malate from [1,4-13C2]fumarate is a marker of cell necrosis and treatment response in tumors. Proc Natl Acad Sci 106:19801–19806. https://doi.org/10.1073/pnas.0911447106
145. Hourani R, Horská A, Albayram S, et al (2006) Proton magnetic resonance spectroscopic imaging to differentiate between nonneoplastic lesions and brain tumors in children. J Magn Reson Imaging 23:99–107. https://doi.org/10.1002/jmri.20480
146. Nelson SJ, Kadambi AK, Park I, et al (2017) Association of early changes in 1H MRSI parameters with survival for patients with newly diagnosed glioblastoma receiving a multimodality treatment regimen. Neuro Oncol 19:430–439. https://doi.org/10.1093/neuonc/now159
147. Govindaraju V, Young K, Maudsley AA (2000) Proton NMR chemical shifts and coupling constants for brain metabolites. NMR Biomed 13:129–153. https://doi.org/10.1002/1099-1492(200005)13:3<129::AID-NBM619>3.0.CO;2-V
148. Tate AR, Griffiths JR, Martinez-Perez I, et al (1998) Towards a method for automated classification of 1H MRS spectra from brain tumours. NMR Biomed 11:177–191. https://doi.org/10.1002/(SICI)1099-1492(199806/08)11:4/5<177::AID-NBM534>3.0.CO;2-U
149. Lindon JC, Holmes E, Nicholson JK (2001) Pattern recognition methods and applications in biomedical magnetic resonance. Prog Nucl Magn Reson Spectrosc 39:1–40. https://doi.org/10.1016/S0079-6565(00)00036-4
150. Ortega-Martorell S, Olier I, Julià-Sapé M, Arús C (2010) SpectraClassifier 1.0: A user friendly, automated MRS-based classifier-development system. BMC Bioinformatics 11:106. https://doi.org/10.1186/1471-2105-11-106
151. Sajda P, Du S, Brown TR, et al (2004) Nonnegative matrix factorization for rapid recovery of constituent spectra in magnetic resonance chemical shift imaging of the brain. IEEE Trans Med Imaging 23:1453–1465. https://doi.org/10.1109/TMI.2004.834626
152. Lee DD, Seung HS (2000) Learning the parts of objects by non-negative matrix factorization. Nature 401:788–791. https://doi.org/10.1038/44565
153. Ortega-Martorell S, Lisboa PJG, Vellido A, et al (2012) Convex Non-Negative Matrix Factorization for Brain Tumor Delimitation from MRSI Data. PLoS One 7:e47824. https://doi.org/10.1371/journal.pone.0047824
154. Ding C, Li T, Jordan MI (2010) Convex and Semi-Nonnegative Matrix Factorizations for Data Clustering. IEEE Trans Pattern Anal Mach Intell 32:45–55.

https://doi.org/10.1109/TPAMI.2008.277

155. Ortega-Martorell S, Ruiz H, Vellido A, et al (2013) A novel semi-supervised methodology for extracting tumor type-specific MRS sources in human brain data. PLoS One 8:e83773. https://doi.org/10.1371/journal.pone.0083773
156. Amari SI (2001) Information geometry on hierarchy of probability distributions. IEEE Trans Inf Theory 47:1701–1711. https://doi.org/10.1109/18.930911
157. Brigger I, Dubernet C, Couvreur P (2012) Nanoparticles in cancer therapy and diagnosis. Adv Drug Deliv Rev 64:24–36. https://doi.org/10.1016/j.addr.2012.09.006
158. Farokhzad OC, Langer R (2009) Impact of nanotechnology on drug delivery. ACS Nano 3:16–20. https://doi.org/10.1021/nn900002m
159. Sethuraman VA, Lee MC, Bae YH (2008) A biodegradable pH-sensitive micelle system for targeting acidic solid tumors. Pharm Res 25:657–666. https://doi.org/10.1007/s11095-007-9480-4
160. Sailor MJ, Park J-H (2012) Hybrid Nanoparticles for Detection and Treatment of Cancer. Adv Mater 24:3779–3802. https://doi.org/10.1002/adma.201200653
161. Mohanraj VJ, Chen Y (2006) Nanoparticles–a review. Trop J Pharm Res 5:561–573. https://doi.org/10.4314/tjpr.v5i1.14634
162. Bhattacharjee S (2016) DLS and zeta potential - What they are and what they are not? J Control Release 235:337–351. https://doi.org/10.1016/j.jconrel.2016.06.017
163. Dobrovolskaia MA, Neun BW, Man S, et al (2014) Protein corona composition does not accurately predict hematocompatibility of colloidal gold nanoparticles. Nanomedicine 10:1453–1463. https://doi.org/10.1016/j.nano.2014.01.009
164. Montes Ruiz-Cabello FJ, Trefalt G, Maroni P, Borkovec M (2014) Electric double-layer potentials and surface regulation properties measured by colloidal-probe atomic force microscopy. Phys Rev E 90:012301. https://doi.org/10.1103/PhysRevE.90.012301
165. Kouchakzadeh H, Shojaosadati SA, Maghsoudi A, Vasheghani Farahani E (2010) Optimization of PEGylation Conditions for BSA Nanoparticles Using Response Surface Methodology. AAPS PharmSciTech 11:1206–1211. https://doi.org/10.1208/s12249-010-9487-8
166. Kiessling F, Mertens ME, Grimm J, Lammers T (2014) Nanoparticles for Imaging: Top or Flop? Radiology 273:10–28. https://doi.org/10.1148/radiol.14131520
167. Eatemadi A, Daraee H, Karimkhanloo H, et al (2014) Carbon nanotubes: Properties, synthesis, purification, and medical applications. Nanoscale Res Lett 9:393. https://doi.org/10.1186/1556-276X-9-393
168. Hernández-Pedro NY, Rangel-López E, Magaña-Maldonado R, et al (2013) Application of nanoparticles on diagnosis and therapy in gliomas. Biomed Res Int 2013:article ID 351031. https://doi.org/10.1155/2013/351031
169. Govindarajan S, Kitaura K, Takafuji M, et al (2013) Gene delivery into human cancer cells by cationic lipid-mediated magnetofection. Int J Pharm 446:87–99. https://doi.org/10.1016/j.ijpharm.2013.01.055
170. Krauze MT, Noble CO, Kawaguchi T, et al (2007) Convection-enhanced delivery of nanoliposomal CPT-11 (irinotecan) and PEGylated liposomal doxorubicin (Doxil) in rodent intracranial brain tumor xenografts. Neuro Oncol 9:393–403. https://doi.org/10.1215/15228517-2007-019
171. Yang FY, Teng MC, Lu M, et al (2012) Treating glioblastoma multiforme with selective high-

dose liposomal doxorubicin chemotherapy induced by repeated focused ultrasound. Int J Nanomedicine 7:965–974. https://doi.org/10.2147/IJN.S29229

172. Li Y, He H, Jia X, et al (2012) A dual-targeting nanocarrier based on poly(amidoamine) dendrimers conjugated with transferrin and tamoxifen for treating brain gliomas. Biomaterials 33:3899–3908. https://doi.org/10.1016/j.biomaterials.2012.02.004
173. An S, Nam K, Choi S, et al (2013) Nonviral gene therapy in vivo with PAM-RG4/ apoptin as a potential brain tumor therapeutic. Int J Nanomedicine 8:821–834. https://doi.org/10.2147/IJN.S39072
174. Lesniak WG, Oskolkov N, Song X, et al (2016) Salicylic Acid Conjugated Dendrimers Are a Tunable, High Performance CEST MRI NanoPlatform. Nano Lett 16:2248–2253. https://doi.org/10.1021/acs.nanolett.5b04517
175. Ouyang M, White EE, Ren H, et al (2016) Metronomic doses of temozolomide enhance the efficacy of carbon nanotube CPG immunotherapy in an invasive glioma model. PLoS One 11:e0148139. https://doi.org/10.1371/journal.pone.0148139
176. Samia ACS, Chen X, Burda C (2003) Semiconductor Quantum Dots for Photodynamic Therapy. J Am Chem Soc 125:15736–15737. https://doi.org/10.1021/ja0386905
177. Jain S, Hirst DG, O'Sullivan JM (2012) Gold nanoparticles as novel agents for cancer therapy. Br J Radiol 85:101–113. https://doi.org/10.1259/bjr/59448833
178. Von Maltzahn G, Park JH, Agrawal A, et al (2009) Computationally guided photothermal tumor therapy using long-circulating gold nanorod antennas. Cancer Res 69:3892–3900. https://doi.org/10.1158/0008-5472.CAN-08-4242
179. Abadeer NS, Murphy CJ (2016) Recent Progress in Cancer Thermal Therapy Using Gold Nanoparticles. J Phys Chem C 120:4691–4716. https://doi.org/10.1021/acs.jpcc.5b11232
180. Day ES, Zhang L, Thompson PA, et al (2012) Vascular-targeted photothermal therapy of an orthotopic murine glioma model. Nanomedicine 7:1133–1148. https://doi.org/10.2217/nnm.11.189
181. Bao C, Conde J, Pan F, et al (2016) Gold nanoprisms as a hybrid in vivo cancer theranostic platform for in situ photoacoustic imaging, angiography, and localized hyperthermia. Nano Res 9:1043–1056. https://doi.org/10.1007/s12274-016-0996-y
182. Hadjipanayis CG, Machaidze R, Kaluzova M, et al (2010) EGFRvIII antibody-conjugated iron oxide nanoparticles for magnetic resonance imaging-guided convection-enhanced delivery and targeted therapy of glioblastoma. Cancer Res 70:6303–6312. https://doi.org/10.1158/0008-5472.CAN-10-1022
183. Jiang W, Xie H, Ghoorah D, et al (2012) Conjugation of functionalized spions with transferrin for targeting and imaging brain glial tumors in rat model. PLoS One 7:e37376. https://doi.org/10.1371/journal.pone.0037376
184. Yen SK, Padmanabhan P, Selvan ST (2013) Multifunctional iron oxide nanoparticles for diagnostics, therapy and macromolecule delivery. Theranostics 3:986–1003. https://doi.org/10.7150/thno.4827
185. Chertok B, Moffat BA, David AE, et al (2008) Iron oxide nanoparticles as a drug delivery vehicle for MRI monitored magnetic targeting of brain tumors. Biomaterials 29:487–496. https://doi.org/10.1016/j.biomaterials.2007.08.050
186. Ma Z, Moulton B (2007) Supramolecular medicinal chemistry: Mixed-ligand coordination complexes. Mol Pharm 4:373–385. https://doi.org/10.1021/mp070013k
187. Novio F, Simmchen J, Vázquez-Mera N, et al (2013) Coordination polymer nanoparticles

in medicine. Coord Chem Rev 257:2839–2847. https://doi.org/10.1016/j.ccr.2013.04.022

188. Amorín-Ferré L, Busqué F, Bourdelande JL, et al (2013) Encapsulation and release mechanisms in coordination polymer nanoparticles. Chemistry (Easton) 19:17508–17516. https://doi.org/10.1002/chem.201302662
189. van der Zee J (2002) Heating the patient: A promising approach? Ann Oncol 13:1173–1184. https://doi.org/10.1093/annonc/mdf280
190. Adkins I, Fucikova J, Garg AD, et al (2014) Physical modalities inducing immunogenic tumor cell death for cancer immunotherapy. Oncoimmunology 3:12. https://doi.org/10.4161/21624011.2014.968434
191. Lal S, Clare SE, Halas NJ (2008) Nanoshell-enabled photothermal cancer therapy: Impending clinical impact. Acc Chem Res 41:1842–1851. https://doi.org/10.1021/ar800150g
192. Hirsch LR, Stafford RJ, Bankson J a, et al (2003) Nanoshell-mediated near-infrared thermal therapy of tumors under magnetic resonance guidance. Proc Natl Acad Sci U S A 100:13549–13554. https://doi.org/10.1073/pnas.2232479100
193. O'Neal DP, Hirsch LR, Halas NJ, et al (2004) Photo-thermal tumor ablation in mice using near infrared-absorbing nanoparticles. Cancer Lett 209:171–176. https://doi.org/10.1016/j.canlet.2004.02.004
194. Day ES, Thompson PA, Zhang L, et al (2011) Nanoshell-mediated photothermal therapy improves survival in a murine glioma model. J Neurooncol 104:55–63. https://doi.org/10.1007/s11060-010-0470-8
195. Schwartz JA, Shetty AM, Price RE, et al (2009) Feasibility study of particle-assisted laser ablation of brain tumors in orthotopic canine model. Cancer Res 69:1659–1667. https://doi.org/10.1158/0008-5472.CAN-08-2535
196. Cheng W, Ping Y, Zhang Y, et al (2013) Magnetic Resonance Imaging (MRI) Contrast Agents for Tumor Diagnosis. J Healthc Eng 4:23–46. https://doi.org/10.1260/2040-2295.4.1.23
197. Gahramanov S, Muldoon LL, Varallyay CG, et al (2013) Pseudoprogression of glioblastoma after chemo- and radiation therapy: diagnosis by using dynamic susceptibility-weighted contrast-enhanced perfusion MR imaging with ferumoxytol versus gadoteridol and correlation with survival. Radiology 266:842–852. https://doi.org/10.1148/radiol.12111472
198. Gaillard PJ, Visser CC, Appeldoorn CCM, Rip J (2012) Enhanced brain drug delivery: Safely crossing the blood-brain barrier. Drug Discov Today Technol 9:e155–e160. https://doi.org/10.1016/j.ddtec.2011.12.002
199. Pardridge WM (2002) Drug and gene delivery to the brain: The vascular route. Neuron 36:555–558. https://doi.org/10.1016/S0896-6273(02)01054-1
200. Oller-Salvia B, Sanchez-Navarro M, Giralt E, Teixido M (2016) Blood-brain barrier shuttle peptides: an emerging paradigm for brain delivery. Chem Soc Rev 45:4690–4707. https://doi.org/10.1039/C6CS00076B
201. European Medicines Agency - Sinerem Withdrawal. http://www.ema.europa.eu/ema/index.jsp?curl=pages/medicines/human/medicines/000801/wapp/Initial_authorisation/human_wapp_000064.jsp#. Accessed 22 Mar 2019
202. Zhao Z, Zhou Z, Bao J, et al (2013) Octapod iron oxide nanoparticles as high-performance T_2 contrast agents for magnetic resonance imaging. Nat Commun 4:2266. https://doi.org/10.1038/ncomms3266

203. Keasberry NA, Bañobre-López M, Wood C, et al (2015) Tuning the relaxation rates of dual-mode T 1 /T 2 nanoparticle contrast agents: a study into the ideal system. Nanoscale 7:16119–16128. https://doi.org/10.1039/C5NR04400F
204. Szpak A, Fiejdasz S, Prendota W, et al (2014) T1-T2 Dual-modal MRI contrast agents based on superparamagnetic iron oxide nanoparticles with surface attached gadolinium complexes. J Nanoparticle Res 16:1–11. https://doi.org/10.1007/s11051-014-2678-6
205. Bae KH, Kim YB, Lee Y, et al (2010) Bioinspired Synthesis and Characterization of Gadolinium-Labeled Magnetite Nanoparticles for Dual Contrast T1- and T2-Weighted Magnetic Resonance Imaging. Bioconjug Chem 21:505–512. https://doi.org/10.1021/bc900424u
206. Maeda H, Wu J, Sawa T, et al (2000) Tumor vascular permeability and the EPR effect in macromolecular therapeutics: A review. J Control Release 65:271–284. https://doi.org/10.1016/S0168-3659(99)00248-5
207. Dobrovolskaia MA, McNeil SE (2007) Immunological properties of engineered nanomaterials. Nat Nanotechnol 2:469–478. https://doi.org/10.1038/nnano.2007.223
208. Kim ST, Saha K, Kim C, Rotello VM (2013) The role of surface functionality in determining nanoparticle cytotoxicity. Acc Chem Res 46:681–691. https://doi.org/10.1021/ar3000647
209. Aggarwal P, Hall JB, McLeland CB, et al (2009) Nanoparticle interaction with plasma proteins as it relates to particle biodistribution, biocompatibility and therapeutic efficacy. Adv Drug Deliv Rev 61:428–437. https://doi.org/10.1016/j.addr.2009.03.009
210. Gref R, Lück M, Quellec P, et al (2000) "Stealth" corona-core nanoparticles surface modified by polyethylene glycol (PEG): Influences of the corona (PEG chain length and surface density) and of the core composition on phagocytic uptake and plasma protein adsorption. Colloids Surfaces B Biointerfaces 18:301–313. https://doi.org/10.1016/S0927-7765(99)00156-3
211. Caliceti P, Veronese FM (2003) Pharmacokinetic and biodistribution properties of poly(ethylene glycol)-protein conjugates. Adv Drug Deliv Rev 55:1261–1277. https://doi.org/10.1016/S0169-409X(03)00108-X
212. Jokerst J V, Lobovkina T, Zare RN, Gambhir SS (2011) Nanoparticle PEGylation for imaging and therapy. Nanomedicine 6:715–728. https://doi.org/10.2217/nnm.11.19
213. Zhang P, Hu L, Yin Q, et al (2012) Transferrin-modified c[RGDfK]-paclitaxel loaded hybrid micelle for sequential blood-brain barrier penetration and glioma targeting therapy. Mol Pharm 9:1590–1598. https://doi.org/10.1021/mp200600t
214. Wilhelm S, Tavares AJ, Dai Q, et al (2016) Analysis of nanoparticle delivery to tumours. Nat Rev Mater 1:16014. https://doi.org/10.1038/natrevmats.2016.14
215. Alkilany AM, Murphy CJ (2010) Toxicity and cellular uptake of gold nanoparticles: What we have learned so far? J Nanoparticle Res 12:2313–2333. https://doi.org/10.1007/s11051-010-9911-8
216. Soenen SJH, Himmelreich U, Nuytten N, De Cuyper M (2011) Cytotoxic effects of iron oxide nanoparticles and implications for safety in cell labelling. Biomaterials 32:195–205. https://doi.org/10.1016/j.biomaterials.2010.08.075
217. Tzeng SY, Green JJ (2013) Therapeutic nanomedicine for brain cancer. Ther Deliv 4:687–704. https://doi.org/10.4155/tde.13.38
218. Naqvi S, Samim M, Abdin MZ, et al (2010) Concentration-dependent toxicity of iron oxide nanoparticles mediated by increased oxidative stress. Int J Nanomedicine 5:983–989.

https://doi.org/10.2147/IJN.S13244

219. Alkilany AM, Nagaria PK, Hexel CR, et al (2009) Cellular uptake and cytotoxicity of gold nanorods: Molecular origin of cytotoxicity and surface effects. Small 5:701–708. https://doi.org/10.1002/smll.200801546
220. Lewinski N, Colvin V, Drezek R (2008) Cytotoxicity of nanoparticles. Small 4:26–49. https://doi.org/10.1002/smll.200700595
221. Aillon KL, Xie Y, El-Gendy N, et al (2009) Effects of nanomaterial physicochemical properties on in vivo toxicity. Adv. Drug Deliv. Rev. 61:457–466. https://doi.org/10.1016/j.addr.2009.03.010
222. Zhang XD, Wu D, Shen X, et al (2011) Size-dependent in vivo toxicity of PEG-coated gold nanoparticles. Int J Nanomedicine 6:2071–2081. https://doi.org/10.2147/IJN.S21657
223. Abdelhalim MAK (2011) Gold nanoparticles administration induces disarray of heart muscle, hemorrhagic, chronic inflammatory cells infiltrated by small lymphocytes, cytoplasmic vacuolization and congested and dilated blood vessels. Lipids Health Dis 10:233. https://doi.org/10.1186/1476-511X-10-233
224. Fröhlich E (2018) Comparison of conventional and advanced in vitro models in the toxicity testing of nanoparticles. Artif Cells, Nanomedicine, Biotechnol 46:1091–1107. https://doi.org/10.1080/21691401.2018.1479709
225. Li Y, Boraschi D (2016) Endotoxin contamination: a key element in the interpretation of nanosafety studies. Nanomedicine 11:269–287. https://doi.org/10.2217/nnm.15.196
226. Copeland S, Warren HS, Lowry SF, et al (2005) Acute inflammatory response to endotoxin in mice and humans. Clin Diagn Lab Immunol 12:60–67. https://doi.org/10.1128/CDLI.12.1.60
227. Karpman D, Connell H, Svensson M, et al (1997) The role of lipopolysaccharide and Shiga-like toxin in a mouse model of Escherichia coli O157:H7 infection. J Infect Dis 175:611–620. https://doi.org/10.1093/infdis/175.3.611
228. Gorbet MB, Sefton M V. (2005) Endotoxin: The uninvited guest. Biomaterials 26:6811–6817. https://doi.org/10.1016/j.biomaterials.2005.04.063
229. Smulders S, Kaiser J-P, Zuin S, et al (2012) Contamination of nanoparticles by endotoxin: evaluation of different test methods. Part Fibre Toxicol 9:41. https://doi.org/10.1186/1743-8977-9-41
230. GABMRN Dynamic MRSI Processing Module. http://gabrmn.uab.es/DMPM. Accessed 22 Mar 2019
231. Candiota AP, Acosta M, Simões RV, et al (2014) A new ex vivo method to evaluate the performance of candidate MRI contrast agents: a proof-of-concept study. J Nanobiotechnology 12:12. https://doi.org/10.1186/1477-3155-12-12
232. Suárez-García S, Arias-Ramos N, Frias C, et al (2018) Dual T1/ T2 Nanoscale Coordination Polymers as Novel Contrast Agents for MRI: A Preclinical Study for Brain Tumor. ACS Appl Mater Interfaces 10:38819–38832. https://doi.org/10.1021/acsami.8b15594
233. Kratz F (2008) Albumin as a drug carrier: Design of prodrugs, drug conjugates and nanoparticles. J Control Release 132:171–183. https://doi.org/10.1016/j.jconrel.2008.05.010
234. Elzoghby AO, Samy WM, Elgindy NA (2012) Albumin-based nanoparticles as potential controlled release drug delivery systems. J Control Release 157:168–182. https://doi.org/10.1016/j.jconrel.2011.07.031

235. Novio F, Lorenzo J, Nador F, et al (2014) Carboxyl group (-CO2H) functionalized coordination polymer nanoparticles as efficient platforms for drug delivery. Chemistry (Easton) 20:15443–15450. https://doi.org/10.1002/chem.201403441
236. Högemann D, Ntziachristos V, Josephson L, Weissleder R (2002) High Throughput Magnetic Resonance Imaging for Evaluating Targeted Nanoparticle Probes. Bioconjug Chem 13:116–121. https://doi.org/10.1021/bc015549h
237. Nador F, Novio F, Ruiz-Molina D (2014) Coordination Polymer Particles with ligand-centred pH-responses and spin transition. Chem Commun 50:14570–14572. https://doi.org/10.1039/c4cc05299d
238. Saldaña-Ruíz S, Soler-Martín C, Llorens J (2012) Role of CYP2E1-mediated metabolism in the acute and vestibular toxicities of nineteen nitriles in the mouse. Toxicol Lett 208:125–132. https://doi.org/10.1016/j.toxlet.2011.10.016
239. Funk F, Ryle P, Canclini C, et al (2010) The new generation of intravenous iron: chemistry, pharmacology, and toxicology of ferric carboxymaltose. Arzneimittelforschung 60:345–353. https://doi.org/10.1055/s-0031-1296299
240. Vermeij EA, Koenders MI, Bennink MB, et al (2015) The In-vivo use of superparamagnetic iron oxide nanoparticles to detect inflammation elicits a cytokine response but does not aggravate experimental arthritis. PLoS One 10:e0126687. https://doi.org/10.1371/journal.pone.0126687
241. LASA/NC3Rs (2009) Guidance on dose level selection for regulatory general toxicology studies for pharmaceuticals. http://www.lasa.co.uk/pdf/lasa-nc3rsdoselevelselection.pdf
242. Wright PJ, Mougin OE, Totman JJ, et al (2008) Water proton T1 measurements in brain tissue at 7, 3, and 1.5 T using IR-EPI, IR-TSE, and MPRAGE: results and optimization. Magn Reson Mater Phy 21:121–130. https://doi.org/10.1007/s10334-008-0104-8
243. de Graaf RA, Brown PB, McIntyre S, et al (2006) High magnetic field water and metabolite proton T1 and T2 relaxation in rat brain in vivo. Magn Reson Med 56:386–394. https://doi.org/10.1002/mrm.20946
244. The Jackson Laboratory. Body weight information for C57BL/6J. https://www.jax.org/jax-mice-and-services/strain-data-sheet-pages/body-weight-chart-000664. Accessed 22 Mar 2019
245. Bradley WG (1993) MR appearance of hemorrhage in the brain. Radiology 189:15–26. https://doi.org/10.1148/radiology.189.1.8372185
246. Sieber MA, Steger-Hartmann T, Lengsfeld P, Pietsch H (2009) Gadolinium-based contrast agents and NSF: Evidence from animal experience. J Magn Reson Imaging 30:1268–1276. https://doi.org/10.1002/jmri.21971
247. Todd DJ, Kay J (2016) Gadolinium-induced fibrosis. Annu Rev Med 67:273–291. https://doi.org/10.1146/annurev-med-063014-124936
248. Shin T-H, Choi J, Yun S, et al (2014) T1 and T2 Dual-Mode MRI Contrast Agent for Enhancing Accuracy by Engineered Nanomaterials. ACS Nano 8:3393–3401. https://doi.org/10.1021/nn405977t
249. Faraji AH, Wipf P (2009) Nanoparticles in cellular drug delivery. Bioorganic Med Chem 17:2950–2962. https://doi.org/10.1016/j.bmc.2009.02.043
250. Yang Y, Liu J, Liang C, et al (2016) Nanoscale Metal-Organic Particles with Rapid Clearance for Magnetic Resonance Imaging-Guided Photothermal Therapy. ACS Nano 10:2774–2781. https://doi.org/10.1021/acsnano.5b07882

251. Na JH, Lee SY, Lee S, et al (2012) Effect of the stability and deformability of self-assembled glycol chitosan nanoparticles on tumor-targeting efficiency. J Control Release 163:2–9. https://doi.org/10.1016/j.jconrel.2012.07.028
252. Gu L, Fang RH, Sailor MJ, Park JH (2012) In vivo clearance and toxicity of monodisperse iron oxide nanocrystals. ACS Nano 6:4947–4954. https://doi.org/10.1021/nn300456z
253. Wei Y, Zhao M, Yang F, et al (2016) Iron overload by Superparamagnetic Iron Oxide Nanoparticles is a High Risk Factor in Cirrhosis by a Systems Toxicology Assessment. Sci Rep 6:29110. https://doi.org/10.1038/srep29110
254. Zúñiga JM, Orellana JM, Tur JM (2008) Ciencia y Tecnología del Animal de Laboratorio. Ed: Universidad de Alcalá de Henares, Sociedad Española para las Ciencias del Animal de Laboratorio (SECAL), Alcalá de Henares
255. Gozzard D (2011) When is high-dose intravenous iron repletion needed? Assessing new treatment options. Drug Des Devel Ther 5:51–60. https://doi.org/10.2147/DDDT.S15817
256. Delgado-Goñi T, Martín-Sitjar J, Simões R V., et al (2013) Dimethyl sulfoxide (DMSO) as a potential contrast agent for brain tumors. NMR Biomed 26:173–184. https://doi.org/10.1002/nbm.2832
257. Bogner W, Hess AT, Gagoski B, et al (2014) Real-time motion- and B0-correction for LASER-localized spiral-accelerated 3D-MRSI of the brain at 3T. Neuroimage 88:22–31. https://doi.org/10.1016/j.neuroimage.2013.09.034
258. van der Graaf M, Julià-Sapé M, Howe FA, et al (2008) MRS quality assessment in a multicentre study on MRS-based classification of brain tumours. NMR Biomed 21:148–158. https://doi.org/10.1002/nbm.1172
259. Ciezka M, Acosta M, Herranz C, et al (2016) Development of a transplantable glioma tumour model from genetically engineered mice: MRI/MRS/MRSI characterisation. J Neurooncol 129:67–76. https://doi.org/10.1007/s11060-016-2164-3
260. Lin A, Tran T, Bluml S, et al (2012) Guidelines for acquiring and reporting clinical neurospectroscopy. Semin Neurol 32:432–453. https://doi.org/10.1055/s-0032-1331814
261. Simonetti AW, Melssen WJ, Van der Graaf M, et al (2003) A Chemometric Approach for Brain Tumor Classification Using Magnetic Resonance Imaging and Spectroscopy. Anal Chem 75:5352–5361. https://doi.org/10.1021/ac034541t
262. Maudsley AA, Domenig C, Govind V, et al (2009) Mapping of brain metabolite distributions by volumetric proton MR spectroscopic imaging (MRSI). Magn Reson Med 61:548–559. https://doi.org/10.1002/mrm.21875
263. Arias-Ramos N, Ferrer-Font L, Lope-Piedrafita S, et al (2017) Metabolomics of Therapy Response in Preclinical Glioblastoma: A Multi-Slice MRSI-Based Volumetric Analysis for Noninvasive Assessment of Temozolomide Treatment. Metabolites 7:20. https://doi.org/10.3390/METABO7020020
264. Rémy C, Arús C, Ziegler A, et al (1994) In Vivo, Ex Vivo, and In Vitro One- and Two-Dimensional Nuclear Magnetic Resonance Spectroscopy of an Intracerebral Glioma in Rat Brain: Assignment of Resonances. J Neurochem 62:166–179. https://doi.org/10.1046/j.1471-4159.1994.62010166.x
265. Barba I, Cabañas ME, Arús C (1999) The relationship between nuclear magnetic resonance-visible lipids, lipid droplets, and cell proliferation in cultured C6 cells. Cancer Res 59:1861–1868. https://doi.org/10.1007/s00268-011-0971-4
266. Barba I, Mann P, Cabañas ME, et al (2001) Mobile lipid production after confluence and

pH stress in perfused C6 cells. NMR Biomed 14:33–40. https://doi.org/10.1002/nbm.688

267. Valverde D, Quintero MR, Candiota AP, et al (2006) Analysis of the changes in the 1H NMR spectral pattern of perchloric acid extracts of C6 cells with growth. NMR Biomed 19:223–230. https://doi.org/10.1002/nbm.1024
268. Davila M, Candiota AP, Pumarola M, Arus C (2012) Minimization of spectral pattern changes during HRMAS experiments at 37 degrees celsius by prior focused microwave irradiation. Magn Reson Mater Phy 25:401–410. https://doi.org/10.1007/s10334-012-0303-1
269. Hulsey KM, Mashimo T, Banerjee A, et al (2015) (1)H MRS characterization of neurochemical profiles in orthotopic mouse models of human brain tumors. NMR Biomed 28:108–115. https://doi.org/10.1002/nbm.3231
270. Candiota AP, Majos C, Bassols A, et al (2004) Assignment of the 2.03 ppm resonance in in vivo 1H MRS of human brain tumour cystic fluid: contribution of macromolecules. Magn Reson Mater Phy 17:36–46. https://doi.org/10.1007/s10334-004-0043-y
271. McKnight TR, Noworolski SM, Vigneron DB, Nelson SJ (2001) An automated technique for the Quantitative assessment of 3D-MRSI data from patients with glioma. J Magn Reson Imaging 13:167–177. https://doi.org/10.1002/1522-2586(200102)13:2<167::AID-JMRI1026>3.0.CO;2-K
272. Ratai E-M, Zhang Z, Snyder BS, et al (2013) Magnetic resonance spectroscopy as an early indicator of response to anti-angiogenic therapy in patients with recurrent glioblastoma: RTOG 0625/ACRIN 6677. Neuro Oncol 15:936–944. https://doi.org/10.1093/neuonc/not044
273. Hattingen E, Jurcoane A, Bähr O, et al (2011) Bevacizumab impairs oxidative energy metabolism and shows antitumoral effects in recurrent glioblastomas: A 31P/ 1H MRSI and quantitative magnetic resonance imaging study. Neuro Oncol 13:1349–1363. https://doi.org/10.1093/neuonc/nor132
274. Provencher SW (2001) Automatic quantitation of localized in vivo1H spectra with LCModel. NMR Biomed 14:260–264. https://doi.org/10.1002/nbm.698
275. Segerman A, Niklasson M, Haglund C, et al (2016) Clonal Variation in Drug and Radiation Response among Glioma-Initiating Cells Is Linked to Proneural-Mesenchymal Transition. Cell Rep 17:2994–3009. https://doi.org/10.1016/j.celrep.2016.11.056
276. Hall DE, Moffat BA, Stojanovska J, et al (2004) Therapeutic efficacy of DTI-015 using diffusion magnetic resonance imaging as an early surrogate marker. Clin Cancer Res 10:7852–7859. https://doi.org/10.1158/1078-0432.CCR-04-1218
277. Oborski MJ, Laymon CM, Qian Y, et al (2014) Challenges and Approaches to Quantitative Therapy Response Assessment in Glioblastoma Multiforme Using the Novel Apoptosis Positron Emission Tomography Tracer F-18 ML-10. Transl Oncol 7:111–119. https://doi.org/10.1593/tlo.13868
278. Xue S, Song G, Yu J (2017) The prognostic significance of PD-L1 expression in patients with glioma: A meta-analysis. Sci Rep 7:4231. https://doi.org/10.1038/s41598-017-04023-x
279. El Meskini R, Iacovelli AJ, Kulaga A, et al (2015) A preclinical orthotopic model for glioblastoma recapitulates key features of human tumors and demonstrates sensitivity to a combination of MEK and PI3K pathway inhibitors. Dis Model Mech 8:45–56. https://doi.org/10.1242/dmm.018168
280. Zheng Y, McFarland BC, Drygin D, et al (2013) Targeting protein kinase CK2 suppresses

prosurvival signaling pathways and growth of glioblastoma. Clin Cancer Res 19:6484–6494. https://doi.org/10.1158/1078-0432.CCR-13-0265

281. Mastronardi L, Guiducci A, Puzzilli F, Ruggeri A (1999) Relationship between Ki-67 labeling index and survival in high-grade glioma patients treated after surgery with tamoxifen. J Neurosurg Sci 43:263–270. https://www.minervamedica.it/en/journals/neurosurgical-sciences/article.php?cod=R38Y1999N04A0263&acquista=1
282. Skjulsvik AJ, Mørk JN, Torp MO, Torp SH (2014) Ki-67/MIB-1 immunostaining in a cohort of human gliomas. Int J Clin Exp Pathol 7:8905–8910. https://www.ncbi.nlm.nih.gov/pmc/articles/PMC4313958/
283. Perry A, Schmidt RE (2006) Cancer therapy-associated CNS neuropathology: An update and review of the literature. Acta Neuropathol 111:197–212. https://doi.org/10.1007/s00401-005-0023-y
284. Lucas DR, Kshirsagar MP, Biermann JS, et al (2008) Histologic Alterations from Neoadjuvant Chemotherapy in High-Grade Extremity Soft Tissue Sarcoma: Clinicopathological Correlation. Oncologist 13:451–458. https://doi.org/10.1634/theoncologist.2007-0220
285. Ferrer-Font L, Villamañan L, Arias-Ramos N, et al (2017) Targeting Protein Kinase CK2: Evaluating CX-4945 Potential for GL261 Glioblastoma Therapy in Immunocompetent Mice. Pharmaceuticals 10:24. https://doi.org/10.3390/PH10010024
286. Wu J, Jordan M, Waxman DJ (2016) Metronomic cyclophosphamide activation of anti-tumor immunity: tumor model, mouse host, and drug schedule dependence of gene responses and their upstream regulators. BMC Cancer 16:623. https://doi.org/10.1186/s12885-016-2597-2
287. Chen DS, Mellman I (2013) Oncology meets immunology: The cancer-immunity cycle. Immunity 39:1–10. https://doi.org/10.1016/j.immuni.2013.07.012
288. Vacchelli E, Aranda F, Eggermont A, et al (2014) Trial Watch: Chemotherapy with immunogenic cell death inducers. Oncoimmunology 3:e27878. https://doi.org/10.4161/onci.27878
289. Balermpas P, Michel Y, Wagenblast J, et al (2014) Tumour-infiltrating lymphocytes predict response to definitive chemoradiotherapy in head and neck cancer. Br J Cancer 110:501–509. https://doi.org/10.1038/bjc.2013.640
290. Tang J, Flomenberg P, Harshyne L, et al (2005) Cancer Therapy : Preclinical Glioblastoma Patients Exhibit Circulating Tumor-Specific CD8+ T Cells. Clin Cancer Res 11:5292–5299. https://doi.org/10.1158/1078-0432.CCR-05-0545
291. Ehtesham M, Samoto K, Kabos P, et al (2002) Treatment of intracranial glioma with in situ interferon-gamma and tumor necrosis factor-alpha gene transfer. Cancer Gene Ther 9:925–934. https://doi.org/10.1038/sj.cgt.7700516
292. Candolfi M, Curtin JF, Nichols WS, et al (2007) Intracranial glioblastoma models in preclinical neuro-oncology: Neuropathological characterization and tumor progression. J Neurooncol 85:133–148. https://doi.org/10.1007/s11060-007-9400-9
293. Nakamura R, Nishimura T, Ochiai T, et al (2013) Availability of a Microglia and Macrophage Marker, Iba-1, for Differential Diagnosis of Spontaneous Malignant Reticuloses from Astrocytomas in Rats. J Toxicol Pathol 26:55–60. https://doi.org/10.1293/tox.26.55
294. Garofalo S, Porzia A, Mainiero F, et al (2017) Environmental stimuli shape microglial plasticity in glioma. Elife 6:pii: e33415. https://doi.org/10.7554/eLife.33415

295. Preciado-Flores S, Wang D, Wheeler DA, et al (2011) Highly reproducible synthesis of hollow gold nanospheres with near infrared surface plasmon absorption using PVP as stabilizing agent. J Mater Chem 21:2344–2350. https://doi.org/10.1039/C0JM03690K
296. Cebrián V, Martín-Saavedra F, Gómez L, et al (2013) Enhancing of plasmonic photothermal therapy through heat-inducible transgene activity. Nanomedicine Nanotechnology, Biol Med 9:646–656. https://doi.org/10.1016/j.nano.2012.11.002
297. Gomez L, Sebastian V, Irusta S, et al (2014) Scaled-up production of plasmonic nanoparticles using microfluidics: from metal precursors to functionalized and sterilized nanoparticles. Lab Chip 14:325–332. https://doi.org/10.1039/c3lc50999k
298. Gomez L, Cebrian V, Martin-Saavedra F, et al (2013) Stability and biocompatibility of photothermal gold nanorods after lyophilization and sterilization. Mater Res Bull 48:4051–4057. https://doi.org/10.1016/j.materresbull.2013.06.034
299. Mazzaccara C, Labruna G, Cito G, et al (2008) Age-related reference intervals of the main biochemical and hematological parameters in C57BL/6J, 129SV/EV and C3H/HeJ mouse strains. PLoS One 3:e3772. https://doi.org/10.1371/journal.pone.0003772
300. Charles River C57BL/6 Mice. https://www.criver.com/products-services/find-model/c57bl6-mouse?region=3661. Accessed 22 Mar 2019
301. Bruehlmeier M, Roelcke U, Bläuenstein P, et al (2003) Measurement of the extracellular space in brain tumors using 76Br-bromide and PET. J Nucl Med 44:1210–8. http://jnm.snmjournals.org/content/44/8/1210.long
302. Kiyatkin EA (2007) Physiological and pathological brain hyperthermia. Prog Brain Res 162:219–243. https://doi.org/10.1016/S0079-6123(06)62012-8
303. Karnatovskaia L V, Wartenberg KE, Freeman WD (2014) Therapeutic Hypothermia for Neuroprotection: History, Mechanisms, Risks, and Clinical Applications. The Neurohospitalist 4:153–163. https://doi.org/10.1177/1941874413519802
304. Mouratidis PXE, Rivens I, Ter Haar G (2015) A study of thermal dose-induced autophagy, apoptosis and necroptosis in colon cancer cells. Int J Hyperth 31:476–488. https://doi.org/10.3109/02656736.2015.1029995
305. Blanco E, Shen H, Ferrari M (2015) Principles of nanoparticle design for overcoming biological barriers to drug delivery. Nat Biotechnol 33:941–951. https://doi.org/10.1038/nbt.3330
306. Wang H, Wang B, Normoyle KP, et al (2014) Brain temperature and its fundamental properties: A review for clinical neuroscientists. Front Neurosci 8:307. https://doi.org/10.3389/fnins.2014.00307
307. Tsai S, Chen Y, Liaw J (2008) Compound cellular imaging of laser scanning confocal microscopy by using gold nanoparticles and dyes. Sensors 8:2306–2316. https://doi.org/10.3390/s8042306
308. Cabada TF, de Pablo CSL, Serrano AM, et al (2012) Induction of cell death in a glioblastoma line by hyperthermic therapy based on gold nanorods. Int J Nanomedicine 7:1511–1523. https://doi.org/10.2147/IJN.S28470
309. Malyala P, Singh M (2008) Endotoxin limits in formulations for preclinical research. J Pharm Sci 97:2041–2044. https://doi.org/10.1002/jps.21152
310. Li Y, Italiani P, Casals E, et al (2014) Optimising the use of commercial LAL assays for the analysis of endotoxin contamination in metal colloids and metal oxide nanoparticles. Nanotoxicology 5390:1–12. https://doi.org/10.3109/17435390.2014.948090

311. Tremoleda JL, Kerton A, Gsell W (2012) Anaesthesia and physiological monitoring during in vivo imaging of laboratory rodents: Considerations on experimental outcomes and animal welfare. EJNMMI Res 2:1–23. https://doi.org/10.1186/2191-219X-2-44
312. Erhardt W, Lendl C, Hipp R, et al (1990) The use of pulse oximetry in clinical veterinary anaesthesia. Vet Anaesth Analg 17:30–31. https://doi.org/10.1111/j.1467-2995.1990.tb00385.x
313. Zhang Z, Hallac RR, Peschke P, Mason RP (2014) A noninvasive tumor oxygenation imaging strategy using magnetic resonance imaging of endogenous blood and tissue water. Magn Reson Med 71:561–569. https://doi.org/10.1002/mrm.24691
314. Hallac RR, Zhou H, Pidikiti R, et al (2014) Correlations of noninvasive BOLD and TOLD MRI with pO2 and relevance to tumor radiation response. Magn Reson Med 71:1863–1873. https://doi.org/10.1002/mrm.24846
315. Dunn AW, Zhang Y, Mast D, et al (2016) In-vitro depth-dependent hyperthermia of human mammary gland adenocarcinoma. Mater Sci Eng C 69:12–16. https://doi.org/10.1016/j.msec.2016.06.026
316. Chen J, Glaus C, Laforest R, et al (2010) Gold nanocages as photothermal transducers for cancer treatment. Small 6:811–817. https://doi.org/10.1002/smll.200902216
317. Shi J, Zhang Y, Fu WM, et al (2015) Establishment of C6 brain glioma models through stereotactic technique for laser interstitial thermotherapy research. Surg Neurol Int 6:51. https://dx.doi.org/10.4103/2152-7806.154451
318. Schulze PC, Adams V, Busert C, et al (2002) Effects of laser-induced thermotherapy (LITT) on proliferation and apoptosis of glioma cells in rat brain transplantation tumors. Lasers Surg Med 30:227–232. https://doi.org/10.1002/lsm.10019
319. Lu W, Melancon MP, Xiong C, et al (2011) Effects of photoacoustic imaging and photothermal ablation therapy mediated by targeted hollow gold nanospheres in an orthotopic mouse xenograft model of glioma. Cancer Res 71:6116–6121. https://doi.org/10.1158/0008-5472.CAN-10-4557
320. Carpentier A, Chauvet D, Reina V, et al (2012) MR-guided Laser-Induced Thermal Therapy (LITT) for recurrent glioblastomas. Lasers Surg Med 44:361–368. https://doi.org/10.1002/lsm.22025
321. Stafford RJ, Price RE, Diederich CJ, et al (2004) Interleaved echo-planar imaging for fast multiplanar magnetic resonance temperature imaging of ultrasound thermal ablation therapy. J Magn Reson Imaging 20:706–714. https://doi.org/10.1002/jmri.20157
322. Wan J, Wang JH, Liu T, et al (2015) Surface chemistry but not aspect ratio mediates the biological toxicity of gold nanorods in vitro and in vivo. Sci Rep 5:11398. https://doi.org/10.1038/srep11398
323. Niidome T, Yamagata M, Okamoto Y, et al (2006) PEG-modified gold nanorods with a stealth character for in vivo applications. J Control Release 114:343–347. https://doi.org/10.1016/j.jconrel.2006.06.017
324. Mendes M, Sousa JJ, Pais A, Vitorino C (2018) Targeted theranostic nanoparticles for brain tumor treatment. Pharmaceutics 10:pii: E181. https://doi.org/10.3390/pharmaceutics10040181
325. Cho WS, Cho M, Jeong JJ, et al (2009) Acute toxicity and pharmacokinetics of 13??nm-sized PEG-coated gold nanoparticles. Toxicol Appl Pharmacol 236:16–24. https://doi.org/10.1016/j.taap.2008.12.023

326. Lopez-Chaves C, Soto-Alvaredo J, Montes-Bayon M, et al (2018) Gold nanoparticles: Distribution, bioaccumulation and toxicity. In vitro and in vivo studies. Nanomedicine 14:1–12. https://doi.org/10.1016/j.nano.2017.08.011
327. Yu Y, Wu Y, Liu J, et al (2016) Metabolizable dopamine-coated gold nanoparticle aggregates: preparation, characteristics, computed tomography imaging, acute toxicity, and metabolism in vivo. J Mater Chem B 4:1090–1099. https://doi.org/10.1039/C5TB02497H
328. Li B, Zhang XY, Yang JZ, et al (2014) Influence of polyethylene glycol coating on biodistribution and toxicity of nanoscale graphene oxide in mice after intravenous injection. Int J Nanomedicine 9:4697–4707. https://doi.org/10.2147/IJN.S66591
329. Zhang XD, Wu HY, Wu D, et al (2010) Toxicologic effects of gold nanoparticles in vivo by different administration routes. Int J Nanomedicine 5:771–781. https://doi.org/10.2147/IJN.S8428
330. Leonov AP, Zheng J, Clogston JD, et al (2008) Detoxification of gold nanorods by treatment with polystyrenesulfonate. ACS Nano 2:2481–2488. https://doi.org/10.1021/nn800466c
331. Stupp R, Roila F (2009) Malignant glioma: ESMO clinical recommendations for diagnosis, treatment and follow-up. Ann Oncol 20:iv126-iv128. https://doi.org/10.1093/annonc/mdp151
332. Patrizii M, Bartucci M, Pine SR, Sabaawy HE (2018) Utility of Glioblastoma Patient-Derived Orthotopic Xenografts in Drug Discovery and Personalized Therapy. Front Oncol 8:23. https://doi.org/10.3389/fonc.2018.00023
333. Joo KM, Kim J, Jin J, et al (2013) Patient-Specific Orthotopic Glioblastoma Xenograft Models Recapitulate the Histopathology and Biology of Human Glioblastomas In Situ. Cell Rep 3:260–273. https://doi.org/10.1016/j.celrep.2012.12.013
334. William D, Mullins CS, Schneider BB, et al (2017) Optimized creation of glioblastoma patient derived xenografts for use in preclinical studies. J Transl Med 15:27. https://doi.org/10.1186/s12967-017-1128-5
335. Reardon DA, Gokhale PC, Klein SR, et al (2016) Glioblastoma Eradication Following Immune Checkpoint Blockade in an Orthotopic, Immunocompetent Model. Cancer Immunol Res 4:124–135. https://doi.org/10.1158/2326-6066.CIR-15-0151
336. Towner RA, Ihnat M, Saunders D, et al (2015) A new anti-glioma therapy, AG119: Pre-clinical assessment in a mouse GL261 glioma model. BMC Cancer 15:522. https://doi.org/10.1186/s12885-015-1538-9
337. Ferrer-Font L, Arias-Ramos N, Lope-Piedrafita S, et al (2017) Metronomic treatment in immunocompetent preclinical GL261 glioblastoma: effects of cyclophosphamide and temozolomide. NMR Biomed 30:e3748. https://doi.org/10.1002/nbm.3748
338. Park JM, Recht LD, Josan S, et al (2013) Metabolic response of glioma to dichloroacetate measured in vivo by hyperpolarized13C magnetic resonance spectroscopic imaging. Neuro Oncol 15:433–441. https://doi.org/10.1093/neuonc/nos319
339. Park I, Bok R, Ozawa T, et al (2011) Detection of early response to temozolomide treatment in brain tumors using hyperpolarized 13C MR metabolic imaging. J Magn Reson Imaging 33:1284–1290. https://doi.org/10.1002/jmri.22563
340. Agnes RS, Broome A-M, Wang J, et al (2012) An Optical Probe for Noninvasive Molecular Imaging of Orthotopic Brain Tumors Overexpressing Epidermal Growth Factor Receptor. Mol Cancer Ther 11:2202–2211. https://doi.org/10.1158/1535-7163.MCT-12-0211

341. Jarzabek MA, Huszthy PC, Skaftnesmo KO, et al (2013) In vivo bioluminescence imaging validation of a human biopsy-derived orthotopic mouse model of glioblastoma multiforme. Mol Imaging 12:161–72. https://doi.org/10.2310/7290.2012.00029
342. Villanueva-Meyer JE, Mabray MC, Cha S (2017) Current Clinical Brain Tumor Imaging. Neurosurgery 81:397–415. https://doi.org/10.1093/neuros/nyx103
343. Olchowy C, Cebulski K, Łasecki M, et al (2017) The presence of the gadolinium-based contrast agent depositions in the brain and symptoms of gadolinium neurotoxicity-A systematic review. PLoS One 12:e0171704. https://doi.org/10.1371/journal.pone.0171704
344. Zhou Z, Lu Z-R (2013) Gadolinium-based contrast agents for magnetic resonance cancer imaging. Wiley Interdiscip Rev Nanomedicine Nanobiotechnology 5:1–18. https://doi.org/10.1002/wnan.1198
345. Jeong Y, Na K (2018) Synthesis of a gadolinium based-macrocyclic MRI contrast agent for effective cancer diagnosis. Biomater Res 22:17. https://doi.org/10.1186/s40824-018-0127-9
346. Zhou Z, Bai R, Munasinghe J, et al (2017) T 1 – T 2 Dual-Modal Magnetic Resonance Imaging: From Molecular Basis to Contrast Agents. ACS Nano 11:5227–5232. https://doi.org/10.1021/acsnano.7b03075
347. Soares MP, Hamza I (2016) Macrophages and Iron Metabolism. Immunity 44:492–504. https://doi.org/10.1016/j.immuni.2016.02.016
348. Sottoriva A, Spiteri I, Piccirillo SGM, et al (2013) Intratumor heterogeneity in human glioblastoma reflects cancer evolutionary dynamics. Proc Natl Acad Sci U S A 110:4009–4014. https://doi.org/10.1073/pnas.1219747110
349. Nemoto EM, Frankel HM (1970) Cerebral oxygenation and metabolism during progressive hyperthermia. Am J Physiol 219:1784–1788. https://doi.org/10.1152/ajplegacy.1970.219.6.1784
350. Eshel G, Safar P, Sassano J, Stezoski W (1990) Hyperthermia-induced cardiac arrest in dogs and monkeys. Resuscitation 20:129–143. https://doi.org/10.1016/0300-9572(90)90048-J
351. Goldie R. E. Boone, Valaparla SK, Ripley EM, Clarke GD (2014) Comparison of N-Acetyl Aspartate and Polyethylene Glycol as Chemical Shift Reference Standards for Proton Magnetic Resonance Spectroscopic Thermometry. In: Proc. Intl. Soc. Mag. Reson. Med. p 3750. https://cds.ismrm.org/protected/14MProceedings/files/3750.pdf
352. Vetten MA, Yah CS, Singh T, Gulumian M (2014) Challenges facing sterilization and depyrogenation of nanoparticles: Effects on structural stability and biomedical applications. Nanomedicine 10:1391–1399. https://doi.org/10.1016/j.nano.2014.03.017
353. Li Y, Liu X, Wei F, et al (2017) An advanced MRI and MRSI data fusion scheme for enhancing unsupervised brain tumor differentiation. Comput Biol Med 81:121–129. https://doi.org/10.1016/j.compbiomed.2016.12.017

11. ANNEXES

ANNEX I:

LABORATORY ANIMALS SUPERVISION

Procedure: CEEAH 530, DMA 2449

MONITORING PARAMETERS (scale: 0-3 points):

Wight loss

0) Normal weight
1) Less than 10% loss
2) Between 10 and 15% loss
3) Consistent or rapid, exceeding 20% loss maintained for 72 h.

Physical appearance

0) Normal
1) More than 10% dehydration, body condition 2 (BC; see further for details), tenting of the skin
2) Piloerection. Cyanosis
3) Hunched back. Loss of muscle mass

Clinical signs

0) None
1) Circular motion of the animal
2) Mucous secretions and/or bleeding from any orifice. Detectable hypertrophy of organs (lymph nodes, spleen, liver).
3) Shortness of breath (particularly if accompanied by nasal discharge and/or cyanosis). Cachexia

Changes in behaviour

0) No
1) Inability to move normally
2) Inability to get food/ drink, isolation from the rest of the animals in the cage
3) Unconsciousness or coma. Lack of response (dying)

Wounds

0) No
1) Scratches
2) Nonhealing wounds. Infection at surgical site
3) Ulcerating, festering wounds. Ulcerating necrotic tumours

The animal condition according to the parameters and overall score:

a) 0 points: Healthy animal
b) 1-2 points: Minor signs, follow stablished protocol
c) 3-11 points: Daily supervision of the animal. Analgesics* or animal euthanization**
d) 12-30 points: euthanization**

*Analgesic: Meloxicam (subcutaneously: 1 mg/kg)

**The *Servei d'Estabulari* veterinary staff will report to a group member as soon as possible to consider halting of the protocol/ experiment.

NOTE: As the tumour grows, it could affect in the motor function of the brain. Animals may suffer from: paresis, decreased strength, plegia, paralysis. In these cases, food and water (i.e. hydrogel or water-soaked food) should be placed inside the cage to facilitate access by the animal.

Body Condition (BC):

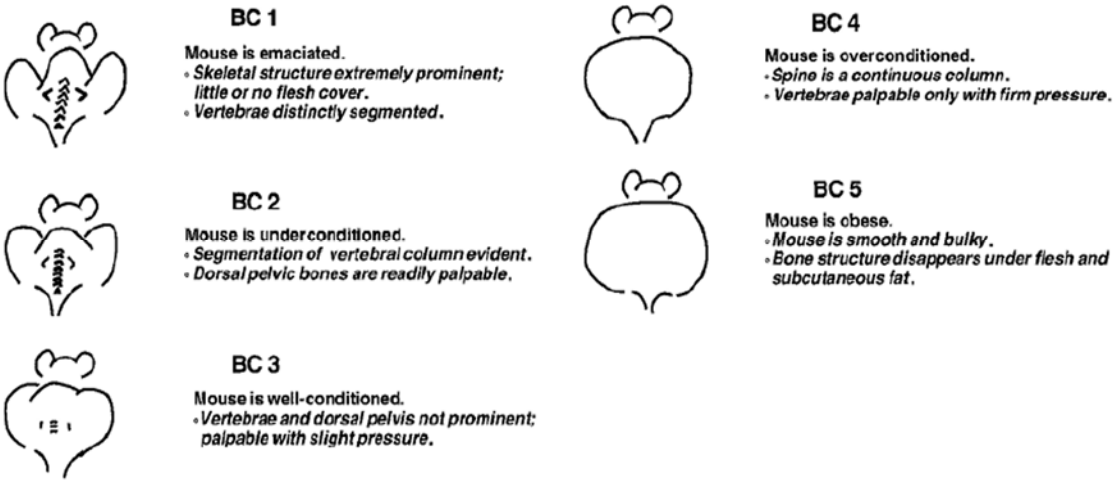

ANNEX II:

Annex II.I:

A. SNR maps for the case C891 (the coloured scale indicates the SNR range). The tumour area is marked by white dashed line.

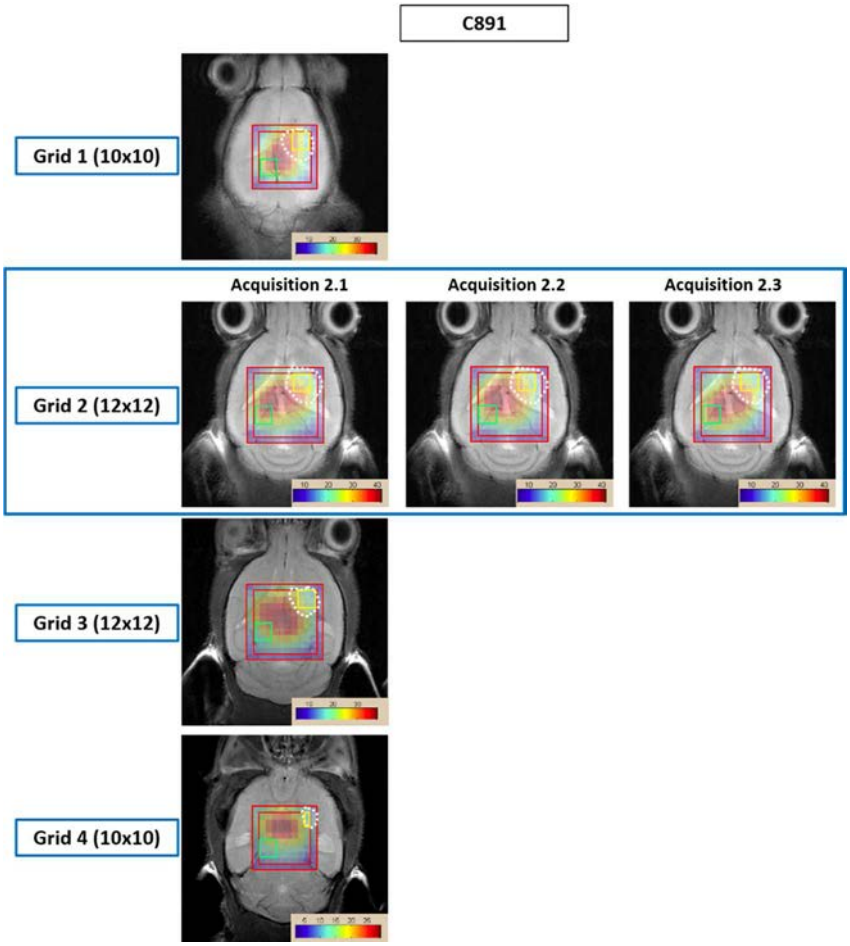

In the case C891, significant differences ($p<0.05$) were observed in the SNR of the voxels from the central part of the grids between Grid 4 (23.0±7.8) and Grids 1 (33.3±8.4), Grid 2 (29.1±8.9) and Grid 3 (30.8±11.7) and also between Grid 1 and Grid 2. No significant differences were observed in this case between Grid 1 and Grid 3 or between Grid 2 and Grid 3. Regarding the SNR from the edges of the grids, significant differences ($p<0.05$) were observed between Grid 1 (19.3±7.7) and Grids 2 (16.0±7.2), Grid 3 (14.6±7.1) and Grid 4 (13.6±6.4) and between Grid 2 and Grid 4. No significant differences were observed between Grids 2 and Grid 3 or between Grid 3 and Grid 4.

B. SNR maps from the case C895 (the coloured scale indicates the SNR range). The tumour area is marked by white dashed line.

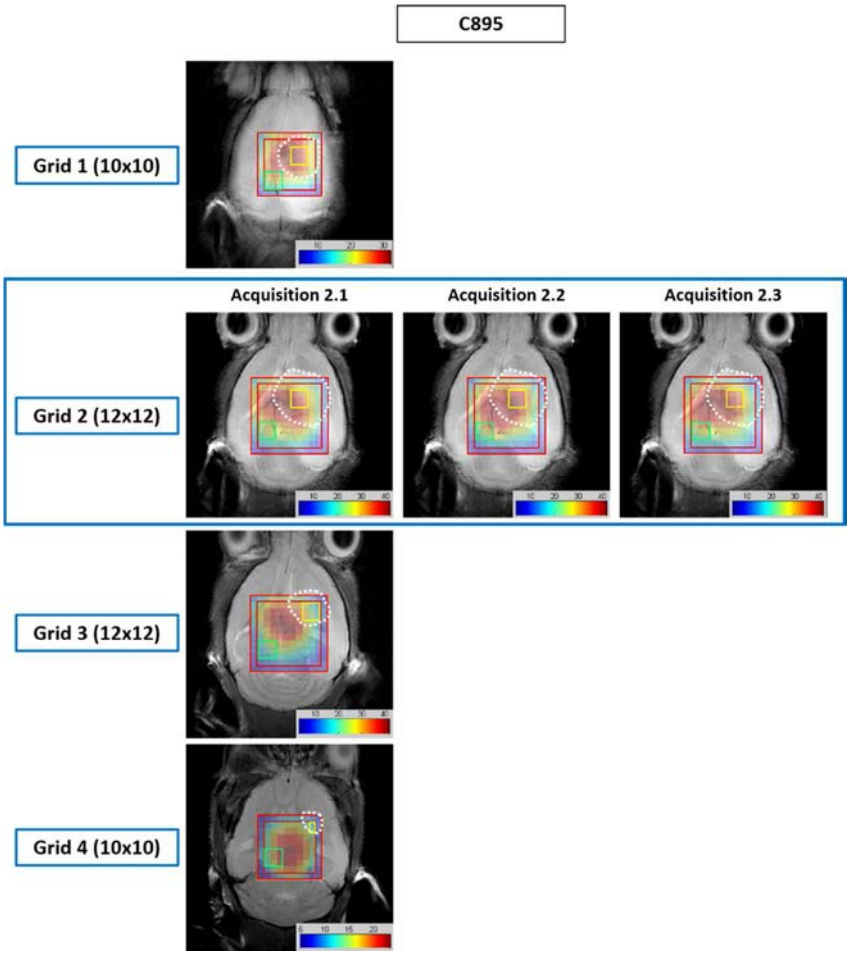

In the case C895, significant differences ($p<0.05$) were observed in the SNR of the voxels from the central part among all grids except between Grid 1 (39.3±11.8) and Grid 2(38.1±15.2), where no significant differences were observed ($p>0.05$). Regarding the SNR from the edges of the grids, significant differences ($p<0.05$) were observed between Grid 1 (22.7±9.9) and Grids 2 (19.8±10.6), Grid 3 (18.5±9.9) and Grid 4 (13.3±3.4) and between Grid 2 and Grid 4. No significant differences ($p>0.05$) were observed between Grids 2 and Grid 3 or between Grid 3 and Grid 4.

Annex II.II:

Mean spectra from tumour and contralateral areas of GL261 tumour-bearing animals. The tumour area is marked by white dashed line.

A: C891

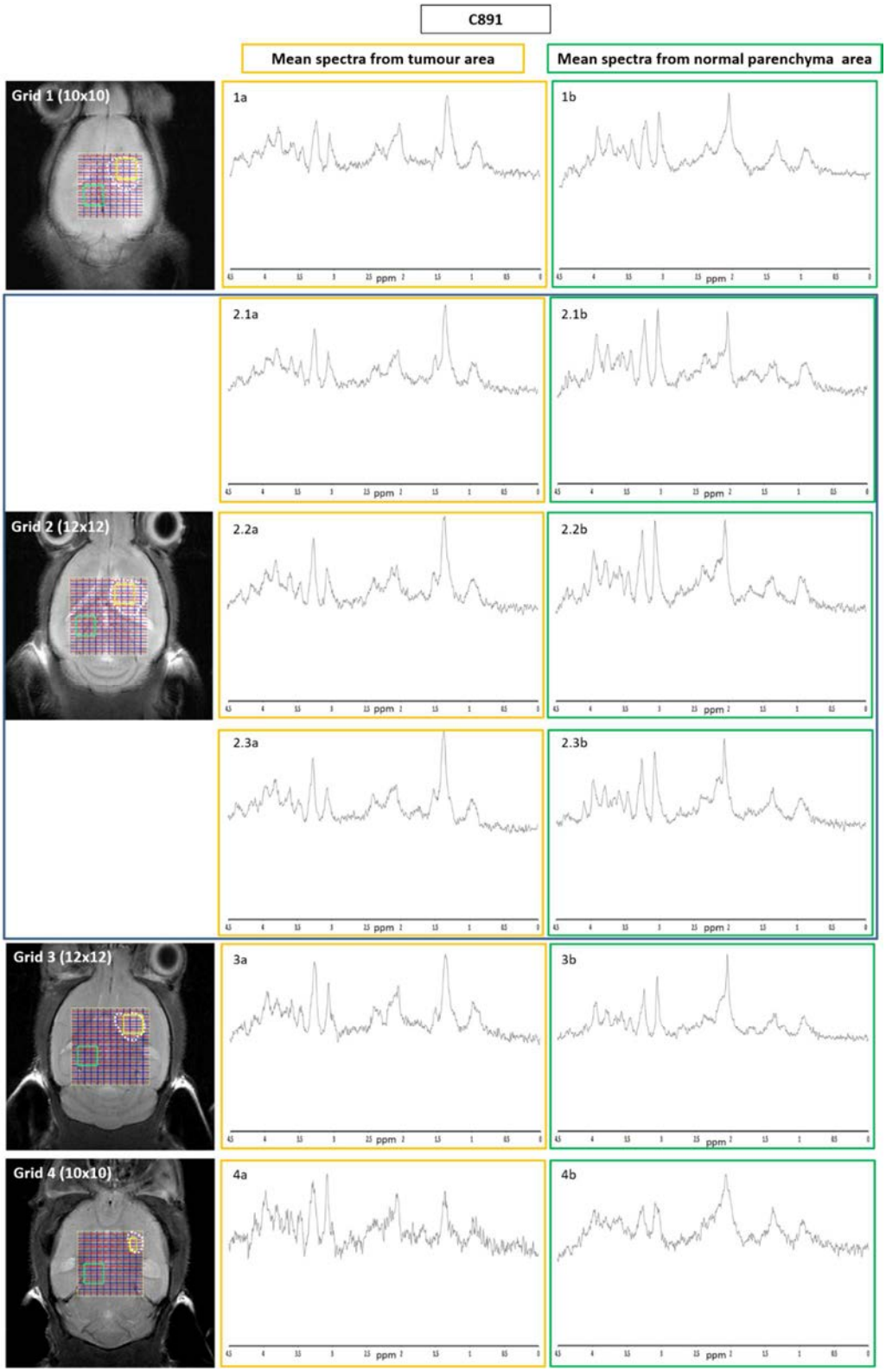

B: C895

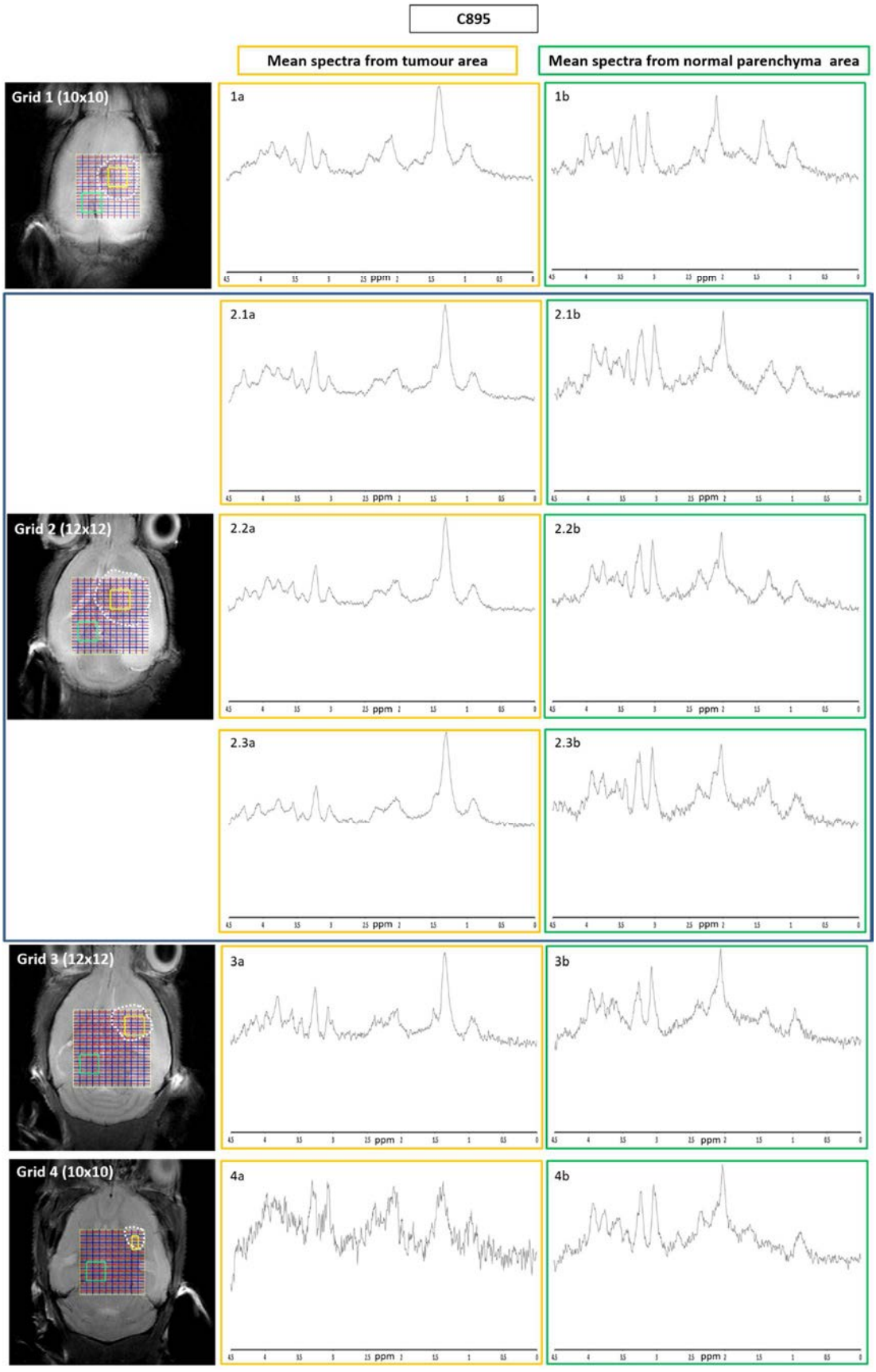
C895
Mean spectra from tumour area
Mean spectra from normal parenchyma area
Grid 1 (10x10)
1a
1b
2.1a
2.1b
Grid 2 (12x12)
2.2a
2.2b
2.3a
2.3b
Grid 3 (12x12)
3a
3b
Grid 4 (10x10)
4a
4b
ppm

Annex II.III:

Unsupervised sources obtained from GL261 tumour-bearing animals. The tumour area is marked by white dashed line and artefacts are pointed by red rectangles.

A: C891

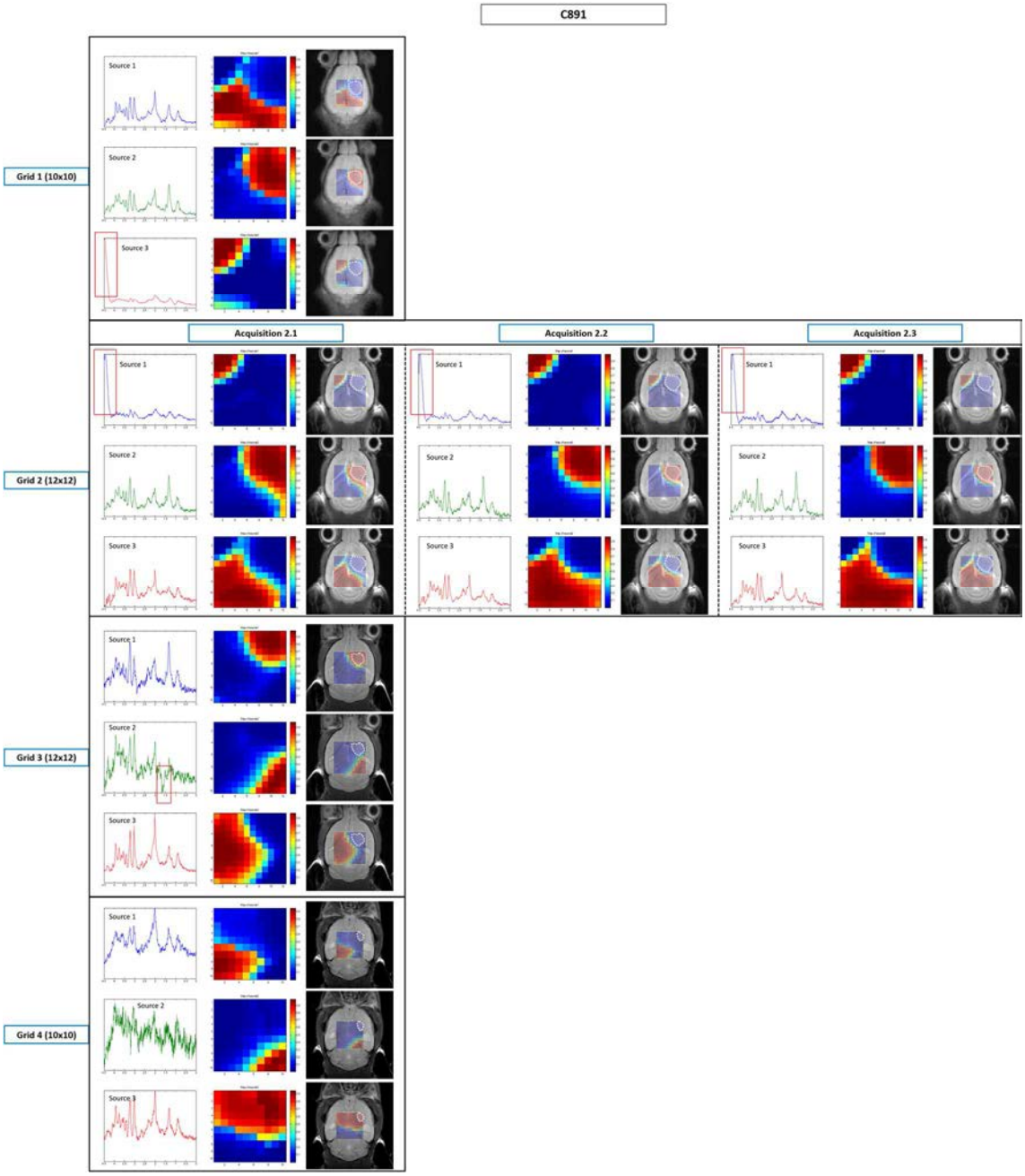

B: C895

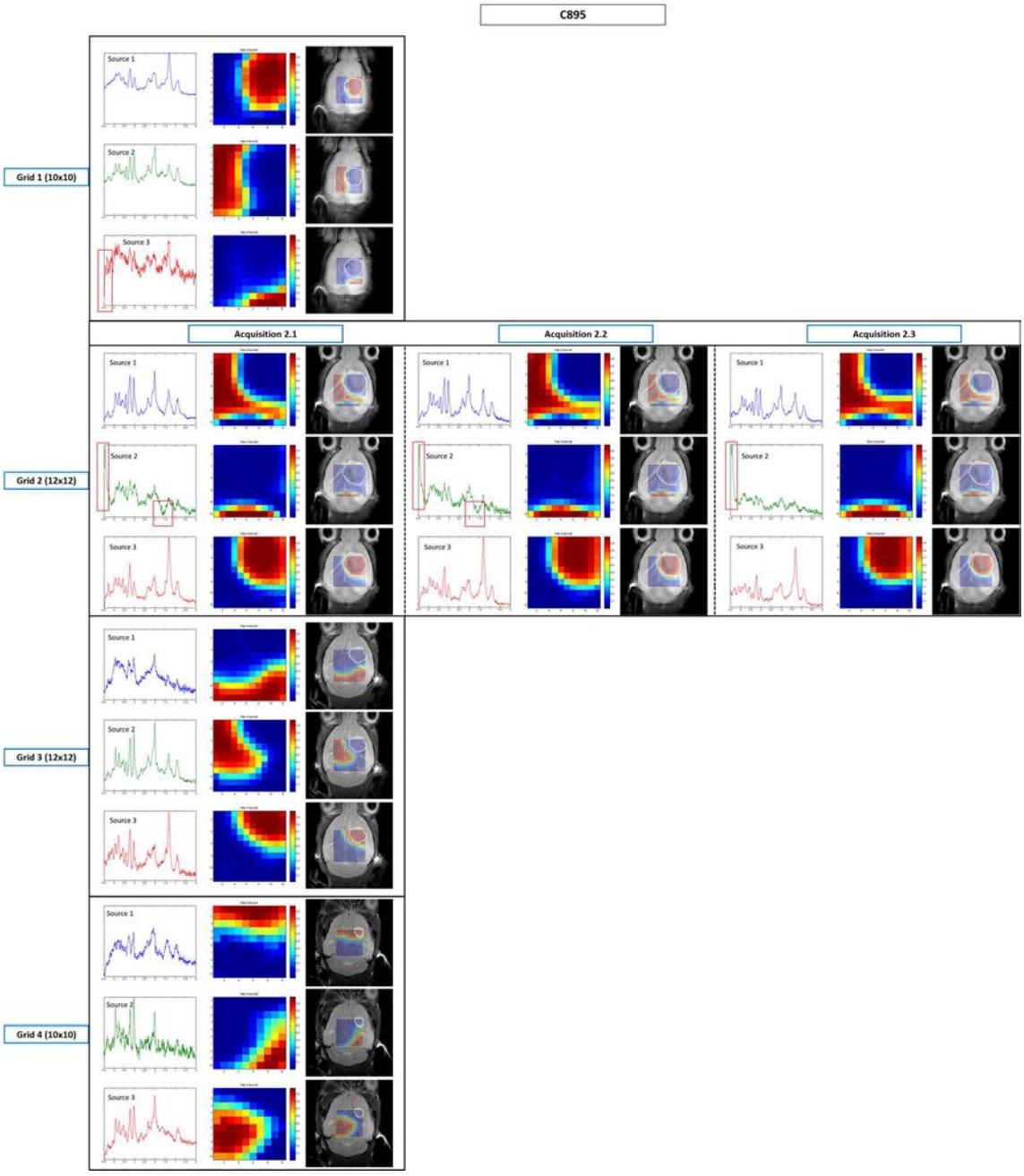
C895
Grid 1 (10x10)
Grid 2 (12x12)
Grid 3 (12x12)
Grid 4 (10x10)
Acquisition 2.1
Acquisition 2.2
Acquisition 2.3
Source 1
Source 2
Source 3

Annex II.IV:

Semi-supervised sources obtained from GL261 tumour-bearing animals, the tumour area is marked by white dashed line.

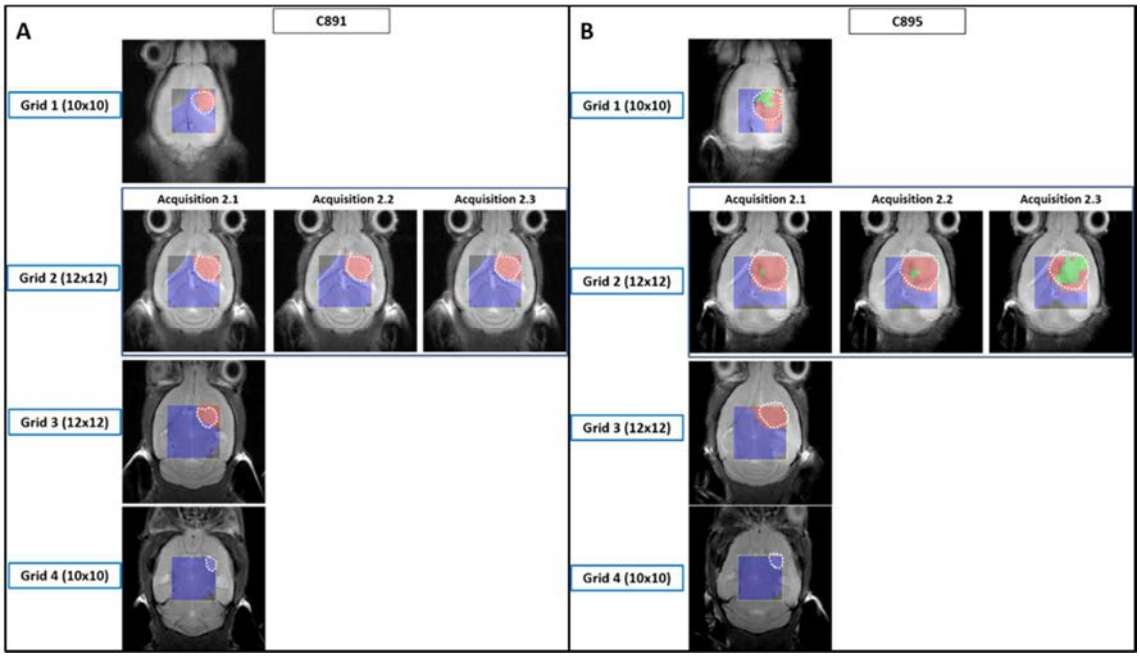

Annex II.V:

Superimposed average spectra of acquisitions 2.1, 2.2 and 2.3 from **A.** C891, **B.** C894 (average spectra from red-tumour pixels in both cases) and **C.** C895 (in this case, image shows average spectra from green-tumour pixels in acquisition 2.3 and pixels from equivalent positions in acquisitions 2.1 and 2.2). Different acquisitions are indicated by different line colours: acquisition 2.1 (green), acquisition 2.2 (red) and acquisition 2.3 (black). The blue rectangle shows a slight difference observed in the spectral pattern of C895 case along the acquisitions.

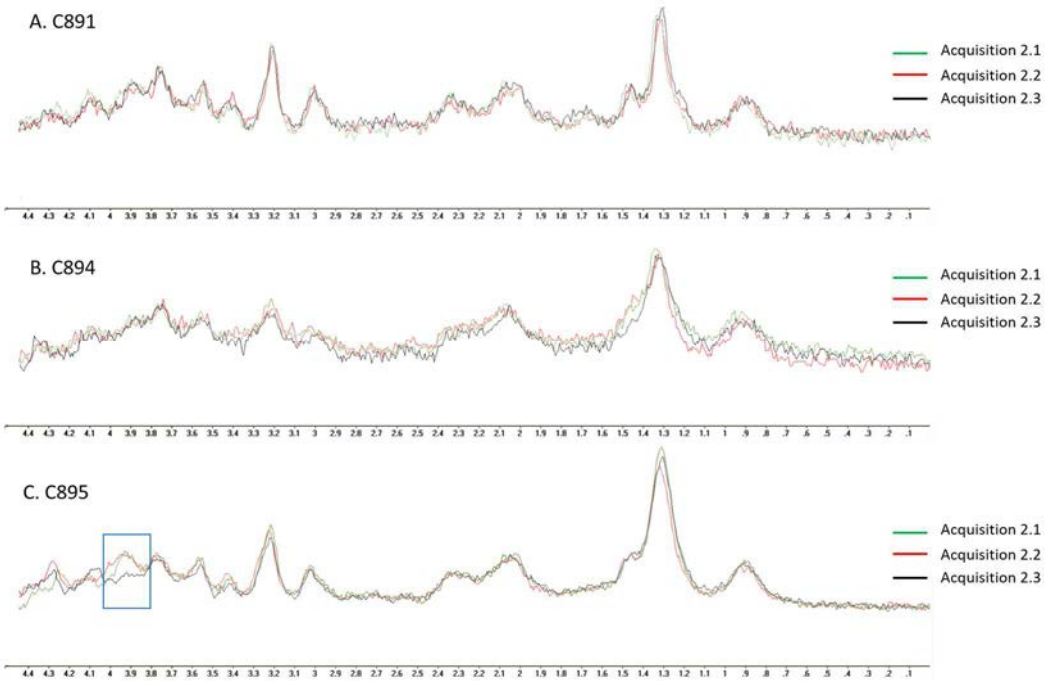

ANNEX III:

Annex III.I:

Adapted RECIST criteria from [124]**.** In [124], the volume is compared to the baseline volume on day 20 p.i., whereas in this study the tumour volume is compared to the tumour volume measured in the previous MRI exploration.

Response category	**Criteria**
Complete response	Total tumour disappearance
Partial response	At least 30% decrease in tumour volume *
Stable disease	Neither sufficient shrinkage nor sufficient increase to qualify for partial response or progressive disease, respectively
Progressive disease	At least 20% increase in tumour volume *

* Response compared to tumour volume measured in the previous MRI exploration

Annex III.II:

Graphical representation of the tumour volume evolution and the percentage of TRI variation in IR cases and the obtained nosological images in the longitudinal study.

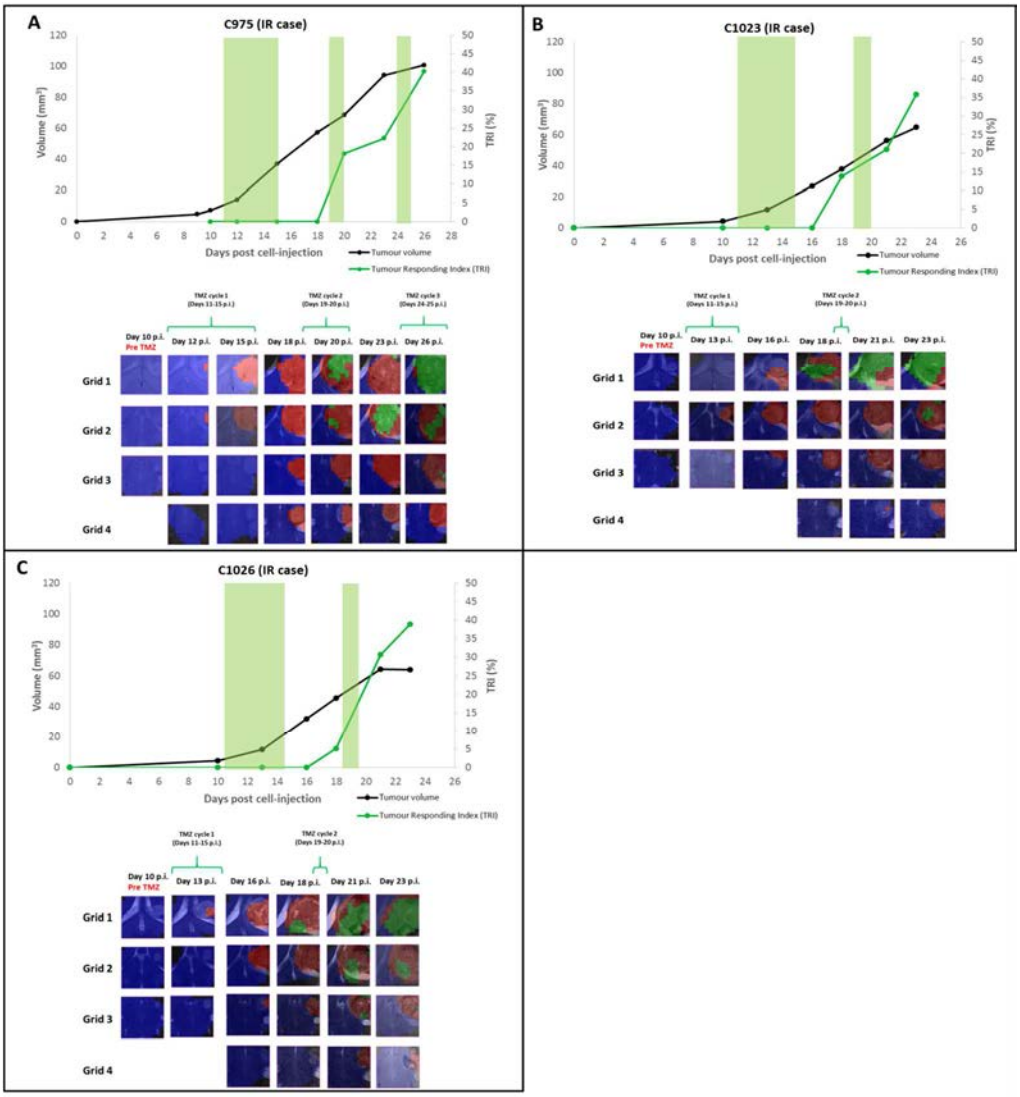

Graphical representation of the tumour volume evolution (in mm3, black line, left axis), and the percentage of TRI (in %, green line, right axis). For chosen time points, the evolution of the nosological images obtained with the semisupervised source extraction system is shown overlaid over T2w-MRI for each slice. The green shaded columns and the keys on top of the nosological images columns indicate TMZ administration periods. A. Corresponds to the IR case C975, green pixels were observed first in grid 1 and a few in grid 2 at day 20 p.i. At day 23 p.i., green pixels were observed only in grid 2 and at day 26 p.i., green pixels were observed in grids 1 and 2 with a TRI = 40.3%. Tumour volume variation meeting criteria for 'stable disease' according to adapted RECIST was observed from day 23 to 26 p.i. B. Corresponds to the IR case C1023, green pixels were observed in grid 1 at days 18 and 21 p.i., at day 23 p.i. green pixels were observed in grids 1 and 2 (TRI = 35.8%), this TRI increase coincides with the possible beginning of a stable disease stage (volume increase with respect to preceding observation of 15.1%). C. Corresponds to the IR case C1026, with an evolution similar to the C1023 case, green pixels were observed only in grid 1 at day 18 p.i. while green pixels were observed in grids 1 and 2 at days 21 and 23 p.i. (TRI = 38.9%, at day 23 p.i.). From day 21 to 23 p.i., the beginning of a stable disease stage was also observed.

Annex III.III:

Comparison of responding/non responding spectral patterns with expansions in some differential zones with tentative metabolite assignment as in Figure 6.8 and Table 6.2:

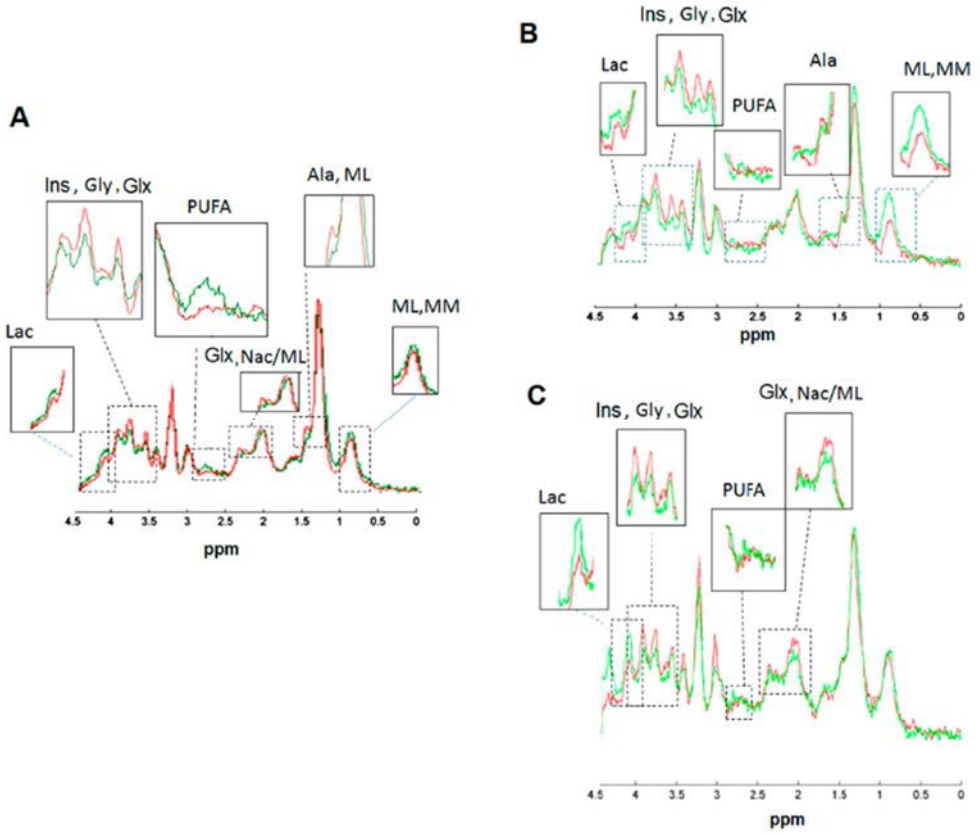

A. Prototypical patterns (sources) extracted from TMZ treated (green) and untreated (read) tumour-bearing mice as described in [116]. B. Superimposition of average spectra from an untreated case (n = 44, red voxels, C1112 day 13 p.i., grid 2) and a treated case (n = 32, green voxels, C1108 day 29 p.i., grid 1). C. Superimposition of average spectra from the zones classified either as non-responding (n = 35, red) or responding (n=26) from mouse C971, an IR case. ML, MM: mobile lipids + macromolecules; Ala, ML: alanine + mobile lipids; NAc/ML: N-acetyl containing compounds + mobile lipids; PUFA: polyunsaturated fatty acids in mobile lipids; Glx, glutamine + glutamate; Gly: glycine (glycine signal is also contributed by myoinositol, Ins); Lac: lactate. Tentative resonance assignment according to [89, 111, 267, 347, 115, 140, 261–266].

Annex III.IV:

Ki67 immunostainings in histological areas corresponding to red or green regions in nosological images, from different grids of chosen cases.

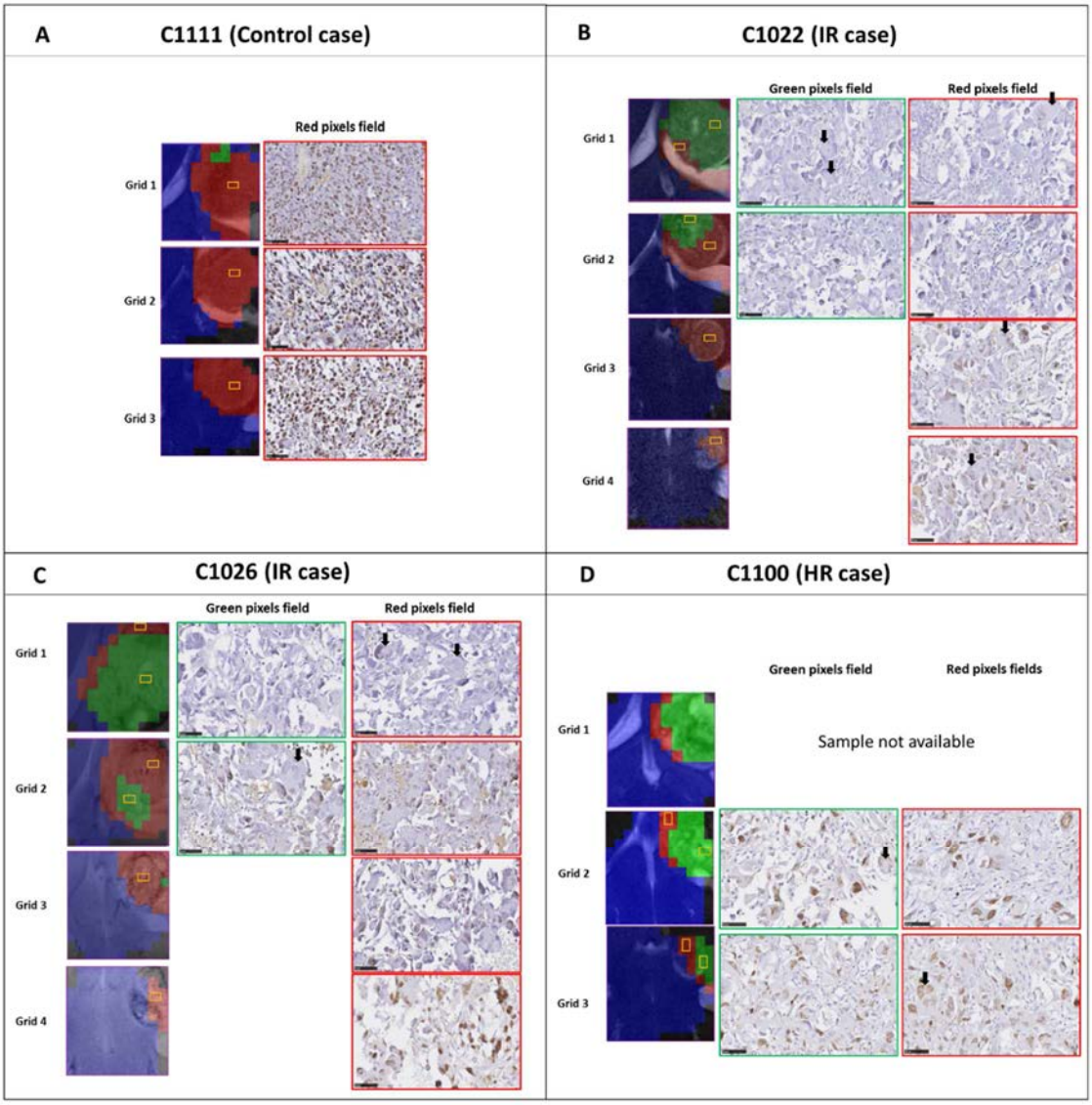

Ki67 immunostainings (40× magnification, the scale bar corresponds to 50 µm) in histological areas corresponding to red or green regions in nosological images, from different grids of chosen cases. The nuclei of Ki67 positive cells are stained in brown. **A.** Control case C1111, with a global Ki67 of 73.3 ± 6.4% and a typical tumour morphology, with small to medium-sized polygonal or irregular cells with rounded nuclei and scanty cytoplasm without any giant cells. **B.** IR case C1022, presented lower Ki67 immunostaining (42.5 ± 33.5%) than control and LR cases, with presence of giant cells with several nuclei (black arrows), and acellular spaces. **C.** IR case C1026, presented as well as in case C1022 with lower Ki67 immunostaining (66.0 ± 39.1%) than control and LR cases, and presence of giant cells (black arrows), and acellular spaces. **D.** HR case C1100, with a higher value of Ki67 (82.2 ± 7.7%) compared to control, LR and IR cases, although large acellular spaces among cells and giant cells (black arrows) were observed. In this case, no histopathological evaluation could be performed from the first grid.

Annex III.V:

Graphical representation of the tumour volume evolution and the percentage of TRI variation of a retrospective longitudinal study of response to TMZ therapy by single-slice MRSI approach. Nosological images obtained in the study are also shown. See Figure 6.5 legend for further details.

A: C819

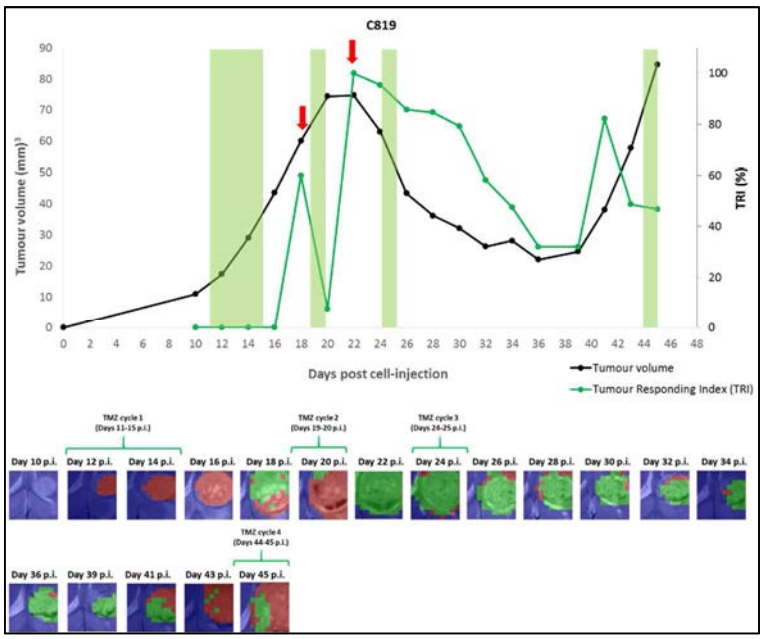

B: C821

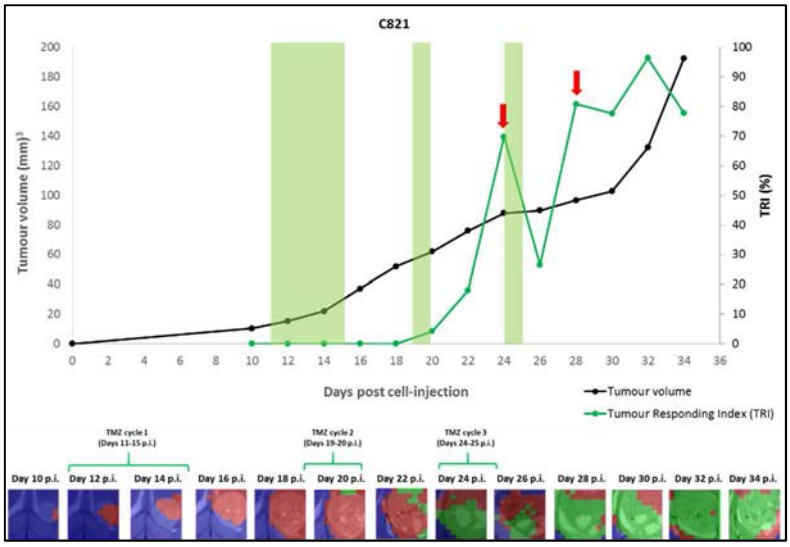

ANNEX IV:

Annex IV.I:

Transmission electron microscopy (TEM) photographs of Gold NPs used in this section. **A:** Non-PEGylated Hollow Gold Nanospheres (Adapted from [296]). **B:** PEGylated Hollow Gold Nanospheres (Adapted from [297]). **C:** PEGylated Gold Nanorods (Adapted from [298]).

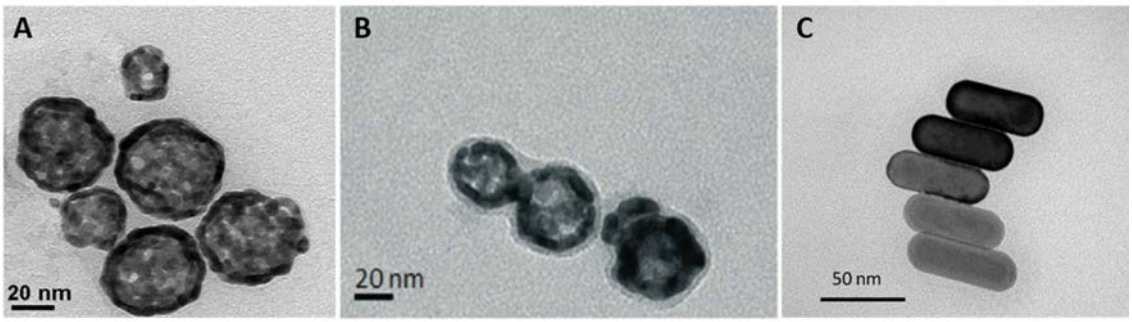

Annex IV.II:

NIR absorbance spectrum of NPs used in the range of interest, around 800 nm. **A:** Non-PEGylated Hollow Gold Nanospheres (Adapted from [296]). **B:** PEGylated Hollow Gold Nanospheres (Adapted from [297]). **C:** PEGylated Gold Nanorods, an additional absorbance peak due to the transverse plasmon band, is observed around 570 nm (Adapted from [298]).

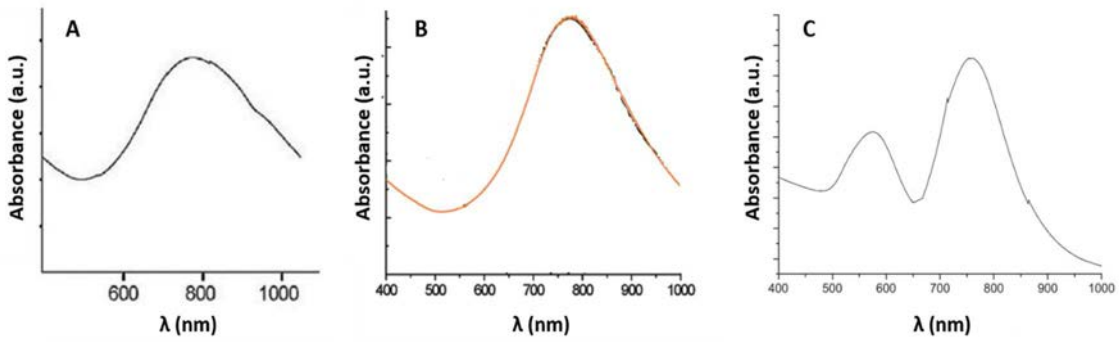

Annex IV.III:

Summary of non-lethal mean temperature slopes calculated in the hyperthermia (*in vivo*) experiments.

Conditions studied	Irradiation Protocol	Nanoparticle administering/ route/ dose	Administration schedule	Mean Temperature slope value
Continuous laser irradiation:				
1 injection with non-PEG HGNPs GL261 (n=2)	Continuous laser irradiation 0.07W (Described in Figure 7.4)	Yes/i.v./ 2.8 mg Au/kg	24h before irradiation	0.16
1 injection with non-PEG HGNPs GL261 (n=2)	Continuous laser irradiation 0.28W (Described in Figure 7.4)	Yes/i.v./ 2.8 mg Au/kg	24h before irradiation	0.37
2 injections with non-PEG HGNPs GL261 (n=2)	Continuous laser irradiation 0.07W (Described in Figure 7.4)	Yes/i.v./ 2.8 mg Au/kg	72h and 24h before irradiation	0.13
2 injections with non-PEG HGNPs GL261 (n=2)	Continuous laser irradiation 0.28W (Described in Figure 7.4 in section 7.2.16.2)	Yes/i.v./ 2.8 mg Au/kg	72h and 24h before irradiation	0.30
GL261 (n=3)	Stepwise power increase approach (Described in section 7.2.16.2)	No	NA	0.08±0.02
wt (n=3)	Stepwise power increase approach (Described in section 7.2.16.2)	No	NA	0.06±0.02
1 injection of PEG-HGNPs, wt35 (n=1)	Stepwise power increase approach (Described in section 7.2.16.2)	Yes/stereotactical/ 20 mg Au/kg	Immediately prior to irradiation	0.24
1 injection of PEG-HGNPs, wt36 (n=1)	Stepwise power increase approach (Described in section 7.2.16.2)	Yes/stereotactical/ 20 mg Au/kg	Immediately prior to irradiation	0.12
Pulsed laser irradiation:				
(wt n=3)	Pulsed laser irradiation, protocol described in section 7.2.16.3	No	NA	0.05±0.02

Annex IV.IV:

Histopathology report summary from necropsy of mice found dead during the PEG-HGNPs tolerability study of section 7.3.2.2.

Macroscopic injuries:

In general, the organs of the studied animals showed dark coloration and soft consistency.

- Animals injected with a dose of 135 mg Au/kg (n=2): the brain of one mouse showed dark parenchyma alternating with pale areas. Transversal sections showed a multifocal dark dotted pattern in the white matter. The other mouse did not show macroscopic changes.
- Animal injected with a dose of 67.5 mg Au/kg (n=1): the chest cavity showed accumulation of a white coloured liquid. No further macroscopic alterations were observed.

Microscopic injuries:

- Animals injected with a dose of 135 mg Au/kg: in one of the animals, the medium sized vessels and capillaries of the brain were enlarged and multifocal extravasation of erythrocytes was observed. This mouse showed dilated sinusoids in the liver parenchyma which were filled with blood cells. Some hepatocytes presented intracytoplasmic brown pigment. The kidneys of the second animal showed interstitial bacterial colonies and intratubular amorphous eosinophilic material. Both animals showed a granular, non-aggregated, brown material inside the sarcoplasm of the cardiocytes (myocytes), and coccoid bacteria were also observed among these fibres.
- The animal injected with a dose of 67.5 mg/Au showed a collapse of most alveolar spaces. The remaining alveolar spaces either presented an acellular amorphous eosinophilic material or were widely dilated.
- The remaining studied organs did not show significant microscopic alterations.

Diagnosis:

A diffuse brain congestion with multifocal haemorrhage. Unspecific cardiopathy and hepatopathy with accumulation of amorphous material. Alveolar collapse, lung oedema with compensatory alveolar emphysema.

The material observed at the cardiocytes may suggest an accumulation of substances associated to PEG-HGNPs due to absence of inflammatory reaction. Nevertheless, it was not possible to identify this accumulated material.

The presence of bacteria in different organs is probably due to *post-mortem* autolysis.

Annex IV.V:

Oxygen and air anaesthesia system for safe hyperthermia experiments using laser irradiation inside the MR scanner:

The new devices incorporated to perform anaesthesia with sterile air instead of oxygen are marked in red squares. **A.** Air conduct. **B.** Double flowmeter for oxygen and air. **C.** Filtration system from the air conduct to the MR magnet.